



Technische Universität München
Fakultät für Luftfahrt, Raumfahrt und Geodäsie
Lehrstuhl für Astronomische und Physikalische Geodäsie

Multi-sensor data fusion for terrestrial 3D-gravity profiling

Peter Wolfgang Schack

Vollständiger Abdruck der von der Fakultät für Luftfahrt, Raumfahrt und Geodäsie der Technischen Universität München zur Erlangung des akademischen Grades eines

Doktor-Ingenieurs (Dr.-Ing.)

genehmigten Dissertation.

Vorsitzender: Prof. Dr. rer. nat. Thomas H. Kolbe
Prüfende der Dissertation: Prof. Dr. techn. Roland Pail
Prof. Dr.-Ing. Matthias Becker
Prof. Dr.-Ing. habil. Thomas Wunderlich

Die Dissertation wurde am 19.01.2021 bei der Technischen Universität München eingereicht und durch die Fakultät für Luftfahrt, Raumfahrt und Geodäsie am 09.03.2021 angenommen.

Abstract

Based on recent developments in moving-base gravimetry utilizing navigation-grade inertial measurement units for gravity field determination, this thesis demonstrates that with today's technical standards it is possible to observe the gravity disturbance vector with high accuracy from a moving car, even through villages and forest sections. Car-based observations allow determining gravity directly on the Earth's surface (no effect of upward continuation), trajectories can be recorded repeatedly for redundancy, and update measurements can be implemented as desired. Reaching root-mean-square errors of 1.5 mGal for the scalar gravity disturbance and 0.2 - 0.5'' for the vertical deflections at a spatial resolution of ~ 200 m (w.r.t. accurate reference data), terrestrial 3D-gravity profiling is a fast, simple and robust way to gain and validate local gravity information of high quality.

In this thesis, modern geodetic equipment is applied to collect accurate astronomical, physical, and geometrical information. The digital astrogeodetic QDaedalus system is capable of quantifying the angular difference between the direction of normal gravity on the ellipsoid and inherent gravity on the Earth's surface with a standard deviation of $\pm 0.2''$. The absolute value of gravity is determined with the Scintrex CG-5 relative gravimeter in combination with an official absolute gravity tie point of the Federal Agency for Cartography and Geodesy. The short-time Scintrex CG-5 observations, conducted right after stopping the car during a terrestrial 3D-gravity profiling campaign, reveal a standard deviation of ± 0.1 mGal. Global Navigation Satellite System (GNSS) devices track American, Russian, European, and Chinese navigation satellites on multiple frequencies. The GNSS setup allows kinematic differential positioning of the car with standard deviations in the centimeter range. The equipment is completed with the iMAR iNAV-RQH inertial measurement unit (RQH), which is equipped with ring laser gyroscopes and pendulous rebalancing accelerometers. It accurately registers the specific force during the car ride including its orientation.

The determination of the gravity disturbance vector is realized by fusing all the sensor data, which are collected either point by point (QDaedalus, Scintrex CG-5) or continuously (GNSS, RQH) along a trajectory, by means of an Extended Kalman Filter in combination with the Rauch-Tung-Striebel smoother.

In the frame of this thesis, three different campaigns have been performed, which are all linked to terrestrial 3D-gravity profiling. A field campaign, conducted in Australia, exemplifies the quick and accurate application of QDaedalus for the determination of vertical deflections as well as its value for the assessment of gravity field models. Then, RQH measurements recorded in different orientations inside a temperature chamber provide insights into the integrated inertial sensors' temperature behavior, which is known to be a driving error component for strapdown gravimetry. Lastly, a dedicated terrestrial 3D-gravity profiling campaign in the Bavarian Estergebirge is realized and assessed to reveal the concept's accuracy potential.

Kurzfassung

Die Entwicklungen der letzten Jahre im Bereich der Flug- und Schiffsgravimetrie waren unter anderem durch den erfolgreichen Einsatz von Inertialmesseinheiten der Navigationsgütekategorie geprägt. Die folgende Arbeit zeigt, dass es mit den heutigen technischen Standards möglich ist, die Schwere störung dreidimensional mit hoher Genauigkeit während einer Autofahrt mit diesen Instrumenten zu bestimmen, ohne dabei Dorfdurchfahrten und Waldabschnitte meiden zu müssen. Fahrzeugbasierte Messungen erlauben es, die Schwere auf der Erdoberfläche zu beobachten (ohne Feldfortsetzung), Trajektorien mehrmals aufzuzeichnen, um redundante Datensätze zu erzeugen und sogenannte Updatemessungen nach Belieben durchzuführen. Mit „root-mean-square“ Ungenauigkeiten von 1.5 mGal für die skalare Schwere störung und 0.2 - 0.5'' für die Lotabweichungen bei einer räumlichen Auflösung von ~200 m (bezüglich genauer Referenzdaten), stellt „terrestrial 3D-gravity profiling“ eine schnelle, einfache und robuste Variante dar, lokale Schwerefeldinformationen zu generieren und zu validieren. In dieser Arbeit kommen moderne geodätische Instrumente zum Einsatz, mit denen akkurate astronomische, physikalische und geometrische Daten gemessen werden. Das digitale, astrogeodätische QDaedalus System beobachtet die Winkeldifferenz zwischen der Normalschwererichtung auf dem Ellipsoid und der Richtung der wahren Schwere auf der Erdoberfläche mit einer Standardabweichung von $\pm 0.2''$. Die absolute Schwere wird durch Relativgravimetermessungen mit einem Scintrex CG-5 in Kombination mit einem offiziellen Absolutschwerpunkt des Bundesamtes für Kartographie und Geodäsie bestimmt. Die Kurzzeitbeobachtungen des Scintrex CG-5, die während einer Kampagne direkt nach dem Anhalten durchgeführt werden, weisen eine Standardabweichung von ± 0.1 mGal auf. Die Global Navigation Satellite System (GNSS) Mehrfrequenzempfänger nutzen amerikanische, russische, europäische und chinesische Navigationssatelliten. Damit werden bei kinematischen, differenziellen Beobachtungen Positionsgenauigkeiten im Zentimeterbereich realisiert. Die iMAR iNAV-RQH Inertialmesseinheit (RQH) vervollständigt das Instrumentarium. Sie ist mit Ringlasern und Pendelakzelerometern ausgestattet, die in der Lage sind, die spezifische Kraft inklusive deren Richtung genau zu registrieren.

Die Bestimmung des Vektors der Schwere störung wird über die Fusion aller Sensordaten gewährleistet. Die Sensordaten werden entweder punktweise (QDaedalus, Scintrex CG-5) oder kontinuierlich (GNSS, RQH) entlang einer Trajektorie aufgezeichnet. Die Fusion wird anhand eines erweiterten Kalman-Filters mit anschließender Rauch-Tung-Striebel-Glättung umgesetzt.

Im Rahmen dieser Arbeit wurden drei unterschiedliche Kampagnen durchgeführt, die zur Realisierung von „terrestrial 3D-gravity profiling“ beitragen. Eine Feldstudie in Australien zeigt die schnelle und einfache Anwendung des QDaedalus Systems zur präzisen Lotabweichungsbestimmung sowie dessen Eignung zur Validierung von Schwere modellen. Des Weiteren werden RQH Messungen in unterschiedlichen Orientierungen in einer Temperaturkammer ausgewertet, um das Temperaturverhalten der verbauten Inertialsensoren zu bestimmen, das bekannterweise einen großen Einfluss auf deren Messgrößen hat. Zuletzt wird eine „terrestrial 3D-gravity profiling“-Kampagne im bayerischen Estergebirge realisiert und ausgewertet, um das Genauigkeitspotenzial dieses Beobachtungs- und Auswertekonzepts zu analysieren.

Acknowledgements

First of all, I want to acknowledge that during the past nine years at the Institute of Astronomical and Physical Geodesy, as a tutor, student assistant, research associate, and Ph.D. student, Prof. Roland Pail and Dr. Thomas Gruber gave me great opportunities to gather experience in many different subject areas. I really appreciate the freedom I had to define my research topic, and I am thankful for the permanent support and guidance from your side throughout this time. Due to the pleasant working atmosphere at the institute and the esteemed colleagues, I enjoyed coming to the office every day.

Special thanks to Prof. Matthias Becker and Prof. Thomas Wunderlich for joining the examination board and to Prof. Thomas Kolbe for chairing my defense.

I want to thank Dr. Christian Gerlach for mentoring me during the last four years. I always enjoyed talking with you about scientific topics. The constructive, detailed feedback and discussions during that time helped a lot to extend my knowledge and to finish this thesis successfully. Furthermore, I highly regard the continuous support of Dr. Anja Schlicht and Dr. Christian Hirt. You were always available for discussions and provided valuable information at any time I needed it.

Without the help of Dr. David Becker and Dr. Tim Jensen, the completion of the thesis would not have been possible in this way. I really enjoyed working with you, and I am very thankful that you were always open to questions. I benefited a lot from your knowledge, your experience, and your cooperativeness.

The calibrations of the inertial measurement unit could only be realized with the support of Mr. v. Hinüber, Mr. Petry and again Dr. David Becker, who granted access to the calibration facility at iMAR Navigation & Control, performed the calibrations and implemented the procedures for the turntables. I highly appreciate your efforts.

The astrogeodetic campaign in Perth, Western Australia, was one of the highlights of my time as a Ph.D. student. I want to thank Dr. Christian Hirt for initiating the DAAD project, as well as Markus Hauk, Prof. Will Featherstone, and Todd Lyon for the enjoyable teamwork.

In this respect, many thanks to 1) DAAD (German Academic Exchange Service) and Universities Australia for funding the Perth project, 2) Jo Jensen of C. R. Kennedy, Perth, for providing a back-up total station, 3) DFG (German Research Foundation) grant Hi1760/1, and 4) Scripps Institution of Oceanography (University of California), the US National Oceanographic and Atmospheric Administration and the National Geospatial-Intelligence Agency for permission to use the marine gravity anomalies from Sandwell et al. (2014).

I appreciate the endeavors of the "Bayerische Staatsforsten, Forstbetrieb Bad Tölz", the "Passamt - Markt Mittenwald" and the "Gemeinde Krün" for granting permission to access roads with restricted admission in the Estergebirge between Walchensee and the Austrian border.

Moreover, I want to thank Prof. Jakob Flury and Dr. Joachim Schwabe for providing valuable data sets, which are an integral part of this thesis.

Finally, I want to point out that the strong support of my wife Corina helped essentially to finish this work. I am very thankful and happy to have her on my side. I also want to thank my parents and my sister for their encouragement from my childhood until today.

Remarks

- This work is simultaneously published by the Committee for Geodesy, formerly German Geodetic Commission, listed as No. 880 in Series C: Dissertations¹ (ISBN: 978-3-7696-5292-5).
- Text passages, figures, and tables in Ch. 1.2.1, Ch. 2.3.4, and Ch. 4.1 are closely related to or identical to the peer-reviewed publication Schack et al. (2018) (original work). For clarification, the content of these chapters will be highlighted by italic letters.
In this paper, the results of a new vertical deflection traverse observed in Perth, Western Australia, are presented. The author's contribution to the paper comprises:
 - Campaign design, preparation and organization: 25 %
 - Measurement campaign and computations: 33 %
 - Analysis and interpretation: 25 %
 - Text, figures and tables: 25 %

All co-authors confirmed the percentages of my contribution (see Ch. B) and agreed that the content of the mentioned paper can be included in this thesis.

- In the field of geodesy, the two terms "precision" and "accuracy" have different meanings. While precision describes the consistency between similar observations without having an absolute character, the term accuracy describes the agreement of observations with a true value. In this work, the two inherent adjectives "precise" and "accurate" will be used synonymously, implicating high quality in general.
- The digital astrogeodetic QDaedalus system, introduced in Ch. 2.2.3, differs from known realizations of zenith cameras. Nevertheless, it is called a zenith camera throughout this work, since it determines identical quantities.

¹<https://dgk.badw.de/publikationen/reihe-c-dissertationen.html>

Contents

Abstract	3
Kurzfassung	4
Acknowledgements and remarks	5
Acronyms	9
Notation	11
1 Introduction	13
1.1 Gravity determination	13
1.2 Related work	14
1.2.1 Astrogeodetic observations	14
1.2.2 Strapdown systems	15
1.3 Motivation, innovation and outline	15
2 Theoretical foundations	17
2.1 Position and orientation	17
2.1.1 Coordinates and frames	17
2.1.2 Attitude representations and derivatives	18
2.2 Instruments and measuring concepts	22
2.2.1 Inertial measurement unit	22
2.2.1.1 Inertial sensors	24
2.2.1.2 Static RQH performance	25
2.2.2 GNSS receivers	27
2.2.3 Zenith camera	28
2.2.4 Relative gravimeter	29
2.3 Gravity disturbance and height anomaly differences	30
2.3.1 Gravity potential and acceleration	31
2.3.2 Disturbing potential	32
2.3.3 Vertical deflections and scalar gravity disturbance	33
2.3.4 Astronomical leveling	34
2.4 Multi-sensor data fusion	35
2.4.1 Linearization and error-state concept	35
2.4.2 Extended Kalman Filter	37
2.4.3 RTS smoother	38
3 Terrestrial 3D-gravity profiling	39
3.1 Implementation details	40
3.1.1 Strapdown navigation	42
3.1.2 Error propagation derivation	43
3.1.3 Kalman Filter setup	51
3.2 Profile refinement	55

4 Campaign analyses	57
4.1 Digital astrogeodetic traverse in Perth	58
4.2 Assessment of RQH calibrations	68
4.2.1 Up and Down analyses	68
4.2.2 Roll and pitch dependencies	76
4.2.3 Strapdown rotation test	80
4.3 Terrestrial 3D-gravity profiling in the Bavarian Alps	87
4.3.1 Geodetic test region Estergebirge	88
4.3.2 Campaign database	90
4.3.3 Gravity extraction	97
4.3.3.1 Accuracy assessment	99
4.3.3.2 3D-gravity disturbance profiles	100
4.3.3.3 Crucial components	110
5 Summary and conclusion	115
5.1 Summary	115
5.2 Conclusion	116
6 Outlook	119
A Appendix	123
B Co-author confirmations	127
List of figures	133
List of tables	137
Bibliography	139

Index of acronyms

AGQG	Australian Gravimetric Quasigeoid
BDS	BeiDou Navigation Satellite System
BKG	Federal Agency for Cartography and Geodesy
BM	benchmark
CCD	charged coupled device
CHAMP	Challenging Minisatellite Payload
CUPT	coordinate update
DCM	direction cosine matrix
DEM	digital elevation model
DGNSS	differential GNSS
ECEF	Earth-centered, Earth-fixed
EGM2008	Earth Gravitational Model 2008
EGM2020	Earth Gravitational Model 2020
EKF	Extended Kalman Filter
ENU	East-North-Up
FLU	Front-Left-Up
GAL	Galileo
GDA94	Geocentric Datum of Australia 1994
GGMplus	Global Gravity Model plus
GLO	Globalnaja nawigazionnaja sputnikowaja sistema
GNSS	Global Navigation Satellite Systems
GOCE	Gravity field and steady-state Ocean Circulation Explorer
GPS	Global Positioning System
GPS SOW	GPS time seconds of week
GRACE	Gravity Recovery And Climate Experiment
GRACE-FO	Gravity Recovery And Climate Experiment Follow-On
GRS80	Geodetic Reference System 1980
GUPT	gravity update
HOT	higher order terms
IAPG	Institute of Astronomical and Physical Geodesy
ICRF	International Celestial Reference Frame
IERS	International Earth Rotation and Reference Systems Service
iMAR	iMAR Navigation & Control
IMU	inertial measurement unit
INS	inertial navigation system
ISA	inertial sensor assembly
ITRF	International Terrestrial Reference Frame
MARS	mean angular rate sensor axes
NMEA	National Marine Electronics Association

PDOP	Positional Dilution of Precision
PPP	precise point positioning
PPS	pulse per second
PVT	position-velocity-time
RCR	remove-compute-restore
RINEX	Receiver Independent Exchange Format
RMS	root-mean-square
RQH	iMAR navigation-grade inertial measurement unit
RTM	residual terrain modeling
RTS	Rauch-Tung-Striebel
SAA	small angle approximation
SAPOS	Satellitenpositionierungsdienst
SGD	scalar gravity disturbance
SOW	seconds of week
SRTM	Shuttle Radar Topography Mission
TUM	Technical University of Munich
VD	vertical deflection
VUPT	velocity update
WGS84	World Geodetic System 1984
ZGUPT	zero gravity gradient update
ZUPT	zero velocity update

Notation

The list is separated into scalars, vectors and matrices.
Notations can appear in combination, e.g., scalar: $\bar{a}_{[bc,d]}$.

SCALAR

a, γ, A, Γ	general representations of a scalar or a function
a^b	a expressed in the b-frame
$a_{[b]}$	component b of vector \mathbf{a}
$a_{[bc,d]}$	component d of vector \mathbf{a} describing a characteristic of the c-frame w.r.t. the b-frame
\bar{a}	mean value of a
$ \mathbf{a} $	representation of the absolute value of vector \mathbf{a}
$a_{[Info]}, a^{[Info]}$	a with added information <i>Info</i>
$R_{b[de]}^c$	matrix element of rotation matrix \mathbf{R}_b^c in row d and column e
$q_{[b]}$	component b of quaternion \check{q}

VECTOR

\mathbf{a}, γ	general representations of a column vector
$\check{\mathbf{a}}$	estimated version of \mathbf{a} or \mathbf{a} containing errors
$\delta\mathbf{a}$	error component or correction term of $\check{\mathbf{a}}$
$\mathbf{a}^{[-]}$	propagated version of \mathbf{a}
$\mathbf{a}^{[+]}$	updated version of \mathbf{a}
$\tilde{\mathbf{a}}$	center of power series if not specified otherwise
\mathbf{a}^b	\mathbf{a} expressed in the b-frame
$\dot{\mathbf{a}}, \ddot{\mathbf{a}}, \dots$	first and second time derivative of \mathbf{a}
$\frac{d\mathbf{a}}{dt}, \frac{d^2\mathbf{a}}{dt^2}, \dots$	first and second time derivative of \mathbf{a}
$\frac{\partial \mathbf{a}}{\partial \mathbf{x}}$	partial derivative of function \mathbf{a} w.r.t. \mathbf{x}
$\mathbf{a}_{[Info]}, \mathbf{a}^{[Info]}$	\mathbf{a} with added information <i>Info</i>
$\boldsymbol{\alpha}_{[bc]}$	$\boldsymbol{\alpha}$ describing a characteristic of the c-frame w.r.t. the b-frame
\check{q}	general representation of a quaternion
\check{q}^b	representation of a pure quaternion defined in the b-frame
\check{q}_b^c	\check{q} describing a rotation of the b- into the c-frame

MATRIX

$\mathbf{A}, \mathbf{\Gamma}$	general representations of a matrix
\mathbf{R}	representation of a rotation matrix
\mathbf{R}_b^c	\mathbf{R} realizing a vector rotation from the b- into the c-frame
$\mathbf{R}(\gamma)$	\mathbf{R} realizing a vector rotation with the magnitude of γ (counterclockwise)
$\dot{\mathbf{R}}$	first time derivative of \mathbf{R}
$[\gamma \times]$	skew-symmetric matrix of γ
$\mathbf{A}_{[Info]}, \mathbf{A}^{[Info]}$	\mathbf{A} with added information <i>Info</i>
$\mathbf{A}^{[-]}$	propagated version of \mathbf{A}
$\mathbf{A}^{[+]}$	updated version of \mathbf{A}

1 Introduction

Geodesy is the scientific discipline of determining and mapping the Earth’s geometrical and physical appearance in the spatio-temporal domain including its orientation in inertial space. A wide range of geodetic disciplines emerged over time that specialized in certain subdivisions of geodesy, like applied geodesy, remote sensing, or cartography. This thesis is a contribution to higher geodesy, which deals with the Earth’s physical figure, called the geoid. Based on various observation techniques, information about the gravity field can be gained that allows defining the geoid. Although the geoid is a global surface, local and regional campaigns provide valuable insight into its high-frequency structure (local details).

Terrestrial 3D-gravity profiling is a concept for local gravity determination by quantifying vertical deflections (VDs) and the scalar gravity disturbance (SGD) on ground from a moving car. This is realized by applying a strapdown inertial measurement unit (IMU) and Global Navigation Satellite Systems (GNSS) equipment that is mounted in the trunk of and on top of the car, respectively. Additionally, a relative gravimeter and a zenith camera are part of the equipment for point-wise gravimetric/astrogeodetic observations. Campaigns are designed along tracks accessible by car in the area of interest. The IMU and GNSS equipment gather data permanently while driving. Gravity and VDs are observed at the start and endpoint as well as in between, to provide gravity updates to the Extended Kalman Filter (EKF), where the data fusion is implemented.

Before diving into details, the following paragraphs are intended to put terrestrial 3D-gravity profiling into the context of gravimetry, to elucidate related work, and to address the motivation, innovation, and outline of the thesis.

1.1 Gravity determination

Several methods and concepts exist to observe gravity field functionals. Koneshov et al. (2016), for instance, provide an overview of methods to determine VDs from a moving-base. A general classification can be made by distinguishing between spaceborne, airborne or shipborne, and terrestrial concepts, implicating different spatial resolution and coverage in the resulting quantity (cf. Koneshov et al. (2016, Fig. 1)). Naturally, the height of a gravimetric instrument above the Earth’s surface dictates the functional’s maximal spatial resolution, while the coverage is defined by the routing/orbit parameters.

Spaceborne data helps to estimate the Earth’s gravity field globally² down to a spatial resolution of 80 - 100 km (Brockmann et al., 2019) and achieves accuracies of ± 1 mGal when data of different satellite missions are combined. Gravimetric satellite missions like Challenging Minisatellite Payload (CHAMP) (Reigber et al., 1999), Gravity Recovery And Climate Experiment (GRACE) (Tapley et al., 2004), Gravity field and steady-state Ocean Circulation Explorer (GOCE) (Drinkwater et al., 2003), and Gravity Recovery And Climate Experiment Follow-On (GRACE-FO) (Flechtner et al., 2016) provide valuable data for tracking seasonal and long-term changes of the geoid on global and regional scales. Airborne and shipborne campaigns are regionally limited but yield an increased resolution between ~ 0.5 km and 5 km at or even below the milligal-accuracy level, see e.g., Becker (2016) or Petrovic et al. (2016). Airborne gravity gradiometry can provide even higher resolutions and accuracies (Jekeli, 2006). Airborne campaigns are particularly suited for geoid modeling in coastal areas, where satellite altimetry data naturally becomes less reliable. Terrestrial gravimetry³ is usually considered to be a static point-wise measurement process. Although such points exist worldwide, terrestrial gravimetry is assigned as a local concept due to the partially large separation of points in combination with the enormous effort to cover greater areas. Modern zenith cameras provide VDs with an angular

²Except for the polar gap.

³Here, gravimetry also stands for astrogeodetic observations.

accuracy below $\pm 0.1''$ (Hirt and Flury, 2008). Absolute and relative gravimeters observe gravity and changes of gravity at an accuracy level of $\sim \pm 1 \mu\text{Gal}^4$ (Torge and Müller, 2012). Moreover, gravity defined in Newtonian mechanics is also explained in the general theory of relativity by the curvature of space-time and thus is observable by optical clocks (e.g., Flury (2016)). Data sets from terrestrial gravimetry allow to analyze temporal gravity changes, to model the regional geoid, to reduce leveling observations, to validate gravity field solutions, to investigate local mass density variations, and they can provide gravity ties e.g., for terrestrial 3D-gravity profiling.

Terrestrial 3D-gravity profiling merges observation methods known from airborne/shipborne as well as terrestrial campaigns. From this point of view, it cannot be assigned to only one of these classes. The coverage is neither strictly local nor regional too. Instead, it yields a very dense gravity sampling along defined trajectories. Concerning the frequency domain, the high-frequency content of the signal is assumed to be superior to airborne data due to the effect of upward continuation but inferior to point-wise measurements that include the full gravity signal spectrum. The accuracy of terrestrial 3D-gravity profiling is investigated in this thesis. But before, a brief overview of related work is given.

1.2 Related work

This section provides a short historical review of astrogeodetic observations and the gravimetric use of strapdown IMUs due to their central role in this thesis (see Chs. 4.1, 4.2, and 4.3). Developments in GNSS positioning and relative gravimetry are elucidated in Teunissen and Montenbruck (2017), and Torge and Müller (2012). The author emphasizes that the gravimetric concept, as it is realized in this thesis, highly depends on the excellent performance of the GNSS equipment and GNSS software in kinematic mode as well as the quick and reliable operation of the Scintrex CG-5, which have continuously improved during the last decades.

1.2.1 Astrogeodetic observations⁵

Astrogeodetic VDs have played several important roles in geodesy and geophysics. Astronomical leveling was the only means for geoid determination prior to gravimetric methods, though combined astrogravimetric methods have also been used (e.g., Fryer (1972) or Marti (1997)). VDs are needed for the reduction of geodetic surveying measurements to the ellipsoid (e.g., Featherstone and Rieger (2000)), have been used to assess global gravity field models (e.g., Jekeli (1999) or Albayrak et al. (2020)), and can be applied to fit gravimetric geoid models (Featherstone and Lichti, 2009). Astrogeodetic VDs also helped to confirm the principle of isostasy (e.g., Watts (2001, Ch. 1)) and have been applied to geophysical studies of intracrustal mass-density anomalies (Bürki, 1989).

Historically, photographic and geodetic surveying techniques were used for astrogeodetic measurements, but over the past 15 years they have been replaced by charged coupled device (CCD) cameras and Global Positioning System (GPS)/GNSS in fully digital systems (e.g., Hirt et al. (2010a) or Guillaume et al. (2012)). With the advent of the digital zenith camera, numerous astrogeodetic VDs have been observed and used to compute (quasi)geoid profiles (e.g., Hirt et al. (2007), Hirt and Seeber (2007), Hirt et al. (2008), Hirt and Flury (2008), Voigt et al. (2009), Voigt (2013), Smith et al. (2013), Guillaume (2015) or Wang et al. (2017)). In the aforementioned works, sub-millimeter-, millimeter- and centimeter-accuracy was achieved for (quasi)geoid height differences depending on the traverse length, VD station spacing, and instrument accuracy. These VD datasets were employed in independent (quasi)geoid validation based on astronomical leveling, error analysis of GNSS heighting (Hirt et al., 2011) and in the assessment of the high-frequency constituents of geopotential models (e.g., Hirt et al. (2010b), Voigt (2013) or Voigt and Denker (2013)).

⁴Except for superconducting gravimeters, which perform better.

⁵Schack et al. (2018), see remarks on p. 6

1.2.2 Strapdown systems

Before the first realizations of airborne gravity campaigns with strapdown systems by Boedecker et al. (1994) and Wei and Schwarz (1998), scientists had already studied and analyzed this concept for a decade (e.g., Forsberg et al. (1986) or Knickmeyer (1990)). Boedecker et al. (1994) state that the "potential of []his approach to strapdown airborne gravimetry is in the mGal-range". In the following years, several papers of different research groups were dedicated to the assessment and improvement of scalar and vector strapdown (mostly airborne) gravimetry, like Jekeli and Kwon (1999), Glennie et al. (2000), Bastos et al. (2002), Gerlach et al. (2010a), Becker (2016) and Jensen (2018). Becker et al. (2015) could improve airborne gravity results significantly from usually several milligal to the (sub-)milligal level by applying a temperature correction to the IMU accelerometer output. Thus, strapdown systems became a serious alternative to stabilized platform systems (Johann et al., 2020). Throughout the last decades, the direct method as well as the indirect method were utilized to extract gravity from IMU data. With the direct method, GNSS derived accelerations are reduced from the IMU accelerations to obtain gravity, while the indirect method uses a Kalman Filter environment to estimate gravity, see Ch. 3. Johann et al. (2019) could demonstrate that both approaches can achieve equivalent results within the specified accuracies.

In parallel, the utilization of IMUs for terrestrial gravimetry advanced. In Gerlach et al. (2005)⁶, the scalar gravity evaluation of a terrestrial campaign in the Estergebirge suffered from the lack of visible positioning satellites (GPS only), which is less severe nowadays due to the increased number of satellite-based positioning systems. Nevertheless, Gerlach et al. (2005) could show that gravity values derived from the IMU during standstill phases deviate from the reference with a standard deviation of ± 2 mGal. Li (2007) was able to obtain 3D-gravity results from a terrestrial campaign in Montana with standard deviations of $\pm 2 - 3$ mGal/ $\pm 1 - 2''$ w.r.t. local control data, by applying a two-stage EKF and wavelet denoising. Yu et al. (2015) achieve 2.3 mGal/1.7 mGal for half wavelengths of 1.1 km/1.7 km. In Eissfeller (1989), the potential accuracy of a terrestrial 3D-gravity profiling concept was estimated to be about 0.2 - 0.4'', based on simulations. As will be shown in this thesis, these values can only be approached by means of the integration of a high-resolution gravity model that contributes the high-frequency components. Without such a model root-mean-square (RMS) errors of 0.5 - 0.8'' are achieved w.r.t. accurate reference data. For the SGD, both variants yield RMS errors between 1.5 - 2.0 mGal, which is commensurate with the numbers of previous studies.

1.3 Motivation, innovation and outline

The motivation for this thesis is driven by the goal of accurate local gravity determination in a simple and fast fashion, by making use of state-of-the-art instruments and scientific progress, being independent of external gravity information to the greatest extent. The realization concept in combination with the compact instruments shall facilitate the determination of gravimetric profiles worldwide, even in remote regions. Thus, the thesis presents an opportunity to increase the worldwide coverage of high-quality gravity profiles, which simultaneously can help to evaluate existing gravity field models locally. The general idea behind terrestrial 3D-gravity profiling is to bridge the disadvantages of moving-base strapdown gravimetry and point-wise terrestrial gravimetry likewise. This mutual complement can either be interpreted from an IMU point of view that gravimetric/astrogeodetic measurements help to quantify IMU errors or from a gravimetric/astrogeodetic point of view that the IMU helps to spatially interpolate 3D-gravity between gravimetric/astrogeodetic observation points.

As already elaborated, the idea of using strapdown IMUs for gravity field determination is anything but new. Due to the recent developments in airborne and shipborne gravimetry, IMUs not only

⁶Here, the same IMU was employed as in this thesis, apart from minor adaptations.

achieve similar accuracies as the matured technique with platform-stabilized gravimeters but also promote other applications e.g., gravimetry from cars or drones (Deurloo et al., 2012). However, for the majority of such campaigns, the 3D-gravity vector is of minor interest because they are designed to provide areal SGDs that already allow local and regional geoid computation. Another reason is that the horizontal gravity components are difficult to distinguish from gyroscope errors during non-accelerated periods along the straight measurement lines, which hampers their accurate estimation. In contrast, terrestrial gravity profiling cannot provide areal data, but it is highly suited for determining the horizontal components for two reasons. A driven trajectory will always contain significant lateral and vertical accelerations that help to distinguish between certain error sources and the VDs, and the on-ground scenario allows to provide superior gravity information that can be included in the processing and analyses. The innovation of this thesis, in comparison to other moving-base terrestrial gravity campaigns like Li (2007) or Yu et al. (2015), is that 1) relative gravity measurements and astrogeodetic observations are integrated into the campaign's realization concept mitigating the requirement of existing gravity data in the study area, 2) the evaluation aims at the determination of accurate 3D-gravity information and 3) the quality assessment of the terrestrial 3D-gravity campaign in Ch. 4.3 is conducted against dense and accurate 3D-gravity observations.

The thesis is composed of six parts. After the introduction (Ch. 1), a brief overview of essential theory and methodology is provided in Ch. 2, which is considered a prerequisite to follow further explications and analyses. Here, the definitions of important reference frames and attitude representations are given, the instruments are characterized, functionals of the gravity potential are derived, and the principle of multi-sensor data fusion with subsequent smoothing is elucidated.

Chapter 3 contains a detailed description of the mathematical realization of the terrestrial 3D-gravity profiling software. The main topics are the strapdown navigation algorithm, the explicit error propagation yielding the system model, the EKF updates including the measurement models, the applied smoother, and the combination of redundant profiles for increased accuracy and robustness of the final results.

The main chapter of this work is Ch. 4, where three measurement campaigns are presented and analyzed. An astrogeodetic campaign in Western Australia illustrates the performance of a compact instrument mounted on a total station called QDaedalus (Guillaume et al., 2012) that was developed by the Eidgenössische Technische Hochschule Zürich in the last decade and that manages to determine VDs with high accuracy. Next, four IMU temperature calibrations are assessed that help to detect temperature-dependent changes in the output of the applied IMU and to determine corresponding calibration parameters. The third section covers a terrestrial 3D-gravity profiling campaign that was conducted in the Bavarian Estergebirge. A description of the utilized data sets and of the profiles' accuracy assessment is included, and the resulting profiles of the 3D-gravity disturbance are presented. Finally, certain errors are introduced to the processing chain in order to investigate their influence on the results.

In Ch. 5, the results obtained in Ch. 4 are recapitulated and thoughts about gained experiences as well as achieved and missed goals are elaborated.

Lastly, Ch. 6 discusses possible extensions of the presented analyses and addresses reasonable adaptations that might lead to improved results in future campaigns. The thesis ends with concluding remarks on 3D-gravimetry.

2 Theoretical foundations

This chapter includes a technical, mathematical, and physical overview of important concepts applied throughout the thesis. The extraction of gravity information from IMU measurements requires a basic understanding of reference frames and attitude representations. The geodetic instruments, as an integral part of this thesis, should also be familiar to the reader. Of course, basic knowledge about the physical meaning of the thesis's results as well as the mathematics behind the data processing is vital. The paragraphs are based on dedicated chapters in Kuipers (1999), Jekeli (2001), Savage (2007), Groves (2008), and Torge and Müller (2012). Although the underlying theory of this thesis fills entire books, this chapter intends to provide a compact theoretical overview to be able to follow the explications in the following chapters. Thus, this chapter has no claim of completeness.

2.1 Position and orientation

To be able to describe the position or orientation of an object, a defined reference is needed. Such a reference is called coordinate system in combination with its realization, the coordinate frame. A coordinate system is defined by its origin, three orthogonal axes including a scaling (usually similar for all axes), and one type of coordinates. Extending the reference, e.g., to gravity, time, or a geometric body, the terms reference system and reference frame are adopted. In the following, important coordinates and frames for inertial navigation and gravimetry are introduced. Afterward, it is focused on the orientation of these frames.

2.1.1 Coordinates and frames

The frames that are addressed throughout the thesis are introduced and associated with a certain type of coordinates, either Cartesian, spherical, ellipsoidal, or natural ones. To get a deeper understanding of the concepts behind each type of frame or coordinate, the reader is referred to Savage (2007) or Torge and Müller (2012). It is started with the description of the different coordinates:

- *Cartesian coordinates* are noted as x , y , and z and represent the distance of the point from the system's origin projected orthogonally onto its first, second, and third axis in [m].
- *Spherical coordinates* consist of the right ascension α and the declination δ , without a third component⁷. W.r.t. the system's origin, α describes the angle between the first axis of the system and the point, projected onto the equatorial plane, and δ represents the angle between the equatorial plane and the point, in [rad].
- *Ellipsoidal or geodetic coordinates* are known as ellipsoidal latitude φ , ellipsoidal longitude λ and ellipsoidal height h . They are linked to an ellipsoid reference body. The longitude is defined similarly to α from above, in [rad]. The latitude is the angle between the equatorial plane and the normal onto the ellipsoid through the point, in [rad]. h is the height of the point above the ellipsoid, orthogonal to the tangential plane, given in [m].
- *Natural or astronomical coordinates* are given as astronomical latitude Φ and astronomical longitude Λ . Both angles are given in [rad] and represent the orientation of a physically leveled surface at that point. Φ is defined as the angle between the equatorial plane and the normal onto the level surface. Λ is the angle between the first axis and the normal onto the level surface, projected onto the equatorial plane. A third component can exist, in terms of physical heights (e.g., normal or orthometric heights).

⁷This definition is restricted to this thesis since the respective coordinate system is based on a unit sphere. In general, a third component is defined as the distance to the origin. Additionally, the angles can be named differently.

Next, the frames are elaborated. Note that the naming of the frames is not standardized and can be defined differently in other publications.

- the *inertial frame* (= *i-frame*) is a non-rotating, space-fixed frame with its origin in the barycenter of the solar system or, as in this thesis, in the Earth's center of mass. The third axis is usually aligned in parallel to the Earth's mean rotation axis, the first axis is pointing towards the vernal equinox (which is by definition orthogonal to the third axis) and the second axis completes the right-handed coordinate system. Spherical coordinates define the positions in the i-frame. The International Celestial Reference Frame (ICRF)⁸, defined by the International Earth Rotation and Reference Systems Service (IERS), is an example of an i-frame.
- the origin of the *terrestrial frame* (= *e-frame*) is situated in the center of mass of the Earth. It is an Earth-fixed frame, rotating synchronously with the Earth around its third axis (= Earth-centered, Earth-fixed (ECEF)-frame). In general, the first axis points towards the Greenwich meridian in the equatorial plane and the second axis completes the right-handed system. Positions are expressed in terms of ellipsoidal coordinates. As examples, the International Terrestrial Reference Frame (ITRF)⁹ and the World Geodetic System 1984 (WGS84) reference frame¹⁰ are mentioned, which both include the reference ellipsoid Geodetic Reference System 1980 (GRS80) (Moritz, 2000) with a minute difference in the flattening.
- the *navigation frame* (= *n-frame*) is coupled to the IMU in such a way that the frame's origin is situated in the reference point of the IMU. The vertical axis is aligned orthogonally to the relevant reference ellipsoid, pointing outwards. The first and second axes proceed tangential to the ellipsoid and are oriented into east and north direction, respectively. A synonym for the n-frame is the East-North-Up (ENU)-frame. Coordinates w.r.t. the n-frame are of no concern in this work. It is the n-frame's position that is of interest, which is usually expressed in the e-frame, in geodetic coordinates.
- the *local-level frame* (= *l-frame*) is defined analogically to the n-frame, with the difference that the equipotential surface in each point builds the reference, see Ch. 2.3.
- the *body frame* (= *b-frame*) is the third frame that is fixed to the IMU with the identical origin as the n-frame and l-frame. The axes are defined parallel to the accelerometer and gyroscope sensor input axis, pointing in front direction, to the left side, and upwards, mutually orthogonal. A synonym for the b-frame is the Front-Left-Up (FLU)-frame. Coordinates in the b-frame are Cartesian coordinates, which are used to describe the position of the GNSS antenna w.r.t. the iMAR navigation-grade inertial measurement unit (RQH), in this work. Moreover, the b-frame axes and the corresponding inertial sensors are labeled as X , Y , and Z .

2.1.2 Attitude representations and derivatives

The content of this paragraph covers direction cosine matrices (DCM), Euler angles, and quaternions. All of them express the relative orientation between two frames and are applied to switch from one frame into a second one or, in other words, to assign vectors/matrices given in one frame to another frame. The three representations are based on different concepts but can be converted into each other as shown in this paragraph. In addition, the derivatives of DCMs and quaternions are included, and the small angle approximation (SAA) is introduced.

⁸<https://www.iers.org/IERS/EN/DataProducts/ICRF/ICRF3/icrf3.html>, accessed: 06.06.2021

⁹https://itrf.ign.fr/ITRF_solutions/2014/, accessed: 06.06.2021

¹⁰file:///C:/Users/PP/AppData/Local/Temp/NGA.STND.0036_1.0.0_WGS84.pdf, accessed: 06.06.2021

• *DCMs* are (3x3) matrices, noted here as \mathbf{R} . It is started with the definition of a vector \mathbf{v} as the sum of its components projected onto any orthogonal set of frame axes, here frame a and b with the identical origin.

$$\mathbf{v} = v^{a[1]}\mathbf{e}_{a[1]} + v^{a[2]}\mathbf{e}_{a[2]} + v^{a[3]}\mathbf{e}_{a[3]} = v^{b[1]}\mathbf{e}_{b[1]} + v^{b[2]}\mathbf{e}_{b[2]} + v^{b[3]}\mathbf{e}_{b[3]}$$

where $\mathbf{e}_{a[1]}, \mathbf{e}_{a[2]}, \mathbf{e}_{a[3]}$ and $\mathbf{e}_{b[1]}, \mathbf{e}_{b[2]}, \mathbf{e}_{b[3]}$ are normalized (unit) vectors along the three orthogonal axes of the a- and b-frame. The following three equations can be generated subsequently due to the orthogonal basis.

$$\begin{aligned} v^{a[1]} &= v^{b[1]}\mathbf{e}_{a[1]}\mathbf{e}_{b[1]} + v^{b[2]}\mathbf{e}_{a[1]}\mathbf{e}_{b[2]} + v^{b[3]}\mathbf{e}_{a[1]}\mathbf{e}_{b[3]} \\ v^{a[2]} &= v^{b[1]}\mathbf{e}_{a[2]}\mathbf{e}_{b[1]} + v^{b[2]}\mathbf{e}_{a[2]}\mathbf{e}_{b[2]} + v^{b[3]}\mathbf{e}_{a[2]}\mathbf{e}_{b[3]} \\ v^{a[3]} &= v^{b[1]}\mathbf{e}_{a[3]}\mathbf{e}_{b[1]} + v^{b[2]}\mathbf{e}_{a[3]}\mathbf{e}_{b[2]} + v^{b[3]}\mathbf{e}_{a[3]}\mathbf{e}_{b[3]} \end{aligned}$$

With the help of the dot or scalar product ($\mathbf{x} \cdot \mathbf{y} = |\mathbf{x}||\mathbf{y}| \cos \mu$) the DCM is defined as follows.

$$\mathbf{v}^a = \begin{pmatrix} \cos \mu_{[11]} & \cos \mu_{[12]} & \cos \mu_{[13]} \\ \cos \mu_{[21]} & \cos \mu_{[22]} & \cos \mu_{[23]} \\ \cos \mu_{[31]} & \cos \mu_{[32]} & \cos \mu_{[33]} \end{pmatrix} \mathbf{v}^b = \mathbf{R}_b^a \mathbf{v}^b \quad (2.1)$$

The elements of \mathbf{R} reflect the angles between the single axes of the a- and b-frame, specified by $_{[11]}$, $_{[12]}$, etc. in Eq. (2.1). It is noted that this matrix is not symmetric and that the inverse rotation can be realized with its transposed. Furthermore, \mathbf{R} has to be an orthogonal matrix with the determinant 1. The transformation of a matrix \mathbf{A} is realized in Eq. (2.2) from Jekeli (2001, Ch. 1.3.1), where \mathbf{w} represents another vector.

$$\begin{aligned} \mathbf{v}^b = \mathbf{A}^b \mathbf{w}^b \Rightarrow \mathbf{R}_a^b \mathbf{v}^a = \mathbf{A}^b \mathbf{R}_a^b \mathbf{w}^a \Rightarrow \mathbf{v}^a = \mathbf{R}_b^a \mathbf{A}^b \mathbf{R}_a^b \mathbf{w}^a \Rightarrow \mathbf{v}^a = \mathbf{A}^a \mathbf{w}^a \\ \mathbf{A}^a = \mathbf{R}_b^a \mathbf{A}^b \mathbf{R}_a^b \end{aligned} \quad (2.2)$$

• *Euler angles* are a triplet of angles that describe the magnitude of three successive rotations around the axes of a frame¹¹. Thereby, it is of major importance to be aware of the axis sequence the angles are assigned to. In this thesis, the three Euler angles ϕ , θ , and ψ are called roll, pitch, and yaw, and they are assigned to the East¹², North¹² and Up axis of the n-frame. $\boldsymbol{\psi}^n$ represents the vector of the three Euler angles in the n-frame and helps to transform a vector from the n- to the b-frame. \mathbf{R}_n^b is created by following the axis sequence of Eq. (2.3).

$$\begin{aligned} \mathbf{R}_n^b &= \mathbf{R}_{n''}^b(\phi^n) \mathbf{R}_{n'}^{n''}(\theta^n) \mathbf{R}_n^{n'}(\psi^n) \\ &= \begin{pmatrix} 1 & 0 & 0 \\ 0 & \cos(\phi^n) & \sin(\phi^n) \\ 0 & -\sin(\phi^n) & \cos(\phi^n) \end{pmatrix} \begin{pmatrix} \cos(\theta^n) & 0 & -\sin(\theta^n) \\ 0 & 1 & 0 \\ \sin(\theta^n) & 0 & \cos(\theta^n) \end{pmatrix} \begin{pmatrix} \cos(\psi^n) & \sin(\psi^n) & 0 \\ -\sin(\psi^n) & \cos(\psi^n) & 0 \\ 0 & 0 & 1 \end{pmatrix} \\ &= \begin{pmatrix} \cos(\theta^n) \cos(\psi^n) & \cos(\theta^n) \sin(\psi^n) & -\sin(\theta^n) \\ \sin(\phi^n) \sin(\theta^n) \cos(\psi^n) - \cos(\phi^n) \sin(\psi^n) & \sin(\phi^n) \sin(\theta^n) \sin(\psi^n) + \cos(\phi^n) \cos(\psi^n) & \sin(\phi^n) \cos(\theta^n) \\ \cos(\phi^n) \sin(\theta^n) \cos(\psi^n) + \sin(\phi^n) \sin(\psi^n) & \cos(\phi^n) \sin(\theta^n) \sin(\psi^n) - \sin(\phi^n) \cos(\psi^n) & \cos(\phi^n) \cos(\theta^n) \end{pmatrix} \end{aligned} \quad (2.3)$$

¹¹The reader should be aware that angles describing a rotation sequence around three different axes are usually called Kardan angles. Angles are called Euler angles if the first and the last rotation axis of a sequence are similar. However, this distinction is not made in the literature quoted at the beginning of this chapter as well as in this work.

¹²Note that the rotations are not conducted around the east and north axis, but around their rotated version, indicated as n' and n'' in Eq. (2.3).

The last matrix represents the conversion of Euler angles into a DCM. Vice versa, the Euler angles can be extracted from \mathbf{R}_n^b according to Eqs. (2.4).

$$\begin{aligned}\phi^n &= \arctan\left(\frac{R_{n[23]}^b}{R_{n[33]}^b}\right) \\ \theta^n &= -\arcsin\left(R_{n[13]}^b\right) \\ \psi^n &= \arctan\left(\frac{R_{n[12]}^b}{R_{n[11]}^b}\right)\end{aligned}\tag{2.4}$$

A disadvantage of the Euler angles is that they exhibit a singularity, also called gimbal-lock. If $\theta = \pm 90^\circ$, then ϕ and ψ cannot be distinguished.

• *Quaternions* are called hyper-complex numbers of rank four, where the three orthonormal axes \mathbf{i} , \mathbf{j} , and \mathbf{k} satisfy the following equations.

$$\begin{aligned}\mathbf{i}^2 &= \mathbf{j}^2 = \mathbf{k}^2 = \mathbf{i}\mathbf{j}\mathbf{k} = -1 \\ \mathbf{i} \times \mathbf{j} &= -\mathbf{j} \times \mathbf{i} = \mathbf{k} \\ \mathbf{j} \times \mathbf{k} &= -\mathbf{k} \times \mathbf{j} = \mathbf{i} \\ \mathbf{k} \times \mathbf{i} &= -\mathbf{i} \times \mathbf{k} = \mathbf{j}\end{aligned}$$

A quaternion is separable into a scalar component $q_{[0]}$ and a vector component \mathbf{q} , as shown in Eq. (2.5).

$$\begin{aligned}\check{q} &= (q_{[0]}, q_{[1]}, q_{[2]}, q_{[3]}) = q_{[0]} + \mathbf{q} \\ \text{where } \mathbf{q} &= \mathbf{i}q_{[1]} + \mathbf{j}q_{[2]} + \mathbf{k}q_{[3]}\end{aligned}\tag{2.5}$$

The idea behind quaternions is that each rotation sequence can be replaced by a single rotation around a single axis. Following Kuipers (1999, Chs. 5.8.2 and 5.10), a quaternion can also be defined w.r.t. a rotation angle α , and a normalized (unit) vector \mathbf{u} representing the axis of rotation, see Eq. (2.6).

$$\check{q} = \cos\left(\frac{\alpha}{2}\right) + \mathbf{u} \sin\left(\frac{\alpha}{2}\right)\tag{2.6}$$

The concept of combining a scalar and a vector needs special consideration when it comes to mathematical operations, which is discussed comprehensively in Kuipers (1999). Transforming a vector is realized by two Hamilton products in Eq. (2.7), where v is called a pure quaternion with a zero scalar part. q^* is the complex conjugate of q .

$$\check{v}^a = \check{q}_b^{a*} \check{v}^b \check{q}_b^a \quad \text{with } \check{v} = \begin{pmatrix} 0 \\ \mathbf{v} \end{pmatrix}\tag{2.7}$$

Quaternions can be transformed to DCMs and Euler angles and vice versa, see Eqs. (2.8) to (2.11). Quaternion to DCM:

$$\mathbf{R} = \begin{pmatrix} q_{[0]}^2 + q_{[1]}^2 - q_{[2]}^2 - q_{[3]}^2 & 2(q_{[1]}q_{[2]} + q_{[0]}q_{[3]}) & 2(q_{[1]}q_{[3]} - q_{[0]}q_{[2]}) \\ 2(q_{[1]}q_{[2]} - q_{[0]}q_{[3]}) & q_{[0]}^2 - q_{[1]}^2 + q_{[2]}^2 - q_{[3]}^2 & 2(q_{[2]}q_{[3]} + q_{[0]}q_{[1]}) \\ 2(q_{[1]}q_{[3]} + q_{[0]}q_{[2]}) & 2(q_{[2]}q_{[3]} - q_{[0]}q_{[1]}) & q_{[0]}^2 - q_{[1]}^2 - q_{[2]}^2 + q_{[3]}^2 \end{pmatrix}\tag{2.8}$$

DCM to quaternion:

$$\begin{aligned}
 q_{[0]} &= \frac{1}{2} \sqrt{R_{[11]} + R_{[22]} + R_{[33]} + 1} \\
 q_{[1]} &= \frac{R_{[23]} - R_{[32]}}{4q_{[0]}} \\
 q_{[2]} &= \frac{R_{[31]} - R_{[13]}}{4q_{[0]}} \\
 q_{[3]} &= \frac{R_{[12]} - R_{[21]}}{4q_{[0]}}
 \end{aligned} \tag{2.9}$$

Quaternion to Euler angles:

$$\begin{aligned}
 \phi &= \arctan\left(\frac{2q_{[1]}q_{[2]} + 2q_{[0]}q_{[3]}}{2q_{[0]}^2 + 2q_{[1]}^2 - 1}\right) \\
 \theta &= \arcsin\left(-2q_{[1]}q_{[3]} - 2q_{[0]}q_{[2]}\right) \\
 \psi &= \arctan\left(\frac{2q_{[2]}q_{[3]} + 2q_{[0]}q_{[1]}}{2q_{[0]}^2 + 2q_{[3]}^2 - 1}\right)
 \end{aligned} \tag{2.10}$$

Euler angles to quaternion:

$$\begin{aligned}
 q_{[0]} &= \cos\left(\frac{\phi}{2}\right) \cos\left(\frac{\theta}{2}\right) \cos\left(\frac{\psi}{2}\right) + \sin\left(\frac{\phi}{2}\right) \sin\left(\frac{\theta}{2}\right) \sin\left(\frac{\psi}{2}\right) \\
 q_{[1]} &= \sin\left(\frac{\phi}{2}\right) \cos\left(\frac{\theta}{2}\right) \cos\left(\frac{\psi}{2}\right) - \cos\left(\frac{\phi}{2}\right) \sin\left(\frac{\theta}{2}\right) \sin\left(\frac{\psi}{2}\right) \\
 q_{[2]} &= \cos\left(\frac{\phi}{2}\right) \sin\left(\frac{\theta}{2}\right) \cos\left(\frac{\psi}{2}\right) + \sin\left(\frac{\phi}{2}\right) \cos\left(\frac{\theta}{2}\right) \sin\left(\frac{\psi}{2}\right) \\
 q_{[3]} &= \cos\left(\frac{\phi}{2}\right) \cos\left(\frac{\theta}{2}\right) \sin\left(\frac{\psi}{2}\right) - \sin\left(\frac{\phi}{2}\right) \sin\left(\frac{\theta}{2}\right) \cos\left(\frac{\psi}{2}\right)
 \end{aligned} \tag{2.11}$$

• *Derivatives or first-order differential equations* of DCMs and quaternions describe the relative change of orientation between frame a and b. In Jekeli (2001, p. 114f), the corresponding formulations can be found, which are repeated in Eqs. (2.12) and (2.13).

$$\dot{\mathbf{R}}_b^a = \mathbf{R}_b^a [\boldsymbol{\omega}_{[ab]}^b \times] = \mathbf{R}_b^a \begin{pmatrix} 0 & -\omega_{[ab,Z]}^b & \omega_{[ab,Y]}^b \\ \omega_{[ab,Z]}^b & 0 & -\omega_{[ab,X]}^b \\ -\omega_{[ab,Y]}^b & \omega_{[ab,X]}^b & 0 \end{pmatrix} \tag{2.12}$$

$$\dot{\check{q}}_b^a = \frac{1}{2} \mathbf{S} \check{q}_b^a = \frac{1}{2} \begin{pmatrix} 0 & \omega_{[ab,X]}^b & \omega_{[ab,Y]}^b & \omega_{[ab,Z]}^b \\ -\omega_{[ab,X]}^b & 0 & \omega_{[ab,Z]}^b & -\omega_{[ab,Y]}^b \\ -\omega_{[ab,Y]}^b & -\omega_{[ab,Z]}^b & 0 & \omega_{[ab,X]}^b \\ -\omega_{[ab,Z]}^b & \omega_{[ab,Y]}^b & -\omega_{[ab,X]}^b & 0 \end{pmatrix} \check{q}_b^a \tag{2.13}$$

• An additional paragraph for *small angle approximations* is added to clarify how small angle rotations can be described, see also Groves (2008, p. 25/152/380). \mathbf{R}_n^b was already defined in Eq. (2.9). When it comes to small rotations α or β , the SAA can be applied. Assigning $\cos(\alpha) = 1$, $\sin(\alpha) = \alpha$ and $\sin(\alpha)\sin(\beta) = 0$ to \mathbf{R}_n^b , the matrix simplifies to

$$\mathbf{R}_n^b = \begin{pmatrix} 1 & \psi^n & -\theta^n \\ -\psi^n & 1 & \phi^n \\ \theta^n & -\phi^n & 1 \end{pmatrix}. \quad (2.14)$$

2.2 Instruments and measuring concepts

As the title of the thesis states, multiple sensors/instruments come into play during terrestrial 3D-gravity profiling campaigns. The four instruments, which are introduced in this section, can be considered as the minimal setup. An IMU and GNSS equipment enable the profiling of gravity in dynamic mode. Thereby, the lever arm, which is the position of the GNSS antenna phase center in the b-frame, must be known accurately to account for differences in the individual dynamics of the IMU and the GNSS antenna. Precise gravity reference data is collected with a zenith camera and a relative gravimeter on selected points. Both instruments are limited to static observations but provide a high-accuracy gravity tie. Other instruments can be incorporated that compensate drawbacks of these four. This could be, e.g., an odometer that provides velocity information independent of sky-visibility or a tiltmeter that measures the direction of the plumb-line w.r.t. the IMU housing.

In the further course, the four instruments are specified, their measuring principles are elucidated and it is coarsely explained how the raw data is transformed to the input data of the algorithm described in Ch. 3. Since the IMU is the main instrument of terrestrial 3D-gravity profiling, its performance is discussed, too.

2.2.1 Inertial measurement unit

A more than 15-year-old iMAR navigation-grade inertial measurement unit (RQH), shown in Fig. 2.1, is incorporated in this thesis. It is a strapdown system equipped with three servo-balanced pendulous QA-2000 accelerometers (Honeywell, a) and three GG1320 dithered ring laser gyroscopes (Honeywell, b), all fabricated by Honeywell. They are rigidly fixed to the sensor mounting plate, which is connected to the RQH housing via shock mounts. The shock mounts absorb impulsive accelerations and thus protect the sensors from damage through external forces. The accelerometer data is digitized by iMAR Navigation & Control (iMAR) analog-to-digital-converter boards, while the gyroscopes directly provide a digital output. A sensor measurement is the mean acceleration or angular rate of the time interval prior to the corresponding time tag. The time interval is defined by the measurement frequency, which is chosen to be 500 Hz in this thesis, but can be increased up to 2000 Hz if needed. The internal oscillator can be synchronized to GPS time via a pulse per second (PPS) input in combination with National Marine Electronics Association (NMEA) time messages. Moreover, the RQH comprises three built-in temperature sensors that will be relevant in Chs. 4.2 and 4.3. Their position inside the RQH is unknown. A dedicated software, called NavCommand, allows the user to adjust a variety of RQH settings, including the RQH output that is defined in this work as:

- internal time count in [s]
- GPS time in seconds of week (SOW) in [s]
- calibrated¹³ accelerometer data in [m s^{-2}]
- calibrated¹³ gyroscope data in [rad s^{-1}]
- temperature output in [K]

¹³Standard calibration method of iMAR

Normally, this output is forwarded to the EKF without any further adaptations. A temperature correction is implemented as an integral part of the EKF software and can be applied optionally. Unfortunately, during the last calibration the accelerometer eccentricity values were not saved inside the RQH. These values describe the offset of each accelerometer from the b-frame's origin. When neglecting this offset, rotations couple into the accelerometer observations. In Ch. 4.3.3.2, the effect of disregarding the accelerometers eccentricity w.r.t. the gravity estimation is evaluated. It reveals the importance of a correction that must be applied by the user to the observations in the post-processing¹⁴. Therefore, the eccentricity components of the accelerometers along the b-frame axes have to be known:

- Accelerometer X: $x^b = 0$ cm, $y^b = 0$ cm, $z^b = 0$ cm
- Accelerometer Y: $x^b = 0$ cm, $y^b = -4.42$ cm, $z^b = 0$ cm
- Accelerometer Z: $x^b = 0$ cm, $y^b = 0$ cm, $z^b = 4.28$ cm



Figure 2.1: RQH housing with cable port on the backside. The b-frame axes are marked on top with the X axis pointing in front direction, the Y axis to the left, and the Z axis upwards.

Every two years, the inertial sensor assembly (ISA) sensors should be calibrated by the manufacturer iMAR, to eliminate the most dominant systematic error sources. During this calibration, the ambient temperature (in a thermal chamber) is adjusted to 30 °C. A rotation sequence is completed with a calibration turntable that allows determining the biases, non-orthogonalities (the combined effect of misalignments and cross-couplings), and linear scale factors of the accelerometers and the gyroscopes. However, when the RQH is operated without warming up and/or exposed to varying ambient temperatures during operation, Becker (2016) could show that the RQH performance degrades due to the temperature dependency of the calibration parameters. The typical RQH temperature behaves as follows. Considering that the RQH was turned off for one day, the whole RQH is cooled down to the ambient temperature. When starting the RQH, its inner temperature will rise, mostly due to the gyroscope dithering (see Ch. 2.2.1.1). Static indoor measurements revealed that it takes around 5 h until the temperature sensors reach 1 °C below the maximum temperature. The maximum temperature, which is between 15 and 20 °C above the ambient temperature, is reached after ~20 h. As soon as the ambient temperature changes, the RQH temperature will slowly adapt.

¹⁴The exact procedure is treated as confidential by the manufacturer.

To mitigate this effect, in 2017 and 2019, the RQH passed not only the standard manufacturer calibration but also an Up and Down calibration (Ch. 4.2.1) at different temperatures as well as either a Roll and Pitch calibration (Ch. 4.2.2) or a strapdown rotation test (Ch. 4.2.3) at different temperatures. Since these calibrations were conducted by iMAR, the opportunity was taken to renew the firm- and software, to replace the hard disk by a new 32 GB Solid-State-Drive and to install a new central processing unit.

2.2.1.1 Inertial sensors The term "inertial sensors" describes instruments that observe some kind of movement w.r.t. the i-frame. The accelerometers and gyroscopes register accelerations $\mathbf{f}_{[ib]}^b$ (called specific force) and angular rates $\omega_{[ib]}^b$ along the three mutually orthogonal b-frame axes w.r.t. i-frame. All six inertial sensors together, accelerometers and gyroscopes, are called ISA. This section continues with a brief introduction of the working principle behind the gyroscopes and accelerometers. It is based on Dorobantu and Gerlach (2004), which provide a more detailed presentation and study of the RQH.

- *Accelerometers:* The QA-2000 (Honeywell, a) built-in accelerometers contain a proof mass attached to a pendulum that is decoupled from the cage via a single-directed hinge. External forces acting along the pendulum’s input axis (= hinge axis) induce a relative displacement of the proof mass w.r.t. the cage, represented by a pick-off. Thereby, the pendulum’s displacement is registered capacitively from the pick-off, which embodies the output quantity on the one hand (neglecting friction and torsion momentum of the hinge) and triggers the servo-rebalancing of the pendulum via a magnetic torque on the other hand. This way, the proof-mass is constantly kept close to its null position, which guarantees good linearity and low hysteresis. Equation (2.15) includes a simplified form of the mathematical relation between the rebalancing torque M and the input acceleration a ,

$$a = \frac{M}{ml} \tag{2.15}$$

where m and l represent the mass of the proof-mass and the length of the pendulum. The descriptive sensor error parameters for the pendulous accelerometers are adopted from tables in Dorobantu and Gerlach (2004) and presented in Table 2.1.

Parameter	Value
Bias repeatability	$<15 \mu\text{g}$
White noise	$8 \mu\text{g Hz}^{-1.5}$
Scale factor error	$\leq 70 \text{ ppm}$
Range	$\pm 2 \text{ g}$
Resolution	$0.2 \mu\text{g}$
Input axis misalignment	$<2 \text{ mrad } (\sim \pm 400'')$
Temperature sensitivity	$3\text{-}25 \mu\text{g } ^\circ\text{C}^{-1}$

Table 2.1: Descriptive sensor parameters of the Honeywell QA-2000 accelerometers (Dorobantu and Gerlach, 2004).

- *Gyroscopes:* The RQH integrates Honeywell dithered ring laser gyroscopes of the type GG1320 (Honeywell, b). The rotation sensing principle behind ring lasers is based on the Sagnac equation, relating the phase difference $\Delta\varphi$ of two light waves propagating in opposite direction for one revolution through a closed light path (index of the medium is set to 1) to the angular velocity ω , see Eq. (2.16) (Lawrence, 1998, Eq. 11.2).

$$\Delta\varphi = \frac{8\pi A}{c\lambda} \omega \tag{2.16}$$

A , c , and λ describe the area surrounded by the ring laser path, the speed of light in a vacuum, and the laser light wavelength, respectively. However, due to the resonator principle of the laser technique, the Sagnac equation has to be adapted to differences in the frequency. In Eq. (2.17) (Lawrence, 1998, Eq. 11.12) the relation between the frequency difference of the two light waves Δf and the angular rate ω becomes apparent.

$$\Delta f = \frac{4A}{\lambda L} \omega \quad (2.17)$$

L is the length of the closed light path. Δf is determined through optical interference.

Another characteristic of ring laser gyroscopes is the lock-in effect, which prevents the accurate determination of small angular rates. The effect occurs if the two bi-directional light-waves couple due to mirror deficiencies and thus assimilate their frequencies. Then, Δf becomes zero. This is only the case during phases with slow angular motion. The solution to this phenomenon is a technique called dithering that keeps the gyroscopes in a steady symmetrical oscillation around their null position. Consequently, the gyroscopes are constantly rotating (except for the moment of reversal) with an adequate known rate even when the RQH is not rotating.

The descriptive sensor error parameters for the ring laser gyroscopes are again adopted from tables in Dorobantu and Gerlach (2004) and presented in Table 2.2.

Parameter	Value
Bias repeatability	$\leq 0.002^\circ \text{ h}^{-1}$
White noise	$\leq 0.0018^\circ \text{ h}^{-0.5}$
Scale factor error	$\leq 10 \text{ ppm}$
Range	$\pm 500^\circ \text{ s}^{-1}$
Resolution	$1.13''$
Input axes misalignment	$\leq \pm 1 \text{ mrad} (\sim \pm 200'')$

Table 2.2: Descriptive sensor parameters of the Honeywell GG1320 gyroscopes (Dorobantu and Gerlach, 2004).

2.2.1.2 Static RQH performance To get an idea about the RQH performance, two static measurements are analyzed that were conducted in the cellar of the Institute of Astronomical and Physical Geodesy (IAPG) at a constant room temperature. During the measurements, the RQH was positioned once with its X axis pointing in downward direction and once with its Z axis pointing in upward direction, to study the influence of gravity on the sensors' performance. The measurements took around 6.5 and 30 h. For a better comparison, the 30 h data set was truncated to 6.5 h, too. While both data sets are used for the calculation of the Allan deviation (Allan (1966) and El-Sheimy et al. (2008)), only one specific section of the second data set is used to calculate sensor autocorrelations.

The Allan deviations of the accelerometers and gyroscopes are illustrated in Figs. 2.2, where four curves of Allan deviations are visualized for each axis. The solid lines represent measurements with the X axis pointing downward, the dashed lines show those where the Z axis is pointing upwards. For the thick lines, the warm-up phase of 5 h was eliminated from the data. For this analysis, slight variations among the curves do not bother, only larger structural differences are relevant that might influence the output of a campaign. Furthermore, it is noted that the Allan deviation gets less reliable towards the right side, where the number of averaging intervals decreases due to larger sections used for the averaging process¹⁵. The short averaging intervals (on the left side) of the accelerometers, up to

¹⁵The different lengths of the thin and thick data set are the reason why the thick lines do not reach the right side of the figures.

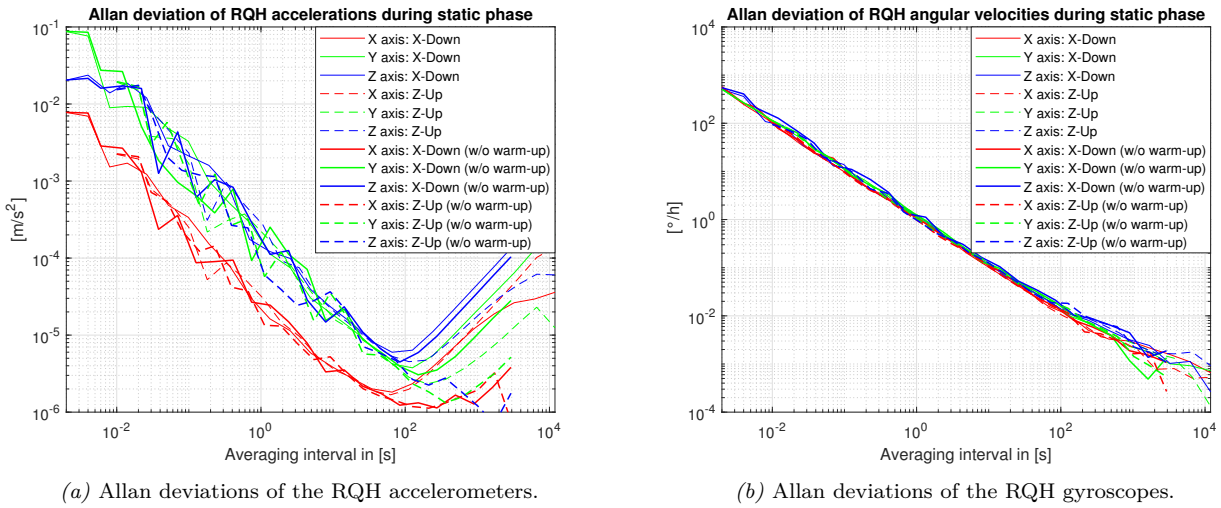


Figure 2.2: Allan deviations of static inertial measurement data exemplified by four static data sets. Thin-solid lines: X axis pointing downwards, RQH cold start. Thin-dashed lines: Z axis pointing upwards, RQH cold start. Thick-solid lines: X axis pointing downwards, RQH after warm-up. Thick-dashed lines: Z axis pointing upwards, RQH after warm-up. Accelerometer data is depicted in (a) and gyroscope data in (b).

10 s, are dominated by quantization noise (slope -1), with superior performance of the X component. White noise behavior (slope -0.5) is hard to identify, maybe between intervals of 10 s to 100 s. This is the area where the bias instability (slope 0) starts to dominate and where the thin and thick curves start to diverge. Overall, it can be stated that the thick curves run below the thin curves, which illustrates the effect of the instruments' warming-up onto the Allan deviation. The bias instabilities reach at least ~ 0.6 mGal with minimum values of $\sim 0.1 - 0.2$ mGal for the data sets excluding the warm-up phase. The minimum values are obtained for averaging intervals between 50 - 400 s. The sub-milligal level is already entered after ~ 5 s and ~ 30 s for X and Y/Z, respectively. This performance qualifies the RQH for sub-milligal gravimetry.

All accelerometers perform slightly better when Z is pointing in upward direction, which is the actual orientation of the RQH w.r.t. the car after installation. However, if the vertical gravity component is of major interest, X pointing downwards might lead to improved results due to the lowest Allan deviation. Another takeaway from Fig. 2.2(a) is that the accelerometers' poor long-term stability (towards the right side) inhibits the instrument from providing high-accuracy output over longer periods.

The gyroscopes illustrate their excellent performance and stability in Fig. 2.2(b). Up to around 100 s averaging intervals quantization noise (slope -1) is still the driving error source. Afterward, white noise (slope -0.5) is slowly flattening the slope of the curves. The bias instability is not reached after 10 000 s. Moreover, there is no warming-up effect visible in the Allan deviations.

To obtain accurate results from terrestrial 3D-gravity profiling campaigns, the biases of the RQH inertial sensors are estimated during the data processing (see Ch. 3) as a separate error-state. An appropriate stochastic model has to be defined that reflects the biases' temporal behavior properly. In recent airborne strapdown gravimetry campaigns with similar IMUs (Becker (2016) and Jensen (2018)) a Gauß-Markov model of first-order established as an appropriate model, see Eq. (2.18).

$$\dot{\mathbf{y}}(t) = -\mathbf{B}\mathbf{y}(t) + \mathbf{w}(t) \quad (2.18)$$

$\mathbf{w}(t)$ is white noise with a spectral density of $2\mathbf{B}\sigma^2$. σ^2 includes the variances of the accelerometer or gyroscope data. \mathbf{B} is a matrix with single β -values on the diagonal. In general, the β -values are

derived from the correlation times τ , in case of a first-order Gauß-Markov process via $\beta = 1/\tau$. τ is always defined as the leftmost intersection point of the autocorrelation curve with the horizontal line at σ/e ($e \hat{=}$ Euler's number). To quantify τ of the RQH ISA sensors, the normalized autocorrelations ($\sigma = 1$) of the static accelerometer and gyroscope data are illustrated in Figs. 2.3. Thereby, a period of ~ 5.5 h of the 30 h data set with decreased noise¹⁶ was selected, at a point in time where the RQH already warmed up (remaining temperature variation: ± 0.2 °C). In both cases, the autocorrelations show large peaks for lag 0, which indicates that all sensors are properly described by white noise behavior instead of a first-order Gauß-Markov model during the static measurement.

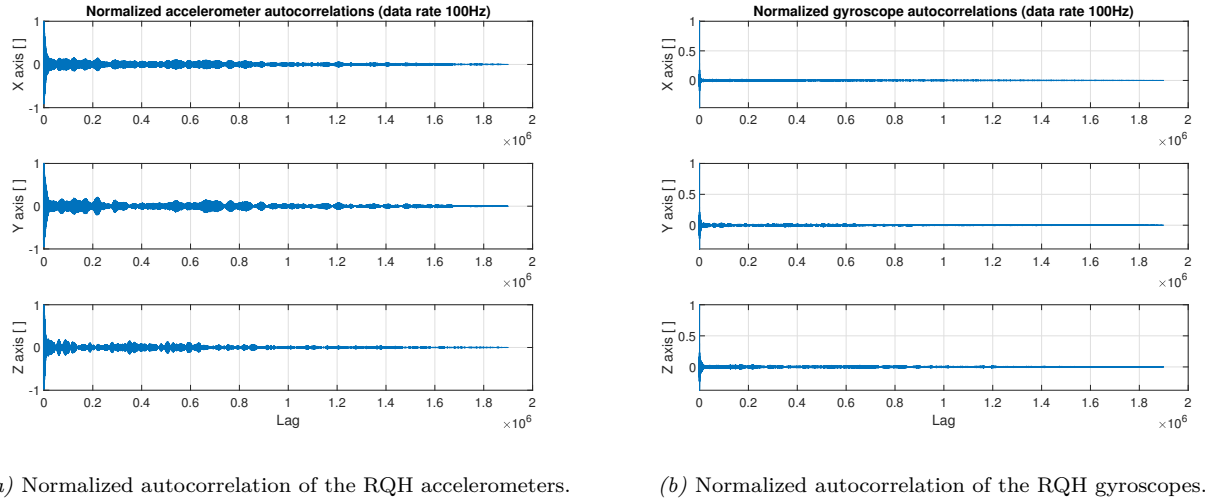


Figure 2.3: Normalized autocorrelation of the RQH ISA sensors. The underlying data originates from the 30 h data set, where a calm period of ~ 5.5 h was selected.

In the field, however, other effects can influence the sensor biases, e.g., Ch. 4.2 will explicitly address the temperature dependency of the accelerometer data. For this reason, empirically determined model parameters (τ and σ^2) have to be found for a proper estimation. The values used in this thesis are defined and listed in Table 4.9.

2.2.2 GNSS receivers

To accurately remove kinematic accelerations from the RQH observations, a sub-decimeter positioning solution in kinematic mode is needed. To fulfill this requirement, two geodetic receivers are applied in this thesis (cf. Ch. 4.3) that record code and phase observations and enable differential GNSS (DGNSS) positioning. Other possibilities would be to use a local positioning service like Satellitenpositionierungsdienst (SAPOS)¹⁷ in Germany for DGNSS or to apply precise point positioning (PPP) (Zumberge et al. (1997) and Kouba and Héroux (2001)) for the rover. For the basic concept of GNSS positioning and the receiver measuring principle, the reader is referred to Teunissen and Montenbruck (2017). The next paragraph outlines the GNSS measuring setup and the processing steps.

The rover is realized with a Septentrio AsteRx-U receiver (antenna: Javad GrAnt-G3) placed in the car. The base station, which should be located in the middle of and close to the trajectory, is a Leica Viva GNSS GS15 receiver (antenna included). Both receivers are able to track GPS, Globalnaja nawigazionnaja sputnikowaja sistema (GLO), Galileo (GAL), and BeiDou Navigation Satellite System (BDS) signals on multiple frequencies. The data is recorded in Receiver Independent Exchange

¹⁶The decreased noise level appears during the night time, probably due to the low traffic volume.

¹⁷<https://sapos.bayern.de/>

Format (RINEX). A mandatory feature of the rover is its ability to forward a PPS signal and NMEA messages that allows synchronizing the RQH with GPS time. The final position-velocity-time (PVT) solution for the rover antenna is acquired in post-processing by a commercial software called Inertial Explorer from NovAtel in version 8.70.8722.

The processing is a combination of PPP and DGNSS. The position of the base station is estimated first via PPP. PPP is a dedicated absolute positioning method for a single dual-frequency receiver. Thereby, the user has to provide "MGEX" final/precise orbits, which are public available¹⁸ with some latency. During PPP calculations, first-order ionospheric effects are removed. Ambiguities and the unmodeled tropospheric delay are estimated. Other error sources/effects are modeled, e.g., Earth tides or antenna offsets (Teunissen and Montenbruck, 2017). The final position of the base station is estimated with centimeter-accuracy for long observation intervals of several hours. During the next processing step, the rover PVT solution is generated with DGNSS positioning. The idea behind this method is to eliminate error sources that similarly affect both receivers, e.g., atmospheric delay and satellite orbit errors (Teunissen and Montenbruck, 2017). However, the assumption of similar impact of certain error sources is restricted to short receiver base-lines <10 km. Basically, two processing strategies can be related to the term DGNSS. The rover observations can be corrected by parameters (either in the state space or the observation space) estimated with the help of the fixed base station (PPP solution) or the observations of both receivers are double-differenced and the resulting relative position is added to the absolute position of the base station. The exact approach of Inertial Explorer is not known. Note that in both cases integer ambiguities still have to be estimated in parallel.

Annotation: GNSS positioning is known to be very stable over long periods, but rather poor over short time intervals. For navigation purposes, the combination with an IMU is beneficial for both systems by compensating the other instrument's stability deficiency. Unfortunately, this is not the case for strapdown gravimetry. Here, the sensors do not provide complementary data. It is the GNSS data that helps to remove the kinematic accelerations from the IMU observations to obtain gravity. Thus, it would be optimal if both sensors perform well over short and long periods.

2.2.3 Zenith camera

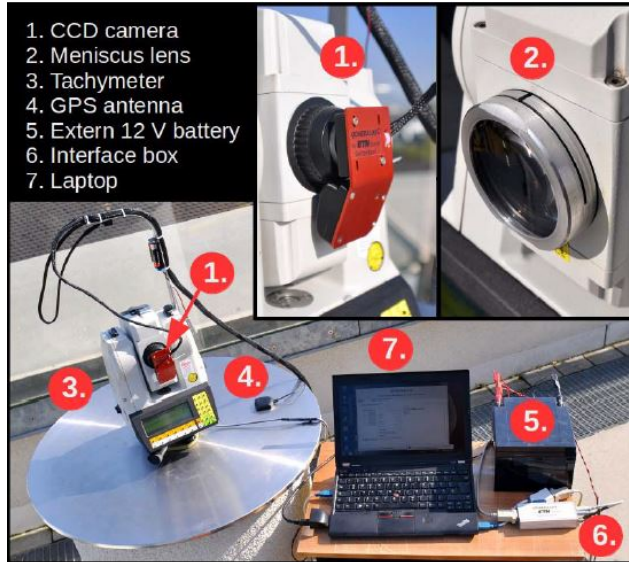
The determination of VDs (in Helmert's definition) for horizontal gravity updates (GUPTs) is realized with the digital QDaedalus zenith camera (Guillaume et al., 2012). This section gives an overview of the instrument. The provided information is based on Hauk (2014) and Hauk et al. (2016), where more detailed information about QDaedalus can be found.

In summary, zenith cameras are capable of calculating their astronomical coordinates by observing topocentric angles (spherical coordinates on topocentric sphere) to known stars, listed in fundamental catalogs. Together with the point's geodetic coordinates, VDs are computed with Eqs. (2.36) and (2.37).

QDaedalus is a unique light-weight realization of a zenith camera, developed by the Eidgenössische Technische Hochschule Zürich. Figure 2.4(a) presents the major components of QDaedalus and Fig. 2.4(b) exemplifies the QDaedalus setup during a measurement campaign. The star camera, a CCD image sensor (AVT Guppy F-080C), is mounted on the ocular of a precise total station. Due to the adapted light path, caused by the CCD image sensor, an additional meniscus lens has to be applied in the front of the total station. The CCD image sensor observes with 30 Hz and transmits the data to a laptop, connected via FireWire. For the correct time synchronization of all observations, and for the determination of ellipsoidal coordinates, a u-blox GPS antenna (ANN-MS) is connected to an u-blox interface box (LEA-6T) that integrates a GPS receiver. The interface box also transmits

¹⁸<https://www.igs.org/mgex/data-products/#products>

steering commands to the total station via a GeoCom-interface to target the reference stars, and control commands to the CCD image sensor. A dedicated software handles the communication and data recording. The data acquired are circle readings from the total station, star images, and GPS time epochs. Thereby, the total station needs to provide accurate angle measurements at least below the $1''$ -accuracy level. Note that additionally, precise geodetic coordinates have to be available for the determination of accurate VDs. The major task of the integrated GPS receiver is to provide precise timing information to the system.



(a) QDaedalus parts, original from Hauk et al. (2016, Fig. 1).



(b) QDaedalus during a campaign in Perth, Western Australia (see Ch. 4.1).

Figure 2.4: Illustration of QDaedalus components (a) and operational setup (b).

Before starting a measurement, QDaedalus has to be leveled, the alignment of the CCD image sensor w.r.t. the total station has to be determined (automated process), and the system has to be oriented along the north direction by observations to known stars. Then, QDaedalus automatically targets stars brighter than magnitude 6 that lie in a defined zenith angle range, uniformly distributed in azimuth directions of $0 - 90^\circ$, $90 - 180^\circ$, $180 - 270^\circ$, and $270 - 360^\circ$. The observation sequence should last ~ 15 min and should be repeated three to four times in a row for redundancy.

The calculation of the astronomical coordinates is realized in an iterative least-squares adjustment. Therefore, the CCD coordinates of each star have to be determined and combined with the total station circle readings to obtain topocentric coordinates. The i-frame coordinates of the observed stars, defined in the FK6 (Sixth Catalogue of Fundamental Stars, Wielen et al. (1999)), are transformed into the e-frame at the epoch of observation. The relation between the topocentric coordinates and the e-frame coordinates can then be expressed in terms of the astronomical coordinates (presented in Eqs. (4.17) and (4.18) in Hauk et al. (2016)).

2.2.4 Relative gravimeter

The determination of gravity values for vertical GUPTs is realized with a Scintrex CG-5 relative gravimeter, shown in Fig. 2.5. The following notes are based on Scintrex Limited (2017), where the interested reader finds more information.

Relative gravimeters can provide accurate absolute gravity when the determined gravity changes are referenced to an absolute gravity tie point. Thereby, the CG-5 fulfills high-accuracy requirements for gravity determination. The standard deviation is listed with ± 0.005 mGal and the daily drift is below 0.02 mGal day⁻¹. For terrestrial 3D-gravimetry, this accuracy level is more than sufficient. It is equally important that the system has a shock mount system, is robust, quickly operational, thermostatically stabilized, and easy to use. The system automatically applies an Earth tide correction after Longman (Longman, 1959), compensates slight level errors, and corrects the internal drift via a software-based automated method.

The sensor of the CG-5 is a spring-mass unit, in this case, a fused quartz spring system. The proof-mass is pulled by a spring against gravity. As soon as gravity changes, a capacitive displacement transducer detects a shift in the position of the proof-mass. A feedback circuit automatically initiates an electrostatic restoring force through capacitor plates to compensate for the gravity changes and to keep the mass close to its null position. The feedback voltage applied to the capacitor plates is multiplied with a calibration factor to obtain an output in milligal, which resembles the CG-5 readings.



Figure 2.5: Scintrex CG-5 relative gravimeter in operation, leveled via tripod.

2.3 Gravity disturbance and height anomaly differences

The gravity field of the Earth, as defined in classical mechanics, is of major interest and importance in geodesy, e.g., the realization of a physical height system or the prediction of satellite orbits depend both on precise knowledge about its physical and geometrical properties. It also provides valuable information to other scientific and social/civil disciplines, locally, regionally, and globally. This includes geophysics, hydrology, glaciology, oceanography, navigation, and water management among others. This thesis is considered as a contribution to the local gravity field determination and validation. Therefore, this section addresses the relation between the gravitational force and the gravity field functionals determined throughout the campaigns described in Chs. 4.1 and 4.3, namely the gravity disturbance in vector form as well as in terms of VDs and the SGD, and the height anomaly differences.

The following explanations are based on Heiskanen and Moritz (1967), Hofmann-Wellenhof and Moritz (2006), and Torge and Müller (2012), where the interested reader finds a comprehensive overview of physical geodesy.

2.3.1 Gravity potential and acceleration

The gravitational force $\mathbf{F}_{[g]}$ between two point masses $m_{[0]}$ and $m_{[1]}$, which are separated by the distance defined by the vector $\mathbf{l}_{[1]}$, is described by Newton's Law of Gravitation in Eq. (2.19).

$$\mathbf{F}_{[g]}(\mathbf{l}_{[1]}) = -G \frac{m_{[0]}m_{[1]}}{|\mathbf{l}_{[1]}|^2} \frac{\mathbf{l}_{[1]}}{|\mathbf{l}_{[1]}|} \quad (2.19)$$

$G = 6.674 \cdot 10^{-11} \text{ m}^3 \text{ kg}^{-1} \text{ s}^{-2}$ is known as the gravitational constant. When applying Eq. (2.19) to the system Earth (including oceans and atmosphere), the Earth can be regarded as an aggregation of an infinite number of such point masses leading to Eq. (2.20).

$$\mathbf{F}_{[g]}(\mathbf{r}) = \mathbf{F}_{[g]}(\mathbf{l}_{[1]}) + \mathbf{F}_{[g]}(\mathbf{l}_{[2]}) + \dots + \mathbf{F}_{[g]}(\mathbf{l}_{[n]}) = -Gm_{[0]} \sum_{i=1}^{n=\infty} \frac{m_{[i]}}{|\mathbf{l}_{[i]}|^2} \frac{\mathbf{l}_{[i]}}{|\mathbf{l}_{[i]}|} \quad (2.20)$$

where \mathbf{r} represents the vector between the center of mass of the Earth and $m_{[0]}$.

With $\mathbf{F}_{[g]}(\mathbf{r}) = m_{[0]}\tilde{\mathbf{g}}(\mathbf{r})$, the gravitational field¹⁹ $\tilde{\mathbf{g}}$ yields

$$\tilde{\mathbf{g}}(\mathbf{r}) = -G \sum_{i=1}^{n=\infty} \frac{m_{[i]}}{|\mathbf{l}_{[i]}|^2} \frac{\mathbf{l}_{[i]}}{|\mathbf{l}_{[i]}|} \Rightarrow -G \iiint_{Earth} \frac{\mathbf{l}}{|\mathbf{l}|^3} dm. \quad (2.21)$$

dm is given by the density times the infinitesimal volume of the mass element i . Since the gravitational field is a conservative vector field, it can be expressed as gradient of the scalar gravitational potential V .

$$\tilde{\mathbf{g}}(\mathbf{r}) = \nabla V(\mathbf{r}) \quad (2.22)$$

$$V(\mathbf{r}) = G \iiint \frac{1}{|\mathbf{l}|} dm \quad (2.23)$$

The gravitational potential contains the identical information as the gravitational field although it is a scalar quantity. Furthermore, V fulfills the Laplace equation outside of the Earth, and its first and second derivatives outside of the Earth are continuous, meaning that it is a harmonic function.

For an observer rotating with the Earth, the centrifugal acceleration \mathbf{z} and potential Z superimpose $\tilde{\mathbf{g}}$ and V , respectively. \mathbf{z} and Z , caused by the Earth's rotation, are defined in Eqs. (2.24) and (2.25).

$$\mathbf{z}(\mathbf{r}) = -\boldsymbol{\omega}_{[ie]} \times (\boldsymbol{\omega}_{[ie]} \times \mathbf{r}) = \omega_{[Earth]}^2 \mathbf{p} = \nabla Z(\mathbf{r}) \quad (2.24)$$

$$Z(\mathbf{r}) = \frac{1}{2} \omega_{[Earth]}^2 \mathbf{p}^2 \quad (2.25)$$

$\omega_{[Earth]}$ and \mathbf{p} represent the magnitude of the Earth's rotation and the orthogonal vector between the rotation axis of the Earth and the point defined by \mathbf{r} . Z does not fulfill Laplace's equation and therefore is not harmonic. Disregarding external gravitational forces, the gravity potential²⁰ is expressed as

$$W(\mathbf{r}) = V(\mathbf{r}) + Z(\mathbf{r}) = G \iiint \frac{1}{|\mathbf{l}|} dm + \frac{1}{2} \omega_{[Earth]}^2 \mathbf{p}^2. \quad (2.26)$$

¹⁹also called gravitational acceleration or gravitation

²⁰ W is not harmonic due to Z .

A surface of identical gravity potential values is called an equipotential surface. From a physical point of view, this surface is leveled in each point and therefore its physical height is constant. In geodesy, the equipotential surface that best fits the mean sea level, called geoid, is of major interest, since it represents the vertical reference surface. Equation (2.26) states that such a surface could be determined if the density and volume of all mass elements are known. Unfortunately, this information is inaccessible and can only be approximated by geophysical models.

To gain information about the gravity potential, potential differences and derivatives of the potential can be observed. The gradient of W , also called gravity field or gravity, is determined with geodetic measurement techniques in Chs. 4.1 and 4.3. The linear relation in Eq. (2.26) allows to define gravity according to Eq. (2.27).

$$\mathbf{g}(\mathbf{r}) = \tilde{\mathbf{g}}(\mathbf{r}) + \mathbf{z}(\mathbf{r}) \quad (2.27)$$

However, analyses are usually based on the disturbing potential, which is a reduction of W by a precisely defined reference potential. This step simplifies mathematical relations (linearization) and generates more intuitive quantities. Therefore, the disturbing potential and the gravity disturbance are introduced next.

2.3.2 Disturbing potential

The disturbing potential T is the difference between W and a chosen normal potential U .

$$T(\mathbf{r}) = W(\mathbf{r}) - U(\mathbf{r}). \quad (2.28)$$

The GRS80 for example, which is used throughout the thesis, is not only a geometric reference (rotational ellipsoid) but also a physical one, equipped with a potential based on its geometrical and physical constants, see Moritz (2000). U can be calculated at any point with Eq. (2.29). Like W , it is not a harmonic function outside the ellipsoid.

$$\begin{aligned} U(\mathbf{r}) &= V_{[Ellipsoid]}(\mathbf{r}) + Z_{[Ellipsoid]}(\mathbf{r}) \\ &= \frac{GM}{E} \arctan(e') + \frac{1}{3}\omega_{[Earth]}^2 a^2 + \frac{1}{2}\omega_{[Earth]}^2 \mathbf{p}^2 \end{aligned} \quad (2.29)$$

where GM stands for the geocentric gravitational constant of the Earth, E for the linear eccentricity, e' for the second eccentricity and a is the semimajor axis of the meridian ellipse. Assuming that the true rotation rate of the Earth does not deviate from $\omega_{[Earth]}$ in Eq. (2.29), Z cancels, and therefore T is harmonic, resembling the difference between $V(\mathbf{r})$ and $V_{[Ellipsoid]}(\mathbf{r})$.

The gravity disturbance \mathbf{dg} is calculated in a similar fashion, based on the corresponding gradients. It is usually expressed in the n-frame, see Eq. (2.30). Here, \mathbf{r} is described in terms of geodetic coordinates.

$$\mathbf{dg}^n(\varphi, \lambda, h) = \mathbf{g}^n(\varphi, \lambda, h) - \boldsymbol{\gamma}^n(\varphi, h) \quad (2.30)$$

Note that the normal gravity $\boldsymbol{\gamma}$ is independent of λ due to the ellipsoidal shape of the potential. The magnitude of $\boldsymbol{\gamma}$ on the ellipsoid can be formulated after Somigliana in Eq. (2.31) (Torge and Müller, 2012, Eq. 4.41a).

$$\gamma_{[0]}(\varphi, h = 0) = \frac{a\gamma_{[a]} \cos^2 \varphi + b\gamma_{[b]} \sin^2 \varphi}{\sqrt{a^2 \cos^2 \varphi + b^2 \sin^2 \varphi}} \quad (2.31)$$

b is the semiminor axis, $\gamma_{[a]}$ and $\gamma_{[b]}$ represent the magnitude of the normal gravity at the equator and the poles, respectively, at $h = 0$ m. In the exterior space, $\boldsymbol{\gamma}$ is calculated according to Eq. (2.32)

(Torge and Müller, 2012, Eq. 4.63), with higher order terms (HOT) neglected.

$$\gamma(\varphi, h) = \gamma_{[0]} \left(1 - \frac{2}{a} \left(1 + f + \frac{\omega_{[Earth]} a^2 b}{GM} - 2f \sin^2 \varphi \right) h + \frac{3}{a^2} h^2 \right) + \text{HOT} \quad (2.32)$$

where f accounts for the flattening of the ellipsoid. On the ellipsoidal surface, no horizontal components of γ exist. As soon as this surface is left, the north-south component deviates from zero. This effect emerges from the property of equipotential surfaces that do not proceed parallel in different heights, which results in a slight curvature of the plumb line w.r.t. the normal of the reference ellipsoid. Equation (2.33) defines the direction of γ in the n-frame. The north component is defined in Jekeli (2001, Eq. 6.92). $h_{[meter]}$ is the ellipsoidal height above the reference surface in meter.

$$\gamma^n(\varphi, h) = \begin{pmatrix} \gamma_{[E]}^n \\ \gamma_{[N]}^n \\ \gamma_{[U]}^n \end{pmatrix} = \begin{pmatrix} 0 \\ 8.08 \cdot 10^{-9} h_{[meter]} \sin(2\varphi) \\ -\gamma(\varphi, h) \end{pmatrix} \quad (2.33)$$

Equation (2.33) must be applied to Eq. (2.30) if the VDs are defined according to the theory of Molodensky. For Helmert's theory, Eq. (2.34) is valid. By setting the north component to zero, the curvature of the plumb line is disregarded. More details follow in the next chapter.

$$\gamma^n(\varphi, h) = \begin{pmatrix} \gamma_{[E]}^n \\ \gamma_{[N]}^n \\ \gamma_{[U]}^n \end{pmatrix} = \begin{pmatrix} 0 \\ 0 \\ -\gamma(\varphi, h) \end{pmatrix} \quad (2.34)$$

As already explained in Ch. 2.1.1, the n-frame axes are aligned w.r.t. the reference ellipsoid. \mathbf{g} , however, is observed perpendicular to the physical equipotential surface in the observation point. The next part illustrates the transformation of \mathbf{g} into the n-frame to be able to solve Eq. (2.30).

2.3.3 Vertical deflections and scalar gravity disturbance

The direction of \mathbf{g} always aligns with the local plumb line, which results in a simple mathematical expression in the l-frame as can be seen in Eq. (2.35).

$$\mathbf{g}^l(\varphi, \lambda, h) = \begin{pmatrix} g_{[E]}^l \\ g_{[N]}^l \\ g_{[U]}^l \end{pmatrix} = \begin{pmatrix} 0 \\ 0 \\ -|\mathbf{g}| \end{pmatrix} \quad (2.35)$$

$|\mathbf{g}|$ can be observed with absolute gravimeters or relative gravimeters in combination with a gravity tie point. To be able to transform \mathbf{g}^l into the n-frame, one has to determine the relative orientation of the l-frame w.r.t. n-frame. This can be realized by observing VDs.

As stated in Schack et al. (2018), "VDs are the angular difference between the direction of the plumbline and some reference direction (e.g., Jekeli (1999)). The direction of the plumbline (true vertical) is defined through the gravity vector. In Molodensky's definition of the VD, the normal plumbline (at the telluroid) serves as the reference direction. In Helmert's definition, VDs are defined as the angle between the direction of the gravity vector at the Earth's surface and the ellipsoidal surface normal through the same point. Each definition differs by the curvature of the normal plumb line (e.g., Torge and Müller (2012, p. 107))." VDs in Helmert's definition thus describe the l- to n-frame orientation and can be obtained from zenith camera observations to fixed stars (e.g., Hirt et al. (2010a)). Thereby,

astronomical coordinates determined by the zenith camera and geodetic coordinates determined via GNSS in the same point are subtracted to reveal the north-south (ξ) and east-west (η) VD components using (e.g., Voigt (2013, p. 27))

$$\begin{aligned}\xi &= \sin \Phi \cos \varphi - \cos \Phi \sin \varphi \cos(\Lambda - \lambda) \\ \eta &= \sin(\Lambda - \lambda) \cos \Phi.\end{aligned}\tag{2.36}$$

in mountainous regions. With flat topography or accuracy demands above a few 0.01'' the first-order Taylor in Eq. (2.37) series suffices.

$$\begin{aligned}\xi &= \Phi - \varphi \\ \eta &= (\Lambda - \lambda) \cos \varphi\end{aligned}\tag{2.37}$$

Neglecting the horizontal VD (frame misalignment around the vertical) and remembering that the SAA can be applied since the VDs are small, leads to

$$\mathbf{g}^n(\varphi, \lambda, h) = \begin{pmatrix} g_{[E]}^n \\ g_{[N]}^n \\ g_{[U]}^n \end{pmatrix} = \mathbf{R}_i^n \mathbf{g}^l = \begin{pmatrix} 1 & 0 & \eta \\ 0 & 1 & \xi \\ -\eta & -\xi & 1 \end{pmatrix} \begin{pmatrix} 0 \\ 0 \\ -|\mathbf{g}| \end{pmatrix} = \begin{pmatrix} -\eta|\mathbf{g}| \\ -\xi|\mathbf{g}| \\ -\sqrt{|\mathbf{g}|^2 - (g_{[E]}^n)^2 - (g_{[N]}^n)^2} \end{pmatrix}.\tag{2.38}$$

With this information, $\mathbf{d}\mathbf{g}^n$, known from Eq. (2.30), can be calculated. Lastly, the SGD is introduced, which resembles the difference between $|\mathbf{g}|$ and $|\boldsymbol{\gamma}|$ at the same point. The combination of VDs and SGD contains similar information as $\mathbf{d}\mathbf{g}^n$.

2.3.4 Astronomical leveling²¹

Following the theory of astronomical leveling (Helmert, 1880/1884), VDs observed at the Earth's surface are numerically integrated along a path to obtain height anomaly differences $\Delta\zeta$ (Torge and Müller, 2012, p. 298).

$$\Delta\zeta_{[AB]} = - \int_A^B \epsilon ds - NC\tag{2.39}$$

A and B denote the endpoints of the path, $\epsilon = \xi \cos \alpha + \eta \sin \alpha$ is the VD component in geodetic azimuth α , ds is the geodesic distance between adjacent VD stations, and NC is the normal correction (Torge and Müller, 2012, p. 254)

$$NC = \int_A^B \frac{|\mathbf{g}| - \gamma}{\gamma} dn + \frac{\bar{\gamma}_{[A]} - \gamma}{\gamma} H_{[A]} - \frac{\bar{\gamma}_{[B]} - \gamma}{\gamma} H_{[B]}\tag{2.40}$$

which depends on surface gravity values $|\mathbf{g}|$, leveled height differences dn between adjacent stations, mean normal gravity values $\bar{\gamma}_{[A]}$, $\bar{\gamma}_{[B]}$ along the plumb lines of the endpoints A and B , and an arbitrary constant normal gravity value $\gamma = \gamma(45^\circ, 0\text{ m})$. $H_{[A]}$ and $H_{[B]}$ are normal heights from the leveling traverse or can be approximated through a digital elevation model (DEM). The combined

²¹Schack et al. (2018), see remarks on p. 6

and discretized form of Eqs. (2.39) and (2.40) is

$$\begin{aligned} \Delta\zeta_{[AB]} \approx & - \sum_{i=1}^{n-1} \left(\frac{\xi_{[i]} + \xi_{[i+1]}}{2} \cos \alpha + \frac{\eta_{[i]} + \eta_{[i+1]}}{2} \sin \alpha \right) ds_{[i,i+1]} \\ & - \sum_{i=1}^{n-1} \left(\frac{0.5(|\mathbf{g}|_{[i]} + |\mathbf{g}|_{[i+1]}) - \gamma}{\gamma} \right) dn_{[i,i+1]} - \frac{\bar{\gamma}_{[A]} - \gamma}{\gamma} H_{[A]} + \frac{\bar{\gamma}_{[B]} - \gamma}{\gamma} H_{[B]} \end{aligned} \quad (2.41)$$

where indices i and $i + 1$ denote adjoining stations with VDs, gravity values and height differences. $\Delta\zeta_{[AB]}$ provides insight into the evolution of the normal height $H^{[N]}$, which is a physical height, in relation to the geometric height h ($h = \zeta + H^{[N]}$). Torge and Müller (2012, Fig. 6.1) provide a visual interpretation of ζ .

2.4 Multi-sensor data fusion

In this thesis, the data collected by the sensors, described in Ch. 2.2, are combined in a Kalman Filter environment. The data fusion is formulated in the time domain using the state-space notation in discrete form. Thereby, the mathematical description of the physical system under investigation is non-linear. The EKF is an appropriate tool for non-linear minimum variance estimation. It is implemented based on error-states in a loosely-coupled, closed-loop manner, wherein general sensor raw data are pre-processed independently, before being forwarded to the EKF. Hereby, the estimated error-state vector is directly fed back to correct the total-state vector.

The next paragraphs have their origin in Gelb (1974), Jekeli (2001), and Groves (2008). In the beginning, the link between the linearization of the functional model and the error-state approach is described. Then, the equations forming the EKF are presented and finally, the smoothing algorithm is defined. Details about the implementation follow in Ch. 3.

2.4.1 Linearization and error-state concept

The EKF handles non-linear systems by linearizing the functional model around the last best guess of the state-vector, assuming linear behavior over short time intervals. It is important to understand that the closed-loop concept is vital in case error-states are used because by directly re-applying the estimated error-states to the total-states the system cannot "drift away".

The linearization process is closely coupled with the idea of an error-state in this work. The IMU observations (cf. Ch. 2.2) and the strapdown navigation (cf. Ch. 3.1.1) are maintained outside of the EKF update phase. Thus, this deterministic part, which is also called "control", is removed from the Kalman Filter. The general non-linear vector-matrix differential equation (Eq. (2.42)) then becomes linear (Eq. (2.43)) w.r.t. the residual error signal that is not or not correctly covered by the IMU observations.

$$\dot{\mathbf{y}}_{[k]} = f(\mathbf{y}_{[k-1]}, dt) + l(\mathbf{u}_{[k-1]}, dt) \quad (2.42)$$

$$\delta\dot{\mathbf{y}}_{[k]} = \mathbf{F}_{[k,k-1]} \delta\mathbf{y}_{[k-1]} \quad (2.43)$$

\mathbf{y} is called the total-state vector, $\delta\mathbf{y}$ the error-state vector, f and l can be any non-linear function, \mathbf{u} is the control input and dt is the constant time interval between $k - 1$ and k . In this case, $l(\mathbf{u}_{[k-1]}, dt)$ covers the IMU signal and is treated separately outside of the EKF update phase. A first-order differential equation remains that describes the evolution of the error-state with the help of the system matrix \mathbf{F} .

The relation between Eqs. (2.42) and (2.43) is briefly deduced. Assuming a non-linear function a in Eq. (2.44) that depends on the total-state vector \mathbf{b} and the constant time interval dt .

$$\dot{\mathbf{b}}_{[k]} = a(\mathbf{b}_{[k-1]}, dt) \quad (2.44)$$

Additionally, the true vectors of \mathbf{b} and $\dot{\mathbf{b}}$ are replaced by the estimated vector ($\check{}$) plus an error/correction vector (δ), as shown in Eqs. (2.45).

$$\mathbf{b}_{[k]} = \check{\mathbf{b}}_{[k]} + \delta\mathbf{b}_{[k]} \quad (2.45a)$$

$$\dot{\mathbf{b}}_{[k]} = \check{\dot{\mathbf{b}}}_{[k]} + \delta\dot{\mathbf{b}}_{[k]} \quad (2.45b)$$

The combination of Eq. (2.44) and Eqs. (2.45) gives

$$\check{\dot{\mathbf{b}}}_{[k]} + \delta\dot{\mathbf{b}}_{[k]} = a(\check{\mathbf{b}}_{[k-1]} + \delta\mathbf{b}_{[k-1]}, dt). \quad (2.46)$$

Describing Eq. (2.46) by means of a first-order Taylor series expansion, Eq. (2.47) is derived.

$$a(\check{\mathbf{b}}_{[k-1]} + \delta\mathbf{b}_{[k-1]}, dt) \approx a(\check{\mathbf{b}}_{[k-1]}, dt) + \left. \frac{\partial a(\mathbf{b}_{[k-1]}, dt)}{\partial \mathbf{b}_{[k-1]}} \right|_{\mathbf{b}_{[k-1]}=\check{\mathbf{b}}_{[k-1]}} \delta\mathbf{b}_{[k-1]} + \text{HOT} \quad (2.47)$$

Then, the relations to Eqs. (2.42) and (2.43) become apparent, see Eqs. (2.48) to (2.50).

$$\check{\dot{\mathbf{b}}}_{[k]} + \delta\dot{\mathbf{b}}_{[k]} = a(\check{\mathbf{b}}_{[k-1]}, dt) + \left. \frac{\partial a(\mathbf{b}_{[k-1]}, dt)}{\partial \mathbf{b}_{[k-1]}} \right|_{\mathbf{b}_{[k-1]}=\check{\mathbf{b}}_{[k-1]}} \delta\mathbf{b}_{[k-1]} \quad (2.48)$$

$$\check{\dot{\mathbf{b}}}_{[k]} = a(\check{\mathbf{b}}_{[k-1]}, dt) \Rightarrow \check{\dot{\mathbf{y}}}_{[k]} = l(\mathbf{u}_{[k-1]}, dt) \quad (2.49)$$

$$\begin{aligned} \delta\dot{\mathbf{b}}_{[k]} &= \left. \frac{\partial a(\mathbf{b}_{[k-1]}, dt)}{\partial \mathbf{b}_{[k-1]}} \right|_{\mathbf{b}_{[k-1]}=\check{\mathbf{b}}_{[k-1]}} \delta\mathbf{b}_{[k-1]} \Rightarrow \delta\dot{\mathbf{y}}_{[k]} = \left. \frac{\partial f(\mathbf{y}_{[k-1]}, dt)}{\partial \mathbf{y}_{[k-1]}} \right|_{\mathbf{y}_{[k-1]}=\check{\mathbf{y}}_{[k-1]}} \delta\mathbf{y}_{[k-1]} \\ &= \mathbf{F}_{[k,k-1]} \delta\mathbf{y}_{[k-1]} \end{aligned} \quad (2.50)$$

\mathbf{F} of terrestrial 3D-gravity profiling is derived in Ch. 3.1.2. By keeping the IMU signal outside of the EKF update phase, computational efforts are reduced in two ways. Firstly, the error-state vector does not have to include the accelerometer and gyroscope errors, which would be necessary for the measurement model in Eq. (2.54). Instead, it is adequate if only the sensor noise is taken into account in terms of attitude and velocity noise. Secondly, the EKF routines do not have to be executed at the measurement rate of the IMU, but only at the rate of available EKF updates.

The differential Eq. (2.50) builds the foundation of the EKF, describing the error-state propagation. It is solved with the help of the transition matrix Φ , which is derived from \mathbf{F} in Eq. (2.51), in this thesis truncated at $n = 1$.

$$\Phi_{[k,k-1]} = e^{\mathbf{F}_{[k,k-1]}dt} = \mathbf{I} + \sum_{i=1}^{n=\infty} \frac{\mathbf{F}_{[k,k-1]}^i dt^i}{i!} \quad (2.51)$$

2.4.2 Extended Kalman Filter

The general idea behind the Kalman Filter is to propagate a linear system state in time and to update the propagated state as soon as additional information, like external observations, are available. The EKF allows to apply the Kalman Filter concept to non-linear systems through linearization (cf. Ch. 2.4.1), in this case in terms of error-states.

In the beginning, $\mathbf{y}_{[0]}$, $\delta\mathbf{y}_{[0]}$, and the error-state covariance matrix $\mathbf{P}_{[0]}$ are initialized by measurements or empirically. With the system noise as Gaussian white noise $\mathbf{w}_{[k]} \sim \mathcal{N}(\mathbf{0}, \mathbf{Q}_{[k]})$ with zero-mean and variance $\mathbf{Q}_{[k]}$, the system model for propagating the error-state is

$$\delta\mathbf{y}_{[k]} = \Phi_{[k,k-1]}\delta\mathbf{y}_{[k-1]} + \mathbf{w}_{[k-1]}. \quad (2.52)$$

When implementing the system model, it is distinguished between the propagation of the error-state estimate and the propagation of the error-state covariance information.

$$\delta\check{\mathbf{y}}_{[k]}^{[-]} = \Phi_{[k,k-1]}\delta\check{\mathbf{y}}_{[k-1]}^{[+]} \quad (2.53a)$$

$$\mathbf{P}_{[k]}^{[-]} = \Phi_{[k,k-1]}\mathbf{P}_{[k-1]}^{[+]} \Phi_{[k,k-1]}^T + \mathbf{Q}_{[k-1]} \quad (2.53b)$$

In Eqs. (2.53), $^{[+]}$ and $^{[-]}$ signify if the matrix or vector is the best guess or if it is a propagated term, respectively. Remember that the closed-loop concept is applied in this thesis, which means that $\delta\check{\mathbf{y}}_{[k-1]}^{[+]}$ is set to zero after being added to the total-state vector, see Eq. (2.57). Thus, Eq. (2.53a) becomes zero and is in fact not implemented. Concerning \mathbf{P} , the propagated term becomes the best guess of the next epoch if no update is available ($\mathbf{P}_{[k]}^{[-]} \rightarrow \mathbf{P}_{[k]}^{[+]}$). If an update is available, $\delta\check{\mathbf{y}}_{[k]}^{[+]}$ and $\mathbf{P}_{[k]}^{[+]}$ are calculated as follows.

Firstly, the measurement model has to be defined as a linear system with the measurement noise $\mathbf{v}_{[k]} \sim \mathcal{N}(\mathbf{0}, \mathbf{R}_{[k]})$, see Eq. (2.54).

$$\mathbf{z}_{[k]} = \mathbf{H}_{[k]}\delta\mathbf{y}_{[k]} + \mathbf{v}_{[k]} \quad (2.54)$$

\mathbf{H} is the measurement matrix associating $\delta\mathbf{y}$ with the observations \mathbf{z} . Then, the Kalman Gain matrix \mathbf{K} is introduced. It is a weighting matrix that realizes a minimum variance estimate. The matrix is mathematically deduced via the cost function of the trace of $\mathbf{P}_{[k]}^{[+]}$, which results in Eq. (2.55).

$$\mathbf{K}_{[k]} = \mathbf{P}_{[k]}^{[-]}\mathbf{H}_{[k]}^T \left[\mathbf{H}_{[k]}\mathbf{P}_{[k]}^{[-]}\mathbf{H}_{[k]}^T + \mathbf{R}_{[k]} \right]^{-1} \quad (2.55)$$

\mathbf{R} is the measurement noise matrix, which characterizes the observation accuracies. Then, $\delta\check{\mathbf{y}}_{[k]}^{[+]}$ and $\mathbf{P}_{[k]}^{[+]}$ are calculated as

$$\begin{aligned} \delta\check{\mathbf{y}}_{[k]}^{[+]} &= \delta\check{\mathbf{y}}_{[k]}^{[-]} + \mathbf{K}_{[k]} \left[\mathbf{z}_{[k]} - \mathbf{H}_{[k]}\delta\check{\mathbf{y}}_{[k]}^{[-]} \right] & (\delta\check{\mathbf{y}}_{[k]}^{[-]} = \mathbf{0}) \\ &= \mathbf{K}_{[k]}\mathbf{z}_{[k]} \end{aligned} \quad (2.56a)$$

$$\mathbf{P}_{[k]}^{[+]} = \left[\mathbf{I} - \mathbf{K}_{[k]}\mathbf{H}_{[k]} \right] \mathbf{P}_{[k]}^{[-]} \quad (2.56b)$$

Next, the closed-loop step is conducted as described in Eq. (2.57).

$$\check{\mathbf{y}}_{[k]} = \check{\mathbf{y}}_{[k]} + \delta\check{\mathbf{y}}_{[k]}^{[+]} \Rightarrow \delta\check{\mathbf{y}}_{[k]}^{[+]} = \mathbf{0} \quad (2.57)$$

This implication is important because after having applied the updated error-state vector $\delta\check{\mathbf{y}}_{[k]}^{[+]}$ the total-state vector $\check{\mathbf{y}}_{[k]}$ is considered as a best guess. Consequently, the corresponding error-state values must be reset to zero.

2.4.3 RTS smoother

The advantage of gravimetric campaigns is that no real-time evaluation/output is needed. Thus far, the EKF solution is based on the chronological processing of observations, which means that one observation in time is only linked with earlier observations through the EKF. The EKF solution can be improved by reprocessing backward in time, which is called smoothing. Presuming that the system noise and measurement noise are normally distributed and uncorrelated, the Rauch-Tung-Striebel (RTS) smoother is an appropriate tool to improve the results of a linear dynamic system. The RTS smoother is originally described in Rauch et al. (1965), where Eqs. (3.28), (3.29), and (3.31) depict the mathematical formulation of the smoother. The equations are repeated here in a different notation, see Eqs. (2.58) - (2.60).

$$\mathbf{P}\Phi\mathbf{P} = \mathbf{P}_{[k]}^{[+]} \Phi_{[k+1,k]}^T (\mathbf{P}_{[k+1]}^{[-]})^{-1} \quad (2.58)$$

$$\delta\mathbf{y}_{[k]}^{[RTS]} = \delta\mathbf{y}_{[k]}^{[+]} + \mathbf{P}\Phi\mathbf{P}(\delta\mathbf{y}_{[k+1]}^{[RTS]} - \delta\mathbf{y}_{[k+1]}^{[-]}) \quad (2.59)$$

$$\mathbf{P}_{[k]}^{[RTS]} = \mathbf{P}_{[k]}^{[+]} + \mathbf{P}\Phi\mathbf{P}(\mathbf{P}_{[k+1]}^{[RTS]} - \mathbf{P}_{[k+1]}^{[-]})(\mathbf{P}\Phi\mathbf{P})^T \quad (2.60)$$

In the final step, the RTS results have to be applied to the EKF total-states. Here, it is important to apply only the residuals between the RTS error-state values and the EKF error-state values, which were already applied due to the closed-loop concept.

3 Terrestrial 3D-gravity profiling

This chapter gives the introduction to terrestrial 3D-gravity profiling and provides the transfer of the content presented so far to the software realization. The basic idea of terrestrial 3D-gravity profiling and a brief outline of the software is presented before more details about the implementation follow in the subsections.

Terrestrial 3D-gravity profiling is closely related to airborne strapdown gravimetry (e.g., Becker (2016) and Jensen (2018)). Instead of operating the classical instruments (IMU and GNSS) onboard an airplane, they are mounted on top of (GNSS antenna) and in the trunk of (GNSS receiver and IMU) a car. Additionally, a relative gravimeter and a zenith camera are part of the equipment for point-wise gravimetric update observations. Campaigns are designed along tracks accessible by car in the area of interest. Gravity and VDs are observed at the start and endpoint as well as in between (with reasonable spacing, see Ch. 4.3), to provide gravimetric updates to the EKF. Thereby, relative gravity data can be gathered in parallel to the IMU and GNSS measurements during so-called zero velocity updates (ZUPTs). VDs have to be determined during a night campaign, given cloudless sky. The data post-processing happens in a loosely-coupled, closed-loop EKF environment, with various types of updates as will be shown in Ch. 3.1.3. The outcome of a campaign are the three profiles of the gravity disturbance vector components expressed in the n-frame. For the Estergebirge campaign, treated in Ch. 4.3, these profiles are transformed into SGD and VD profiles for comparison with accurate reference data. Thereby, RMS errors of 1.5 mGal for the SGD and 0.2 - 0.5'' for the VDs are reached.

Major advantages of this method, compared to airborne campaigns, are the ability to update the EKF with gravimetric information along the track, to observe a larger spectrum of the gravity signal, and to rerun exact tracks. The update option reduces the demand on the IMU long-term bias stability and allows the determination of the long-wavelength gravity signal more accurately. The larger spectrum results from observing on the Earth's surface (no effect of upward continuation), in combination with the reduced speed of the vehicle. Furthermore, the planning and the organization of such terrestrial campaigns are less elaborate. It can be mastered by a single person, the equipment fits into one car and most roads can be driven without special permission. Disadvantages are that campaigns are limited to accessible roads, that investigations of large areas are far more time consuming, and that GNSS visibility plays a critical role.

Figure 3.1 shows the basic structure of the software and links the content of Ch. 2 (gray) with Ch. 3 (blue). The software is divided into six parts as visualized in the middle column. The first part is meant for user interaction to adapt campaign-dependent settings, like sensor noise characteristics, while the other five parts run autonomously. The second part handles general preparations e.g., the definition of the reference frame (see Ch. 3.1). The main part of the software is the EKF, represented by the propagation and update phase (see Chs. 3.1.1 - 3.1.3) as well as by the right side of Fig. 3.1. At the beginning of each propagation phase, the gravity disturbance vector is projected in time and the current position, velocity, and attitude are determined via IMU strapdown navigation (dead reckoning principle). The latter is realized by means of mechanization equations. Moreover, the error covariance information is propagated. As soon as an update is available, the EKF applies the propagated error covariances to spread discrepancies between observation data (or empirical assumptions, e.g., ZUPTs) and the current solution optimally on all error-states. After the serial EKF processing is finished, the RTS smoother is applied to smooth the results backward in time (see Ch. 2.4.3), which eliminates sudden jumps in the total- and error-states induced by the EKF updates. Depicted as "Refinement" is the combination of data collected in two different directions of a trajectory and different runs (in both directions) along the same trajectory. In the following, the reader is introduced to the first five parts. The profile refinement is treated separately in Ch. 3.2.

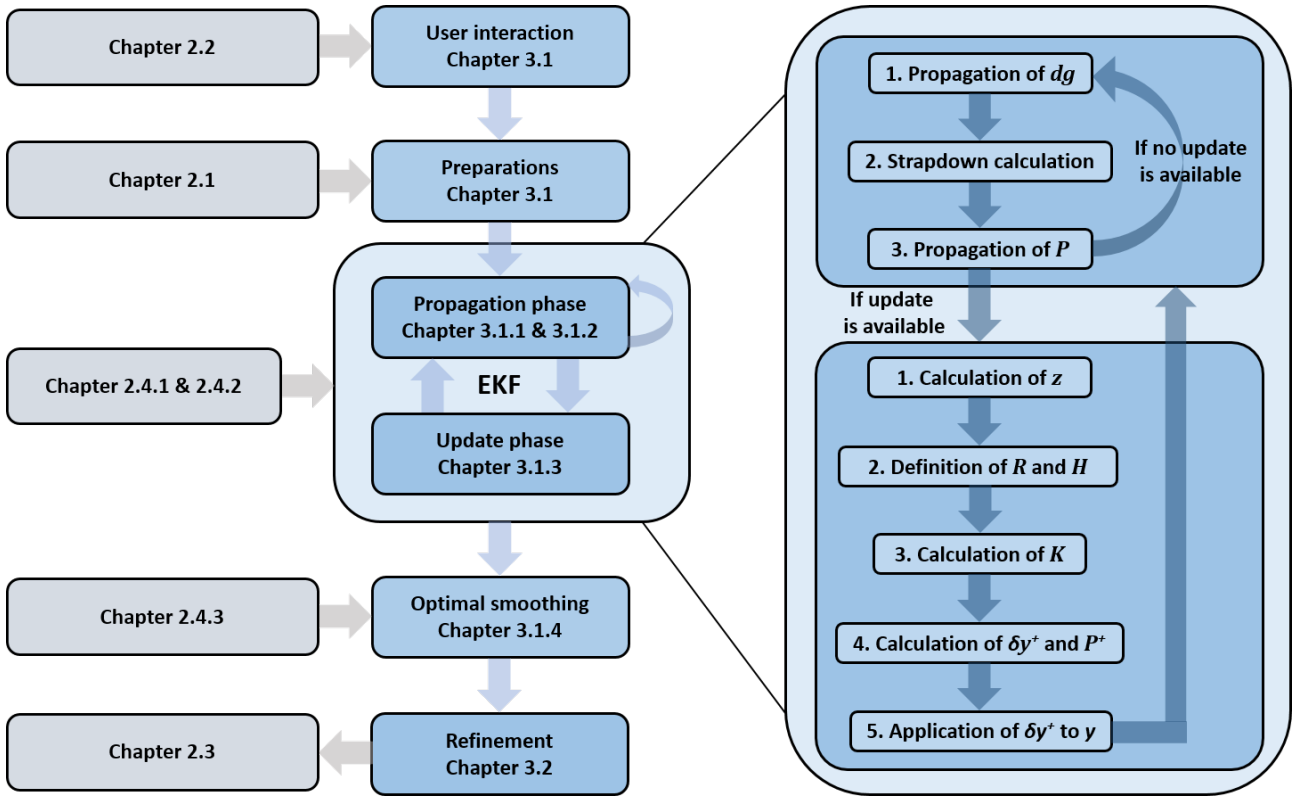


Figure 3.1: Schematic overview of the terrestrial 3D-gravity profiling software. Theory components are linked in gray and the EKF sequence is depicted in more detail on the right side of the figure.

3.1 Implementation details

Before diving into the details of the implementation, the setup of the error-state vector has to be introduced for the sake of clarity. It consists of 24 elements, where a group of three represents one error-state in three dimensions. The states are errors of the position, velocity, attitude, gyroscope, and accelerometer biases of the IMU as well as the gravity disturbance. Since the gravity disturbance is chosen to be represented by a third-order Gauß-Markov model²², the first and second derivatives of the gravity disturbance are added to the error-state vector. Table 3.1 presents the mathematical notation of each error-state and the frame it is defined in. Concerning the attitude, ψ^n stands for three Euler angles, as explained in Ch. 2.1.2.

At the beginning of the processing, the user chooses the variances of the initial error-state estimates, describes the stochastic noise of the propagation process, also known as process noise, and defines the β -values for the Gauß-Markov models (Gelb, 1974) of the gyroscope and accelerometer biases as well as the gravity disturbances for each component. All these values might vary from campaign to campaign, depending on the instruments used and the characteristics of the gravity disturbance in the area of interest. Normally, approximate values are known from manufacturer sheets and auto-correlation analyses. Additionally, a temperature calibration can be applied. Of course, calibration parameters have to be determined separately since they are unique for each IMU. All these settings will be discussed for the Estergebirge campaign in more detail in Ch. 4.3.

²²More details follow in Ch. 3.1.2

Error-state	Representation	Unit of error-state	Unit of covariance
Position	$\delta \mathbf{r}^e$	rad, rad, m	cm, cm, cm
Velocity	$\delta \mathbf{v}^n$	m/s	cm/s
Attitude	$\delta \psi^n$	rad	$^\circ$
Gyroscope biases	$\delta \mathbf{b}_{[g]}$	rad/s	$^\circ/h$
Accelerometer biases	$\delta \mathbf{b}_{[a]}$	m/s^2	$mGal$
Gravity disturbance	$\delta \mathbf{d}g^n$	$mGal$	$mGal$
First derivative of gravity disturbance	$\delta \dot{\mathbf{d}}g^n$	$mGal/s$	$\mu Gal/s$
Second derivative of gravity disturbance	$\delta \ddot{\mathbf{d}}g^n$	$mGal/s^2$	$\mu Gal/s^2$

Table 3.1: Error-state vector setup together with its mathematical notation and the selected physical units of the error-state vector and the error covariance information.

The processing starts with the preparations part, which is handling a variety of tasks. It predefines the ECEF reference system (WGS84), the time system (GPS time seconds of week (GPS SOW)), the local reference system (n-frame = ENU-frame), and the units of the error-state vector elements, including their corresponding covariances. For numerical reasons, the units of the error covariances are adapted w.r.t. the units of the error-state vector (see Table 3.1). Since the EKF is loosely-coupled, a GNSS positioning solution has to be provided by the user. All relevant data/information (IMU and GNSS data, gravity ties, ZUPT times, lever arm details, model-based gravity data along the track) are imported, their units partly transformed, the data rates of the IMU and GNSS are detected, plus the initial position is declared as the median position value of the first 60 s of GNSS positions. For run time efficiency, GNSS, CG-5, and ZUPT observations are allocated to IMU observations via indices. Next, the coarse alignment of the b-frame w.r.t. the n-frame must be determined. The strapdown navigation (or inertial navigation) and also the success of the EKF are depending on a solid estimation of the initial IMU orientation. Static gyroscope and accelerometer data of a navigation-grade IMU allow estimating its coarse orientation w.r.t. n-frame²³. The respective reference quantities are the vectors of the Earth's rotation and gravity. The alignment formulas are presented in Eqs. (3.1). Here, the orientation is expressed in terms of Euler angles in the n-frame. Keep in mind, that this method is restricted to static, coarse leveled systems and navigation-grade IMUs or superior ones.

$$\begin{aligned}
\phi^n &= \arctan\left(\frac{\bar{f}_{[ib,Y]}^b}{\bar{f}_{[ib,Z]}^b}\right) \\
\theta^n &= -\arctan\left(\frac{\bar{f}_{[ib,X]}^b}{\sqrt{\bar{f}_{[ib,Y]}^b{}^2 + \bar{f}_{[ib,Z]}^b{}^2}}\right) \\
\psi^n &= \arctan\left(\frac{\bar{\omega}_{[ib,X]}^b}{\bar{\omega}_{[ib,Y]}^b}\right)
\end{aligned} \tag{3.1}$$

²³Actually, the l-frame is the reference. But since the alignment is just needed to obtain a coarse orientation and since IMU data is comprised by sensor errors anyway, it is justifiable to declare these angles as the Euler angles between b- and n-frame.

$\bar{f}_{[ib,K]}^b$ and $\bar{\omega}_{[ib,K]}^b$ represent the mean accelerometer output (specific force) and mean angular velocity output of the b-frame axis K of the designated alignment phase. The n- to b-frame rotation matrix \mathbf{R}_n^b is then calculated by Eq. (2.3).

Lastly, all prerequisite quantities and covariances are allocated and initialized. The initial value of the targeted quantity, the 3D-gravity disturbance, is defined by the reference gravity vector minus the normal gravity vector at the start point of the survey. If a reduction of the gravity signal is applied, a gravity model value is subtracted, additionally. Then, the residual gravity disturbance $\mathbf{dg}_{[residual]}^n$ in Eq. (3.2) replaces \mathbf{dg}^n in the error-state vector.

$$\mathbf{dg}^n = \mathbf{g}^n - \boldsymbol{\gamma}^n = \mathbf{dg}_{[residual]}^n + \mathbf{dg}_{[GGMplus]}^n \quad (3.2)$$

$\mathbf{dg}_{[GGMplus]}^n$ stands for any modeled gravity disturbance vector but hints at the Global Gravity Model plus (GGMplus), which is used for the Estergebirge campaign in Ch. 4.3.

Next, a for-loop is entered that covers all IMU observations. Each epoch starts with the projection of the gravity disturbance and its first derivative from one IMU time-tag to the next, by integrating the total-states of \mathbf{dg}^n and $\dot{\mathbf{d}}\mathbf{g}^n$ over the time interval between the two IMU observations. Then, the current IMU observation is processed. The inertial data is used to calculate the current position, velocity, and orientation of the IMU, see Ch. 3.1.1.

3.1.1 Strapdown navigation

Strapdown navigation describes the dead reckoning principle of positioning when a trajectory calculation is solely based on IMU data. It is an important part of the software since it tracks the position, velocity, and orientation of the IMU between GNSS observations and thus works as control for the position and velocity error-state calculation. The following equations are called navigation or mechanization equations (expressed in the n-frame)²⁴. There is plenty of literature treating this topic, e.g., Jekeli (2001), Groves (2008), and Wendel (2011).

The first step inside this algorithm is the elimination of estimated biases of the gyroscopes and accelerometers. Then, the attitude calculation is performed based on the gyroscope observations $\boldsymbol{\omega}_{[ib]}^b$. To interpret this quantity correctly in terms of b- to n-frame changes, $\boldsymbol{\omega}_{[nb]}^b$ is needed (Eq. (3.3)).

$$\boldsymbol{\omega}_{[nb]}^b = \boldsymbol{\omega}_{[ib]}^b - \mathbf{R}_n^b(\boldsymbol{\omega}_{[ie]}^n + \boldsymbol{\omega}_{[en]}^n) \quad (3.3)$$

$$\text{with } \boldsymbol{\omega}_{[ie]}^n = \begin{pmatrix} 0 \\ \omega_{[Earth]} \cos \varphi \\ \omega_{[Earth]} \sin \varphi \end{pmatrix} \quad \boldsymbol{\omega}_{[en]}^n = \begin{pmatrix} \frac{-v_{[eb,N]}^n}{R_{[N]}+h} \\ \frac{v_{[eb,E]}^n}{R_{[E]}+h} \\ \frac{v_{[eb,E]}^n \tan \varphi}{R_{[E]}+h} \end{pmatrix}$$

$\mathbf{v}_{[eb]}^n$ represents the so-called transport rate, the velocity of the b-frame w.r.t. the ECEF-frame. $R_{[E]}$ and $R_{[N]}$ describe the radii of curvature of the ellipsoid in east-west and north-south direction, called prime vertical and meridian radii of curvature.

The change of orientation can be expressed as a first-order differential equation on the basis of quaternions, see Eq. (2.13). The relation between DCMs and quaternions is treated in Ch. 2.1.2. Numerical integration, using the fourth-order Runge-Kutta method, gives the new IMU orientation that allows rotating the observed specific force $\mathbf{f}_{[ib]}^b$ from the b- into the n-frame. At this stage, the estimated

²⁴The equations are only briefly introduced here. A derivation follows, since it is an integrated part of the next section.

gravity values and the Coriolis acceleration $(\boldsymbol{\omega}_{[en]}^n + 2\boldsymbol{\omega}_{[ie]}^n) \times \mathbf{v}_{[eb]}^n$ are reduced from the specific force (Eq. (3.4), compare also Eq. (3.19)). Assuming a perfect system, the remaining term contains pure kinematic acceleration ($\mathbf{a}_{[eb]}^n$) between the b- and the ECEF²⁵-frame represented in the n-frame.

$$\mathbf{a}_{[eb]}^n = \mathbf{R}_b^n \mathbf{f}_{[ib]}^b + \boldsymbol{\gamma}^n + d\mathbf{g}^n + d\mathbf{g}_{[GGMplus]}^n - (\boldsymbol{\omega}_{[en]}^n + 2\boldsymbol{\omega}_{[ie]}^n) \times \mathbf{v}_{[eb]}^n \quad (3.4)$$

The strapdown navigation ends by projecting the velocity and the position in time via the differential Eqs. (3.5) and (3.6).

$$\dot{\mathbf{v}}_{[eb]}^n = \mathbf{a}_{[eb]}^n \quad (3.5)$$

$$\begin{pmatrix} \dot{\varphi} \\ \dot{\lambda} \\ \dot{h} \end{pmatrix} = \begin{pmatrix} \frac{v_{[eb,N]}^n}{R_{[N]}+h} \\ \frac{v_{[eb,E]}^n}{(R_{[E]}+h)\cos\varphi} \\ v_{[eb,U]}^n \end{pmatrix} \quad (3.6)$$

Before \mathbf{F} and Φ from Ch. 2.4.1 come into play, the β -values of the gravity disturbance Gauß-Markov process ($\beta_{[dg]}$) are recalculated. As will be shown in Ch. 4.3.1, $\beta_{[dg]}$ is defined as inverse correlation distance. Thus, it has to be transformed into the time domain, from m^{-1} to s^{-1} . This is realized by multiplying $\beta_{[dg]}$ with the current horizontal velocity, each epoch.

3.1.2 Error propagation derivation

This section deduces the elements of the system matrix \mathbf{F} of Eq. (2.43). Principally, \mathbf{F} allows propagating the error-state vector $\delta\mathbf{y}$ and its covariance matrix \mathbf{P} from one point in time to the next²⁶. It originates from a set of first-order differential equations describing the vehicle's motion, inertial sensor bias changes, and gravity disturbance variations. Part of these equations (the navigation/mechanization equations) were already formulated in the previous section. In the following, all equations are deduced from scratch based on Jekeli (2001) and Hofmann-Wellenhof et al. (2003).

In an inertial frame, Newton's laws of motion hold. The first law states that if there is no force applied to an object, the components of its kinematic acceleration vector are zero. This circumstance is expressed by Eq. (3.7).

$$\frac{d^2 \mathbf{x}^i}{dt^2} = \ddot{\mathbf{x}}^i = 0 \quad (3.7)$$

\mathbf{x}^i is representing the object's position in the ICRF, $\frac{d^2 \mathbf{x}^i}{dt^2}$ and $\ddot{\mathbf{x}}^i$ its kinematic acceleration.

The second law describes the linear relation between applied forces ($\mathbf{F}_{[app]}^i$) and the resulting acceleration on inertial masses ($m_{[inertial]}$), given that the mass itself remains constant.

$$\mathbf{F}_{[app]}^i = m_{[inertial]} \ddot{\mathbf{x}}^i \quad (3.8a)$$

It has to be kept in mind that an i-frame is only existent far off gravitational masses. Close to large masses, the effect of gravitational field forces must be accounted for. Consequently, when measuring

²⁵The centrifugal acceleration due to the Earth's rotation is an integral part of the gravity terms.

²⁶Remember from Ch. 2.4.2, $\delta\mathbf{y}$ is zero outside the EKF update phase due to its closed-loop implementation. The transition matrix thus only propagates \mathbf{P} .

on/close to the Earth Eq. (3.8a) extends to

$$\mathbf{F}_{[app]}^i + m_{[grav]}\tilde{\mathbf{g}}^i = m_{[inertial]}\ddot{\mathbf{x}}^i. \quad (3.8b)$$

$\tilde{\mathbf{g}}^i$ represents the gravitational acceleration inherent to the Earth's mass (cf. Ch. 2.3). Making use of Einstein's principle of equivalence by assuming that there is no difference between gravitational masses $m_{[grav]}$ and inertial masses $m_{[inertial]}$, it can be concluded from Eq. (3.8b) that

$$\ddot{\mathbf{x}}^i = \mathbf{f}^i + \tilde{\mathbf{g}}^i. \quad (3.9)$$

\mathbf{f}^i is called specific force, although it is an acceleration. It describes the force per unit mass ($\text{N kg}^{-1} = \text{kg m kg}^{-1} \text{s}^{-2} = \text{m s}^{-2}$). Leaving sensor errors aside for the moment, \mathbf{f}^i is the output of the orthogonal accelerometer triad of an IMU ($\mathbf{f}_{[ib]}^b$; from here on $[ib]$ is neglected for \mathbf{f}) that is rotated into the ICRF. Equation (3.9) yields two vital conclusions in the fields of navigation and gravimetry. The first one is that a trajectory of an IMU, which is the result of orientation-dependent double-integration of $\ddot{\mathbf{x}}^i$, relies on gravity information. For low accuracy requirements, the integration of normal gravity field information is sufficient. With rising demands on the trajectory's accuracy, a more precise knowledge of the Earth's gravity field is indispensable. The other conclusion is that the Earth's gravity field is observable by combining accelerometer data of an IMU with the data of a second sensor observing the kinematic movement ($\ddot{\mathbf{x}}^i$) of the IMU, e.g., GNSS equipment.

Keeping Eq. (3.9) in mind, another definition for $\ddot{\mathbf{x}}^i$ is deduced, starting from the relation that a position in inertial space can be obtained by rotating the ECEF position \mathbf{x}^e , see Eq. (3.10).

$$\mathbf{x}^i = \mathbf{R}_e^i \mathbf{x}^e \quad (3.10)$$

with \mathbf{R}_e^i transforming the vector \mathbf{x}^e from the ECEF-frame to the ICRF. Differentiation w.r.t. time, once and twice with the help of Eq. (2.12), leads to Eqs. (3.11) and (3.12), respectively.

$$\dot{\mathbf{x}}^i = \mathbf{R}_e^i (\dot{\mathbf{x}}^e + \boldsymbol{\omega}_{[ie]}^e \times \mathbf{x}^e) \quad (3.11)$$

$$\ddot{\mathbf{x}}^i = \mathbf{R}_e^i (\ddot{\mathbf{x}}^e + 2\boldsymbol{\omega}_{[ie]}^e \times \dot{\mathbf{x}}^e + \dot{\boldsymbol{\omega}}_{[ie]}^e \times \mathbf{x}^e + \boldsymbol{\omega}_{[ie]}^e \times (\boldsymbol{\omega}_{[ie]}^e \times \mathbf{x}^e)) \quad (3.12)$$

For strapdown gravimetry, gyroscopes of high accuracy are needed. Those sensors are able to observe the Earth's rotation, but they are unable to resolve variations of this rotation. Thus, the simplification for the Euler acceleration $\dot{\boldsymbol{\omega}}_{[ie]}^e \times \mathbf{x}^e = 0$ is applied. The fusion of Eqs. (3.9) and (3.12) yields

$$\mathbf{f}^i + \tilde{\mathbf{g}}^i = \mathbf{R}_e^i (\ddot{\mathbf{x}}^e + 2\boldsymbol{\omega}_{[ie]}^e \times \dot{\mathbf{x}}^e + \boldsymbol{\omega}_{[ie]}^e \times (\boldsymbol{\omega}_{[ie]}^e \times \mathbf{x}^e)). \quad (3.13)$$

Here, the ICRF is left and Eq. (3.13) is formulated in the ECEF-frame (Eq. (3.14)). Additionally, \mathbf{g} is introduced by adding \mathbf{z} to $\tilde{\mathbf{g}}$ ($\mathbf{g}^e = \mathbf{R}_i^e \tilde{\mathbf{g}}^i + (-\boldsymbol{\omega}_{[ie]}^e \times (\boldsymbol{\omega}_{[ie]}^e \times \mathbf{x}^e))$).

$$\ddot{\mathbf{x}}^e = \mathbf{f}^e + \mathbf{g}^e - 2\boldsymbol{\omega}_{[ie]}^e \times \dot{\mathbf{x}}^e \quad (3.14)$$

For a more intuitive interpretation, Eq. (3.14) is converted to the n-frame. But before moving on, a feature of the n-frame is discussed and a new variable has to be defined. It is the fact that the n-frame itself moves with the IMU as its origin is fixed to the center of the IMU. Consequently, there is no movement inside the n-frame by definition, and also the components of \mathbf{x}^n are always zero. To circumvent this characteristic of the n-frame, \mathbf{v}^n (or synonymous $\mathbf{v}_{[en]}^n$) is introduced. It represents the velocity of the n-frame w.r.t. the ECEF-frame coordinated in the n-frame and projects the velocity of the IMU inside the ECEF-frame onto the n-frame axes. Actually, \mathbf{v}^n was already introduced before as

the transport rate $\mathbf{v}_{[eb]}^n$ (Eq. (3.4)) which is equal to $\mathbf{v}_{[en]}^n$, because the b- and n-frame have the same origin. Apart from that, \mathbf{r}^e is defined, which equals \mathbf{x}^e expressed in geodetic coordinates. This short paragraph brings us to Eqs. (3.15) and (3.16), resembling the first navigation equation.

$$\dot{\mathbf{x}}^e = \mathbf{R}_n^e \mathbf{v}^n \quad (3.15)$$

$$\dot{\mathbf{r}}^e = \mathbf{D}_n^e \mathbf{v}^n \quad (3.16)$$

$$\text{with} \quad \mathbf{D}_n^e = \begin{pmatrix} 0 & \frac{1}{R_{[N]+h}} & 0 \\ \frac{1}{(R_{[E]+h}) \cos \varphi} & 0 & 0 \\ 0 & 0 & 1 \end{pmatrix}$$

Note the assignment of the ENU components of \mathbf{v}^n to the North-East-Up ($\dot{\varphi}, \dot{\lambda}, \dot{h}$; cf. Eq. (3.6)) components of $\dot{\mathbf{r}}^e$. Further temporal differentiation of Eq. (3.15) leads to

$$\ddot{\mathbf{x}}^e = \mathbf{R}_n^e (\dot{\mathbf{v}}^n + \boldsymbol{\omega}_{[en]}^n \times \mathbf{v}^n). \quad (3.17)$$

The fusion of Eqs. (3.14), (3.15), and (3.17) leads to Eq. (3.18), and finally after some transformation to the second navigation equation for the n-frame, see Eq. (3.19)²⁷.

$$\mathbf{R}_n^e (\dot{\mathbf{v}}^n + \boldsymbol{\omega}_{[en]}^n \times \mathbf{v}^n) = \mathbf{f}^e + \mathbf{g}^e - 2[\boldsymbol{\omega}_{[ie]}^e \times] \mathbf{R}_n^e \mathbf{v}^n \quad (3.18)$$

$$\dot{\mathbf{v}}^n = \mathbf{f}^n + \mathbf{g}^n - (\boldsymbol{\omega}_{[in]}^n + \boldsymbol{\omega}_{[ie]}^n) \times \mathbf{v}^n \quad (3.19)$$

The navigation equations are completed with the differential equation for the orientation of the IMU. Therefore, Eq. (2.12) is adapted to \mathbf{R}_b^n to obtain the third navigation equation.

$$\dot{\mathbf{R}}_b^n = \mathbf{R}_b^n [\boldsymbol{\omega}_{[nb]}^b \times] = \mathbf{R}_b^n [(\boldsymbol{\omega}_{[ib]}^b - \boldsymbol{\omega}_{[in]}^b) \times] \quad (3.20)$$

From a navigation point of view, derivations are completed. But, up to this point IMU sensor errors were ignored and for gravimetric purposes, the gravity disturbance has to be modeled additionally. The IMU sensor errors are approximated by stochastically modeled bias variations. Over the last decades Gauss-Markov models (see Gelb (1974), Jekeli (2001), and Brown and Hwang (2012)) turned out to be a solid tool to model bias variations of high-accuracy inertial sensors and also to extract variations of gravity disturbances, e.g., Jekeli (1994), Becker (2016) and Jensen (2018). A Gauss-Markov process is completely characterized by its variance σ^2 and correlation parameter β of the exponential-shaped autocorrelation function. This shape implies that the process decorrelates with time/distance/etc. From a mathematical standpoint, the latest value of a n^{th} -order Gauss-Markov process only depends on the previous n values (Gelb, 1974, p. 42ff) plus a Gaussian white noise component.

In this work, bias variations are modeled as first-order Gauss-Markov processes (Eqs. (3.21a) and (3.21b), cf. Eq. (2.18)), while the gravity disturbance is described by a third-order Gauss-Markov process (Eq. (3.21c)) inside the EKF. The third-order Gauss-Markov model is chosen, as it is the standard model to describe the gravity disturbance of airborne campaigns. Furthermore, in Jekeli (1994) it is stated that a third-order model outperforms a first-order model in the shorter wavelengths, which

²⁷For a better understanding the intermediate steps are listed here:

$$\mathbf{f}^n = \mathbf{R}_e^n \mathbf{f}^e, \mathbf{g}^n = \mathbf{R}_e^n \mathbf{g}^e, [\boldsymbol{\omega}_{[ie]}^n \times] = \mathbf{R}_e^n [\boldsymbol{\omega}_{[ie]}^e \times] \mathbf{R}_n^e, [\boldsymbol{\omega}_{[en]}^n \times] = [(\boldsymbol{\omega}_{[in]}^n - \boldsymbol{\omega}_{[ie]}^n) \times], [(\boldsymbol{\omega}_{[in]}^n + \boldsymbol{\omega}_{[ie]}^n) \times] = [(\boldsymbol{\omega}_{[en]}^n + 2\boldsymbol{\omega}_{[ie]}^n) \times]$$

is beneficial for terrestrial 3D-gravity profiling.

$$\dot{\mathbf{b}}_{[g]} = -\mathbf{B}_{[g]}\mathbf{b}_{[g]} + \mathbf{w}_{[b_{[g]}]} \quad (3.21a)$$

$$\dot{\mathbf{b}}_{[a]} = -\mathbf{B}_{[a]}\mathbf{b}_{[a]} + \mathbf{w}_{[b_{[a]}]} \quad (3.21b)$$

$$\ddot{\mathbf{d}}\mathbf{g}^n = -3\mathbf{B}_{[dg]}\ddot{\mathbf{d}}\mathbf{g}^n - 3\mathbf{B}_{[dg]}^2\dot{\mathbf{d}}\mathbf{g}^n - \mathbf{B}_{[dg]}^3\mathbf{d}\mathbf{g}^n + \mathbf{w}_{[dg]} \quad (3.21c)$$

$\mathbf{b}_{[g]}$, $\mathbf{b}_{[a]}$, and $\mathbf{d}\mathbf{g}$ stand for gyroscope and accelerometer biases, and the gravity disturbance. $\mathbf{B}_{[k]}$ is a matrix with the corresponding $\beta_{[k,i]}$ ($k = g, a$, or dg , $i = X, Y$, or Z) elements on the diagonal. The correlation in $\mathbf{B}_{[dg]}$ is described w.r.t. distance and therefore has to be transformed into the time domain, from m^{-1} to s^{-1} . This is realized by multiplication with the current horizontal velocity, as was already mentioned in Ch. 3.1.1. The β -values are defined as $\beta_{[g/a]} = 1/\tau_{[g/a]}$ and $\beta_{[dg]} = 2.903/\tau_{[dg]}$. Explicit β -values follow in Ch. 4.3. $\mathbf{w}_{[b_{[g/a]}]}$ is white noise with a spectral density of $2\mathbf{B}_{[g/a]}\sigma_{[g/a]}^2$. $\mathbf{w}_{[dg]}$ is white noise with a spectral density of $\frac{16}{3}\mathbf{B}_{[dg]}^5\sigma_{[dg]}^2$. The first-order differential equations for $\mathbf{d}\mathbf{g}^n$ and $\dot{\mathbf{d}}\mathbf{g}^n$ are shown in Eq. (3.22).

Summary of terrestrial 3D-gravity profiling differential equations

$$\frac{d\mathbf{y}}{dt} = \begin{pmatrix} \frac{d\mathbf{r}^e}{dt} \\ \frac{d\mathbf{v}^n}{dt} \\ \frac{d\mathbf{R}_b^n}{dt} \\ \frac{d\mathbf{b}_{[g]}}{dt} \\ \frac{d\mathbf{b}_{[a]}}{dt} \\ \frac{d\mathbf{d}\mathbf{g}^n}{dt} \\ \frac{d\dot{\mathbf{d}}\mathbf{g}^n}{dt} \\ \frac{d\ddot{\mathbf{d}}\mathbf{g}^n}{dt} \end{pmatrix} = \begin{pmatrix} \mathbf{D}_n^e \mathbf{v}^n \\ \mathbf{f}^n + \mathbf{g}^n - (\boldsymbol{\omega}_{[in]}^n + \boldsymbol{\omega}_{[ie]}^n) \times \mathbf{v}^n \\ \mathbf{R}_b^n [(\boldsymbol{\omega}_{[ib]}^b - \boldsymbol{\omega}_{[in]}^b) \times] \\ -\mathbf{B}_{[g]}\mathbf{b}_{[g]} + \mathbf{w}_{[b_{[g]}]} \\ -\mathbf{B}_{[a]}\mathbf{b}_{[a]} + \mathbf{w}_{[b_{[a]}]} \\ \mathbf{d}\mathbf{g}^n \\ \dot{\mathbf{d}}\mathbf{g}^n \\ -3\mathbf{B}_{[dg]}\ddot{\mathbf{d}}\mathbf{g}^n - 3\mathbf{B}_{[dg]}^2\dot{\mathbf{d}}\mathbf{g}^n - \mathbf{B}_{[dg]}^3\mathbf{d}\mathbf{g}^n + \mathbf{w}_{[dg]} \end{pmatrix} \quad (3.22)$$

Having derived the driving differential equations for terrestrial 3D-gravity profiling in Eq. (3.22), it is now focused on the associated error propagation or rather the linearization via first-order Taylor approximations. The final equations are then combined to obtain the system matrix \mathbf{F} of Eq. (2.51). The following approach is based on Schwarz and Wei (2001), Noureldin et al. (2013), and Ch. 2.4.1.

POSITION

Since \mathbf{D}_n^e only depends on the position, there are only the following two partial derivatives needed in Eq. (3.23). Hereby, the variations of $R_{[E]}$ and $R_{[N]}$ caused by small changes in position are neglected.

$$\begin{aligned} \delta \dot{\mathbf{r}}^e &= \left. \frac{\partial \mathbf{D}_n^e \mathbf{v}^n}{\partial \mathbf{r}^e} \right|_{\bar{\mathbf{r}}^e} \delta \mathbf{r}^e + \left. \frac{\partial \mathbf{D}_n^e \mathbf{v}^n}{\partial \mathbf{v}^n} \right|_{\bar{\mathbf{v}}^n} \delta \mathbf{v}^n \\ &= \begin{pmatrix} 0 & 0 & -\frac{v_{[eb,N]}^n}{(R_{[N]}+h)^2} \\ \frac{v_{[eb,E]}^n \tan \varphi}{(R_{[E]}+h) \cos \varphi} & 0 & -\frac{v_{[eb,E]}^n}{(R_{[E]}+h)^2 \cos \varphi} \\ 0 & 0 & 0 \end{pmatrix} \begin{pmatrix} \delta \varphi \\ \delta \lambda \\ \delta h \end{pmatrix} + \begin{pmatrix} 0 & \frac{1}{R_{[N]}+h} & 0 \\ \frac{1}{(R_{[E]}+h) \cos \varphi} & 0 & 0 \\ 0 & 0 & 1 \end{pmatrix} \begin{pmatrix} \delta v_{[eb,E]}^n \\ \delta v_{[eb,N]}^n \\ \delta v_{[eb,U]}^n \end{pmatrix} \end{aligned} \quad (3.23)$$

VELOCITY

The effect of certain error-states onto the velocity is more complex to describe, as shown in Eq. (3.24).

$$\begin{aligned} \delta \dot{\mathbf{v}}^n &= \left. \frac{\partial (\mathbf{f}^n + \mathbf{g}^n - (\boldsymbol{\omega}_{[in]}^n + \boldsymbol{\omega}_{[ie]}^n) \times \mathbf{v}^n)}{\partial \mathbf{r}^e} \right|_{\bar{\mathbf{r}}^e} \delta \mathbf{r}^e + \left. \frac{\partial (\mathbf{f}^n + \mathbf{g}^n - (\boldsymbol{\omega}_{[in]}^n + \boldsymbol{\omega}_{[ie]}^n) \times \mathbf{v}^n)}{\partial \mathbf{v}^n} \right|_{\bar{\mathbf{v}}^n} \delta \mathbf{v}^n \\ &+ \left. \frac{\partial (\mathbf{f}^n + \mathbf{g}^n - (\boldsymbol{\omega}_{[in]}^n + \boldsymbol{\omega}_{[ie]}^n) \times \mathbf{v}^n)}{\partial \psi^n} \right|_{\bar{\psi}^n} \delta \psi^n + \left. \frac{\partial (\mathbf{f}^n + \mathbf{g}^n - (\boldsymbol{\omega}_{[in]}^n + \boldsymbol{\omega}_{[ie]}^n) \times \mathbf{v}^n)}{\partial \mathbf{b}_{[a]}} \right|_{\bar{\mathbf{b}}_{[a]}} \delta \mathbf{b}_{[a]} \\ &+ \left. \frac{\partial (\mathbf{f}^n + \mathbf{g}^n - (\boldsymbol{\omega}_{[in]}^n + \boldsymbol{\omega}_{[ie]}^n) \times \mathbf{v}^n)}{\partial d\mathbf{g}^n} \right|_{\bar{d}\mathbf{g}^n} \delta d\mathbf{g}^n \\ &= \frac{\partial (\mathbf{g}^n - (\boldsymbol{\omega}_{[in]}^n + \boldsymbol{\omega}_{[ie]}^n) \times \mathbf{v}^n)}{\partial \mathbf{r}^e} \delta \mathbf{r}^e - \frac{\partial (\boldsymbol{\omega}_{[in]}^n + \boldsymbol{\omega}_{[ie]}^n) \times \mathbf{v}^n}{\partial \mathbf{v}^n} \delta \mathbf{v}^n + \frac{\partial \mathbf{R}_b^n \mathbf{f}^b}{\partial \psi^n} \delta \psi^n + \frac{\partial \mathbf{R}_b^n \mathbf{f}^b}{\partial \mathbf{b}_{[a]}} \delta \mathbf{b}_{[a]} \\ &+ \frac{\partial \mathbf{g}^n}{\partial d\mathbf{g}^n} \delta d\mathbf{g}^n \end{aligned} \quad (3.24)$$

Developing Eq. (3.24) leads to Eq. (3.25).

$$\begin{aligned} \delta \dot{\mathbf{v}}^n &= \begin{pmatrix} \frac{v_{[eb,E]}^n v_{[eb,N]}^n}{(R_{[E]}+h) \cos^2 \varphi} + 2v_{[eb,N]}^n \omega_{[Earth]} \cos \varphi + 2v_{[eb,U]}^n \omega_{[Earth]} \sin \varphi & 0 & -\frac{v_{[eb,E]}^n v_{[eb,N]}^n \tan \varphi}{(R_{[E]}+h)^2} + \frac{v_{[eb,E]}^n v_{[eb,U]}^n}{(R_{[E]}+h)^2} \\ -\frac{v_{[eb,E]}^n}{(R_{[E]}+h) \cos^2 \varphi} - 2v_{[eb,E]}^n \omega_{[Earth]} \cos \varphi & 0 & \frac{v_{[eb,E]}^n \tan \varphi}{(R_{[E]}+h)^2} + \frac{v_{[eb,N]}^n v_{[eb,U]}^n}{(R_{[N]}+h)^2} \\ -2v_{[eb,E]}^n \omega_{[Earth]} \sin \varphi & 0 & -\frac{v_{[eb,E]}^n}{(R_{[E]}+h)^2} - \frac{v_{[eb,N]}^n}{(R_{[N]}+h)^2} - \frac{d\gamma}{dh} \end{pmatrix} \begin{pmatrix} \delta \varphi \\ \delta \lambda \\ \delta h \end{pmatrix} \\ &- \begin{pmatrix} -\frac{v_{[eb,N]}^n \tan \varphi}{R_{[E]}+h} + \frac{v_{[eb,U]}^n}{R_{[E]}+h} & -\frac{v_{[eb,E]}^n \tan \varphi}{R_{[E]}+h} - 2\omega_{[Earth]} \sin \varphi & \frac{v_{[eb,E]}^n}{R_{[E]}+h} + 2\omega_e \cos \varphi \\ \frac{2v_{[eb,E]}^n \tan \varphi}{R_{[E]}+h} + 2\omega_{[Earth]} \sin \varphi & \frac{v_{[eb,U]}^n}{R_{[N]}+h} & \frac{v_{[eb,N]}^n}{R_{[N]}+h} \\ -\frac{2v_{[eb,E]}^n}{R_{[E]}+h} - 2\omega_{[Earth]} \cos \varphi & \frac{-2v_{[eb,N]}^n}{R_{[N]}+h} & 0 \end{pmatrix} \begin{pmatrix} \delta v_{[eb,E]}^n \\ \delta v_{[eb,N]}^n \\ \delta v_{[eb,U]}^n \end{pmatrix} \\ &+ \begin{pmatrix} 0 & f_{[U]}^n & -f_{[N]}^n \\ -f_{[U]}^n & 0 & f_{[E]}^n \\ f_{[N]}^n & -f_{[E]}^n & 0 \end{pmatrix} \begin{pmatrix} \delta \phi^n \\ \delta \theta^n \\ \delta \psi^n \end{pmatrix} + \begin{pmatrix} R_{b[11]}^n & R_{b[12]}^n & R_{b[13]}^n \\ R_{b[21]}^n & R_{b[22]}^n & R_{b[23]}^n \\ R_{b[31]}^n & R_{b[32]}^n & R_{b[33]}^n \end{pmatrix} \begin{pmatrix} \delta b_{[a,X]} \\ \delta b_{[a,Y]} \\ \delta b_{[a,Z]} \end{pmatrix} + \begin{pmatrix} 1 & 0 & 0 \\ 0 & 1 & 0 \\ 0 & 0 & 1 \end{pmatrix} \begin{pmatrix} \delta d\mathbf{g}_{[E]}^n \\ \delta d\mathbf{g}_{[N]}^n \\ \delta d\mathbf{g}_{[U]}^n \end{pmatrix} \end{aligned} \quad (3.25)$$

It is clarified, that \mathbf{g}^n is equivalent to $(\gamma^n + \mathbf{d}\mathbf{g}^n)$. The variation of gravity due to horizontal position errors is negligible. $\frac{d\gamma}{dh}$, the vertical normal gravity gradient of $-0.3086 \text{ mGal m}^{-1}$, has to be considered. \mathbf{f}^n was substituted by $\mathbf{R}_b^n \mathbf{f}^b$, because \mathbf{f}^b is the actual quantity observed by the IMU. $\delta \mathbf{f}^b$ represents the accelerometer errors and is replaced by $\delta \mathbf{b}_{[a]}$ in Eq. (3.25).

For a facilitated tracking of the previous derivatives, a few quantities are formulated in vector form and $\mathbf{R}_b^n \mathbf{f}^b$ is expanded.

$$\begin{aligned} \boldsymbol{\omega}_{[ie]}^n &= \begin{pmatrix} 0 \\ \omega_{[Earth]} \cos \varphi \\ \omega_{[Earth]} \sin \varphi \end{pmatrix} & \boldsymbol{\omega}_{[en]}^n &= \begin{pmatrix} \frac{-v_{[eb,N]}^n}{R_{[N]}+h} \\ \frac{v_{[eb,E]}^n}{R_{[E]}+h} \\ \frac{v_{[eb,E]}^n \tan \varphi}{R_{[E]}+h} \end{pmatrix} & \boldsymbol{\omega}_{[in]}^n &= \begin{pmatrix} \frac{-v_{[eb,N]}^n}{R_{[N]}+h} \\ \frac{v_{[eb,E]}^n}{R_{[E]}+h} + \omega_{[Earth]} \cos \varphi \\ \frac{v_{[eb,E]}^n \tan \varphi}{R_{[E]}+h} + \omega_{[Earth]} \sin \varphi \end{pmatrix} \\ \boldsymbol{\omega}_{[in]}^n + \boldsymbol{\omega}_{[ie]}^n &= \begin{pmatrix} \frac{-v_{[eb,N]}^n}{R_{[N]}+h} \\ \frac{v_{[eb,E]}^n}{R_{[E]}+h} + 2\omega_{[Earth]} \cos \varphi \\ \frac{v_{[eb,E]}^n \tan \varphi}{R_{[E]}+h} + 2\omega_{[Earth]} \sin \varphi \end{pmatrix} \\ (\boldsymbol{\omega}_{[in]}^n + \boldsymbol{\omega}_{[ie]}^n) \times \mathbf{v}^n &= \begin{pmatrix} -\left(\frac{v_{[eb,E]}^n \tan \varphi}{R_{[E]}+h} + 2\omega_{[Earth]} \sin \varphi\right)v_{[eb,N]}^n + \left(\frac{v_{[eb,E]}^n}{R_{[E]}+h} + 2\omega_{[Earth]} \cos \varphi\right)v_{[eb,U]}^n \\ \left(\frac{v_{[eb,E]}^n \tan \varphi}{R_{[E]}+h} + 2\omega_{[Earth]} \sin \varphi\right)v_{[eb,E]}^n + \frac{v_{[eb,N]}^n}{R_{[N]}+h}v_{[eb,U]}^n \\ -\left(\frac{v_{[eb,E]}^n}{R_{[E]}+h} + 2\omega_{[Earth]} \cos \varphi\right)v_{[eb,E]}^n + \frac{-v_{[eb,N]}^n}{R_{[N]}+h}v_{[eb,N]}^n \end{pmatrix} \\ \mathbf{R}_b^n \mathbf{f}^b &= \delta \mathbf{R}_b^n \check{\mathbf{R}}_b^n (\check{\mathbf{f}}^b + \delta \mathbf{f}^b) = (\mathbf{I} + [\delta \psi^n \times]) \check{\mathbf{R}}_b^n (\check{\mathbf{f}}^b + \delta \mathbf{f}^b) \\ &= \check{\mathbf{f}}^n + \begin{pmatrix} 0 & f_{[U]}^n & -f_{[N]}^n \\ -f_{[U]}^n & 0 & f_{[E]}^n \\ f_{[N]}^n & -f_{[E]}^n & 0 \end{pmatrix} \begin{pmatrix} \delta \phi^n \\ \delta \theta^n \\ \delta \psi^n \end{pmatrix} + \check{\mathbf{R}}_b^n \delta \mathbf{f}^b + \text{HOT} \end{aligned}$$

ATTITUDE

For the attitude, a different derivation of the error propagation equations is chosen instead of first-order Taylor approximations. Equation (3.20) represents the evolution of \mathbf{R}_b^n in an error-free scenario. By introducing observations to this equation, associated errors have to be taken into account. Attitude errors can be interpreted as small angle rotations (cf. Ch. 2.1.2). The error $\delta \mathbf{R}$ has to be applied to the estimated quantity $\check{\mathbf{R}}$ to retrieve the true value \mathbf{R} .

$$\mathbf{R}_b^b = \delta \mathbf{R}_b^b \check{\mathbf{R}}_b^b = \begin{pmatrix} 1 & \delta \psi^b & -\delta \theta^b \\ -\delta \psi^b & 1 & \delta \phi^b \\ \delta \theta^b & -\delta \phi^b & 1 \end{pmatrix} \check{\mathbf{R}}_b^b \quad (3.26)$$

Diving into that equation one can imagine that $\delta \mathbf{R}_b^b$ is defined in the b-frame since it is applied after transforming a vector from the n-frame into the b-frame. Because the n-frame is chosen inside the algorithm, the attitude error is (finally) defined in the n-frame.

$$\mathbf{R}_b^n = \delta \mathbf{R}_b^n \check{\mathbf{R}}_b^n = \begin{pmatrix} 1 & -\delta \psi^n & \delta \theta^n \\ \delta \psi^n & 1 & -\delta \phi^n \\ -\delta \theta^n & \delta \phi^n & 1 \end{pmatrix} \check{\mathbf{R}}_b^n = (\mathbf{I} + [\delta \psi^n \times]) \check{\mathbf{R}}_b^n \quad (3.27)$$

$$\Rightarrow \delta \mathbf{R}_b^n = \mathbf{I} + [\delta \boldsymbol{\psi}^n \times] \quad (3.28a)$$

$$\Rightarrow [\delta \boldsymbol{\psi}^n \times] = \delta \mathbf{R}_b^n - \mathbf{I} \quad (3.28b)$$

Note that $\delta \mathbf{R}_n^b \neq (\delta \mathbf{R}_b^n)^T$. The matrices and their elements are defined in different frames. With the matrix rule that $(\mathbf{A}\mathbf{B})^T = \mathbf{B}^T \mathbf{A}^T$, it can be shown that $\delta \mathbf{R}_b^n$ and $\delta \mathbf{R}_n^b$ have to be rotated for equality.

$$\delta \mathbf{R}_n^b = \check{\mathbf{R}}_n^b (\delta \mathbf{R}_b^n)^T \check{\mathbf{R}}_b^n = \check{\mathbf{R}}_n^b (\mathbf{I} + [\delta \boldsymbol{\psi}^n \times])^T \check{\mathbf{R}}_b^n \quad (3.29)$$

Applying $\mathbf{R}_b^n = \delta \mathbf{R}_b^n \check{\mathbf{R}}_b^n$ and $[\boldsymbol{\omega}_{[nb]}^b \times] = [(\check{\boldsymbol{\omega}}_{[nb]}^b + \delta \boldsymbol{\omega}_{[nb]}^b) \times]$ to Eq. (3.20) leads to

$$\begin{aligned} \dot{\mathbf{R}}_b^n &= \delta \mathbf{R}_b^n \check{\mathbf{R}}_b^n [(\check{\boldsymbol{\omega}}_{[nb]}^b + \delta \boldsymbol{\omega}_{[nb]}^b) \times] = (\mathbf{I} + [\delta \boldsymbol{\psi}^n \times]) \check{\mathbf{R}}_b^n [(\check{\boldsymbol{\omega}}_{[nb]}^b + \delta \boldsymbol{\omega}_{[nb]}^b) \times] \\ &= \check{\mathbf{R}}_b^n [\check{\boldsymbol{\omega}}_{[nb]}^b \times] + \check{\mathbf{R}}_b^n [\delta \boldsymbol{\omega}_{[nb]}^b \times] + [\delta \boldsymbol{\psi}^n \times] \check{\mathbf{R}}_b^n [\check{\boldsymbol{\omega}}_{[nb]}^b \times] + [\delta \boldsymbol{\psi}^n \times] \check{\mathbf{R}}_b^n [\delta \boldsymbol{\omega}_{[nb]}^b \times] \end{aligned} \quad (3.30)$$

In parallel, Eq. (3.27) is differentiated with the help of Eq. (3.20).

$$\dot{\mathbf{R}}_b^n = \dot{\check{\mathbf{R}}}_b^n + [\delta \dot{\boldsymbol{\psi}}^n \times] \check{\mathbf{R}}_b^n + [\delta \boldsymbol{\psi}^n \times] \dot{\check{\mathbf{R}}}_b^n = \check{\mathbf{R}}_b^n [\boldsymbol{\omega}_{[nb]}^b \times] + [\delta \dot{\boldsymbol{\psi}}^n \times] \check{\mathbf{R}}_b^n + [\delta \boldsymbol{\psi}^n \times] \dot{\check{\mathbf{R}}}_b^n [\boldsymbol{\omega}_{[nb]}^b \times] \quad (3.31)$$

Comparing Eq. (3.30) with Eq. (3.31), it can be approximated that $[\delta \dot{\boldsymbol{\psi}}^n \times] \check{\mathbf{R}}_b^n = \check{\mathbf{R}}_b^n [\delta \boldsymbol{\omega}_{[nb]}^b \times] + \dot{\check{\mathbf{R}}}_b^n [\delta \boldsymbol{\omega}_{[nb]}^b \times] \approx \check{\mathbf{R}}_b^n [\delta \boldsymbol{\omega}_{[nb]}^b \times]$, since the last term of Eq. (3.30) is of second order and can be dismissed. The resulting propagation of attitude errors are shown in matrix (Eq. (3.32a)) and vector (Eq. (3.32b)) form.

$$[\delta \dot{\boldsymbol{\psi}}^n \times] = \check{\mathbf{R}}_b^n [\delta \boldsymbol{\omega}_{[nb]}^b \times] \check{\mathbf{R}}_b^n \quad (3.32a)$$

$$\delta \dot{\boldsymbol{\psi}}^n = \check{\mathbf{R}}_b^n \delta \boldsymbol{\omega}_{[nb]}^b \quad (3.32b)$$

To specify $\delta \boldsymbol{\omega}_{[nb]}^b$, $\boldsymbol{\omega}_{[nb]}^b$ is defined in Eqs. (3.33).

$$\boldsymbol{\omega}_{[nb]}^b = \boldsymbol{\omega}_{[ib]}^b - \mathbf{R}_n^b \boldsymbol{\omega}_{[in]}^n \quad (3.33a)$$

$$\begin{aligned} \check{\boldsymbol{\omega}}_{[nb]}^b + \delta \boldsymbol{\omega}_{[nb]}^b &= (\check{\boldsymbol{\omega}}_{[ib]}^b + \delta \boldsymbol{\omega}_{[ib]}^b) - \delta \mathbf{R}_n^b \check{\mathbf{R}}_n^b (\check{\boldsymbol{\omega}}_{[in]}^n + \delta \boldsymbol{\omega}_{[in]}^n) \\ &= (\check{\boldsymbol{\omega}}_{[ib]}^b + \delta \boldsymbol{\omega}_{[ib]}^b) - \check{\mathbf{R}}_n^b (\mathbf{I} + [\delta \boldsymbol{\psi}^n \times])^T \check{\mathbf{R}}_b^n \check{\mathbf{R}}_n^b (\check{\boldsymbol{\omega}}_{[in]}^n + \delta \boldsymbol{\omega}_{[in]}^n) \end{aligned} \quad (3.33b)$$

$$\begin{aligned} \delta \boldsymbol{\omega}_{[nb]}^b &= \delta \boldsymbol{\omega}_{[ib]}^b - \check{\mathbf{R}}_n^b \delta \boldsymbol{\omega}_{[in]}^n - \check{\mathbf{R}}_n^b [\delta \boldsymbol{\psi}^n \times]^T \check{\boldsymbol{\omega}}_{[in]}^n - \check{\mathbf{R}}_n^b [\delta \boldsymbol{\psi}^n \times]^T \delta \boldsymbol{\omega}_{[in]}^n \\ &= \delta \boldsymbol{\omega}_{[ib]}^b - \check{\mathbf{R}}_n^b \delta \boldsymbol{\omega}_{[in]}^n + \check{\mathbf{R}}_n^b \delta \boldsymbol{\psi}^n \times \check{\boldsymbol{\omega}}_{[in]}^n + \check{\mathbf{R}}_n^b \delta \boldsymbol{\psi}^n \times \delta \boldsymbol{\omega}_{[in]}^n \\ &\approx \delta \boldsymbol{\omega}_{[ib]}^b - \check{\mathbf{R}}_n^b \delta \boldsymbol{\omega}_{[in]}^n - \check{\mathbf{R}}_n^b \check{\boldsymbol{\omega}}_{[in]}^n \times \delta \boldsymbol{\psi}^n + \text{HOT} \end{aligned} \quad (3.33c)$$

$$\Rightarrow \delta \dot{\boldsymbol{\psi}}^n \approx \check{\mathbf{R}}_b^n \delta \boldsymbol{\omega}_{[ib]}^b - \delta \boldsymbol{\omega}_{[in]}^n - \check{\boldsymbol{\omega}}_{[in]}^n \times \delta \boldsymbol{\psi}^n \quad (3.34)$$

Since $\boldsymbol{\omega}_{[in]}^n$ in Eq. (3.34) is not part of the state vector, this term (its vector form is defined in VELOCITY) is also expressed as first-order Taylor approach in Eq. (3.35).

$$-\delta \boldsymbol{\omega}_{[in]}^n = - \left. \frac{\partial \boldsymbol{\omega}_{[in]}^n}{\partial \mathbf{r}^e} \right|_{\tilde{\mathbf{r}}^e} \delta \mathbf{r}^e - \left. \frac{\partial \boldsymbol{\omega}_{[in]}^n}{\partial \mathbf{v}^n} \right|_{\tilde{\mathbf{v}}^n} \delta \mathbf{v}^n \quad (3.35)$$

Then, Eq. (3.34) can be formulated in detail, as shown in Eq. (3.36).

$$\begin{aligned}
 \delta\dot{\psi}^n &\approx \begin{pmatrix} R_{b[11]}^n & R_{b[12]}^n & R_{b[13]}^n \\ R_{b[21]}^n & R_{b[22]}^n & R_{b[23]}^n \\ R_{b[31]}^n & R_{b[32]}^n & R_{b[33]}^n \end{pmatrix} \begin{pmatrix} \delta\omega_{[ib,X]}^b \\ \delta\omega_{[ib,Y]}^b \\ \delta\omega_{[ib,Z]}^b \end{pmatrix} \\
 &- \begin{pmatrix} 0 & 0 & \frac{-v_{[eb,N]}^n}{(R_{[N]}+h)^2} \\ -\omega_{[Earth]} \sin \varphi & 0 & \frac{v_{[eb,E]}^n}{(R_{[E]}+h)^2} \\ \frac{v_{[eb,E]}^n}{(R_{[E]}+h) \cos^2 \varphi} + \omega_{[Earth]} \cos \varphi & 0 & \frac{v_{[eb,E]}^n \tan \varphi}{(R_{[E]}+h)^2} \end{pmatrix} \begin{pmatrix} \delta\varphi \\ \delta\lambda \\ \delta h \end{pmatrix} - \begin{pmatrix} 0 & \frac{-1}{R_{[N]}+h} & 0 \\ \frac{1}{R_{[E]}+h} & 0 & 0 \\ \frac{\tan \varphi}{R_{[E]}+h} & 0 & 0 \end{pmatrix} \begin{pmatrix} \delta v_{[eb,E]}^n \\ \delta v_{[eb,N]}^n \\ \delta v_{[eb,U]}^n \end{pmatrix} \\
 &- \begin{pmatrix} 0 & -\frac{v_{[eb,E]}^n \tan \varphi}{R_{[E]}+h} - \omega_{[Earth]} \sin \varphi & \frac{v_{[eb,E]}^n}{R_{[E]}+h} + \omega_{[Earth]} \cos \varphi \\ \frac{v_{[eb,E]}^n \tan \varphi}{R_{[E]}+h} + \omega_{[Earth]} \sin \varphi & 0 & \frac{v_{[eb,N]}^n}{R_{[N]}+h} \\ -\frac{v_{[eb,E]}^n}{R_{[E]}+h} - \omega_{[Earth]} \cos \varphi & \frac{-v_{[eb,N]}^n}{R_{[N]}+h} & 0 \end{pmatrix} \begin{pmatrix} \delta\phi^n \\ \delta\theta^n \\ \delta\psi^n \end{pmatrix} \tag{3.36}
 \end{aligned}$$

GYROSCOPE AND ACCELEROMETER BIASES

The differential equations for the biases of the gyroscope and accelerometers as first-order Gauß-Markov processes are shown in Eqs. (3.37) and (3.38).

$$\delta\dot{\mathbf{b}}_{[g]} = \frac{\partial(-\mathbf{B}_{[g]}\mathbf{b}_{[g]} + \mathbf{w}_{[b_{[g]}]})}{\partial\mathbf{b}_{[g]}} \Big|_{\tilde{\mathbf{b}}_{[g]}} \delta\mathbf{b}_{[g]} = \begin{pmatrix} -\beta_{[g,X]} & 0 & 0 \\ 0 & -\beta_{[g,Y]} & 0 \\ 0 & 0 & -\beta_{[g,Z]} \end{pmatrix} \begin{pmatrix} \delta b_{[g,X]} \\ \delta b_{[g,Y]} \\ \delta b_{[g,Z]} \end{pmatrix} \tag{3.37}$$

$$\delta\dot{\mathbf{b}}_{[a]} = \frac{\partial(-\mathbf{B}_{[a]}\mathbf{b}_{[a]} + \mathbf{w}_{[b_{[a]}]})}{\partial\mathbf{b}_{[a]}} \Big|_{\tilde{\mathbf{b}}_{[a]}} \delta\mathbf{b}_{[a]} = \begin{pmatrix} -\beta_{[a,X]} & 0 & 0 \\ 0 & -\beta_{[a,Y]} & 0 \\ 0 & 0 & -\beta_{[a,Z]} \end{pmatrix} \begin{pmatrix} \delta b_{[a,X]} \\ \delta b_{[a,Y]} \\ \delta b_{[a,Z]} \end{pmatrix} \tag{3.38}$$

GRAVITY DISTURBANCES

This chapter is completed with the last equations comprising the differential equations for the gravity disturbance, modeled as a Gauß-Markov process of third-order, and derivatives (Eqs. (3.39) - (3.41)).

$$\delta\dot{\mathbf{d}}\mathbf{g}^n = \frac{\partial\dot{\mathbf{d}}\mathbf{g}^n}{\partial\mathbf{d}\mathbf{g}^n} \Big|_{\tilde{\mathbf{d}}\mathbf{g}^n} \delta\mathbf{d}\mathbf{g}^n = \begin{pmatrix} 1 & 0 & 0 \\ 0 & 1 & 0 \\ 0 & 0 & 1 \end{pmatrix} \begin{pmatrix} \delta\dot{d}g_{[E]}^n \\ \delta\dot{d}g_{[N]}^n \\ \delta\dot{d}g_{[U]}^n \end{pmatrix} \tag{3.39}$$

$$\delta\ddot{\mathbf{d}}\mathbf{g}^n = \frac{\partial\ddot{\mathbf{d}}\mathbf{g}^n}{\partial\mathbf{d}\mathbf{g}^n} \Big|_{\tilde{\mathbf{d}}\mathbf{g}^n} \delta\mathbf{d}\mathbf{g}^n = \begin{pmatrix} 1 & 0 & 0 \\ 0 & 1 & 0 \\ 0 & 0 & 1 \end{pmatrix} \begin{pmatrix} \delta\ddot{d}g_{[E]}^n \\ \delta\ddot{d}g_{[N]}^n \\ \delta\ddot{d}g_{[U]}^n \end{pmatrix} \tag{3.40}$$

$$\begin{aligned}
 \delta \ddot{\mathbf{d}}\mathbf{g}^n &= \frac{\partial \ddot{\mathbf{d}}\mathbf{g}^n}{\partial \mathbf{d}\mathbf{g}^n} \bigg|_{\tilde{\mathbf{d}}\mathbf{g}^n} \delta \mathbf{d}\mathbf{g}^n + \frac{\partial \ddot{\mathbf{d}}\mathbf{g}^n}{\partial \dot{\mathbf{d}}\mathbf{g}^n} \bigg|_{\tilde{\mathbf{d}}\mathbf{g}^n} \delta \dot{\mathbf{d}}\mathbf{g}^n + \frac{\partial \ddot{\mathbf{d}}\mathbf{g}^n}{\partial \ddot{\mathbf{d}}\mathbf{g}^n} \bigg|_{\tilde{\mathbf{d}}\mathbf{g}^n} \delta \ddot{\mathbf{d}}\mathbf{g}^n \\
 &= \begin{pmatrix} -\beta_{[dg,E]}^3 & 0 & 0 \\ 0 & -\beta_{[dg,N]}^3 & 0 \\ 0 & 0 & -\beta_{[dg,U]}^3 \end{pmatrix} \begin{pmatrix} \delta dg_{[E]}^n \\ \delta dg_{[N]}^n \\ \delta dg_{[U]}^n \end{pmatrix} + \begin{pmatrix} -3\beta_{[dg,E]}^2 & 0 & 0 \\ 0 & -3\beta_{[dg,N]}^2 & 0 \\ 0 & 0 & -3\beta_{[dg,U]}^2 \end{pmatrix} \begin{pmatrix} \delta \dot{dg}_{[E]}^n \\ \delta \dot{dg}_{[N]}^n \\ \delta \dot{dg}_{[U]}^n \end{pmatrix} \\
 &+ \begin{pmatrix} -3\beta_{[dg,E]} & 0 & 0 \\ 0 & -3\beta_{[dg,N]} & 0 \\ 0 & 0 & -3\beta_{[dg,U]} \end{pmatrix} \begin{pmatrix} \delta \ddot{dg}_{[E]}^n \\ \delta \ddot{dg}_{[N]}^n \\ \delta \ddot{dg}_{[U]}^n \end{pmatrix} \quad (3.41)
 \end{aligned}$$

With this information the system matrix \mathbf{F} is defined by merging the derived error relations in Eqs. (3.23), (3.25), (3.36), and (3.37) to (3.41) into one matrix.

$$\frac{d\delta\mathbf{y}}{dt} = \begin{pmatrix} \frac{d\delta\mathbf{r}^e}{dt} \\ \frac{d\delta\mathbf{v}^n}{dt} \\ \frac{d\delta\mathbf{R}_b^n}{dt} \\ \frac{d\delta\mathbf{b}_{[g]}}{dt} \\ \frac{d\delta\mathbf{b}_{[a]}}{dt} \\ \frac{d\delta\mathbf{d}\mathbf{g}^n}{dt} \\ \frac{d\delta\dot{\mathbf{d}}\mathbf{g}^n}{dt} \\ \frac{d\delta\ddot{\mathbf{d}}\mathbf{g}^n}{dt} \end{pmatrix} = \mathbf{F} \begin{pmatrix} \delta\mathbf{r}^e \\ \delta\mathbf{v}^n \\ \delta\mathbf{R}_b^n \\ \delta\mathbf{b}_{[g]} \\ \delta\mathbf{b}_{[a]} \\ \delta\mathbf{d}\mathbf{g}^n \\ \delta\dot{\mathbf{d}}\mathbf{g}^n \\ \delta\ddot{\mathbf{d}}\mathbf{g}^n \end{pmatrix} \quad (3.42)$$

The next step is the calculation of the transition matrix Φ either via Eq. (2.51) or via the van Loan method (please see van Loan (1978) or Brown and Hwang (2012, p. 126)). The advantage of van Loan's method is that in this approach the system noise matrix \mathbf{Q} is quantified simultaneously. Finally, the error covariance matrix is propagated, which is realized by Eq. (2.53b)²⁸. In case of an available update measurement, the EKF update routine is entered, which is treated in the next section. Otherwise, the next epoch of the for-loop mentioned on p. 42 is re-entered.

3.1.3 Kalman Filter setup

The execution of the EKF update routine is initiated as soon as external update information is available. For terrestrial 3D-gravity profiling, this can be either a coordinate update (CUPT) normally plus velocity update (VUPT) from GNSS observations, a ZUPT plus zero gravity gradient update (ZGUPT) during standstill phases, or a 1D-, 2D-, or a 3D-GUPT if the car is close to a gravity tie point. While the CUPT, VUPT, ZUPT, and ZGUPT are referenced by time tags, a GUPT is either referenced by time or by its location. Thus, before running the update routines, it has to be determined if a gravity tie point is close by. "Close by" is defined as less than 25 m horizontal distance between the current IMU position and any gravity tie point. This criterion is based on a gradient analysis of reference data in the Estergebirge, see Ch. 4.3.2, and might be adapted for other campaigns. After having determined the type(s) of available updates, the EKF update is executed. Step one is to quantify the difference between the update value(s) and the current total-state. The differences are used as observations inside the EKF.

²⁸Remember from Ch. 2.4.1 that the error-state vector is zero outside the EKF update phase in this realization and is not propagated.

- In case a CUPT is available, the position error is determined by removing the IMU-based strap-down position (plus lever arm) from the GNSS position. The same procedure is conducted for a VUPT. Here, the lever arm affects the IMU-based velocity through angular motion, which has to be accounted for, before the difference to the GNSS-based velocities can be calculated. As measurement noise, the standard deviations of the GNSS software solution are used.
- If the time tag of a ZUPT, and ZGUPT coincides with the IMU time tag, the velocity of the car, as well as the changes in the gravity disturbance, are supposed to be zero. In this case, the observation is the negative IMU-based velocity and the negative value of the propagated $\dot{\mathbf{d}}\mathbf{g}^n$. Empirical accuracy estimates are used that should absorb smaller oscillations from wind or closing doors, etc.
- Lastly, for GUPTs absolute gravity is continued upward from the ground to the IMU level with the normal gravity gradient (free-air gradient). Then, the gravity tie values are transformed into the n-frame where the projected gravity disturbance, the normal gravity, and, if a gravity reduction is applied, the model-based gravity disturbance of this point are reduced. The residuals form the EKF observations.

In the next step, the measurement matrix \mathbf{H} is created. Normally, this matrix links the propagated EKF (error-)states (here $\delta\mathbf{y}_{[k]}^{[-]}$) with the observations, cf. Eq. (2.54), which are set to zero in the closed-loop scenario. However, the \mathbf{H} matrix is still required to calculate the Kalman Gain matrix \mathbf{K} and the updated error covariance matrix \mathbf{P} , cf. Eqs. (2.55) and (2.56b). This also means that the mathematical units of the \mathbf{H} matrix entries have to be adapted according to Table 3.1. Possible matrix entries are derived in the following for a CUPT, a VUPT, a ZUPT, a ZGUPT and a GUPT from Eqs. (3.43) to (3.52). The derivation is based on observed quantities ($\check{\cdot}$) that are split into the true and the error (δ) component. The true quantities always cancel out, indicated by e.g., $\check{\mathbf{R}}$. Depending on the available update information, the number of rows of the measurement matrix is varying. The matrices below have to be combined accordingly if more than one type of update is available at one point in time.

CUPT

The position of the GNSS antenna reference point should be equal to the IMU position plus the lever arm. Therefore, the lever arm has to be expressed in the n-frame, with the east and north component in radiant, to be able to assign its components to the geodetic latitude, longitude, and height of the IMU solution. A possible lever arm error is not considered in the following, since it hardly affects²⁹ the outcome when determined better than some centimeters, see Becker (2016).

$$\begin{aligned}
 \delta\mathbf{r}^e &= \check{\mathbf{r}}_{[GNSS]}^e - (\check{\mathbf{r}}_{[IMU]}^e + (\check{\mathbf{R}}_b^n \mathbf{l}^b)_{[12 \rightarrow 21, rad]}) \\
 &= \mathbf{r}_{[GNSS]}^e - \delta\mathbf{r}_{[GNSS]}^e - (\mathbf{r}_{[IMU]}^e - \delta\mathbf{r}_{[IMU]}^e + ((\delta\mathbf{R}_b^n)^T \mathbf{R}_b^n \mathbf{l}^b)_{[12 \rightarrow 21, rad]}) \\
 &= \mathbf{r}_{[GNSS]}^e - \delta\mathbf{r}_{[GNSS]}^e - (\mathbf{r}_{[IMU]}^e - \delta\mathbf{r}_{[IMU]}^e + ((\mathbf{I} - [\delta\psi^n \times]) \mathbf{R}_b^n \mathbf{l}^b)_{[12 \rightarrow 21, rad]}) \\
 &= \cancel{\mathbf{r}_{[GNSS]}^e} - \delta\mathbf{r}_{[GNSS]}^e - \cancel{\mathbf{r}_{[IMU]}^e} + \delta\mathbf{r}_{[IMU]}^e - \cancel{(\mathbf{R}_b^n \mathbf{l}^b)_{[12 \rightarrow 21, rad]}} + (\delta\psi^n \times \mathbf{l}^n)_{[12 \rightarrow 21, rad]} \\
 &= \delta\mathbf{r}_{[combined]}^e - (\mathbf{l}^n \times \delta\psi^n)_{[12 \rightarrow 21, rad]} \\
 &= \begin{pmatrix} \delta\varphi \\ \delta\lambda \\ \delta h \end{pmatrix} - \begin{pmatrix} l_{[U]} & 0 & -l_{[E]} \\ 0 & -l_{[U]} & l_{[N]} \\ -l_{[N]} & l_{[E]} & 0 \end{pmatrix} \begin{pmatrix} \delta\phi^n \\ \delta\theta^n \\ \delta\psi^n \end{pmatrix} \tag{3.43}
 \end{aligned}$$

*Row 1 and 2 are swapped and the east and north components are expressed in radiant.

$$\mathbf{H}_{[CUPT]} = \begin{pmatrix} \mathbf{I} & \mathbf{0} & -[\mathbf{l}^n \times]_{[12 \rightarrow 21, rad]} & \mathbf{0} & \mathbf{0} & \mathbf{0} & \mathbf{0} & \mathbf{0} \end{pmatrix} \tag{3.44}$$

²⁹The outcome of Ch. 4.3 indicates that the VDs are more sensitive to such an error compared to the SGD.

VUPT

The time derivative of $\check{\mathbf{r}}_{[IMU]}^e + (\check{\mathbf{R}}_b^n \mathbf{l}^b)_{[12 \rightarrow 21, rad]}$ (see CUPT) leads to the velocity measurement model. Again, a lever arm error is not considered. Furthermore, errors of second order are dismissed and $[(\boldsymbol{\omega}_{[in]}^b - \delta\boldsymbol{\omega}_{[in]}^b) \times]$ is disregarded, because the rotations $[(\boldsymbol{\omega}_{[ie]}^b + \boldsymbol{\omega}_{[en]}^b) \times]$ (Earth's rotation plus transport rate) are some orders of magnitude smaller than $[\boldsymbol{\omega}_{[ib]}^b \times]$ ($^\circ \text{ h}^{-1}$ vs. $^\circ \text{ s}^{-1}$).

$$\begin{aligned}
 \delta\mathbf{v}^n &= \check{\mathbf{v}}_{[GNSS]}^n - (\check{\mathbf{v}}_{[IMU]}^n + \check{\mathbf{R}}_b^n \mathbf{l}^b) \\
 &= \check{\mathbf{v}}_{[GNSS]}^n - (\check{\mathbf{v}}_{[IMU]}^n + \check{\mathbf{R}}_b^n (\check{\boldsymbol{\omega}}_{[ib]}^b - \check{\boldsymbol{\omega}}_{[in]}^b) \times \mathbf{l}^b) \\
 &= \mathbf{v}_{[GNSS]}^n - \delta\mathbf{v}_{[GNSS]}^n - (\mathbf{v}_{[IMU]}^n - \delta\mathbf{v}_{[IMU]}^n + (\mathbf{I} - [\delta\boldsymbol{\psi}^n \times]) \mathbf{R}_b^n (\boldsymbol{\omega}_{[ib]}^b - \delta\boldsymbol{\omega}_{[ib]}^b - \boldsymbol{\omega}_{[in]}^b + \delta\boldsymbol{\omega}_{[in]}^b) \times \mathbf{l}^b) \\
 &= \mathbf{v}_{[GNSS]}^n - \delta\mathbf{v}_{[GNSS]}^n - \mathbf{v}_{[IMU]}^n + \delta\mathbf{v}_{[IMU]}^n - \mathbf{R}_b^n (\boldsymbol{\omega}_{[ib]}^b - \delta\boldsymbol{\omega}_{[ib]}^b) \times \mathbf{l}^b \\
 &+ \mathbf{R}_b^n (\boldsymbol{\omega}_{[in]}^b - \delta\boldsymbol{\omega}_{[in]}^b) \times \mathbf{l}^b + [\delta\boldsymbol{\psi}^n \times] \mathbf{R}_b^n (\boldsymbol{\omega}_{[ib]}^b - \delta\boldsymbol{\omega}_{[ib]}^b) \times \mathbf{l}^b - [\delta\boldsymbol{\psi}^n \times] \mathbf{R}_b^n (\boldsymbol{\omega}_{[in]}^b - \delta\boldsymbol{\omega}_{[in]}^b) \times \mathbf{l}^b \\
 &= \cancel{\mathbf{v}_{[GNSS]}^n} - \delta\mathbf{v}_{[GNSS]}^n - \cancel{\mathbf{v}_{[IMU]}^n} + \delta\mathbf{v}_{[IMU]}^n - \cancel{\mathbf{R}_b^n \boldsymbol{\omega}_{[ib]}^b \times \mathbf{l}^b} + \mathbf{R}_b^n \delta\boldsymbol{\omega}_{[ib]}^b \times \mathbf{l}^b + \cancel{\mathbf{R}_b^n \boldsymbol{\omega}_{[in]}^b \times \mathbf{l}^b} \\
 &- \cancel{\mathbf{R}_b^n \delta\boldsymbol{\omega}_{[in]}^b \times \mathbf{l}^b} + [\delta\boldsymbol{\psi}^n \times] \mathbf{R}_b^n \boldsymbol{\omega}_{[ib]}^b \times \mathbf{l}^b - [\delta\boldsymbol{\psi}^n \times] \mathbf{R}_b^n \delta\boldsymbol{\omega}_{[ib]}^b \times \mathbf{l}^b - [\delta\boldsymbol{\psi}^n \times] \mathbf{R}_b^n \boldsymbol{\omega}_{[in]}^b \times \mathbf{l}^b \\
 &+ [\delta\boldsymbol{\psi}^n \times] \mathbf{R}_b^n \delta\boldsymbol{\omega}_{[in]}^b \times \mathbf{l}^b \\
 &= \delta\mathbf{v}_{[combined]}^n - [(\mathbf{R}_b^n \boldsymbol{\omega}_{[ib]}^b \times \mathbf{l}^b) \times] \delta\boldsymbol{\psi}^n - \mathbf{R}_b^n \mathbf{l}^b \times \delta\boldsymbol{\omega}_{[ib]}^b \\
 &= \begin{pmatrix} \delta v_{[eb,E]}^n \\ \delta v_{[eb,N]}^n \\ \delta v_{[eb,U]}^n \end{pmatrix} - \left[\mathbf{R}_b^n \begin{pmatrix} 0 & -\omega_{[ib,Z]}^b & \omega_{[ib,Y]}^b \\ \omega_{[ib,Z]}^b & 0 & -\omega_{[ib,X]}^b \\ -\omega_{[ib,Y]}^b & \omega_{[ib,X]}^b & 0 \end{pmatrix} \begin{pmatrix} l_{[X]} \\ l_{[Y]} \\ l_{[Z]} \end{pmatrix} \times \right] \begin{pmatrix} \delta\phi^n \\ \delta\theta^n \\ \delta\psi^n \end{pmatrix} \\
 &- \mathbf{R}_b^n \begin{pmatrix} 0 & -l_{[Z]} & l_{[Y]} \\ l_{[Z]} & 0 & -l_{[X]} \\ -l_{[Y]} & l_{[X]} & 0 \end{pmatrix} \begin{pmatrix} \delta b_{[g,X]} \\ \delta b_{[g,Y]} \\ \delta b_{[g,Z]} \end{pmatrix} \tag{3.45}
 \end{aligned}$$

$$\mathbf{H}_{[VUPT]} = \begin{pmatrix} \mathbf{0} & \mathbf{I} & -[(\mathbf{R}_b^n \boldsymbol{\omega}_{[ib]}^b \times \mathbf{l}^b) \times] & \mathbf{0} & -\mathbf{R}_b^n [\mathbf{l}^b \times] & \mathbf{0} & \mathbf{0} & \mathbf{0} \end{pmatrix} \tag{3.46}$$

ZUPT and ZGUPT

During static periods, the velocity of the IMU is supposed to be zero. The same is valid for changes in the gravity disturbance. Residual movement of the instruments due to wind, etc., must be absorbed by the corresponding accuracy estimation. The lever arm does not have to be taken into account assuming no rotations. Note that this observation is considered more reliable than the GNSS velocity observations during standstill phases.

$$\begin{aligned}
 \delta\mathbf{v}^n &= \check{\mathbf{0}} - \check{\mathbf{v}}_{[IMU]}^n \\
 &= \mathbf{v}_{[true]}^n - \delta\mathbf{v}_{[empirical]}^n - (\mathbf{v}_{[IMU]}^n - \delta\mathbf{v}_{[IMU]}^n) \\
 &= \cancel{\mathbf{v}_{[true]}^n} - \delta\mathbf{v}_{[empirical]}^n - \cancel{\mathbf{v}_{[IMU]}^n} + \delta\mathbf{v}_{[IMU]}^n \\
 &= \delta\mathbf{v}_{[combined]}^n \\
 &= \begin{pmatrix} \delta v_{[eb,E]}^n \\ \delta v_{[eb,N]}^n \\ \delta v_{[eb,U]}^n \end{pmatrix} \tag{3.47}
 \end{aligned}$$

$$\mathbf{H}_{[ZUPT]} = \begin{pmatrix} \mathbf{0} & \mathbf{I} & \mathbf{0} & \mathbf{0} & \mathbf{0} & \mathbf{0} & \mathbf{0} & \mathbf{0} \end{pmatrix} \tag{3.48}$$

$$\begin{aligned}
 \delta \dot{\mathbf{d}}\mathbf{g}^n &= \check{\mathbf{0}} - \dot{\check{\mathbf{d}}}\mathbf{g}_{[projected]}^n \\
 &= \dot{\mathbf{d}}\mathbf{g}_{[true]}^n - \delta \dot{\mathbf{d}}\mathbf{g}_{[empirical]}^n - (\dot{\mathbf{d}}\mathbf{g}_{[projected]}^n - \delta \dot{\mathbf{d}}\mathbf{g}_{[projected]}^n) \\
 &= \cancel{\dot{\mathbf{d}}\mathbf{g}_{[true]}^n} - \delta \dot{\mathbf{d}}\mathbf{g}_{[empirical]}^n - \cancel{\dot{\mathbf{d}}\mathbf{g}_{[projected]}^n} + \delta \dot{\mathbf{d}}\mathbf{g}_{[projected]}^n \\
 &= \delta \dot{\mathbf{d}}\mathbf{g}_{[combined]}^n \\
 &= \begin{pmatrix} \delta \dot{\mathbf{d}}\mathbf{g}_{[E]}^n \\ \delta \dot{\mathbf{d}}\mathbf{g}_{[N]}^n \\ \delta \dot{\mathbf{d}}\mathbf{g}_{[U]}^n \end{pmatrix}
 \end{aligned} \tag{3.49}$$

$$\mathbf{H}_{[ZGUP T]} = \begin{pmatrix} \mathbf{0} & \mathbf{0} & \mathbf{0} & \mathbf{0} & \mathbf{0} & \mathbf{0} & \mathbf{I} & \mathbf{0} \end{pmatrix} \tag{3.50}$$

GUPT

Lastly, the \mathbf{H} matrix for gravity updates is introduced.

$$\begin{aligned}
 \delta \mathbf{d}\mathbf{g}^n &= \mathbf{d}\mathbf{g}_{[gravity\ tie]}^n - \check{\mathbf{d}}\mathbf{g}_{[projected]}^n \\
 &= \mathbf{d}\mathbf{g}_{[gravity\ tie]}^n - \delta \mathbf{d}\mathbf{g}_{[gravity\ tie]}^n - (\mathbf{d}\mathbf{g}_{[projected]}^n - \delta \mathbf{d}\mathbf{g}_{[projected]}^n) \\
 &= \cancel{\mathbf{d}\mathbf{g}_{[gravity\ tie]}^n} - \delta \mathbf{d}\mathbf{g}_{[gravity\ tie]}^n - \cancel{\mathbf{d}\mathbf{g}_{[projected]}^n} + \delta \mathbf{d}\mathbf{g}_{[projected]}^n \\
 &= \delta \mathbf{d}\mathbf{g}_{[combined]}^n \\
 &= \begin{pmatrix} \delta \mathbf{d}\mathbf{g}_{[E]}^n \\ \delta \mathbf{d}\mathbf{g}_{[N]}^n \\ \delta \mathbf{d}\mathbf{g}_{[U]}^n \end{pmatrix}
 \end{aligned} \tag{3.51}$$

$$\mathbf{H}_{[GUPT]} = \begin{pmatrix} \mathbf{0} & \mathbf{0} & \mathbf{0} & \mathbf{0} & \mathbf{0} & \mathbf{I} & \mathbf{0} & \mathbf{0} \end{pmatrix} \tag{3.52}$$

After the measurement matrix is determined, the Kalman Gain matrix \mathbf{K} is calculated by using Eq. (2.55), which is applied to the innovation (cf. Eq. (2.56a)) to define the updated error-state vector. Then, the error covariance matrix is updated with Eq. (2.56b) and the error-state vector $\delta \mathbf{y}^{[+]}$, the transition matrix Φ , the propagated and the updated error covariance matrices ($\mathbf{P}^{[-]}$ and $\mathbf{P}^{[+]}$) have to be saved for the RTS smoothing process. Before the next epoch is entered, the error-states are applied to the total-states after adequate unit transformation and the error-state vector is set to zero again, cf. Eq. (2.57).

Chapters 3.1.1, 3.1.2, and 3.1.3 are repeatedly executed as long as there is unprocessed IMU data, before finally the RTS smoother is run on the EKF results, see Ch. 2.4.3.

After having applied the residual corrections of the RTS to the gravity disturbance estimates, it is important to reapply the gravity disturbance of the gravity model, which was used for reducing the gravity disturbances signal inside the EKF. Of course, this step is omitted when no gravity reduction was conducted.

3.2 Profile refinement

Unfortunately, in the case of terrestrial 3D-gravity profiling, the RTS output does not meet the accuracy expectations for the 3D-gravity disturbance along the trajectory. A direct indication of the decreased quality is the large difference between the results when driving in opposite directions, as will be shown in Ch. 4.3.3.2 (Figs. 4.25(a), (c), and (e)).

The enormous advantage of terrestrial campaigns to repeatedly measure a trajectory in both directions comes into play at this point. For example, for the Estergebirge campaign (see Ch. 4.3), a trajectory was observed in both directions three times to extract gravity disturbance profiles. The final result of this thesis is created by a combination of the single-direction gravity disturbance profiles of each run followed by the combination of these results from different runs³⁰ to mitigate random errors. This way more robust results are gained due to averaging/redundancy. Details of the applied approach are explained in the following.

For a single run (including both directions):

- Division of the latitude-range into 0.001° (~ 111 m) segments³¹. This value is chosen as it is about half of the spatial resolution of GGMplus.
- Calculation of the mean gravity disturbance of the RTS smoother output for each segment, for each direction. For the segments including turning points, only one mean value is calculated.
- Calculation of the corresponding mean latitudes of the RTS smoother output.
- Averaging of the mean gravity disturbances of both directions for each segment, except for turning points.
- Averaging of the corresponding mean latitudes, except for turning points.
- Linear interpolation onto the original GNSS latitudes, not positions³².

For the combination of multiple runs, items 1 - 5 are executed for each run separately. Then, the segments of the different runs are averaged, before item 6, the linear interpolation, is performed.

³⁰If the reader needs more information about the Estergebirge campaign to better understand the explained refinement approach, the beginning of Ch. 4.3 gives a short introduction to the Estergebirge campaign.

³¹A specialty of the Estergebirge trajectory, the author took advantage of, is its north-south alignment. For other campaigns, the length of the trajectory should be used to define the length of a segment instead.

³²This approach is only applicable due to the dominant and steady north-south orientation of the trajectory.

4 Campaign analyses

The following subsections build the centerpiece of this thesis. The reader is introduced to three thematically different measurement campaigns. All of them contribute important insights to the main subject of terrestrial 3D-gravity profiling. At first, the QDaedalus zenith camera, its performance, and its added value for gravity model validation are exemplified. Therefore, an astrogeodetic campaign conducted in February/March 2017 in Perth (Western Australia) is evaluated in Ch. 4.1. The next section deals with the temperature calibration of the RQH. Three different calibration schemes were conducted with the RQH, which are presented, visualized, and assessed in Ch. 4.2. Lastly, in Ch. 4.3 a terrestrial 3D-gravity profiling campaign is analyzed. It involves the QDaedalus zenith camera as well as the deduced temperature calibration parameters. The campaign was realized in the Estergebirge, around 100 km south of Munich (Germany) in the northern part of the Alps.

The main takeaways from this chapter are that

... the QDaedalus zenith camera

- allows observing precise astronomical coordinates ($\sigma \approx \pm 0.2''$) in a fast and low-cost manner
- allows evaluating gravity field models locally in terms of VD and/or height anomaly profiles
- is able to capture and locate large crustal density contrasts
- is easy to handle and its transport is uncomplicated

... the RQH

- exhibits relevant temperature dependencies in the estimated accelerometer biases and scale factors
- gyroscope observations are only slightly affected by the temperature
- ISA orientation w.r.t. the housing varies with changing temperature
- is not susceptible to larger temperature-induced movement between sensor triads or single axes of the accelerometers and gyroscopes

... terrestrial 3D-gravity profiling

- allows mapping the SGD and VDs along a given trajectory with RMS errors of 1.5 mGal and 0.2 - 0.5'' w.r.t. accurate reference data at a spatial resolution of ~ 200 m, if:
 - * 3D-gravity tie points are provided every 10 - 15 km
 - * a high-resolution (~ 200 m) gravity field model, like GGMplus, is chosen to reduce the gravity disturbance inside the EKF. The EKF will estimate inconsistencies between the model and real gravity, e.g., due to density anomalies.
 - * the inertial sensor output is corrected for temperature-induced errors (important for the vertical component)
 - * the \mathbf{Q} -matrix is tuned to match the IMU behavior and local gravity disturbance characteristics
 - * the trajectory is measured in both directions, at least twice, to benefit from redundancy

4.1 Digital astrogeodetic traverse in Perth³³

Historical VD traverses have been conducted in Australia for astrogeodetic geoid determination (e.g., Fischer et al. (1968) or Fryer (1972)), but were analog, and of lower precision than modern VD measurements. Thus, the following traverse is the first of its kind in the Southern Hemisphere. The digital QDaedalus zenith camera (Guillaume et al. (2012)), introduced in Ch. 2.2, was deployed in February 2017 to measure VDs with $\sim \pm 0.2''$ precision at 39 benchmarks (BMs) with a ~ 1 km spacing in Perth, Western Australia (see Fig. 4.1). This study area was deliberately chosen because it hosts one of the steepest geoid gradients in the world due to the juxtaposition of the low bulk density Perth Basin and the high bulk density Yilgarn Craton (topographic bulk density contrasts reach 480 kg m^{-3} (Middleton et al. (1993)) that are separated by the near-vertical 15 km-deep Darling Fault, and because of its proximity to the ocean where problems associated with coastal marine gravity quality and the sea-land transition can affect the quality of gravimetric quasigeoid models. The objective of this study is to introduce a new VD data set acquired with digital instrumentation in the Southern Hemisphere and to exemplify the use of this data set for validation of existing global and regional gravity field models in this "gravimetrically challenging" region. For interested readers, this VD data set is freely available via <https://mediatum.ub.tum.de/1399846>.

Annotation: The VD campaign in Perth was designed as a low-cost effort (less than AU\$10,000), possibly allowing replication in other Southern Hemisphere countries (e.g., Asia, Africa, South America, and Antarctica), where VD data are particularly scarce, to improve the global VD data coverage, and to rectify the current geographical VD imbalance between Northern and Southern Hemispheres. In turn, this will allow for improved global testing of high-degree gravity field models (such as the anticipated Earth Gravitational Model 2020 (EGM2020)). For the measurement campaign, the logistical requirements were comparatively low. The measurement equipment was transported by commuter aircraft and moved between stations with a small car.

Data

The data part includes information about the observed astrogeodetic VDs and auxiliary measurements before the models used for comparisons are introduced. Subsequently, a short description of the applied astronomical-topographical leveling method follows. Its outcome is used to convert VDs to height anomaly differences. For information about the method of astronomical leveling, the reader is referred to Ch. 2.3.4. Lastly, the quality of the VDs and height anomaly differences are assessed.

The measurement process and data processing of the QDaedalus zenith camera are summarized in Ch. 2.2 and explained in detail in Hauk et al. (2016) and Guillaume et al. (2012), so not replicated here. From February 15 to March 1, 2017, weather conditions (predominantly clear summer skies over Perth) permitted QDaedalus observations of astronomical coordinates on 13 nights at 39 different BMs along an east-west traverse (up to four BMs per night). The location of the astrogeodetic traverse is shown in Fig. 4.1, together with the surface geology (Davidson, 1995), the Australian Gravimetric Quasigeoid (AGQG) heights 2017 (Featherstone et al., 2018), and the AGQG2017 VDs. For the astronomical orientation of the system, stars of the Crux, Triangulum Australe, or Carina constellations were targeted, depending on local time and sky-visibility. A set of three consecutive observation sessions was performed at or near each BM, each taking ~ 15 minutes and resulting in ~ 300 angular measurements. The observations from all sessions were averaged to reduce random error sources (e.g., atmospheric scintillation). For internal validation and evaluation of the results, observations were repeated at six BMs on different nights. The quality assessment yielded standard deviations of $\pm 0.17''$ for ξ and $\pm 0.23''$ for η . These numbers are in agreement with the standard deviations of $\pm 0.15''$ to $\pm 0.20''$, which were determined based on repeat and comparison measurements in Germany prior to the campaign (Hauk et al. (2016)).

³³Schack et al. (2018), see remarks on p. 6

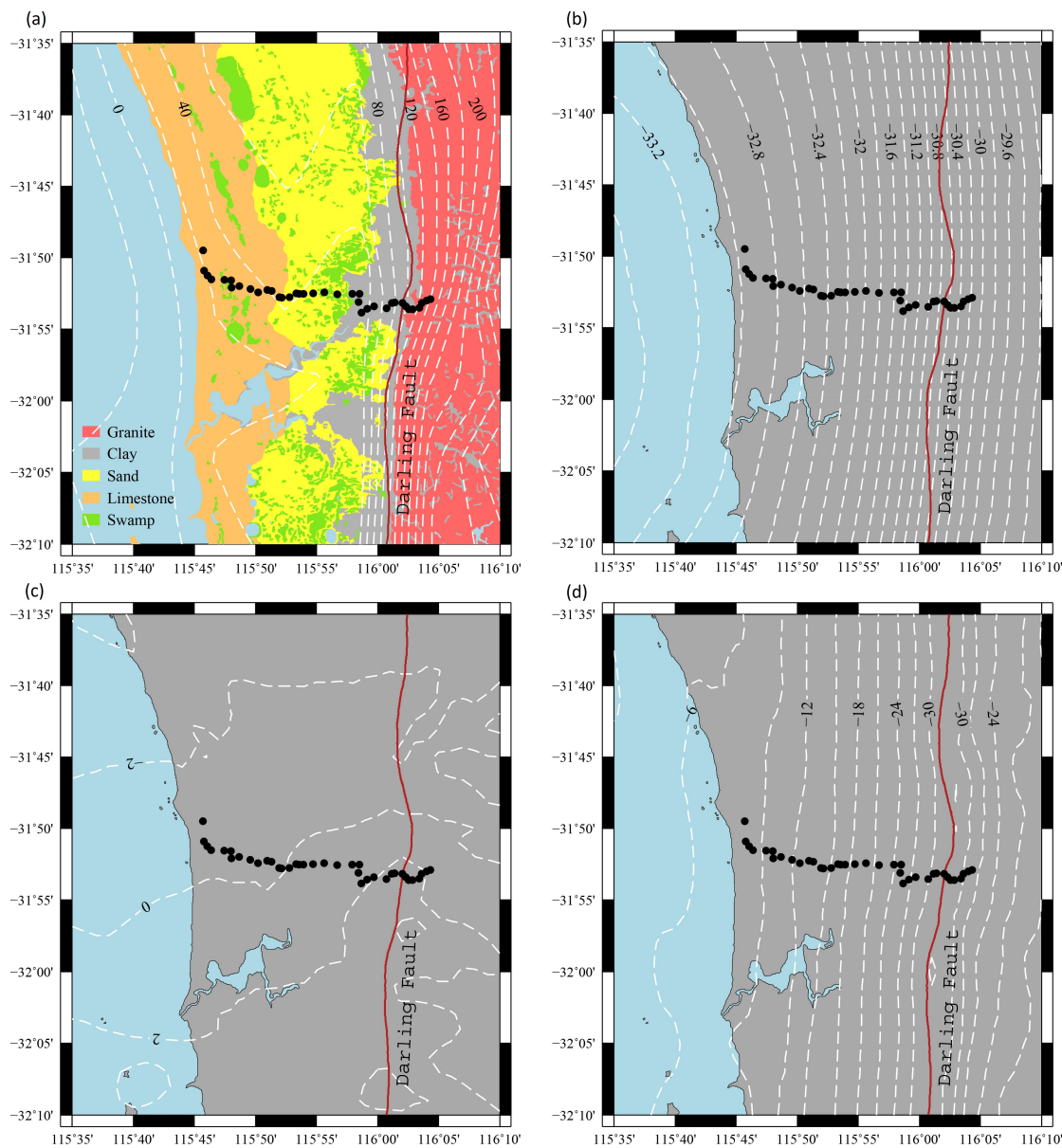


Figure 4.1: Study area in Perth, Western Australia. (a) Surface geology digitized from Davidson (1995) with elevations contoured from Shuttle Radar Topography Mission (SRTM), (b) AGQG2017 height anomaly in meters, showing the steep east-west gradient (~ 70 ppm) due to the juxtaposition of the Perth Basin and Yilgarn Craton along the north-south Darling Fault, (c) AGQG2017 north-south VDs in arcsecond, (d) AGQG2017 east-west VDs in arcsecond. The astrogeodetic traverse is represented by black dots. (Schack et al., 2018)

Geodetic coordinates (Geocentric Datum of Australia 1994 (GDA94)) for the majority of BMs were available from the State's register of surveying control marks, most of them having been previously coordinated by relative carrier-phase GNSS surveys with a mean horizontal precision of ± 7 mm at one-sigma. At BMs with less accurate geodetic coordinates (e.g., BMs with horizontal coordinates scaled from maps), or when the QDaedalus zenith camera had to be deployed eccentrically for better sky-visibility, co-located short-occupation static GNSS baselines were observed simultaneously with the astrogeodetic observations relative to two International GNSS Station control points (PERT and CUT0) in "fast-static" mode, with fixed integer ambiguity solutions, and a mean horizontal precision of ± 56 mm at one-sigma. These standard deviations translate to an angular uncertainty of $\sim \pm 0.002''$ in the geodetic coordinates.

Surface gravity measurements along the profile, with a mean standard deviation of ± 0.01 mGal, provide auxiliary data for the astronomical leveling (see Ch. 2.3.4). They were collected during a relative gravity survey conducted in December 2015 using a Scintrex CG-5 relative gravimeter (cf. Ch. 2.2), connected to a base station of the Australian Absolute Gravity Datum 2007, but have not been used in any of the gravimetric quasigeoid models tested here.

GGMplus (Hirt et al., 2013) is used as model for comparisons with 1) measured VDs, 2) modeled height anomaly differences, and 3) for test computations in the remove-compute-restore (RCR) combination with measured VDs. GGMplus is a composite gravity model that relies on satellite data (GRACE, GOCE), Earth Gravitational Model 2008 (EGM2008) (Pavlis et al. (2012), Pavlis et al. (2013)), terrestrial gravity information at spatial scales of $\sim 10\,000$ km to ~ 10 km and topography-implied gravity values at spatial scales of ~ 10 km to ~ 200 m. VDs (in Helmert's definition) and height anomalies from GGMplus are available at <http://ddfe.curtin.edu.au/models/GGMplus/>. Additionally, the AGQG2017 (Featherstone et al., 2018), a regional gravimetric quasigeoid model based on EGM2008, is integrated. It includes location-specific error estimates propagated from EGM2008 and the local gravity and terrain data. Over the study area, the uncertainty is ~ 90 mm. Lastly, the AGQG2009 regional gravimetric quasigeoid model (Featherstone et al., 2011), the predecessor to AGQG2017, is also used. Opposed to GGMplus, the two AGQG models are based on gravimetric information (marine and terrestrial) at spatial scales less than ~ 10 km.

To calculate height anomaly differences from Eq. (2.41), densely spaced VDs are required such that the deflection data of adjacent stations can be interpolated linearly. The method of astronomical-topographical leveling (Bosch and Wolf (1974), Hirt and Flury (2008)) is applied using a RCR technique. This method, as described e.g., by Hirt and Flury (2008), uses topographic reductions of VDs prior to the interpolation between astrogeodetic stations. Different from the original description of Hirt and Flury (2008), the observed and reduced VDs are not linearly interpolated but interpolated with modeled VDs (also topographically reduced), from

- 1) residual terrain modeling (RTM) (Forsberg, 1984) data instead of topographic forward modeling. Our RTM is based on a $1''$ SRTM model with a degree-2160 spherical harmonic digital elevation model reference surface removed.
- 2) GGMplus (Hirt et al., 2013) that merges GRACE, GOCE, and EGM2008 gravity information at long- and medium-wavelengths (harmonic degrees 2 to 2190) with short-wavelength gravity information obtained from a RTM based on $7.2''$ SRTM topography.

The RTM was computed with the Fortran software "TC" (Forsberg, 1984), along with a ~ 200 km integration cap radius and the residual SRTM topography. The height differences dn (Eq. (2.40)) were interpolated from the SRTM model and the gravity values obtained through the application of the RCR technique with observed gravity and SRTM-predicted gravity. In this topographically low-lying region (max. ~ 200 m, Fig. 4.1a), the normal correction term NC (Eq. (2.40)) is < 5 mm.

At this point, the different character of the astronomical and gravimetric solutions is emphasized. While the astronomical solution is unbiased from a conceptual point of view, gravimetric solutions may suffer from biases (here via low-accuracy coastal marine gravity, see later) that propagate via the geodetic convolution integral (modified Stokes integration in case of the Australian models) into the quasi-geoid solutions. The astronomical solution provides height anomaly differences along a profile (1D), while the gravimetric solution delivers a grid of height anomalies (2D), cf. Torge and Müller (2012). Concerning the quality of data, the standard deviation of the VDs is at the level of $\pm 0.15 - 0.20''$ (Hauk et al., 2016), as already mentioned. This random error in the VD data translates into a $\sim 0.8 - 1$ mm error in height anomalies over 1 km, and accumulates with the square root of the number of stations (e.g., Hirt and Flury (2008)) to $\sim \pm 4 - 6$ mm standard deviation in the height anomaly differences (over 38 km). From Hirt and Flury (2008, Table 9), the impact of the signal omission error due to the ~ 1 km spacing is estimated to reach the ~ 1 mm level over the traverse. This simple precision assessment does not take into account errors associated with the topographic VDs used in the interpolation, which are at the millimeter level. The uncertainty of the NC computation is estimated not to exceed 1 mm. This estimate is based on empirical results from other astronomical surveys in more rugged terrain and over longer traverses (Hirt et al., 2008).

Systematic errors in the observed VDs propagate linearly along the length of the traverse, contaminating the height anomaly differences. For instance, a systematic error of $0.01''$ falsifies $\Delta\zeta_{[AB]}$ by 0.05 mm (over 1 km) and 1.9 mm (over 38 km). Accordingly, a systematic error of $0.05''$ would cause a 10 mm bias in $\Delta\zeta_{[AB]}$ towards the end of the traverse.

Regarding the source of biases or residual errors in the VD data, some possible effects are as follows. 1) The effect of Earth tides on the direction of the physical plumbline may reach maximum values of $0.01 - 0.02''$ (cf. Jekeli (1999) or Voigt (2013)). Earth tide corrections were not applied in this study because they remain mostly below $\sim 5 - 10$ % of the observational accuracy. 2) The effect of anomalous atmospheric refraction might cause amplitudes of a few $0.05''$ at time scales of hours (Hirt, 2006), but smaller amplitudes at time scales of several days or weeks (e.g., $0.01''$, Hirt and Seeber (2007)). Explicit modeling of parts of the refraction effects through ray-tracing through 3D atmospheric weather models is possible in principle (Guillaume, 2015, p. 241ff), but was not envisaged here due to the demanding requirements in terms of temporal and spatial resolution of the atmospheric data that would be required. 3) As far as instrumental systematic effects are concerned, comparisons between VDs from QDaedalus measured at digital zenith camera sites (Hauk et al., 2016) and a control site at the Technical University of Munich (TUM) before and after the campaign did not provide any evidence of observational biases (e.g., systematic instrumental errors). 4) Another effect that can cause biases between gravity field observations and models is the underlying reference frames (Kotsakis (2009), Featherstone (1995)). In the case of the observed VDs, the underlying reference frame for the geodetic coordinates in GDA94 is ITRF92 (epoch 1994.0). This differs from ITRF2014 by ~ 2 m in a north-east direction, which would translate to a systematic $\sim 0.06''$ in each deflection component if it were to be compared to a gravity model with ITRF2014 as the underlying reference frame. For satellite-only global gravity models, the reference frame is implicit from the tracking stations. For combined gravity models such as GGMplus, AGQG2009, and AGQG2017, it also depends on the underlying reference frames for the gravity data and terrain data used. For AGQG2009 and AGQG2017, the horizontal coordinates of the gravity and terrain data were GDA94 (ITRF92 epoch 1994.0), so the underlying reference frame of the high-frequency model constituents is compatible with the GDA94 geodetic coordinates used to calculate the astrogeodetic VDs. In the case of GGMplus, the high-frequency constituents depend on SRTM elevation data, which is assumed to refer to WGS84 (G873) (Brown et al., 2005). The underlying reference frame is therefore ITRF94 (epoch 1997) and the effect on the VDs is estimated to be below $0.01''$. However, in all models there is also a dependency on the underlying reference frames of EGM2008, assumed to be GDA94 for Australian gravity data and ITRF94 for SRTM. In summary, the upper limit of the reference frame inconsistency can be constrained to

$\sim 0.06''$, but is likely to be less because the epochs of the input data sets of the gravity models used in this study are closer to 1994.0 than 2014.0, or identical with 1994.0.

Based on all stochastic information available, a standard deviation of $\pm 10 - 15$ mm for $\Delta\zeta_{[AB]}$ over the 38 km traverse length is considered to be realistic.

Illustration

Figure 4.2 shows the observed VDs along the Perth traverse including their RCR-based combination with RTM-data and with GGMplus. The ξ component shows a dominant linear behavior and reaches values from $-1.4''$ in the west to $3.1''$ in the east (Table 4.1 and Fig. 4.2(a)). Short-scale variations remain less than $1''$. The η component exhibits a large decrease from $-7.0''$ to $-32.5''$ (Table 4.1 and Fig. 4.2(b)) from the west up to the Darling Fault (32 - 33 km along the profile), followed by a sharp peak and slowly increasing VD values eastward of the Fault. The combined deflections for the two variants (GGMplus and RTM modeling based on 30 m SRTM) are very similar, with RMS differences of $0.07''$ for ξ and $0.09''$ for η , due to the flat topography. The differences primarily reflect high-frequency signals associated with the higher spatial resolution of the $1''$ -resolution SRTM data set. To be independent of gravimetric data sets (used in EGM2008 and AGQG models), only the combined VD solutions based on $1''$ -resolution SRTM data (blue line in Fig. 4.2) are used for the model validation.

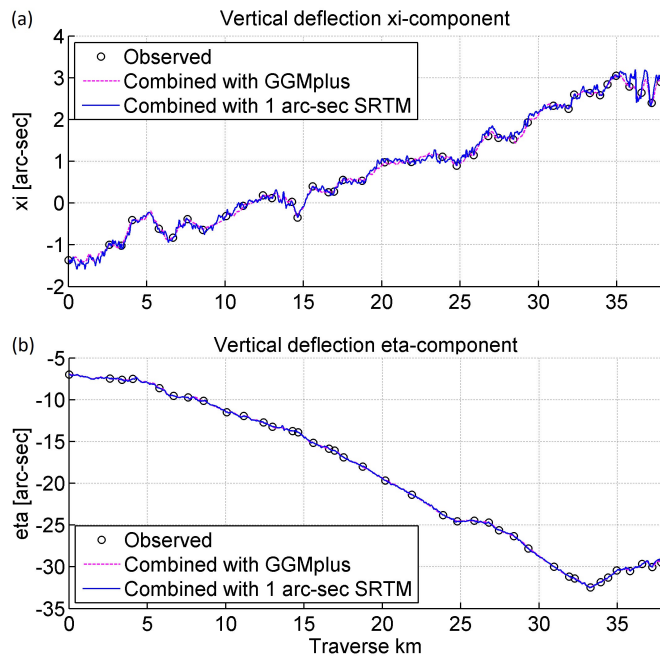


Figure 4.2: VDs along the Perth traverse. Units in arcsecond. (a) north-south component ξ , (b) east-west component η . Astronomically measured VDs (black circles), GGMplus RCR-combination (magenta), and SRTM RCR-combination (blue). The large east-west VDs reflect the steep quasigeoid gradient in the Perth region due to the Darling Fault. (Schack et al., 2018)

Figure 4.3 includes the observed VDs together with AGQG2009, AGQG2017, and GGMplus-only VDs, which are independent of the observed VDs and vice versa, while Fig. 4.4 shows the differences between the astrogeodetic VDs and those from the models (for the descriptive statistics of the VDs and their differences, see Table 4.1). From Figs. 4.3 and 4.4, and Table 4.1, for all three models, the RMS of the ξ differences are about $0.3''$. There are larger discrepancies at the eastern end of the traverse (toward the right in Fig. 4.4) that coincides with the location of the Darling Fault, with larger

differences exhibited in the η component than in ξ . The η differences exceed $1''$ and show RMS values ranging from $0.6''$ to $0.9''$, reflecting the presence of large bulk density anomalies in the east-west direction (cf. Fig. 4.1a). The differences along the first 30 km are predominantly positive, at the level of a few $0.1''$ (between 0 km and 30 km, the offset in the η differences is $0.43''$ for GGMplus, $0.33''$ for AGQG2009 and $0.39''$ for AGQG2017). This may indicate a bias, either in the observed VDs or in the VDs calculated from the three quasigeoid models (see discussion of this chapter).

Component	Source	Min	Max	Mean	RMS
ξ	Observed	-1.37	3.05	0.93	1.61
	GGMplus	-0.98	3.44	0.96	1.62
	AGQG2009	-1.37	2.68	0.91	1.57
	AGQG2017	-1.15	2.51	0.78	1.45
	Observed - GGMplus	-0.63	0.40	-0.04	0.30
	Observed - AGQG2009	-0.41	0.79	0.02	0.23
	Observed - AGQG2017	-0.28	1.10	0.15	0.31
η	Observed	-32.47	-7.00	-20.08	21.88
	GGMplus	-30.87	-8.08	-20.16	21.82
	AGQG2009	-30.64	-8.10	-20.04	21.62
	AGQG2017	-31.88	-7.79	-20.30	21.99
	Observed - GGMplus	-2.46	1.39	0.08	0.89
	Observed - AGQG2009	-1.89	1.22	-0.04	0.71
	Observed - AGQG2017	-1.30	1.21	0.22	0.56

Table 4.1: Descriptive statistics of the VDs along the Perth traverse: observed, GGMplus, AGQG2009, and AGQG2017, and differences between the observations and models. Units in arcsecond. (Schack et al., 2018)

The RMS values of the differences never exceed $1''$ for any of the three models (Table 4.1), which is commensurate with investigations using astrogeodetic VDs in Northern Hemisphere countries (e.g., Hirt et al. (2010b), Smith et al. (2013), or Wang et al. (2017)).

Annotation: Astrogeodetic VDs can be directly compared with GGMplus VDs, given both are in Helmert definition (Hirt et al. (2013), supplementary materials). For the comparison with VDs from the AGQG models, the model VDs were derived from horizontal quasigeoid gradients and transformed to the Helmert definition $(\xi, \eta)_{[QG]}^{[H]}$ as follows.

In the first step, the gridded quasigeoid values were used to compute VDs in Molodensky definition $(\xi, \eta)_{[QG]}^{[M]}$ (Eqs. (4.1), cf. Heiskanen and Moritz (1967, p. 313), Voigt (2013, p. 63))

$$\begin{aligned}\xi_{[QG]}^{[M]} &= -\frac{1}{R_{[N]} + h} \frac{\partial \zeta}{\partial \varphi} - \Delta \xi \\ \eta_{[QG]}^{[M]} &= -\frac{1}{(R_{[E]} + h) \cos \varphi} \frac{\partial \zeta}{\partial \lambda} - \Delta \eta\end{aligned}\quad (4.1)$$

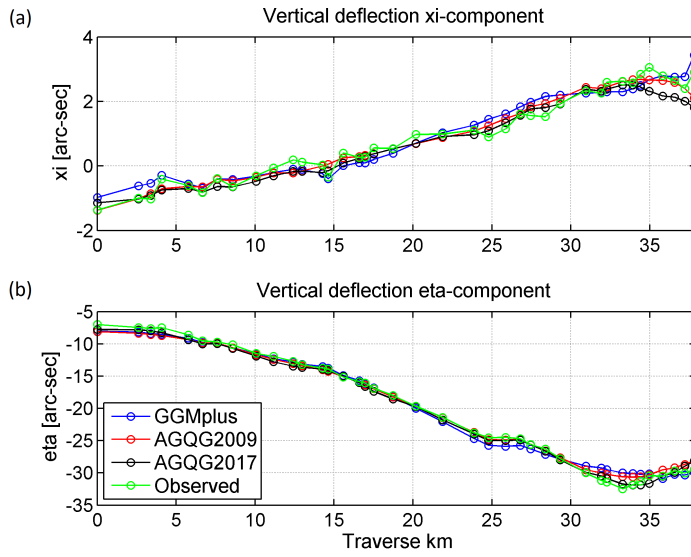


Figure 4.3: VDs along the Perth traverse. Units in arcsecond. (a) north-south component ξ , (b) east-west component η . GGMplus-predicted deflections (blue), AGQG2009-predicted deflections (red), AGQG2017-predicted deflections (black), astronomically observed VDs (green). (Schack et al., 2018)

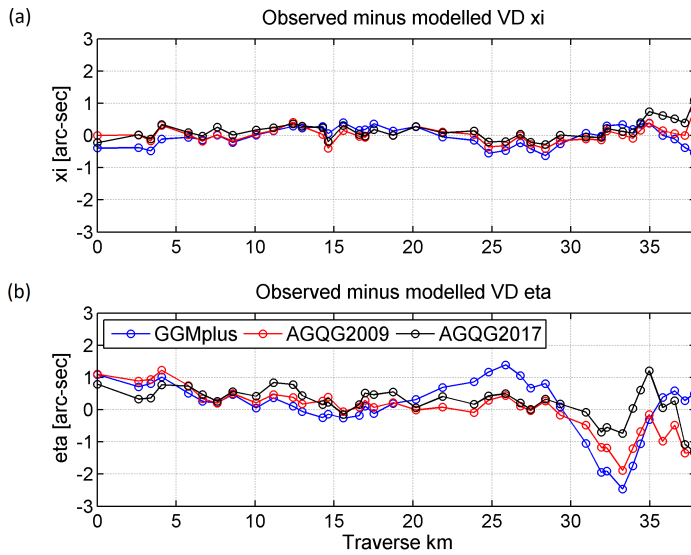


Figure 4.4: Differences between observed and modelled VDs. Units in arcsecond. (a) north-south component ξ , (b) east-west component η . (Schack et al., 2018)

$\Delta\xi$ and $\Delta\eta$ are terrain slope correction terms, see Eqs. (4.2),

$$\begin{aligned}\Delta\xi &= \frac{\Delta g}{\gamma} \frac{1}{R_{[N]} + h} \frac{\partial h}{\partial \varphi} \\ \Delta\eta &= \frac{\Delta g}{\gamma} \frac{1}{(R_{[E]} + h) \cos \varphi} \frac{\partial h}{\partial \lambda}\end{aligned}\quad (4.2)$$

that take into account that the Earth's topographic surface is not an equipotential surface. The terrain slope correction terms depend on the gravity anomaly Δg , normal gravity γ and the terrain slopes in north-south $(R_{[N]} + h)^{-1} \delta h / \delta \varphi$ and east-west direction $((R_{[E]} + h) \cos \varphi)^{-1} \delta h / \delta \lambda$, respectively. In the second step, VDs are transformed from Molodensky $(\xi, \eta)_{[QG]}^{[M]}$ to Helmert $(\xi, \eta)_{[QG]}^{[H]}$ definition via

$$\begin{aligned}\xi^{[H]} &= \xi^{[M]} + 0.17'' H \sin 2\varphi \\ \eta^{[H]} &= \eta^{[M]}\end{aligned}\quad (4.3)$$

where H is the normal height in kilometer (Jekeli, 1999) and the difference in ξ is due to the curvature of the normal plumbline. VDs from Eqs. (4.3) can then be compared with the (Helmert) astrogeodetic VDs.

According to Voigt (2013, p. 106), the terrain slope terms (Eqs. (4.2)) are a "central problem" because the "limited accuracy of the terrain slopes, particularly in rough topography, leads to systematic deviations" in their computation. It was attempted to calculate the terrain slope correction terms with digital elevation models of different resolution, and gravity anomalies from high-resolution global models. However, because of the large amplitudes of gravity anomalies over most of the traverse (~ 100 mGal), errors of a few meters in the digital elevation models were found to translate into several $0.1''$ -errors in the $\Delta\xi$, $\Delta\eta$ correction terms, deteriorating the quality of the VDs in Eqs. (4.1) along the traverse.

A principal problem appears to be the spectral inconsistency between quasigeoid grids (e.g., $1'$ -resolution) and digital elevation models to consistently model the difference between the level surfaces and terrain surface. Therefore, it was decided not to apply the slope correction terms in this study. The encountered difficulties suggest that the accurate prediction of Helmert VDs from quasigeoid models using the formalism of Eq. (4.1) to Eq. (4.3) can be problematic where large gravity anomalies "amplify" errors in the terrain slopes. It is noted that the comparison of height anomaly differences from astronomical leveling with gravimetric quasigeoid information (see below) does not require slope correction terms, thus avoiding such difficulties with their computation.

Figure 4.5(a) presents the height anomalies along the traverse for all three quasigeoid models and the new VD data set. At the starting point (0 km), all height anomalies were set to zero. Over the entire traverse, the height anomaly changes by ~ 2.7 m, corresponding to a gradient of 71 ppm. The differences in the height anomalies are shown in Fig. 4.5(b). The RMS differences between the observed and modeled height anomalies remain at the 20 - 30 mm level (Table 4.2). The AGQG2017 differences reach their maximum value at the eastern end of the traverse, while the AGQG2009 and GGMplus reach their maximum, of up to ~ 50 mm, between 25 km and 30 km along the traverse. Up to 15 km, the differences among the height anomalies show little variation but exhibit a steady decrease. This is a direct translation of the biases in the η differences, shown in the previous paragraph, into the quasigeoid domain, which causes a trend in the height anomaly differences. From 15 km onwards, the curves start to diverge. From this point on, the GGMplus differences show a wave-like signal (~ 15 mm amplitude), likely reflecting the impact of unmodeled bulk density across the Darling Fault. In contrast, the AGQG2017 curve is largely dominated by a trend and only shows short-scale variations.

With formally propagated AGQG2017 gravimetric quasigeoid errors (Featherstone et al., 2018) ranging between 83 mm and 98 mm along the traverse, the differences in Fig. 4.5b lie within the expected error budgets.

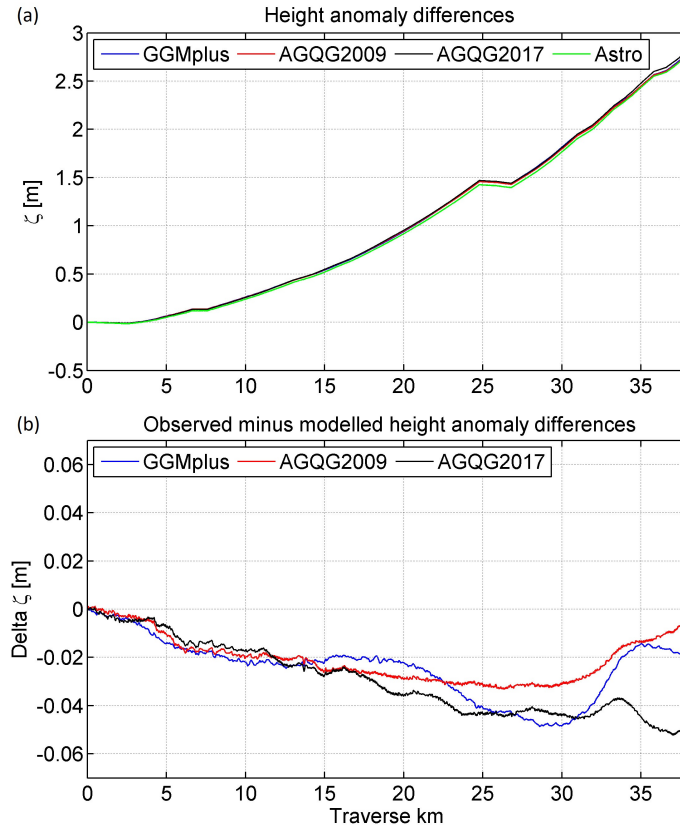


Figure 4.5: (a) Height anomaly differences (in meters) along the Perth traverse from GGMplus (blue), AGQG2009 (red), AGQG2017 (black), and VD survey (green). (b) Differences between height anomalies (in meters) from the astronomical-topographical solution and from the models (GGMplus, AGQG2009, and AGQG2017). The height anomaly of each solution or model was set to zero at the beginning of the traverse. (Schack et al., 2018)

$\Delta\zeta$	Min	Max	Mean	RMS
Observed - GGMplus	-49	0	-24	27
Observed - AGQG2009	-33	1	-21	23
Observed - AGQG2017	-52	1	-29	33

Table 4.2: Descriptive statistics of the height anomaly differences along the traverse. Units in millimeter. (Schack et al., 2018)

Discussion

Based on Table 4.1, the study corroborates the ability of global or regional models to predict VDs at the 1''-precision level or better over topographically flat areas. Over the Darling Fault (~33 km along the profile), the gravity field models are not able to capture the quasigeoid variations as consistently as in the western part, which is indicated by the larger discrepancies and the higher variability in the η differences from ~20 km to ~35 km (cf. Fig. 4.4). Here, AGQG2017 maps the quasigeoid's fine structure more reliable than GGMplus. Also, the smaller RMS values of the AGQG models in Table 4.1 indicate that the inclusion of local gravity observations is a preferable modeling technique

in areas of steep geoid gradients and low-lying topography. GGMplus employs a constant topographic mass density in the forward modeling at spatial scales of less than ~ 10 km, which prohibits a detailed description of the high-frequency gravitational signature of the mass-density variations associated with the Darling Fault.

However, tilt-like biases of ~ 1 mm over ~ 1 km (1 ppm) are present for all quasigeoid models within ~ 20 km of the coastline, which might either point at inconsistencies in the model-underlying coastal zone gravity data sets (e.g., offsets in the transition between altimeter and land gravity data), or remaining systematic errors in the VD observations. Since no evidence for the bias in Fig. 4.4 was found in Hauk et al. (2016, Fig. 4) when assessing the quality of QDaedalus measurements, the cause of the bias is more likely to be associated with the GGMplus, AGQG2009, and AGQG2017 models of the very steep east-west quasigeoid gradient in Perth. A plausible explanation for the bias and the subsequent tilts in the quasigeoid models is that the traverse is in a coastal area, where marine gravity field information derived from satellite altimetry data is less reliable (e.g., Vignudelli et al. (2011)). If the altimetry data are incorrect, the introduction of a tilt in the quasigeoid of some $0.1''$ is possible. Figure 4.6 shows a subset of the point gravity anomaly errors used in AGQG2017, comprising formally propagated errors for land gravity observations and the error grids that accompany the Sandwell et al. (2014) marine gravity anomalies.

From Fig. 4.6, the advantage of the astronomical method becomes clear: while only local data along the traverse is needed to compute the astronomical solution, the numerical integration in two coordinate directions requires gravity data outside the study area. The degradation of the marine gravity data is the prime suspect for the tilts in the quasigeoid models, adding yet more evidence that airborne gravimetry should be used to bridge this deficiency (e.g., Schwarz and Li (1996), Li et al. (2016) or Jamil et al. (2017)). AGQG2017 uses an integration cap of 55 km, so the extents of Fig. 4.6 correspond to the local gravity data errors used in its computation.

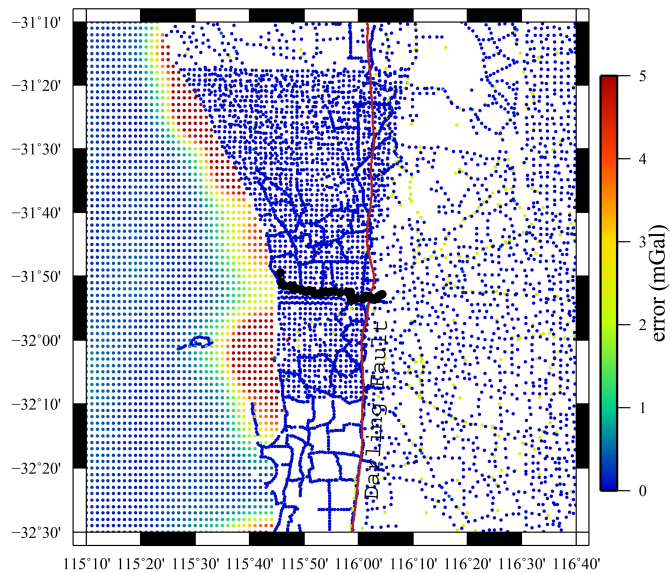


Figure 4.6: Gravity anomaly errors used in AGQG2017. Units in mGal. Rectangular projection. (Schack et al., 2018)

An unintended outcome of this study is that the QDaedalus zenith camera has proven capable of mapping the horizontal location of the Darling Fault. The Fault is obscured by weathered regolith that prevents accurate mapping from surface geology observations. The inflections in η at 33 km (Fig. 4.4) indicate that this is the location of the near-vertical fault line. However, this is a dramatic density contrast, so QDaedalus may not be capable of mapping other less prominent faults.

4.2 Assessment of RQH calibrations

Investigations in Becker (2016) show that for a RQH IMU the accelerometer standard calibration of iMAR does not suffice for sub-milligal airborne gravimetry. The reason is that the sensor temperature and the unit's orientation affect the accelerometer performance beyond the simulated error margins in Becker (2016, Table 5.3). Since the RQH of the IAPG is equipped with similar inertial sensors, it is supposed that the temperature and orientation dependencies are driving error components, too. Therefore, in spring 2017 an Up and Down calibration followed by a Roll and Pitch calibration (known as sample-based TRP calibration from Becker (2016)) were completed with the RQH. The analyses revealed internal sensor movement, which could not be assigned to one single source. After correspondence with Dr. D. Becker and iMAR, a more expedient calibration approach, the strapdown rotation test (including another Up and Down calibration), was scheduled for summer 2019 to detect the source of the sensor movement.

Each of the calibrations was executed with the "Two-Axis Test System with thermal chamber Series TES-4H4o_TM" at several temperatures, see Table 4.3, with the RQH at the iMAR calibration facilities. During the calibrations, a stable sensor temperature output was reached (± 0.3 °C, except for 0 °C in July 2019) before a single calibration sequence was started. This means that no internal temperature gradient is assumed and that error characteristics due to temperature gradients are not detectable. The RQH installation is sketched and elucidated in Fig. 4.7. The calibrations are described and assessed in the following sections. It is noted that these calibrations shall eliminate remaining sensor errors after the standard manufacturer's calibration parameters are applied to the raw IMU observations.

Type	Date	Temperatures in °C
Up and Down (Ch. 4.2.1)	June 2017	10 - 14 - 18 - 21 - 24 - 28 - 32 - 36
Roll and Pitch (Ch. 4.2.2)	June 2017	0 - 5 - 10 - 14 - 18 - 21 - 24 - 28 - 32 - 36
Up and Down (Ch. 4.2.1)	July 2019	0 - 5 - 10 - 14 - 18 - 21 - 24 - 28 - 33 - 38
Strapdown rotation (Ch. 4.2.3)	July 2019	0 - 5 - 10 - 14 - 18 - 21 - 24 - 28 - 33 - 38

Table 4.3: Temperature stages for calibrations conducted in 2017 and 2019.

4.2.1 Up and Down analyses

The Up and Down calibration represents the six-position static acceleration test proposed by El-Diasty and Pagiatakis (2008) and Shin and El-Sheimy (2002). It is based on acceleration measurements collected during standstill phases in which each of the nominal b-frame axes is aligned along the gravity vector successively, positive and negative. It allows determining biases, linear scale factors, and non-orthogonalities of the accelerometer axes³⁴. Table 4.4 includes the sensor orientation details during the calibration procedure.

³⁴ El-Diasty and Pagiatakis (2008) mention that this calibration method can also be used to determine scale factors of high-grade gyroscopes with the Earth's rotation rate as reference. As will be seen in Ch. 4.2.3, these parameters are rather small for the used RQH.

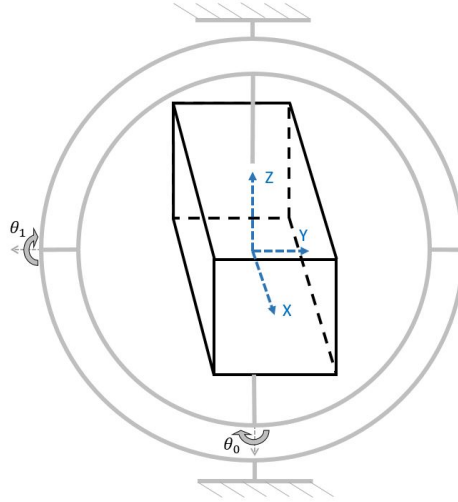


Figure 4.7: Sketch of the calibration scenario. In black the RQH is depicted with its b-frame indicated in blue. The gray parts abstract the two-axis calibration turntable. When $\theta_{[0]}$ and $\theta_{[1]}$ are set to 0 rad the platform is nominally leveled and the RQH X axis points southward (to the reader), the Z axis upwards, and the Y axis eastward.

Up axis	Turntable angles: $\theta_{[0]}/\theta_{[1]}$ in $^\circ$
+X	0/+90
-X	0/-90
+Y	+90/+90
-Y	+90/-90
+Z	0/0
-Z	0/+180

Table 4.4: Upwards pointing b-frame axes and nominal turntable orientation angles during Up and Down calibration.

Data

For the calculation of calibration parameters averaged acceleration values during the standstill phases are used. The averaging time is 100 s, based on the sensors' bias instability, see Fig. 2.2(a). An average value $\check{\mathbf{f}}^b$ of the measured accelerations is modeled by Eq. (4.4) in the b-frame.

$$\check{\mathbf{f}}^b = \mathbf{b}_{[a]} - (\mathbf{S} + \mathbf{M})\mathbf{R}(\theta_{[0]}, \theta_{[1]})\mathbf{g}^l \quad (4.4)$$

$$= \begin{pmatrix} b_{[a,X]} \\ b_{[a,Y]} \\ b_{[a,Z]} \end{pmatrix} - \left(\begin{pmatrix} sf_{[X]} & 0 & 0 \\ 0 & sf_{[Y]} & 0 \\ 0 & 0 & sf_{[Z]} \end{pmatrix} + \begin{pmatrix} 1 & \epsilon_{[XY]} & \epsilon_{[XZ]} \\ \epsilon_{[YX]} & 1 & \epsilon_{[YZ]} \\ \epsilon_{[ZX]} & \epsilon_{[ZY]} & 1 \end{pmatrix} \right) \begin{pmatrix} \cos \theta_{[0]} \cos \theta_{[1]} & -\sin \theta_{[0]} \cos \theta_{[0]} \sin \theta_{[1]} \\ \sin \theta_{[0]} \cos \theta_{[1]} & \cos \theta_{[0]} \sin \theta_{[0]} \sin \theta_{[1]} \\ -\sin \theta_{[1]} & 0 & \cos \theta_{[1]} \end{pmatrix} \begin{pmatrix} 0 \\ 0 \\ -|g| \end{pmatrix}$$

$$\begin{aligned} \text{with } \mathbf{R}(\theta_{[0]}, \theta_{[1]}) &= \mathbf{R}_{[tt_1]}(\theta_{[1]})\mathbf{R}_{[tt_0]}(\theta_{[0]}) = [\mathbf{R}_{[Z]}(-\theta_{[0]})\mathbf{R}_{[Y]}(-\theta_{[1]})\mathbf{R}_{[Z]}(\theta_{[0]})]\mathbf{R}_{[Z]}(-\theta_{[0]}) \\ &= \mathbf{R}_{[Z]}(-\theta_{[0]})\mathbf{R}_{[Y]}(-\theta_{[1]}) \\ \mathbf{M} &= \mathbf{R}_{[X]}(\epsilon_{[YZ]}/\epsilon_{[ZY]})\mathbf{R}_{[Y]}(\epsilon_{[ZX]}/\epsilon_{[XZ]})\mathbf{R}_{[Z]}(\epsilon_{[XY]}/\epsilon_{[YX]}) \quad (\text{SAA}) \end{aligned}$$

$\mathbf{b}_{[a]}$ represents the accelerometer biases, \mathbf{S} the deviation of each accelerometer linear scale factor from 1. \mathbf{M} includes accelerometer non-orthogonalities, actually a mixture of misalignments and cross-couplings. $\epsilon_{[XZ]}$ e.g., describes the deviation of the true b-frame X axis from orthogonality w.r.t. the nominal b-frame Z axis. $\mathbf{R}(\theta_{[0]}, \theta_{[1]})$ ($\mathbf{R}_{[tt_0/t_1]} \hat{=}$ turntable axes, $\mathbf{R}_{[X/Y/Z]} \hat{=}$ nominal b-frame axes) maps the reference acceleration, which is gravity pointing in physical downward direction (\mathbf{g}^l), onto the nominal b-frame orientation.

The biases, linear scale factors, and non-orthogonalities can be extracted from the averaged acceleration values as follows:

$$\mathbf{b}_{[a]} = \begin{pmatrix} (\check{f}_{[X]}^{b[X_{up}]} + \check{f}_{[X]}^{b[X_{down}]})/2 \\ (\check{f}_{[Y]}^{b[Y_{up}]} + \check{f}_{[Y]}^{b[Y_{down}]})/2 \\ (\check{f}_{[Z]}^{b[Z_{up}]} + \check{f}_{[Z]}^{b[Z_{down}]})/2 \end{pmatrix} \quad (4.5)$$

$$\mathbf{S} + \mathbf{M} = \frac{1}{2|\mathbf{g}|} \begin{pmatrix} (\check{f}_{[X]}^{b[X_{up}]} - \check{f}_{[X]}^{b[X_{down}]})^T \\ (\check{f}_{[Y]}^{b[Y_{up}]} - \check{f}_{[Y]}^{b[Y_{down}]})^T \\ (\check{f}_{[Z]}^{b[Z_{up}]} - \check{f}_{[Z]}^{b[Z_{down}]})^T \end{pmatrix}^T \quad (4.6)$$

Illustration

In the following, the accelerometer standstill averages and the extracted parameters are visualized for all temperatures of the 2017 and 2019 Up and Down calibrations. Their characteristics are briefly described as well. A more detailed discussion follows afterward.

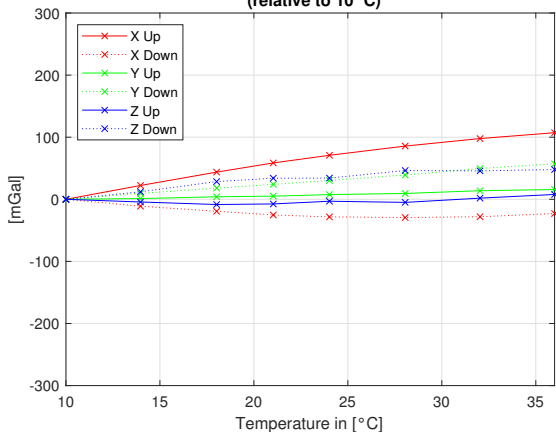
Figures 4.8 show the mean accelerometer values over the 100 s standstill phases of the six orientations (referenced to 10 °C)³⁵. An optimal sensor output would result in curves with a value of zero. Several error effects are responsible for the deviations from zero, but since a correlation with temperature is visible for all sensors, it is supposed to be a dominant error source. The curves mostly stay below 100 mGal, except for the blue curve in Fig. 4.8(c) and the green curve in Fig. 4.8(e). A comparison of the 2017 data with the 2019 data reveals that some accelerometer outputs changed significantly, while others show only minor differences.

The biases are visualized in Figs. 4.9 after removing the bias value at 10 °C. Remember from Ch. 3 that the biases are estimated inside the EKF for gravimetric purposes. For this reason, the absolute bias values are not considered in this calibration. Each plot includes three bias curves for one accelerometer, which originate from the X/Y/Z up and down measurements (Eq. (4.5) is also applicable for horizontal measurements). The first thing to state is that the curves of each sensor spread with increasing temperature. In X and Y, differences of up to 20 mGal, and in Z even larger differences are visible. Secondly, the curves of 2017 and 2019 show a high correlation, meaning that the temperature effect on the biases does not change immensely. Still, the differences might influence gravimetry campaigns (largest difference in X bias at 35 °C about 10 - 15 mGal).

Figures 4.10(a) and (b), depicting the absolute linear scale factor values, manifest a range below ± 100 ppm. Evidently, a temperature-induced effect exists. For a better comparison of this effect, in Figs. 4.10(c) and (d) the linear scale factors of 2017 and 2019 are referenced to the 10 °C value. The curves let assume that the temperature effect on the linear scale factors does not change significantly over time. The curves of 2017 and 2019 deviate by less than ± 10 ppm.

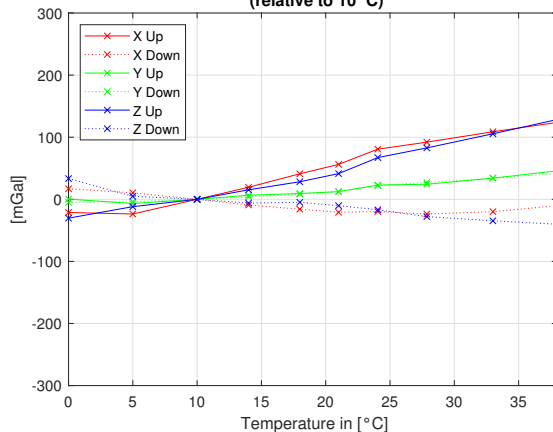
³⁵Several figures in this work are referenced to 10 °C, which is the lowest common temperature of the four calibrations.

Evolution of accelerometer X averages during Up and Down calibration 2017 (relative to 10°C)



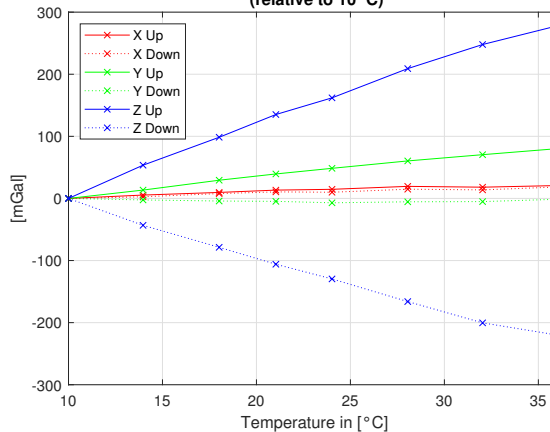
(a) Accelerometer X output 2017

Evolution of accelerometer X averages during Up and Down calibration 2019 (relative to 10°C)



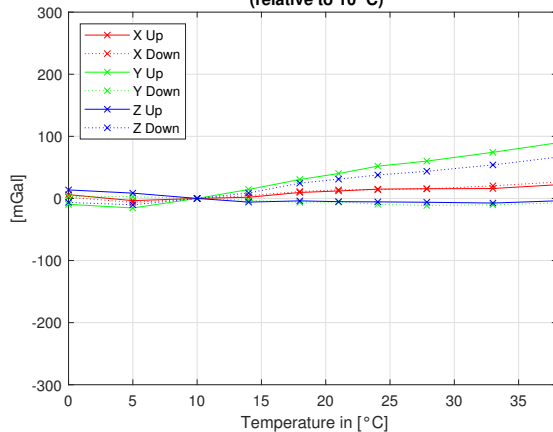
(b) Accelerometer X output 2019

Evolution of accelerometer Y averages during Up and Down calibration 2017 (relative to 10°C)



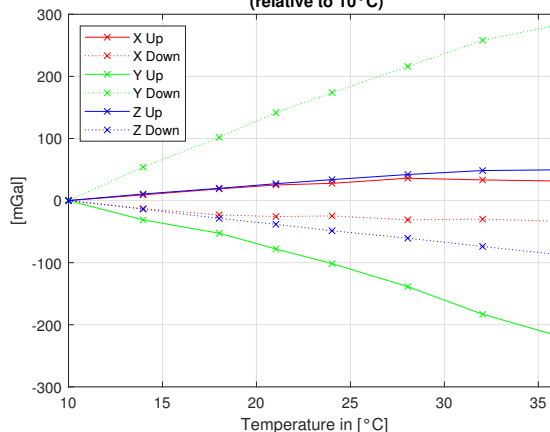
(c) Accelerometer Y output 2017

Evolution of accelerometer Y averages during Up and Down calibration 2019 (relative to 10°C)



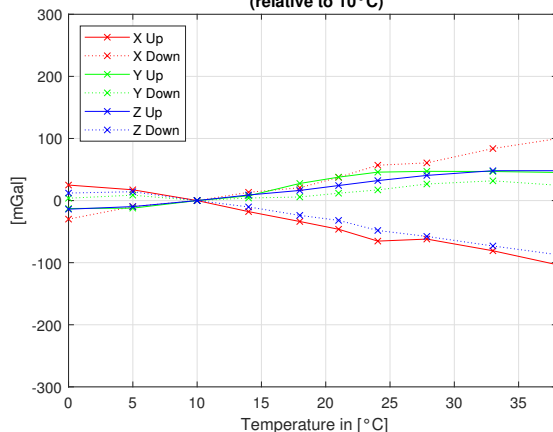
(d) Accelerometer Y output 2019

Evolution of accelerometer Z averages during Up and Down calibration 2017 (relative to 10°C)



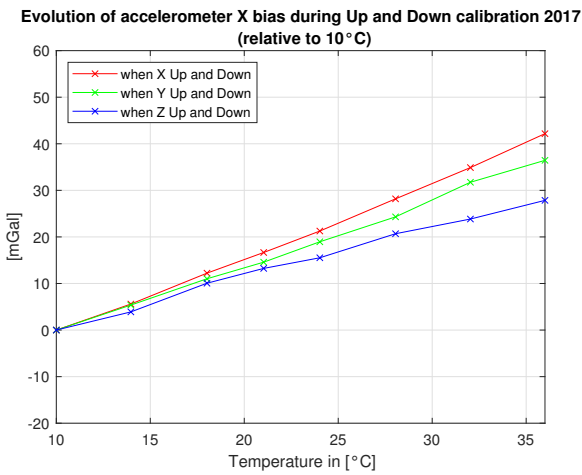
(e) Accelerometer Z output 2017

Evolution of accelerometer Z averages during Up and Down calibration 2019 (relative to 10°C)

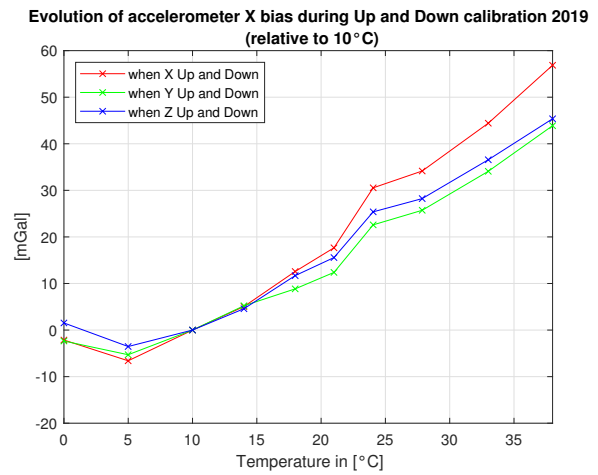


(f) Accelerometer Z output 2019

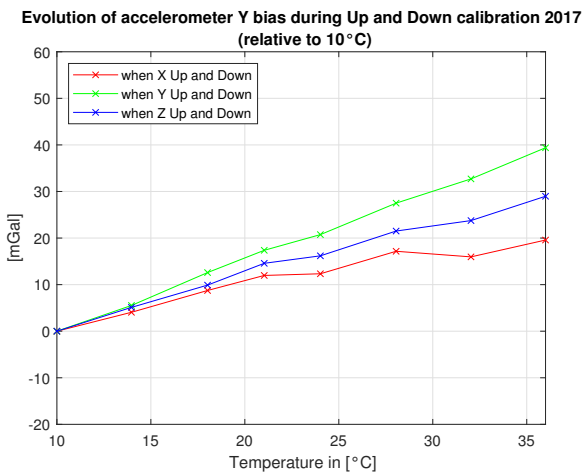
Figure 4.8: Up and Down calibration: Averaged accelerometer output over temperature in six different orientations (each axis pointing up and down once) in 2017 and 2019.



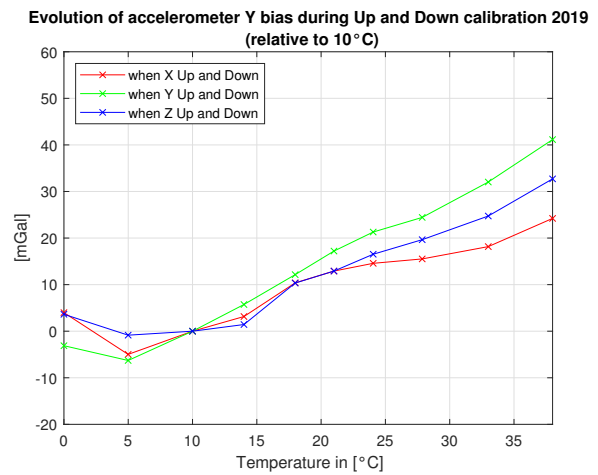
(a) Accelerometer X bias 2017 (relative)



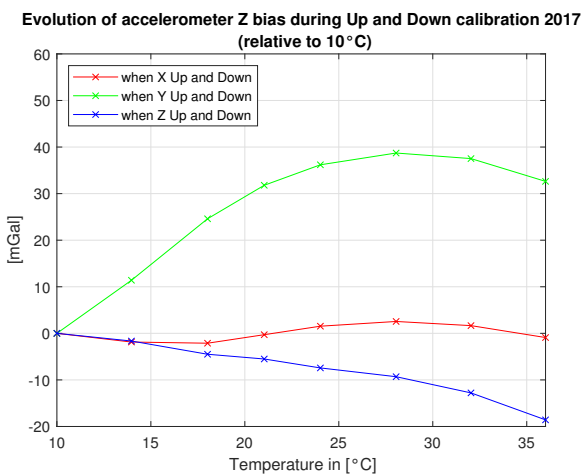
(b) Accelerometer X bias 2019 (relative)



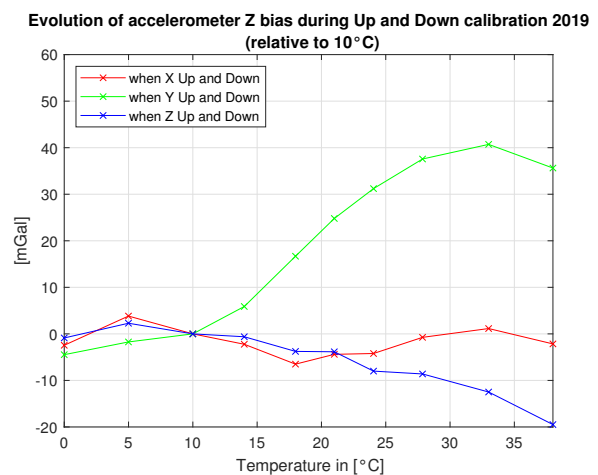
(c) Accelerometer Y bias 2017 (relative)



(d) Accelerometer Y bias 2019 (relative)

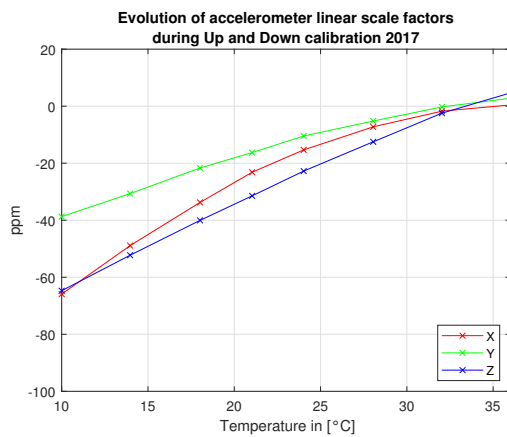


(e) Accelerometer Z bias 2017 (relative)

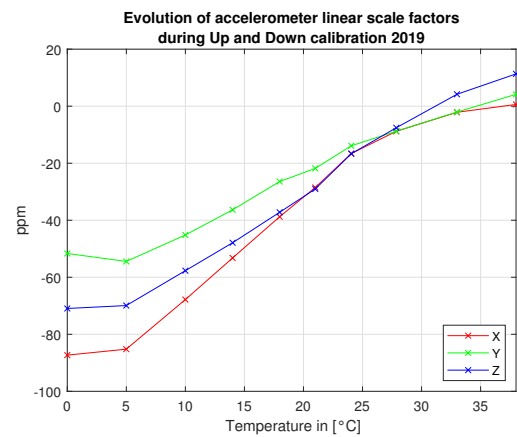


(f) Accelerometer Z bias 2019 (relative)

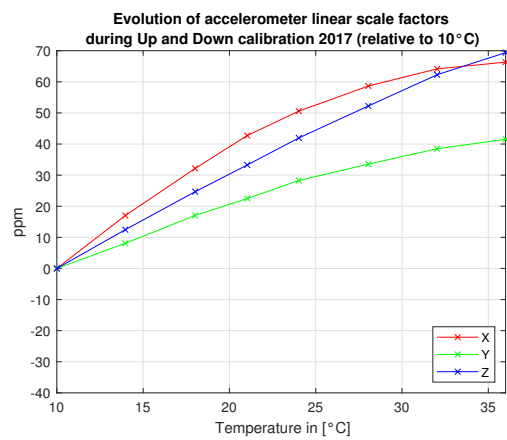
Figure 4.9: Up and Down calibration: Accelerometer biases over temperature in 2017 and 2019.



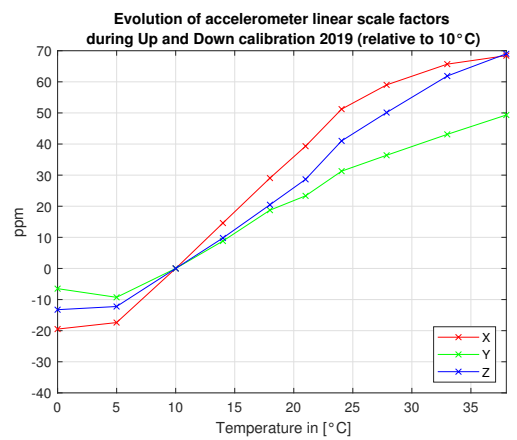
(a) Accelerometer linear scale factors 2017 (absolute)



(b) Accelerometer linear scale factors 2019 (absolute)



(c) Accelerometer linear scale factors 2017 (relative)



(d) Accelerometer linear scale factors 2019 (relative)

Figure 4.10: Up and Down calibration: Accelerometer linear scale factors over temperature in 2017 and 2019.

The evaluation of the non-orthogonality plots (Figs. 4.11) is not trivial. Therefore, some clarifications are preceded. In this thesis, the term "non-orthogonality" stands for the combined effect of a triad misalignment and sensor axes cross-couplings. A misalignment describes the deviation of orthogonal triad axes from their nominal axes, while cross-coupling stands for a non-orthogonality between two axes of a triad. Both quantities are hidden in the elements of M from Eq. (4.6) and are represented by small rotation angles.

The absolute non-orthogonality values are not visualized, since the manufacturer's calibration is supposed to reduce these imperfections accurately enough³⁶. Only the temperature variation is of interest. Curves with the same color were reduced with the same absolute value, to keep the offsets between the two lines, see e.g., $\epsilon_{[YZ]}$ and $\epsilon_{[ZY]}$ ³⁷ in Fig. 4.11(a). For the interpretation, it can be stated that a cross-coupling exists if lines of the same color do not coincide, that the misalignment is varying when two lines of the same color change in a similar manner, and that the cross-coupling is varying when the offset between two lines of the same color changes. However, with the Up and Down calibration, it is not possible to determine exact misalignment and cross-coupling values separately.

Starting with 2017, it can be seen that with rising temperatures a rotation around the X axis by about 50'' and roughly 8'' around the Y axis are indicated. Differences between curves of the same color stay below 5'' for all axes with only slight variations. For 2019, the characteristics of the curves change significantly. There is hardly any misalignment or cross-coupling visible in $\epsilon_{[XY]}/\epsilon_{[YX]}$. The misalignment alteration for $\epsilon_{[ZX]}/\epsilon_{[XZ]}$ and $\epsilon_{[YZ]}/\epsilon_{[ZY]}$ change direction, and while the rotation around X became smaller in magnitude (10''), the rotation around Y increased to 20 - 25''.

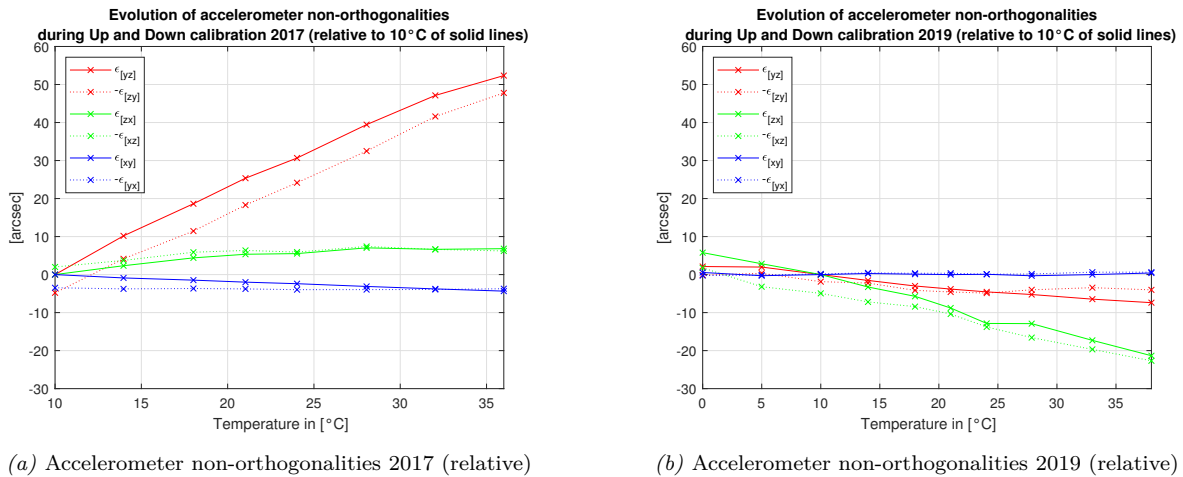


Figure 4.11: Up and Down calibration: Accelerometer non-orthogonalities over temperature in 2017 and 2019.

Discussion

Figures 4.8 partly show large differences in the sensor output from 2017 and 2019. The biases and linear scale factors cannot be made responsible for those changes, but the non-orthogonality curves exhibit high variability. The 50'' non-orthogonality in Fig. 4.11(a) explains the large and symmetric trend of the blue and green curves in Figs. 4.8(c) and (e) and visualizes its large impact on observations in horizontal orientations. And exactly this circumstance is of great concern. Do the 50'' originate

³⁶The absolute values in these calibrations are not zero and can vary by several magnitudes, due to details in the calibration procedure. It is the only exception from the introductory part where the standard manufacturer calibration parameters were not applied.

³⁷ $-\epsilon_{[ZY]}/-\epsilon_{[XZ]}/-\epsilon_{[YX]}$ are plotted for better comparison.

from angular motion of the whole ISA or is this a movement of the accelerometers only? A misalignment of the ISA w.r.t. the RQH housing (and even variations that can be resolved by the gyroscopes) are not problematic, since the ISA-frame resembles the b-frame, which is the nominal frame during campaigns. And, the relative position of the GNSS antenna w.r.t. the RQH is only slightly affected. Whereas a rotation of the accelerometer triad w.r.t. the gyroscope triad can cause a severe decrease in the accuracy of the gravity disturbance by assigning a wrong orientation to the accelerometer axes.

The 2017 calibration results were the reason to repeat the Up and Down calibration together with the strapdown rotation test since the large rotation about the X axis ($\epsilon_{[YZ]}/\epsilon_{[ZY]}$) was not assignable to one source in 2017. Now, comparing the 2017 Up and Down data with 2019, it seems that this observed phenomenon is not reproducible³⁸. A rotation of the accelerometer triad only (w.r.t. the gyroscope axes) could not be calibrated then. The strapdown rotation test in Ch. 4.2.3 will give more insight since it allows to observe both, ISA rotations w.r.t. the housing and accelerometer triad rotations w.r.t. the gyroscope triad³⁹.

The bias changes from 2017 to 2019 signify that for gravimetric applications with large temperature variations a two-year calibration interval is not sufficient. To find a reasonable calibration interval a series of monthly calibrations would be needed, to observe the bias variations in more detail. Furthermore, the circumstance that three bias correction curves are extracted for each accelerometer axis opens the question of which curve to use as the proper correction. Two points can be considered here. Firstly, in a nominal horizontal position, a slight non-orthogonality of the horizontal sensor axes would have a large impact on the measured acceleration (see again Fig. 4.8). In this case, however, measuring up and down, a possible non-orthogonality effect on the bias estimation is neutralized. Secondly, Savage (2007) states that scale factors can drastically affect bias estimation when gravity is used as the reference. But as the non-orthogonality effect, the linear scale factor effect is eliminated, too, by Eq. (4.5). Consequently, the different bias curves must resemble an effect of the sensor orientation on to the biases (see Ch. 4.2.2), which seems to be rather constant, since the 2017 curves (except for the X axis when Z is pointing up and down) show high correlation with those of 2019. Finally, one would choose the blue curves as calibration curves since they represent the standard RQH usage orientation during terrestrial 3D-gravity profiling, with X and Y oriented (nearly) horizontally and Z aligned in upwards direction. Equation (4.5) is adapted to Eq. (4.5a) accordingly.

$$\mathbf{b}_{[a]} = \begin{pmatrix} (\check{f}_{[X]}^{b[Z_{up}]} + \check{f}_{[X]}^{b[Z_{down}]})/2 \\ (\check{f}_{[Y]}^{b[Z_{up}]} + \check{f}_{[Y]}^{b[Z_{down}]})/2 \\ (\check{f}_{[Z]}^{b[Z_{up}]} + \check{f}_{[Z]}^{b[Z_{down}]})/2 \end{pmatrix} \quad (4.5a)$$

Simulations in Becker (2016) could show that constant accelerometer scale factors below 100 ppm lead to sub-mGal/sub-arcsecond effects in the gravity disturbances of an airborne campaign with roll and pitch variations of $\pm 8^\circ$ and $\pm 3^\circ$. For terrestrial campaigns the roll range is comparable. However, the pitch range must be extended to $\pm 8^\circ$. It is assumed that this extended pitch variation does not change the result of Becker (2016) since this pitch range does not exceed the roll range. In that case, it would be acceptable to neglect the linear scale factors of the accelerometers for terrestrial 3D-gravity profiling if they remain constant during a campaign. But, Figs. 4.10 show that already slight temperature variations lead to substantial scale factor changes. Those variations would mainly degrade the down component, due to gravity. An unnoticed change in the linear scale factor of 1 ppm might be interpreted as approx. 1 mGal decrease/increase in the SGD.

³⁸Remember from Ch. 2.2 that in 2019 parts of the RQH were renewed. Another calibration in 2021 seems reasonable to investigate if the 2019 results are reproducible.

³⁹The gyroscope data of the Up and Down calibration is not capable of detecting such a small rotation over a measurement period of two days.

4.2.2 Roll and pitch dependencies

This calibration was initiated by Becker (2016, Ch. 6.6.1) after realizing that the accelerometer errors of a similar RQH depend on its orientation. The idea behind this calibration is to calculate the difference between the nominal and the measured acceleration for a chosen number of orientations to create a two-dimensional (roll- and pitch-dependent) correction matrix. The orientations are defined by a grid that covers the range of airborne and ground-based maneuvers, as visualized in Fig. 4.12. All in all, 83 orientations were selected and were recorded for ten different temperatures, see Table 4.3. Note that the correction matrix itself is not illustrated, assessed, or applied in this work. The reason is that the analyses of the Up and Down calibration 2017 indicate an unexpected behavior of the accelerometer triad. As mentioned before, for a 3D-gravimetry campaign it would be critical if the relative orientation of the accelerometer axes changes w.r.t. the gyroscope axes. Furthermore, the Roll and Pitch calibration itself would be meaningless when the accelerometer orientation is not constant w.r.t. the turntable. Unfortunately, this calibration is not capable of tracking such behavior, as for example the strapdown rotation test (Ch. 4.2.3). The Roll and Pitch calibration is only used to confirm the insights of the Up and Down analyses via least square adjustment. The benefit of this calibration w.r.t. the Up and Down calibration is that the results are based on normal usage orientations. But, when determining calibration parameters this way, the limited sensor inclination becomes problematic e.g., to separate bias and scale factors properly.

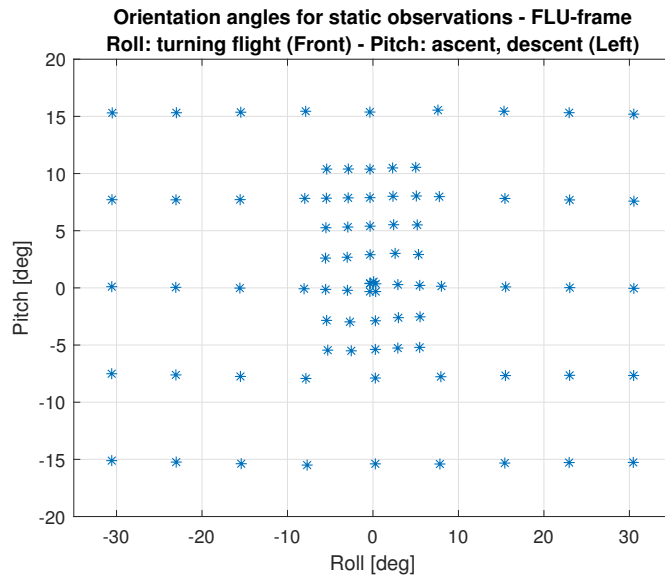


Figure 4.12: Roll and Pitch calibration: RQH orientations during calibration, for all temperatures. The FLU-frame states that the roll and pitch rotations are assigned to the b-frame X and Y axes, respectively.

Data

The following equation is used to estimate the accelerometer biases, non-orthogonalities, and level errors of the turntable. Note that scale factors are missing since they are not properly separable from biases due to the limited range of orientation angles and that it is not distinguished between $\epsilon_{[XY]}/\epsilon_{[ZX]}/\epsilon_{[YZ]}$ and $\epsilon_{[YX]}/\epsilon_{[XZ]}/\epsilon_{[ZY]}$, so no cross-couplings are extracted.

$$\check{\mathbf{f}}^b = \mathbf{b}_{[a]} - \mathbf{M}\mathbf{R}(\theta_{[0]}, \theta_{[1]})\mathbf{R}(\alpha, \beta)\mathbf{g}^l \quad (4.7)$$

$$= \begin{pmatrix} b_{[a,X]} \\ b_{[a,Y]} \\ b_{[a,Z]} \end{pmatrix} - \begin{pmatrix} 1 & \epsilon_{[XY]} & -\epsilon_{[ZX]} \\ -\epsilon_{[XY]} & 1 & \epsilon_{[YZ]} \\ \epsilon_{[ZX]} & -\epsilon_{[YZ]} & 1 \end{pmatrix} \begin{pmatrix} \cos \theta_{[0]} \cos \theta_{[1]} & -\sin \theta_{[0]} \cos \theta_{[0]} \sin \theta_{[1]} \\ \sin \theta_{[0]} \cos \theta_{[1]} & \cos \theta_{[0]} \sin \theta_{[0]} \sin \theta_{[1]} \\ -\sin \theta_{[1]} & 0 & \cos \theta_{[1]} \end{pmatrix} \begin{pmatrix} 1 & 0 & \beta \\ 0 & 1 & \alpha \\ -\beta & -\alpha & 1 \end{pmatrix} \begin{pmatrix} 0 \\ 0 \\ -|\mathbf{g}| \end{pmatrix}$$

$$\text{with } \mathbf{R}(\alpha, \beta) = \mathbf{R}_{[Y']}(-\beta)\mathbf{R}_{[X']}(\alpha) \quad (\text{SAA})$$

$$\begin{aligned} \mathbf{R}(\theta_{[0]}, \theta_{[1]}) &= \mathbf{R}_{[tt_1]}(\theta_{[1]})\mathbf{R}_{[tt_0]}(\theta_{[0]}) = [\mathbf{R}_{[Z]}(-\theta_{[0]})\mathbf{R}_{[Y]}(-\theta_{[1]})\mathbf{R}_{[Z]}(\theta_{[0]})]\mathbf{R}_{[Z]}(-\theta_{[0]}) \\ &= \mathbf{R}_{[Z]}(-\theta_{[0]})\mathbf{R}_{[Y]}(-\theta_{[1]}) \end{aligned}$$

$$\mathbf{M} = \mathbf{R}_{[X]}(\epsilon_{[YZ]})\mathbf{R}_{[Y]}(\epsilon_{[ZX]})\mathbf{R}_{[Z]}(\epsilon_{[XY]}) \quad (\text{SAA})$$

Observations inside the least square adjustment are the average acceleration values ($\check{\mathbf{f}}^b$) during the standstill phases. The length of these phases is based on the sensors' bias instability again. $\mathbf{b}_{[a]}$ represents the accelerometer biases but is also affected by scale factor variations. \mathbf{M} (with $\mathbf{R}_{[X'/Y'/Z]} \hat{=}$ nominal b-frame axes) includes accelerometer non-orthogonalities (actually mean axes misalignments in this case) w.r.t. the nominal axes. $\epsilon_{[ZX]}$ describes the deviation of the angle between the b-frame Z and X axes from the nominal b-frame X and Z axes from orthogonality. $\mathbf{R}(\theta_{[0]}, \theta_{[1]})\mathbf{R}(\alpha, \beta)$ ($\mathbf{R}_{[X'/Y']}$ $\hat{=}$ l-frame axes, $\mathbf{R}_{[tt_0/1]}$ $\hat{=}$ turntable axes) maps the reference acceleration, which is gravity pointing in physical downward direction (\mathbf{g}^l), into the nominal b-frame orientation. α and β express the deviation of the turntable $0^\circ/0^\circ$ -position from the local-level. A dedicated rotation sequence was executed at each temperature to be able to determine α and β , which can cause systematic errors in the parameter estimation of the Roll and Pitch calibration. With an internal positioning precision (repeatability) of the turntable of $0.36''$, the resulting deviations from the plumb line are between $0''$ and $4''$ and show a correlation with rising temperatures. The two angles are not presented, but the outcome tells that due to the absolute turntable instability, α and β should always be estimated during a Roll and Pitch calibration⁴⁰. An inclination of $4''$ falsifies the horizontal accelerometer readings between $\sim \pm 20$ mGal, depending on the yaw angle.

Illustration

Figures 4.13 include the average values of the three accelerometers for each orientation at the different temperatures, referenced to 10°C . On the left side, the curves are clustered in three roll intervals, on the right in three pitch intervals, as noted in the legend. The X component does neither show a correlation with the roll nor with the pitch angle. But, there is a linear trend and a spreading of the curves visible with rising temperatures. The mean trend is ~ 1 mGal $^\circ\text{C}^{-1}$, while the curves spread around this trend with approximately ± 2 mGal. In each orientation, the measured values seem to evolve differently within this range. This is an example where the Roll and Pitch calibration might bring benefits. A similar statement is valid for the Y accelerometer. The most significant differences are that there is a coarse clustering with roll and pitch angles and that the mean linear trend is about ten times larger (~ 10 mGal $^\circ\text{C}^{-1}$). At first sight, a pure temperature-dependent correction could reduce the largest portion of the error. The last two figures depict the Z accelerometer data. The overall pattern of the curves is completely different. There is a correlation with the roll angle,

⁴⁰The Up and Down calibration is not affected by this phenomenon, due to the reversing of the sensor axes (up and down). The strapdown rotation test in Ch. 4.2.3 is not affected, too. During this calibration, a separate alignment of the ISA is calculated for each temperature and the gyroscope are used to track angular motion instead of turntable readings.

while the pitch angle shows only a minor correlation. Figure 4.13(e) reveals an asymmetric behavior for the positive and negative roll angles with varying temperatures. This result is discussed in detail later on. Additionally, from the red curves ($\pm 1^\circ$ to local-level) in this figure a general linear trend of $\sim 2 \text{ mGal } ^\circ\text{C}^{-1}$ can be deduced.

The results for the biases and non-orthogonalities are presented in Figs. 4.14. A comparison with the Up and Down calibration 2017 results indicate that except for the Z bias (see Discussion), the coarse shape of the curves can be determined with both methods, and thus the results from the Up and Down calibration are confirmed.

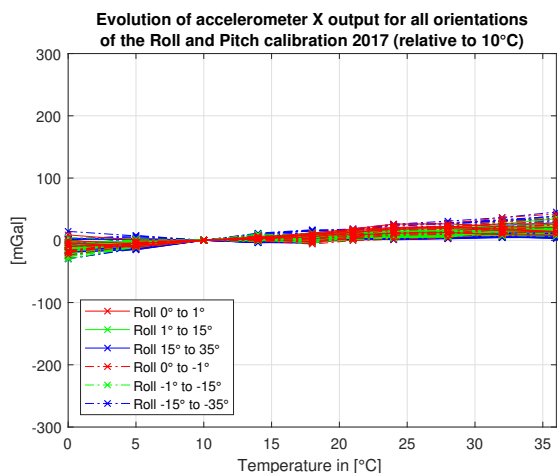
Discussion

Conclusions from Figs. 4.13 are that there is at least no dominant pitch dependency for all accelerometers, and no systematic influence of the roll angle onto the measurements exists for the X accelerometer (cf. Figs. 4.13(a), (b), (d), and (f)). From this perspective, a correction matrix is a promising candidate to reduce errors, which are unique for different orientations. The analysis gets more complicated when analyzing Figs. 4.13(c) and (e). From the Y component, it could be concluded that the sensor is strongly influenced by the temperature, independently of its orientation. So, a temperature correction might be a promising option. However, when analyzing both figures in combination, it is possible to confirm the interpretation from the Up and Down non-orthogonality plot (Fig. 4.11(a)). Considering a rotation of the accelerometer triad or the ISA with increasing temperatures around the X axis, the results would look alike. The reason why a rotation manifests differently in Y and Z is their orientation w.r.t. the gravity vector. Y senses gravity positive or negative depending on the roll angle, while Z measures gravity always with a positive sign. In this case, a correction matrix would not tackle the original cause and might even deteriorate the quality of the RQH output if the true cause is a rotating ISA.

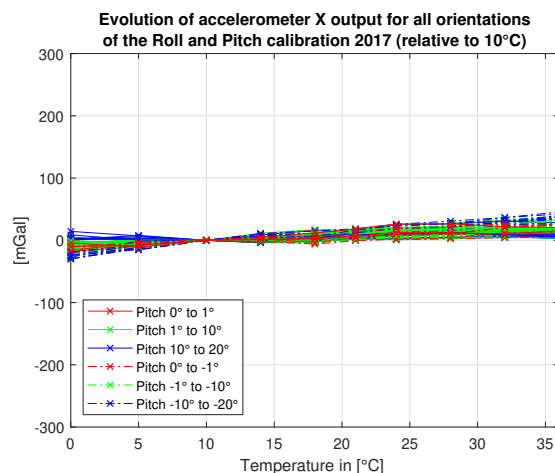
The different shape of the Z bias compared to the Up and Down calibration 2017 result reveals the influence of the scale factor when large accelerations like gravity are acting on the accelerometer. In this case, scale factor changes of 1 ppm mix into the bias estimation with $\sim 1 \text{ mGal}$. Consequently, extracting bias or non-orthogonality information from the Roll and Pitch calibration is less trustworthy than from the Up and Down calibration, having all accelerometers in the horizontal position twice. For the latter, the scale factor effect can be detected and a non-orthogonality will be amplified⁴¹. Nevertheless, confirming the main structure of the non-orthogonality changes was the reason to believe that high-precision measurements are potentially impossible if the movement is originating from an ISA instability. Unfortunately, with the two presented calibrations, a complete picture of this behavior can not be derived. This is why only the least square adjustment is covered by this chapter to compare it with the Up and Down calibration results, and why the calibration matrix itself is not presented. And remember that the Up and Down calibration 2019 already revealed that the RQH behavior changed drastically, so the temperature calibration results from 2017 are not valid anymore. To get a deeper insight, in 2019 the strapdown rotation test was performed, which is treated in the next chapter.

Annotation: Some numbers are added to understand why the gyroscopes are not capable of tracking a small rotation during these calibrations. If a rotation of the ISA is assumed between the steady-state of two temperatures, an angular velocity of $50''$ in 56 h (time between first and last calibration sequence) is considered from the non-orthogonality trend in Fig. 4.11(a). The gyroscopes exhibit an angular random walk/white noise of $0.0018^\circ \text{ h}^{-0.5}$ according to the manufacturer (RQH details in Table 2.2), which equals an uncertainty of $\sim 48.5''$ over a 56 h period. Therefore, such a rotation cannot be reliably resolved. For shorter periods, e.g., between the first and second calibration sequence, the problem becomes even more clear: $6.5''$ in 8 h against the uncertainty of $18.3''$ due to the sensor noise.

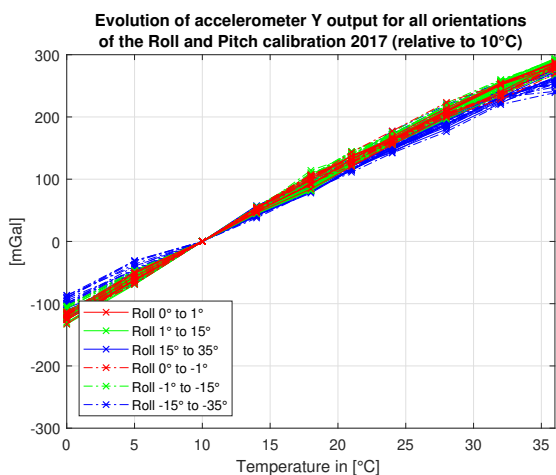
⁴¹Effect of non-orthogonality of $40''$ horizontal: $9.81 \text{ m s}^{-2} * \sin(40'' / 3600'' / 180^\circ * \pi) = 190 \text{ mGal}$
 Effect of non-orthogonality of $40''$ vertical: $9.81 \text{ m s}^{-2} - 9.81 \text{ m s}^{-2} * \cos(40'' / 3600'' / 180^\circ * \pi) = 0.018 \text{ mGal}$



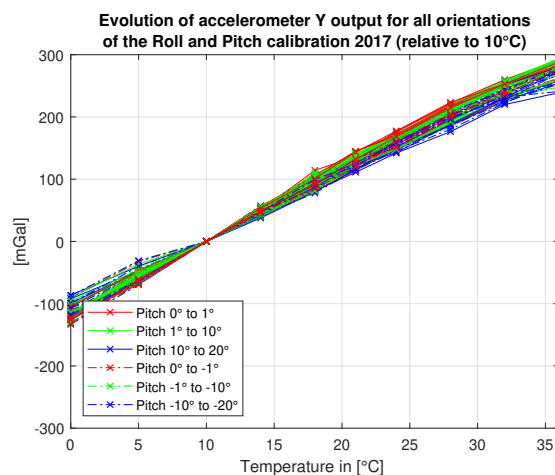
(a) Accelerometer X output - Roll dependencies



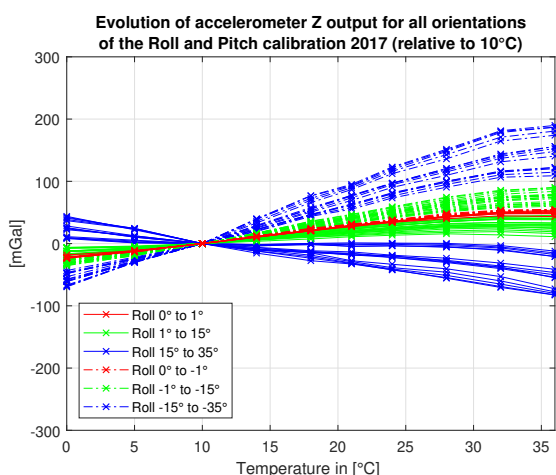
(b) Accelerometer X output - Pitch dependencies



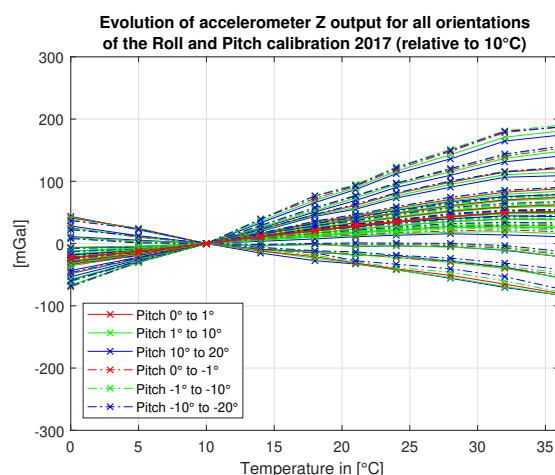
(c) Accelerometer Y output - Roll dependencies



(d) Accelerometer Y output - Pitch dependencies



(e) Accelerometer Z output - Roll dependencies



(f) Accelerometer Z output - Pitch dependencies

Figure 4.13: Roll and Pitch calibration: Accelerometer output (averaged values) over temperature for all orientations. Additionally, roll (left) and pitch (right) angles are clustered and color-coded.

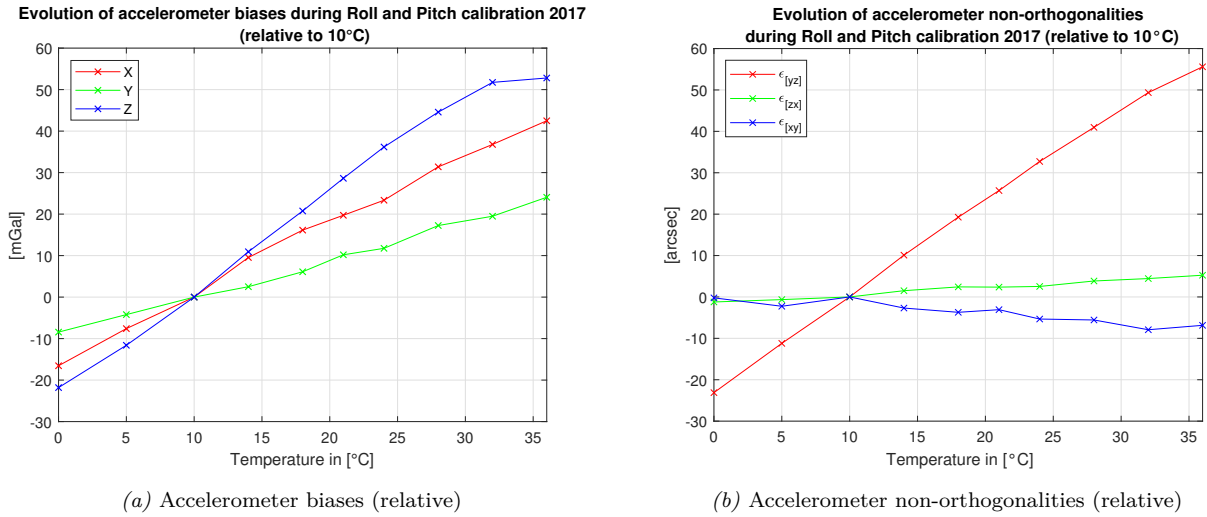


Figure 4.14: Roll and Pitch calibration: Accelerometer biases and non-orthogonalities over temperature, based on all roll and pitch combinations during the calibration.

4.2.3 Strapdown rotation test

The strapdown rotation test, as described in Savage (2007, Ch. 18.4), is capable of determining gyroscope linear scale factors and cross-couplings as well as accelerometer biases, linear scale factors, and scale factor asymmetries. Furthermore, this method allows to analyze non-orthogonalities of the accelerometer axes w.r.t. the mean gyroscope axes ($\hat{=}$ mean angular rate sensor axes (MARS)) and movements of the ISA w.r.t. the housing. With this information, it is possible to determine whether the accelerometer and gyroscope axes diverge or if the ISA rotates w.r.t. the housing. This section includes a summary of the strapdown rotation test and presents the results obtained with the RQH. For more details about the test and the mathematical derivation, the reader is referred to Savage (2007). Note that in Savage (2007) descriptions are related to NED-frame calculations.

The calibration consists of 21 dedicated rotation sequences⁴², as shown in Table 4.5, and makes use of standstill accelerometer data before and after each rotation sequence in combination with gyroscope data collected during the rotations, via an "attitude-integrating/acceleration-transformation" algorithm, as it is called in Savage (2007). The measured acceleration values before and after each rotation sequence are averaged separately (based on the sensors' bias instability), transformed into the n-frame with the help of an initial alignment in combination with the subsequent gyroscope observations, and finally reduced by gravity. Non-zero n-frame average values reflect some sort of sensor error, an error in the initial alignment, or an error in the magnitude of the Earth's rotation rate. With the rapid execution of single rotation sequences and by taking the difference between the horizontal acceleration average values of the "before" and "after" measurements, the impact of an Earth rotation rate error and an initial alignment error is minimized, see Savage (2007). Accelerometer and gyroscope errors dominate the remaining signal. The rotation sequences are designed such that a minimum of error sources is amplified by each sequence, which makes the extraction of single calibration parameters simpler and more robust. In this thesis, a least square adjustment was implemented additionally to extract the calibration parameters apart from the equations in Savage (2007, Fig. 18.4.4-1). Both methods show consistent results.

⁴²There is also a version with only 16 rotation sequences. For advantages and disadvantages, see Savage (2007).

No.	Up axis	Turntable angles: $\theta_{[0]}/\theta_{[1]}$ in $^{\circ}$	Nominal b-frame rotation axis and angle in $^{\circ}$
1	+Z	0/0	Y: -360
2	+Z	+90/0	X: +360
3	+Z	0/0	Y: -90, Z: -360, Y: +90
4	+Z	0/0	Y: -180, Z: -90, X: +180, Z: +90
5	+Z	+90/0	X: +180, Z: -90, Y: +180, Z: +90
6	+Z	0/0	Y: -90, Z: -90, X: -90, Z: +90
7	+Z	0/0	Y: -180
8	-Z	0/+180	Y: -180
9	+Z	+90/0	X: +90
10	+Y	+90/+90	X: +90
11	-X	0/-90	Z: -180
12	+Z	+90/0	X: +180
13	-Z	+90/+180	X: +180
14	+Z	0/0	Y: -90
15	+X	0/+90	Y: -90
16	+Y	+90/+90	Z: -180
17	-Y	+90/-90	X: +180
18	+Y	+90/+90	X: +180
19	-Y	+90/-90	Z: -90
20	+X	+180/-90	Z: -90
21	+Z	+90/0	X: +180

Table 4.5: Upwards pointing accelerometer axes and nominal turntable orientation angles at the start of each sequence of the strapdown rotation test. Additionally, rotations executed during the calibration are listed in terms of the nominal b-frame rotation axis and angle.

Data

In Savage (2007, Fig. 18.4.3.5) each observation is expressed in terms of sensor errors, and Savage (2007, Fig. 18.4.4.2) shows how to extract the sensor calibration parameters from the observations. In this work, the parameters of each temperature are deduced via least square adjustment, linearly interpolated, and then applied to the RQH measurement data as shown in Eqs. (4.8) and (4.9).

$$\mathbf{f}^b = (\mathbf{S} + \mathbf{M} + \mathbf{SA})^{-1}(\check{\mathbf{f}}^b - \mathbf{b}_{[a]}) \quad (4.8)$$

$$= \left(\left(\begin{pmatrix} sf_{[X]} & 0 & 0 \\ 0 & sf_{[Y]} & 0 \\ 0 & 0 & sf_{[Z]} \end{pmatrix} + \begin{pmatrix} 1 & \epsilon_{[XY]} & \epsilon_{[XZ]} \\ \epsilon_{[YX]} & 1 & \epsilon_{[YZ]} \\ \epsilon_{[ZX]} & \epsilon_{[ZY]} & 1 \end{pmatrix} + \begin{pmatrix} s^{43}(\check{f}_{[X]}^b)sf_{a[X]} & 0 & 0 \\ 0 & s(\check{f}_{[Y]}^b)sf_{a[Y]} & 0 \\ 0 & 0 & s(\check{f}_{[Z]}^b)sf_{a[Z]} \end{pmatrix} \right)^{-1} \left(\begin{pmatrix} \check{f}_{[X]}^b \\ \check{f}_{[Y]}^b \\ \check{f}_{[Z]}^b \end{pmatrix} - \begin{pmatrix} b_{[a,X]} \\ b_{[a,Y]} \\ b_{[a,Z]} \end{pmatrix} \right)$$

$$\text{with } \mathbf{M} = \mathbf{R}_{[X]}(\epsilon_{[YZ]}/\epsilon_{[ZY]})\mathbf{R}_{[Y]}(\epsilon_{[ZX]}/\epsilon_{[XZ]})\mathbf{R}_{[Z]}(\epsilon_{[XY]}/\epsilon_{[YX]}) \quad (\text{SAA})$$

$$\boldsymbol{\omega}_{[ib]}^b = (\mathbf{T} + \mathbf{N})^{-1}(\check{\boldsymbol{\omega}}_{[ib]}^b - \mathbf{b}_{[g]}) \quad (4.9)$$

$$= \left(\left(\begin{pmatrix} SF_{[X]} & 0 & 0 \\ 0 & SF_{[Y]} & 0 \\ 0 & 0 & SF_{[Z]} \end{pmatrix} + \begin{pmatrix} 1 & \frac{1}{2}N_{[XY]} & \frac{1}{2}N_{[ZX]} \\ \frac{1}{2}N_{[XY]} & 1 & \frac{1}{2}N_{[YZ]} \\ \frac{1}{2}N_{[ZX]} & \frac{1}{2}N_{[YZ]} & 1 \end{pmatrix} \right)^{-1} \left(\begin{pmatrix} \check{\omega}_{[ib,X]}^b \\ \check{\omega}_{[ib,Y]}^b \\ \check{\omega}_{[ib,Z]}^b \end{pmatrix} - \begin{pmatrix} b_{[g,X]} \\ b_{[g,Y]} \\ b_{[g,Z]} \end{pmatrix} \right)$$

In Eqs. (4.8) and (4.9) variables are defined in the same way as in the preceding calibrations, although the inverse calculation is presented. The calibrated sensor measurements \mathbf{f}^b and $\boldsymbol{\omega}_{[ib]}^b$ are listed on the left side of the equations. The measurement data is represented by $\check{\mathbf{f}}^b$ and $\check{\boldsymbol{\omega}}_{[ib]}^b$. $\mathbf{b}_{[a]}$ represents the accelerometer biases and $\mathbf{b}_{[g]}$ the gyroscope biases. \mathbf{S} , \mathbf{M} (with $\mathbf{R}_{[X/Y/Z]} \hat{=}$ nominal b-frame axes), and \mathbf{SA} stand for the deviation of the accelerometer linear scale factors from 1, the accelerometer non-orthogonalities w.r.t. the MARS and the accelerometer asymmetrical scale factors, respectively. \mathbf{T} and \mathbf{N} include the gyroscope linear scale factors and cross-couplings. $N_{[XZ]}$ expresses the deviation of the gyroscopes X and Z axes from perpendicularity. By setting the elements of \mathbf{N} to $\frac{1}{2}N_{[YZ/ZX/XY]}$ the gyroscope observations are referenced to the MARS.

Illustration

The first two figures of the strapdown rotation test in Figs. 4.15 include the linear scale factors and cross-couplings of the gyroscopes. The linear scale factors range between ± 4 ppm, with marginal trends (~ 0.1 ppm $^{\circ}\text{C}^{-1}$) over temperature. The calculated cross-couplings stay far below $10''$. However, a distinct trend of $\sim 0.2''$ $^{\circ}\text{C}^{-1}$ of the angle between the X and Z axis with rising temperature is apparent from $-1''$ to $6''$.

⁴³ $s(\dots)$ represents the sign(\dots)-function: output equals +1 in case of positive input and -1 in case of negative input.

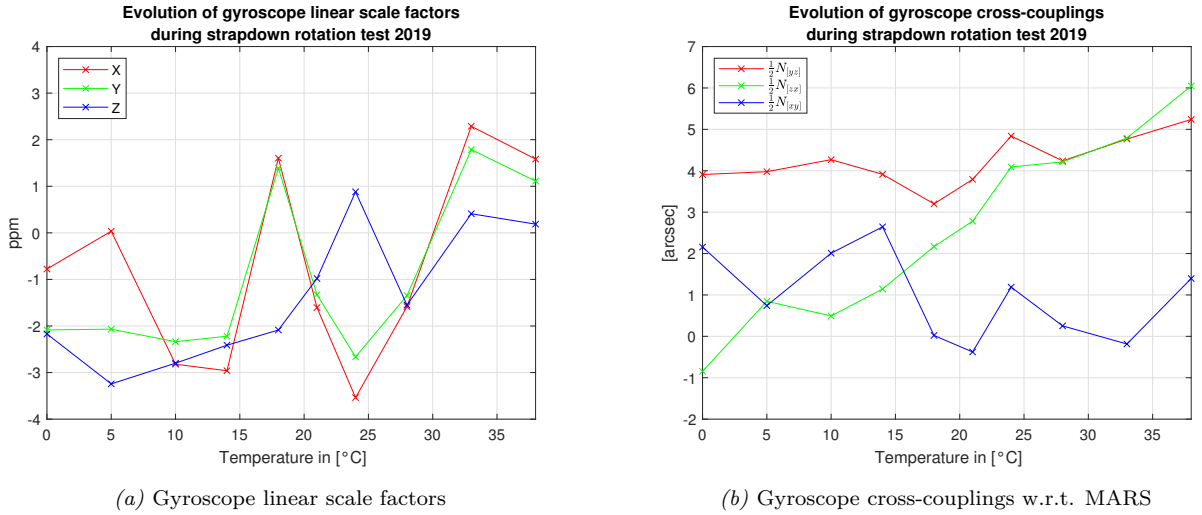


Figure 4.15: Strapdown rotation test: Gyroscope linear scale factors and cross-couplings over temperature.

All parameters concerning the accelerometers are presented in Figs. 4.16. The linear scale factors agree with the results of the Up and Down calibration 2019 (Figs. 4.10). The three scale factor asymmetries look very similar in terms of relative changes (the trend of Z is just negative). The curves clearly depend on the temperature with changes of ~ 0.5 ppm $^{\circ}\text{C}^{-1}$. The absolute values of X and Y remain between 10 - 30 ppm while Z exhibits a range between -30 ppm and -50 ppm.

Also the bias curves in Fig. 4.16(e) show a high correlation with the blue bias estimation curves from the Up and Down calibration 2019 (Figs. 4.9(b), (d), and (f)). Minor differences are expected due to the extended list of estimated parameters for the strapdown rotation test.

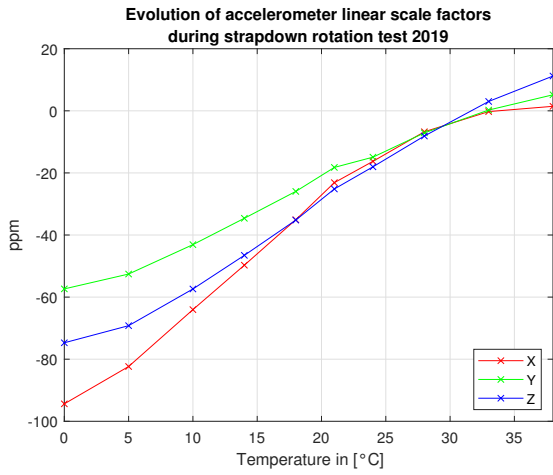
Lastly, Fig. 4.16(f) shows the most important information about the calibration. It depicts the movement of the accelerometer sensor axes w.r.t. the MARS⁴⁴. The absolute values are not shown but stay in the range of $\pm 10''$. All curves show minor variations with rising temperature in combination with systematic temperature-related trends. In case of $\epsilon_{[ZX/XZ]}$ and $\epsilon_{[XY/YX]}$, these trends are dominated by a change of the misalignment by 1 - 2'', while for $\epsilon_{[YZ/ZY]}$ the cross-coupling changes by $\sim 7''$, dominated by a change in $\epsilon_{[ZY]}$.

Discussion

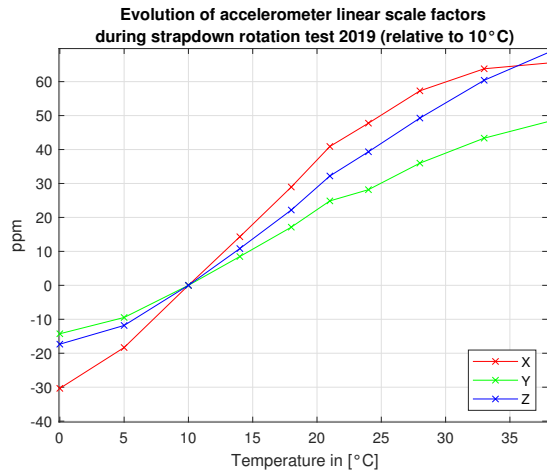
The estimated gyroscope parameters do not indicate a critical behavior, especially when the temperature range of the sensors is kept small, for instance by avoiding cold starts of the RQH. The cross-coupling values stay below the error margins for 3D-gravimetry mentioned in Becker (2016). The only unsatisfying point is the slightly larger cross-coupling drift in $\frac{1}{2}N_{[ZX]}$. However, resulting effects on the final gravity estimates cannot be stated without performing further analysis. This point will be addressed as part of the Estergebirge campaign in Ch. 4.3.

From the accelerometer scale factor illustrations, three conclusions can be derived. Firstly, the close correlations of Figs. 4.16(a) and (b) with Figs. 4.10(b) and (d), which are combined in Fig. 4.17(a), confirm that the Up and Down calibration is as reliable as the least square adjustment of the strapdown rotation test for detecting and quantifying linear scale factors. Anyhow, this result is not surprising since the strapdown rotation test is also based on several up and down measurements without any inclined measurement data. Secondly, it could be observed that the Z accelerometer is built-in in

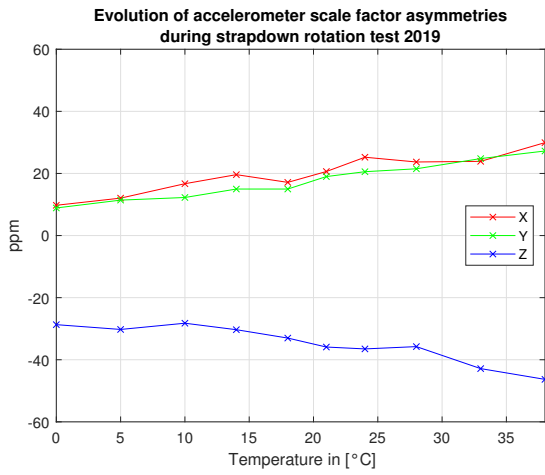
⁴⁴ $-\epsilon_{[ZY]}/-\epsilon_{[XZ]}/-\epsilon_{[YX]}$ are plotted for better comparison.



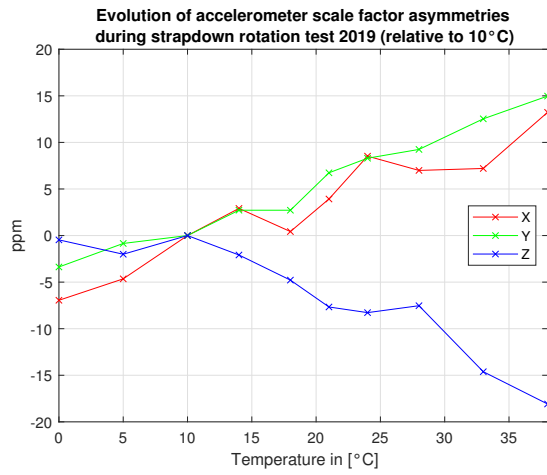
(a) Accelerometer linear scale factors (absolute)



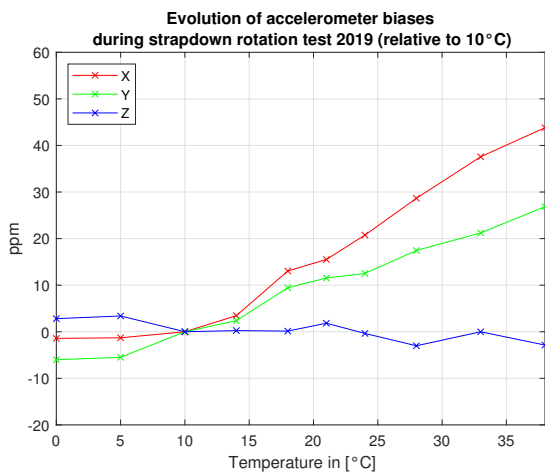
(b) Accelerometer linear scale factors (relative)



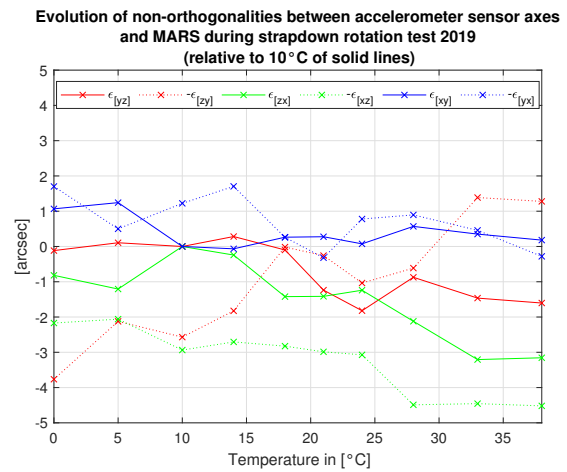
(c) Accelerometer linear scale factor asymmetries (absolute)



(d) Accelerometer scale factor asymmetries (relative)



(e) Accelerometer biases (relative)



(f) Non-orthogonalities: Accelerometer sensor axes to MARS (relative)

Figure 4.16: Strapdown rotation test: Accelerometer parameters over temperature.

opposite direction as X and Y (checked by the author in standard calibration description), which then reveals very similar temperature dependencies of the scale factor asymmetry for all QA-2000 sensors. Lastly, the scale factor asymmetries $> \pm 10$ ppm may cause larger errors in the state vector components of terrestrial 3D-gravimetry if they are not considered, due to positive and negative kinematic accelerations along the horizontal axes. The larger absolute values in Z are of minor concern as long as this axis is nominally pointing in up direction, resulting in only positive accelerations as shown in Fig. A.1(a).

As stated before, the accelerometer bias curves do not contradict the results from the Up and Down calibration 2019, but they are supposed to be more reliable due to the fact that scale factor asymmetries are considered in the strapdown rotation test, but omitted in the Up and Down calibration.

Figure 4.16(f) rules out the worst-case scenario. There is only a minor movement between the two sensor triads observable, which is not responsible for the drift of $\epsilon_{[ZX/XZ]}$ in Fig. 4.11(b). The extracted absolute non-orthogonalities lie within the error margin of $10''$ for gravity results of $1 \text{ mGal}/''$ -accuracy, as noted in Becker (2016). Nevertheless, the rather strong trend in $\epsilon_{[ZY]}$ was not expected and it can definitely degrade the results. Fortunately, in this thesis, the Z axis usually points in upward direction ($\pm 8^\circ$), where misalignments are less critical than in the horizontal plane⁴⁰.

To affirm that the drift of $\epsilon_{[ZX/XZ]}$ in Fig. 4.11(b) is of different origin, the computation described in Savage (2007, Ch. 18.4.7.4) is implemented for six orientations. It allows to extract a movement of the ISA w.r.t. the turntable mount from three independent combinations of two orientations. When considering the connection of the RQH housing to the turntable mount as exceptional stable, then actually ISA movements w.r.t. the RQH housing can be investigated. The three solutions are combined in a least square manner, where the correlation with temperature is modeled as a linear trend. The final result is shown in Fig. 4.17(b). Although the blue and red curves do not completely agree with the curves in Fig. 4.11(b), it becomes clear that the main rotation of the green curve in Fig. 4.11(b) represents a movement of the ISA w.r.t. the housing. The rotation is likely caused by a thermal reaction of the shock mounts (internal communication with iMAR). Shock mounts connect the ISA with the housing and prevent the sensors from being damaged by external impacts (damping capacity). Such a movement of the ISA generally is of no concern, since the sensors build their own mathematical frame and do not have to be referenced to the housing. And, effects onto the lever arm in the b-frame are normally small for car-based applications because of the limited distance between IMU and GNSS antenna. However, it can be problematic if the gyroscopes are not able to track this movement due to the angular random walk of the gyroscopes, as was pointed out in the previous "**Annotation**". Yet, during terrestrial 3D-gravity profiling campaigns, this phenomenon is not critical (tested and confirmed by the author). Firstly, because the temperature range is rather small (cf. Ch. 4.3). Secondly, 3D-gravity updates are provided regularly, removing the major part of this rotation that affects the gravity disturbance. Lastly, the continuous GNSS updates in combination with horizontal accelerations improve the separation between orientation errors and VDs inside the EKF.

Apart from that, the ISA rotation is critical for calibrations similar to the Roll and Pitch calibration, where reference accelerations are calculated based on the turntable orientation (no gyroscope data integrated), without considering the true ISA orientation, see e.g., Fig. 4.13(e).

Finally, it can be recapitulated from Figs. 4.11(a) and 4.11(b) that this rotation of the ISA w.r.t. the housing due to variations in the temperature is of complex nature. The characteristics changed completely from 2017 to 2019, as already mentioned. If for any application, the precise orientation of the RQH housing/vehicle is needed, this phenomenon has to be further investigated. The rotation can be depending on several influences, e.g., internal temperature gradients, opening of housing for service, aging of shock mounts, etc.

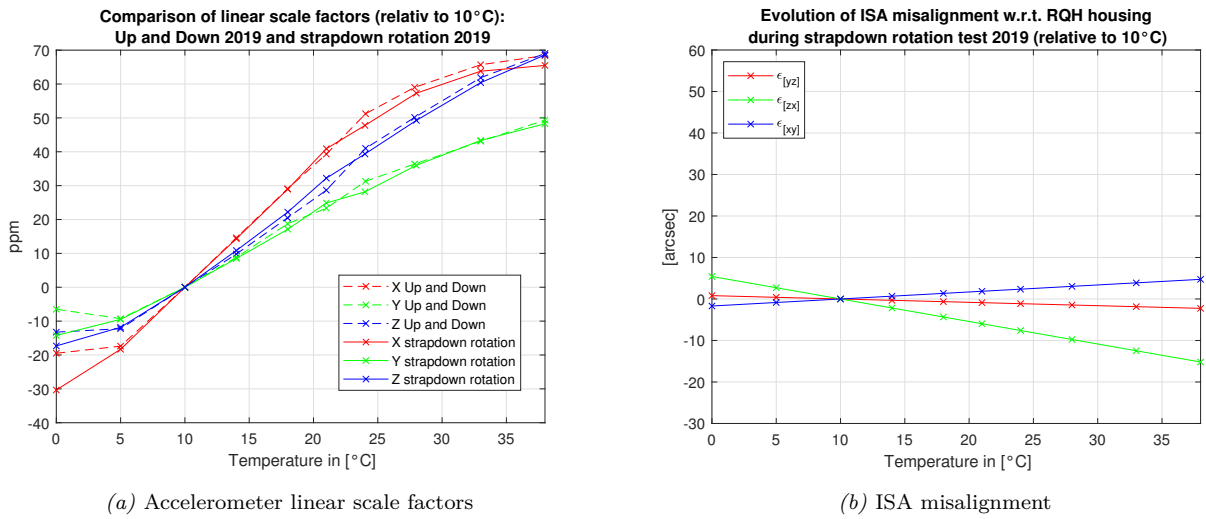


Figure 4.17: (a) Comparison of linear scale factors, determined with the Up and Down calibration and the strapdown rotation test, referenced to 10 °C. (b) Misalignments: ISA - RQH housing (relative).

4.3 Terrestrial 3D-gravity profiling in the Bavarian Alps

This section comprises detailed information about a terrestrial 3D-gravity profiling campaign in the Estergebirge, a mountainous region around 100 km south of Munich in the Northern Alps. In the beginning, the reader is introduced to the test region, and it is elucidated why a geodetic test region was established by the IAPG in the Estergebirge, followed by a brief insight into the region's geodetic history. Additionally, a dedicated trajectory for terrestrial 3D-gravity profiling, depicted in Fig. 4.18, is presented and characterized. The campaign along this trajectory, conducted in November/December 2019, is elaborated subsequently. All the data utilized during the processing are addressed before gravity information is finally extracted from the measurements and illustrated. This part also covers some considerations about the results' accuracy assessment and analyses about certain errors influencing the quality of the results.

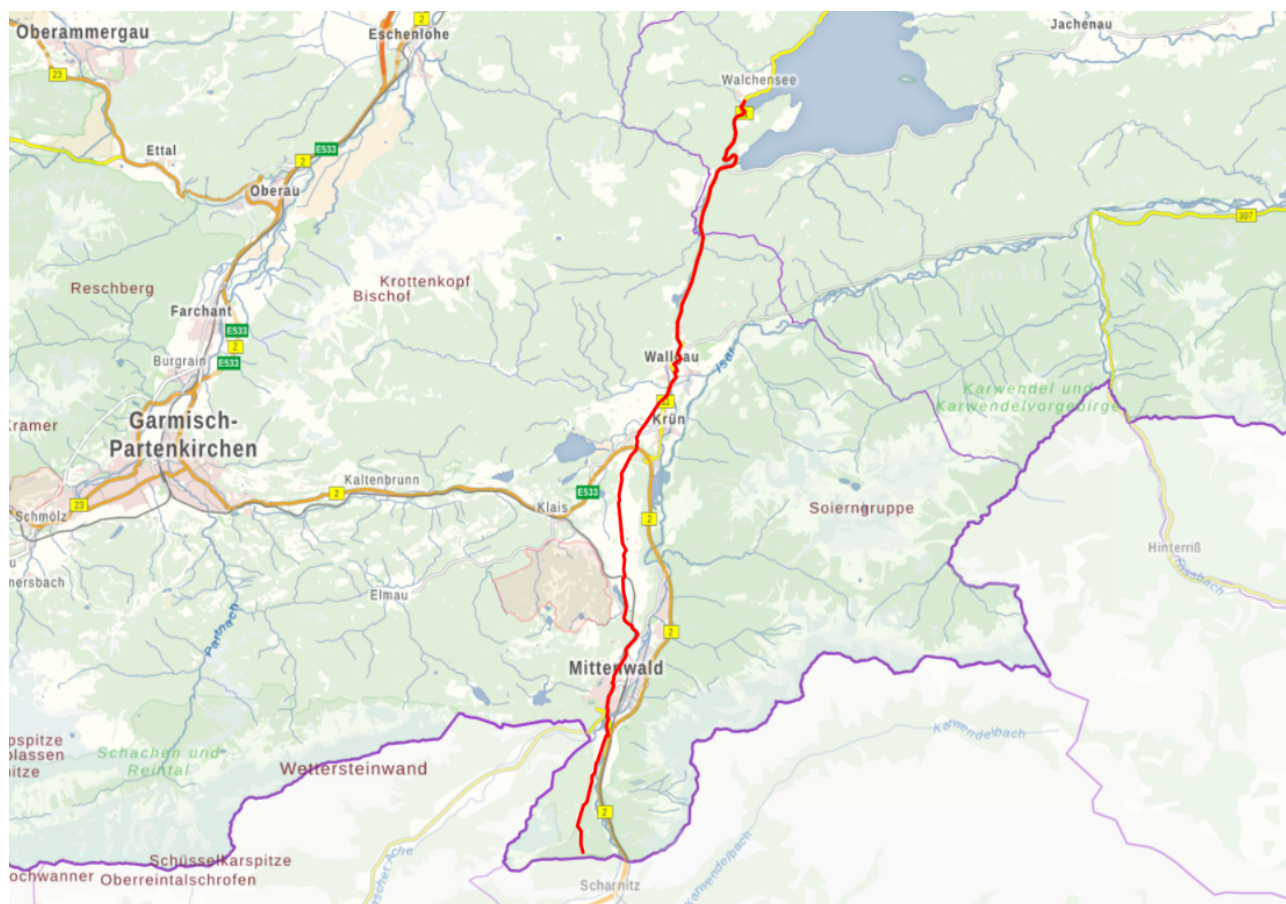


Figure 4.18: Location of the terrestrial 3D-gravity profiling trajectory east of Garmisch-Partenkirchen, in the Estergebirge. The trajectory (red) starts at lake Walchensee towards Mittenwald and ends just north of the Austrian border. The map was created with the help of the "Bayern Atlas" and can be viewed online via <https://v.bayern.de/Myxvg>.

4.3.1 Geodetic test region Estergebirge

The value of a test region like the Estergebirge, where considerable effort was performed to establish a dense geodetic database with diverse measurement techniques lies in its exploitation as precise reference/ground truth e.g., for testing new measurement technologies or the regional validation of any kind of gravity field model, in an area with unique geological, geophysical, and geodetic characteristics. Its proximity to Munich, as part of the Northern Alps, with ellipsoidal height variations between ~ 700 m and ~ 2100 m, its alpine geology (folded rock layers), and the good accessibility qualified the Estergebirge as a valuable geodetic test region.

Stoll (2014) lists the historic geodetic developments in the test region. Her research is based on several diploma projects and intern communication of the IAPG. Observations reach back to the year 1994 and end in 2010. In this period, overall more than 500 point-wise observations were conducted comprising GPS measurements, relative gravity observations, VD campaigns, and leveling lines surrounding and crossing the mountain Wank. Moreover, a terrestrial strapdown inertial scalar gravimetry campaign (cf. Gerlach et al. (2004) and Gerlach et al. (2005)) and an airborne gravimetry campaign (cf. Gerlach et al. (2010a) and Gerlach et al. (2010b)) were conducted in the Estergebirge. Thus, the Estergebirge qualified for a variety of geodetic studies, which comprise e.g.,

- modeling the regional geoid
- investigating regional height anomalies and density anomalies
- analyzing topographically reduced gravity disturbances/topographic modeling
- calibrating gravimeters
- testing the kinematic RQH performance for gravimetry

A VD campaign from 2005 is mentioned in particular. The TZK2-D DZCS zenith camera, developed at the University of Hannover, recorded VDs at 103 points along the ~ 23 km trajectory shown in Fig. 4.18, with an accuracy between $0.05 - 0.1''$ (see Hirt and Flury (2008)). The observations helped to investigate the method of astronomical-topographical leveling. Due to the dense observation spacing over a rather long distance, the VD campaign data perfectly suits the assessment of a terrestrial 3D-gravity profiling campaign, which was already stated by Hirt and Flury (2008): "A further interesting application field is the calibration and validation of INS/GPS vector gravimetric measurement systems. Currently, minor use is being made of the vertical deflections as obtained by those systems (Jekeli and Li, 2006). A dense set of precise predicted vertical deflections, provided by astronomical-topographic levelling, may help to obtain a proper accuracy assessment of INS/GPS systems for 3D-vector gravimetry."⁴⁵ This leads to the latest campaign in the Estergebirge and the main subject of this work, the terrestrial 3D-gravity profiling campaign conducted in 2019 along this trajectory. Details about the practical realization follow in Ch. 4.3.2. The general campaign concept was already addressed at the beginning of Ch. 3. It involves static measurements with the CG-5, QDaedalus, and GS15 as well as measurements with the RQH and AsteRx-U⁴⁶, conducted on a car while driving to determine profiles of the VDs and the SGD.

Since the trajectory in the Estergebirge in Fig. 4.18 is of major interest for this work, it is characterized in the following. The dominant direction is clearly north-south⁴⁷ oriented with only a slight

⁴⁵inertial navigation system (INS)

⁴⁶More details about the instruments can be found in Ch. 2.2

⁴⁷Due to the strong north-south orientation, most subsequent illustrations are plotted against latitude. This leads to one ambiguous latitude mapping at the south-west end of lake Walchensee when the trajectory turns around for more than 90° (against the main direction), and smaller scaling effects that do not affect the upcoming interpretations. The author is aware of this circumstance and suggests an evaluation w.r.t. the length of the trajectory for future campaigns.

east-west trend. The northern part proceeds on the national primary road "B11" until the village of Wallgau. From Wallgau on, it follows smaller tarred roads, through residential and agricultural areas. Behind the village of Mittenwald the trajectory turns from a village road into a forest road. Unfortunately, the given trajectory does not allow to maintain a constant velocity. Furthermore, it includes sections with large and sections with little lateral acceleration.

The recorded ellipsoidal heights and the RQH Euler angles (driven in both directions) are illustrated in Figs. 4.19. Figure 4.19(a) reveals a rather variable height profile. From south to north, the dominant height trend is downward from ~ 990 m to ~ 850 m, including three separate hills with about ~ 90 m, ~ 40 m and ~ 50 m ascents/descents. For the interpretation of Fig. 4.19(b) the reader is reminded that the RQH is installed with its X axis (roll axis) pointing in front direction of the car, the Y axis (pitch axis) pointing to the left, and its Z axis (yaw axis) pointing upwards. The Euler angles manifest that the orientation spectrum of the RQH along the trajectory agrees with the assumption of roll and pitch variations between $\pm 8^\circ$ from Ch. 4.2. A slight positive bias is visible in both angles. The pitch offset ($\sim 1^\circ$) expresses the mean angle between the RQH, mounted on the car's floor, and the local-level, while the roll offset ($\sim 0.5^\circ$) is probably a result of the shape of tarred roads, with a small lateral slope towards the roadside.

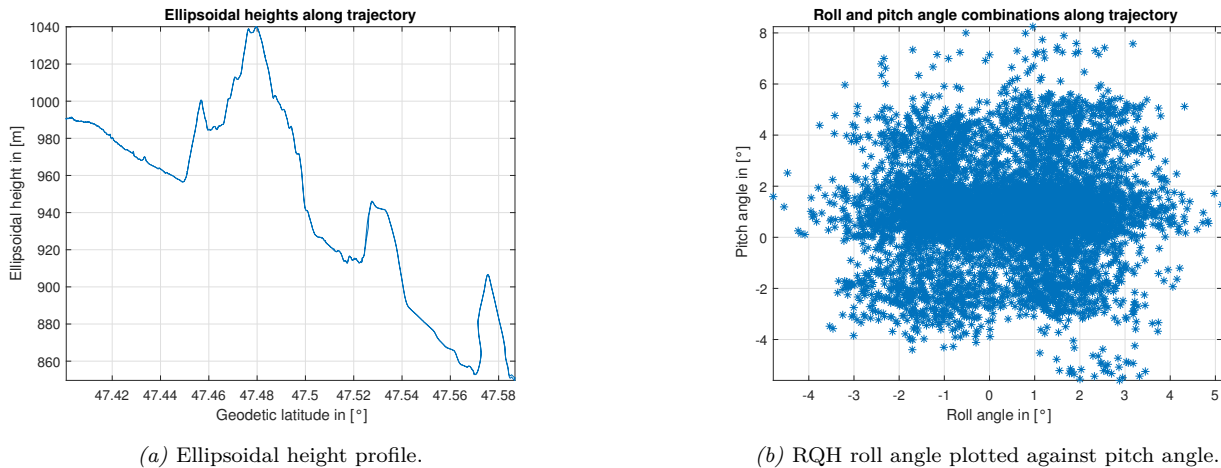
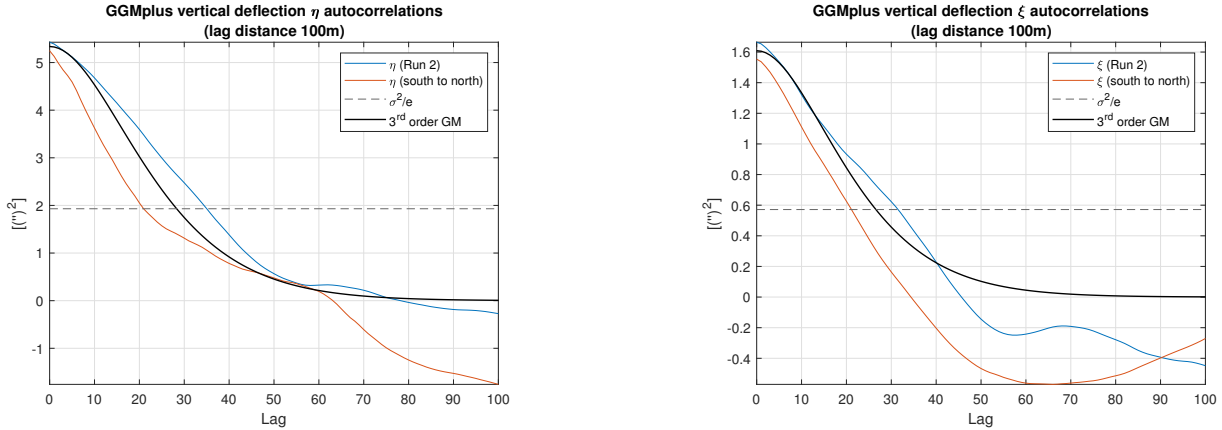


Figure 4.19: Ellipsoidal heights and roll-pitch orientations of the RQH along the trajectory (both directions) in the Estergebirge.

A first impression of the VDs and SGD along the trajectory can be obtained from Figs. 4.24 in Ch. 4.3.2. The η component reaches from $\sim -3''$ to $\sim 6''$ with a sharp trend reversal at $\sim 47.43^\circ$ N. The ξ component varies between $\sim 11''$ and $\sim 16''$. The deflection offset in ξ is due to the large masses of the Central Alps and their inherent attraction towards the south. The vertical component increases from ~ -20 mGal in the south up to ~ 6 mGal after the first third. From then on variations remain between ~ -8 mGal and ~ 6 mGal. All components show smaller overlaying high-frequency structures.

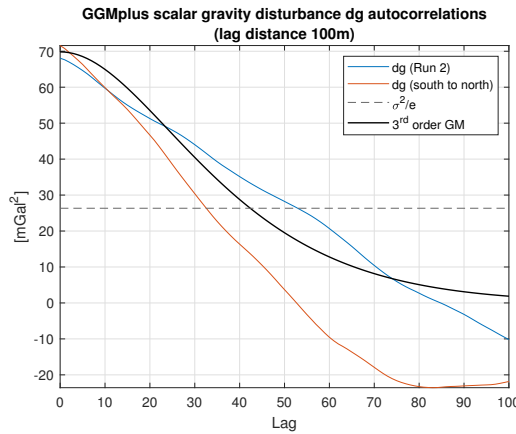
Figures 4.20 illustrate two autocorrelation functions of the VDs and the SGD along the trajectory, obtained from GGMplus. The blue one is based on a complete measurement session, driving along the trajectory in both directions. In this case, the car stopped and turned around two times (at the southern and northern points). The red one presents the autocorrelation of the south-to-north gravity functionals. The results are quite similar and are modeled as third-order Gauß-Markov processes (cf. Eq. (3.21c)). For an initial guess of the model parameters empirical values are chosen. σ^2 is defined as the mean of both functions at lag zero. The correlation distances are extracted in the middle of

the intersections of the blue and red lines with the σ^2/e -lines. e is Euler's number. Inside the EKF algorithm, the correlation distances are converted to correlation times $\tau_{[dg]}$ each epoch by multiplication with the absolute value of the current horizontal vehicle velocity. The β -values of the third-order Gauß-Markov processes are derived from $\tau_{[dg]}$ via $\beta_{[dg]} = 2.903/\tau_{[dg]}$. The numerical values of the empirical parameters, visualized by the black curves, are listed inside the caption of Figs. 4.20 and can also be found in Table 4.9.



(a) Autocorrelation of the GGMplus vertical deflection η .

(b) Autocorrelation of the GGMplus vertical deflection ξ .



(c) Autocorrelation of the GGMplus SGD dg .

Figure 4.20: VD and SGD autocorrelations of a complete measurement session (blue) and along the trajectory from south to north (red). The underlying data originates from GGMplus. Also included is a horizontal line at σ^2/e to determine the correlation distances and an empirical "intermediate" third-order Gauß-Markov model. The variance σ^2 and the Gauß-Markov β -values of the black curves for η , ξ , and dg are: $\sigma^2 = 5.33(")^2$; $1.61(")^2$; 69.83 mGal^2 and $\beta = \frac{2.903}{2.8} \text{ km}^{-1}$; $\frac{2.903}{2.6} \text{ km}^{-1}$; $\frac{2.903}{4.3} \text{ km}^{-1}$

4.3.2 Campaign database

The campaign processing and its evaluation comprise several measured as well as modeled data sets. For the measurements, the author drove along the defined trajectory three times in both directions, on two different days. The goal was to avoid large acceleration spikes and to drive as slow as possible without interfering with the traffic to increase the spatial resolution of the gravity estimates. Velocity

mostly remained between $\sim 15 \text{ km h}^{-1}$ to $\sim 50 \text{ km h}^{-1}$ with spikes of up to $\sim 70 \text{ km h}^{-1}$. The first day (November 11, 2019, Run 1), GNSS and RQH data were collected while relative gravity measurements were conducted in parallel on 15 selected points. On this day, a part of the trajectory was inaccessible (just north of Mittenwald). For this reason, a steep and curvy detour had to be driven. On the second day (December 5, 2019), the trajectory was measured twice (Run 2 and 3) with the GNSS equipment and the RQH on board, without detour. No relative gravity data were collected on that day. While Run 2 was executed with a minimum of standstill phases, during Run 3, the car was stopped at (or close by) most of the relative gravity spots from Run 1. This strategy should reveal the benefits of stopovers for gravity determination. VDs have not been observed during these two days, instead, the VDs determined by Hirt and Flury (2008) are used in the following. Additionally, modeled gravity disturbances play an important role for an improved gravity determination with the EKF/RTS routine and also for the assessment of the final results. The following pages provide a closer look at the various data sets.

iMAR iNAV-RQH When recording, the RQH is mounted in the trunk of the institute’s car at a defined position, where the lever arm w.r.t. the GNSS antenna on the roof is well known. Its X axis points in front direction, its Y axis to the left side, and the Z axis is directed upwards. The raw RQH accelerations and angular velocities are conducted with a frequency of 500 Hz. For Run 2, the accelerometer and gyroscope observations are shown in Figs. A.1, to introduce the reader to the original signal from which the final gravity disturbance is extracted.

Figure 4.21 presents the temperature curve of the three temperature sensors inside the RQH for the three runs. These are important for the application of the temperature calibration parameters determined by the strapdown rotation test from Ch. 4.2.3, which relies on this input information. The RQH was already switched on in the morning at TUM, around 3 h before the measurement in the Estergebirge started, to warm up as long as possible, and thus to keep the temperature spectrum of the sensors small. The temperatures remain between $30 \text{ }^\circ\text{C}$ and $40 \text{ }^\circ\text{C}$, and show a different behavior during the two days of observation. The temperature of Run 1 imitates a sine wave, while Run 2 and 3 are constantly increasing (except right after the measurement start). During Run 1, the car doors had to be opened several times for the CG-5 measurements, which led to a lower inner car temperature due to the low outer temperature in the morning. Lastly, the temperature sensors (T1, T2, and T3) show systematic offsets. The temperature differences arise from their individual location inside the RQH. When applying the temperature calibration parameters of the strapdown rotation test (Ch. 4.2.3), the T1 sensor provides the reference temperature. T1 was chosen randomly since the author does not know the exact position of the temperature sensors inside the RQH.

As a side note, Fig. 4.21 also depicts the duration of the three runs. Run 1 took about double the time of the other runs due to the parallel CG-5 measurements. Moreover, it can be seen that Run 3 in yellow followed closely after Run 2 in red.

Septentrio AsteRx-U The positioning is based on a DGNSS processing solution, meaning an evaluation of a rover and base station constellation as summarized in Ch. 2.2. The rover setup consists of the Septentrio AsteRx-U receiver in combination with a Javad GrAnt-G3 antenna mounted in and on the institute’s car, respectively. The base station was realized with a Leica Viva GNSS GS15 receiver, which was placed in the middle area of the trajectory ($\sim 47.48^\circ \text{ N}$). A measurement rate of 10 Hz was chosen to achieve an improved mapping of the strong dynamics, compared to a 1 Hz solution. Both receivers are able to track GPS, GLO, GAL, and BDS satellites on multiple frequencies. The DGNSS processing was realized by a commercial software called Inertial Explorer from NovAtel in the version 8.70.8722. The cut-off angle is set to only 5° , to increase the number of available satellites along the trajectory, especially in urban and tree-covered sections. Overall, the GNSS coverage is better than expected. During Run 2, e.g., a complete signal loss occurred 84 times with a maximum length of

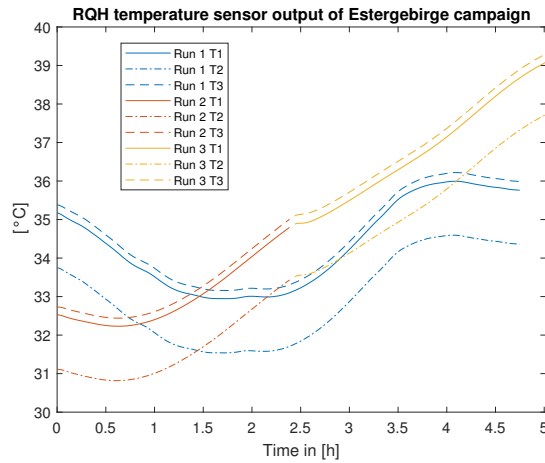


Figure 4.21: RQH temperature sensor outputs during the three runs in the Estergebirge.

7.4 s for a single loss. All signal outages together add up to a duration of 148.7 s (out of 2.5 h) where positioning was not possible. Hereby, GAL, and BDS satellites play a critical role for the increase of visible satellites and thus for the success of the campaign. The maximum number of used satellites is limited to 24 by Inertial Explorer, as can be seen in Fig. 4.22(a) where the blue dots represent the number of all satellites (GPS, GLO, GAL, and BDS) used for positioning. The red curve in this figure represents the mean amount of used satellites over 10 s intervals and illustrates their high short-term variability during the drive. Figure 4.22(b) includes the Positional Dilution of Precision (PDOP) values of each position solution. The PDOP is a quality grade for the satellite-receiver geometry. A small PDOP value thus corresponds to minor scattering around the estimated 3D-position. ~90 % of the time, the PDOP is smaller than three. A comparison with Fig. 4.22(a) (naturally) reveals a negative correlation between the two quantities. Lastly, Table 4.6 presents a summary of the accuracy estimation of Inertial Explorer for the 3D-positions. More than 75 % of the positions are estimated with a standard deviation below $\pm 2/\pm 5$ cm for the horizontal/vertical component(s). The larger standard deviations are spread over the whole trajectory except for sections with excellent sky-visibility (not shown).

Component	$ \sigma < 0.02$ m	$ \sigma > 0.02$ m & < 0.05 m	$ \sigma > 0.05$ m & < 0.1 m	$ \sigma > 0.1$ m
Longitude	76.7 %	17.6 %	2.9 %	2.8 %
Latitude	77.9 %	16.7 %	2.3 %	3.1 %
Height	7.4 %	71.4 %	12.9 %	8.3 %

Table 4.6: Classification of Inertial Explorer standard deviations (σ) for each component of the GNSS positions of Run 2.

Scintrex CG-3 & CG-5 Two absolute gravity data sets are available at the IAPG, which partly include the trajectory. They were gathered in the years 2005 (by M. Schmeer and J. Flury) and 2014 (see Stoll (2014)) with the Scintrex CG-3. Unfortunately, these existing gravity values did not cover the whole trajectory. Consequently, 15 points were chosen to be recorded with the Scintrex CG-5 within the terrestrial 3D-gravity profiling campaign. These observations should not only cover

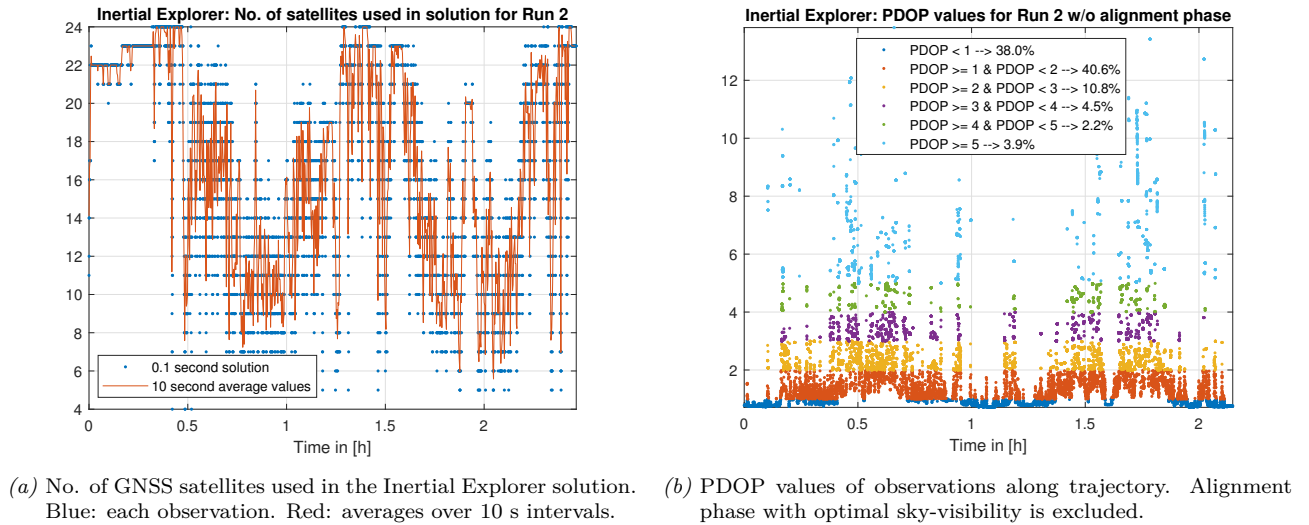


Figure 4.22: Inertial Explorer output: number of GNSS satellites used in solution and PDOP for Run 2.

the whole trajectory but were also selected with a proper spacing of ~ 1.5 km for an evaluation of how frequent gravity updates are needed for accurate profiling results. Most of these points coincide with points from earlier campaigns, either VD-only-, gravity-only-, or 3D-gravity-points. The 2019 observations are not only meant for EKF gravity updates, they also help to assess the profiling results of the SGD, together with 2005 and 2014 data sets. The gravity points, which are integrated in this work, are located within a few meters of the trajectory and are shown in Fig. 4.23 (together with VD observation points from 2005). The corresponding SGD values are visualized in Fig. 4.24(c). The geodetic coordinates can be found in Table 4.7, Table A.1, and Table A.2, including the absolute gravity values.

For comparison and validation of the three mentioned data sets, eight differences of the SGD can be formed with measurements on identical points (see bold entries in Tables 4.7, A.1, and A.2). A maximum discrepancy of 0.085 mGal was observed. Keeping in mind that in 2019 the measurements were performed in a short amount of time (overall ~ 5 min) immediately after stopping the car and that CG-5 leveling and air pressure are not considered (see below), the differences are acceptable and still below the expected accuracies achievable with the RQH. With this performance, it can be stated that the campaign's concept with parallel CG-5 measurements is viable.

Concerning the 2019 data, the official Federal Agency for Cartography and Geodesy (BKG) gravity tie point on the floor of the cellar of the IAPG is chosen as absolute gravity reference for the relative CG-5 measurements. It is named "München 18-4" and the absolute gravity is $9.807\,254\,87\text{ m s}^{-2}$. The absolute value is transferred to the CG-5 "parking slot", where the CG-5 is placed when it is not actively used. It is the point where relative gravity campaigns start. The two points are about 2 m apart horizontally with a height difference of 96.8 cm, which leads to a decrease in gravity of 0.247 mGal. Note that the air pressure is not considered in the whole RQH gravity processing.

Starting from the "parking slot" in Munich, CG-5 measurements were performed on or close to VD/gravity observation spots from earlier campaigns. They were realized in such a way that the car stopped at the defined positions during Run 1. While the RQH and GNSS equipment kept on recording, the gravity measurement was conducted either above an old measurement mark or close to the car if the old mark was not detectable. Precise (static) GNSS coordinates were not determined for these points to save time. Instead, the GNSS position of the antenna on the roof of the car is used. Moreover, due to the limited sensitivity of the RQH, air pressure and CG-5 height variations from

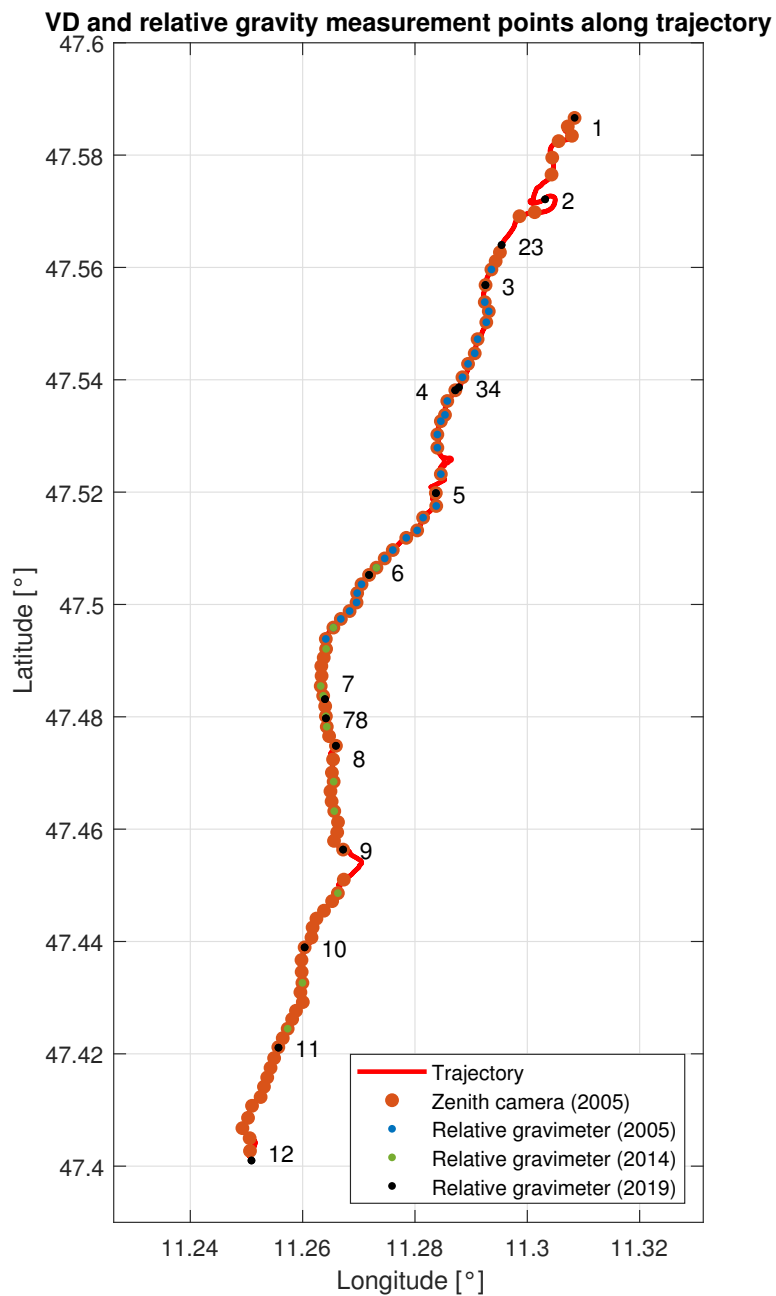


Figure 4.23: Gravimetric and astrogeodetic observation points along the trajectory (red). Orange: VD observation points from 2005. Blue, green, and black: Relative gravimeter observation points from 2005, 2014, and 2019, respectively.

the instrument leveling were not recorded. Tidal effects are removed internally by the CG-5. The last measurement took place in Munich on the "parking slot", to rule out an erroneous behavior of the CG-5. The difference between the measurement in the morning and the evening was 0.026 mGal. This is a reasonable value considering measurement noise, air pressure variation plus instrument leveling, and an internal drift. A correction due to this difference was not applied to the observations.

In the post-processing, the CG-5 observations are all geo-referenced to ellipsoidal coordinates on the ground either directly via point coordinates from earlier campaigns or via the measured GNSS position by subtracting the antenna height above ground, which was determined before (constant value: 2.12 m). The gravity values do not have to be reduced in this case, because the author assumes a constant CG-5 height above ground, also above the reference point in Munich. The error introduced by this approach arises from the different gravity gradients above each point and the height variation of the leveling process. A difference of 0.1 mGal m^{-1} in the gradients above two points leads to an error of 0.0265 mGal, using a constant CG-5 height of 0.265 m, as defined by the author. The height variation can be assumed to be smaller than 10 cm in reality, which corresponds to an error of 0.0309 mGal (using the free-air gradient of $-0.3086 \text{ mGal m}^{-1}$). Both values are far below the expected accuracies for the estimated gravity disturbance vector.

In the EKF, a gravity update is performed w.r.t. the RQH, located in the trunk of the car, about 63 cm above the ground. Therefore, the reference value is continued upward by applying the free-air gravity gradient. Overall, the gravity update accuracies are estimated with a constant measurement uncertainty of $\pm 0.1 \text{ mGal}$ and a distance-related part of maximal $\pm 0.5 \text{ mGal}$ at a horizontal distance of 25 m, linearly scaled. The second term is based on a gradient analysis along the trajectory with a maximum value of 20 mGal km^{-1} . Beyond 25 m, no update is executed inside the EKF.

QDaedalus - simulated The QDaedalus zenith camera was chosen as part of the terrestrial 3D-gravity profiling equipment due to its compactness and performance (cf. Ch. 4.1). However, the author did not collect any VD data along the trajectory in the Estergebirge, because there is a dense data set available from Hirt and Flury (2008), which was observed with a more accurate zenith camera. It originates from measurements with the TZK2-D DZCS zenith camera collected during a 4-week-period in autumn 2005 and is defined according to Helmert. It includes 103 points along the trajectory with an average spacing of 230 m and an angular accuracy level $< 0.1''$. The VD locations and the VD values between points No. 1 and 12 are visualized in Figs. 4.23 and 4.24, respectively. The data optimally suit to find a reasonable spacing between gravity updates for the EKF and are therefore used to simulate QDaedalus measurements. This is simply realized by increasing the standard deviation of the VD updates inside the EKF from $\pm 0.1''$ to $\pm 0.25''$, plus a distance related part of maximal $\pm 0.1''$ at a horizontal distance of 25 m, linearly scaled. The second term is based on a gradient analysis along the trajectory with a maximum value of $5'' \text{ km}^{-1}$. It is noted that only ten observed VDs and two predicted VDs (No. 7 and 12, see next paragraph) are selected as possible EKF updates, cf. Table 4.7. The remaining VDs, which are not forwarded to the EKF, help to assess the quality of the profiling results.

Modeled 3D-gravity The last database component is modeled 3D-gravity information along the trajectory. It is utilized inside the processing for a gravity reduction step and/or for the quality assessment/comparison of/with the final 3D-gravity profiling results. Moreover, two predicted VDs come into play as EKF updates.

Three modeled data sets are used: 1) "Predicted" represents modeled 3D-gravity information based on the local Estergebirge observations, 2) "bkg2016g" describes VDs and SGDs based on an official German gravimetric quasigeoid model, and 3) "GGMplus" VDs and SGDs originate from a (nearly) global gravity model, see also Ch. 4.1. In Figs. 4.24, all data sets are presented (based on Run 2).

No.	Geodetic latitude [°]	Geodetic longitude [°]	Ellipsoidal height [m]	East-West VD η ["]	North-South VD ξ ["]	Absolute gravity [$\frac{m}{s^2}$]
1	47.58663595	11.30842180	850.13	6.301	12.785	9.80585078
2	47.57213045	11.30317075	869.30	5.486	13.941	9.80579608
23	47.56399828	11.29541839	858.16	n.a.	n.a.	9.80579625
3	47.55686725	11.29253405	868.23	3.611	13.994	9.80578141
34	47.53864233	11.28782353	912.87	n.a.	n.a.	9.80568201
4	47.53813115	11.28716555	917.46	2.699	12.471	9.80567321
5	47.51981950	11.28373108	914.03	1.785	10.814	9.80557633
6	47.50525690	11.27182360	926.31	0.241	11.884	9.80552313
7	47.48314420	11.26397666	1024.08	-0.964	13.515	9.80529366
78	47.47972780	11.26414371	1039.36	n.a.	n.a.	9.80525659
8	47.47484370	11.26592630	1027.02	-0.801	13.736	9.80529035
9	47.45636110	11.26720430	998.79	-1.113	13.735	9.80532050
10	47.43895510	11.26035440	962.80	-1.409	12.905	9.80529304
11	47.42109501	11.25569722	977.61	0.972	11.726	9.80517154
12	47.40100460	11.25088841	989.69	5.084	12.282	9.80510039

Table 4.7: VDs and absolute gravity values based on the measurements that were performed in 2005 and on November 7, 2019. The standard deviation of the VDs is set to $\pm 0.25''$ and those of the absolute gravity values are empirically estimated with ± 0.1 mGal. Bold: Identical points of 2005 and/or 2014. Note: No. 7 and 12 got assigned with predicted VDs.

The predicted data is supposed to be the most accurate data set, apart from the static observations, and fulfills two tasks. Firstly, it is added to the figures to have a more continuous visual coverage of the gravity disturbance signal along latitude. Secondly, two predicted VDs are forwarded to the EKF as QDaedalus updates. This is the case for points 7 and 12 in Table 4.7. During Run 1, no VD point mark from 2005 was found there. However, the algorithm needs to have VD update values at these points because the survey starts at No. 7 (initial value needed), and No. 12 is an important update location at the turning point of the trajectory.

The predicted VDs and SGDs were calculated by Prof. Dr. Jakob Flury in a RCR manner with the help of the gravity data of the Estergebirge. In a first step, this method calculates topographic gravity effects for existing, surrounding gravity data points and the ones which should be predicted, see Flury (2002, Ch. 6). Then, the topographic effect is reduced from the observed values together with normal gravity. The remaining signal is interpolated onto the point locations, where gravity should be predicted. In the last step, the topographic effect and normal gravity are added to all points again. The accuracy of the method is in the sub-mGal range (intern communication), which could be proved by the CG-5 measurements⁴⁸. The differences between the vertical components of measured and predicted values are mostly below 0.2 - 0.3 mGal and reach a maximum value of 0.6 mGal. The VD standard deviations of point 7 and 12 are set to $\pm 0.25''$ for the EKF update, which equals a standard deviation of $\sim \pm 1.25$ mGal. The VDs are supposed to be defined according to Helmert.

⁴⁸An approval is not possible for the VDs because no independent data set is available.

GGMplus (Hirt et al., 2013) gravity functionals are used for a visual and numerical comparison of the final results, and it helps to specify gravity more precisely inside the strapdown navigation algorithm, see Eq. (3.2). By removing the GGMplus signal from the specific force, the remaining gravity signal, which is estimated inside the EKF as a third-order Gauß-Markov model, fits a stochastic process more properly since a large portion of systematic effects are reduced by GGMplus. Consequently, the estimation process gets more robust. For this application, the accuracy of the GGMplus data is of minor interest, since the EKF/RTS is supposed to improve the GGMplus values anyhow. Actually, the GGMplus and RQH observations benefit from each other in different frequency bands. The RQH detects long-wavelength deficiencies in the topographic density model of GGMplus while GGMplus provides high-frequency signal from topography to the RQH estimates.

GGMplus is selected for the gravity reduction since it provides nearly global coverage, and VDs (in Helmert's definition) as well as SGDs from GGMplus are freely available at <http://ddfe.curtin.edu.au/models/GGMplus/>. Thus, the approach of this work is not limited to the Estergebirge. As already introduced in Ch. 4.1, GGMplus is a composite gravity model that relies on satellite data (GRACE, GOCE), EGM2008 (Pavlis et al. (2012), Pavlis et al. (2013)), terrestrial gravity information at spatial scales of $\sim 10\,000$ km to ~ 10 km and topography-implied gravity values at spatial scales of ~ 10 km to ~ 200 m. The SGD is defined as the radial derivative of the disturbing potential, which leads to a slight inconsistency w.r.t. the terrestrial 3D-gravity profiling results, where the SGD resembles the difference between \mathbf{g} and $\boldsymbol{\gamma}$ along the normal on the ellipsoid in the same point⁴⁹.

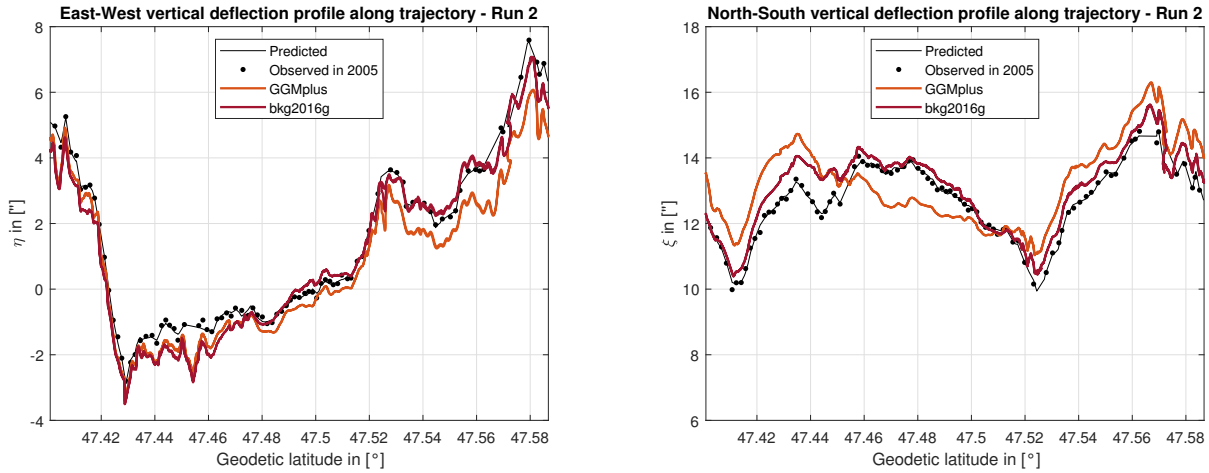
The VDs (Helmert definition) and SGDs called bkg2016g were provided by Dr.-Ing. Joachim Schwabe from the BKG. The data is derived from the same BKG-internal model on which the bkg2016g-height anomalies are based on (described in Schirmer et al. (2018, Ch. IV, 11.3.1 - 11.3.8)). It incorporates local gravity data, the digital terrain model DGM25 of the BKG, and the EIGEN-6C4 (Förste et al. (2014)) global gravity field model. Formally propagated errors were attached with ranges between 0.5 - 0.8 mGal and 0.08 - 0.13". These bkg2016g VDs and SGDs are included for a visual and numerical assessment of the 3D-gravity profiling results.

4.3.3 Gravity extraction

The result of separating the specific force into the gravity components and kinematic accelerations (and errors) with the algorithm described in Ch. 3 is assessed in this section. For a reliable and precise extraction of the gravity components an appropriate adjustment of the noise characteristics of each error-state component inside the EKF is vital. The reader is referred to Ch. 2.2.1.2 for a detailed view on the RQH performance, described by Allan deviations and correlation times. The correlation times of the gravity disturbance along the trajectory are addressed in Ch. 4.3.1. The quality of the resulting gravity estimation also relies on the proper incorporation/compensation of systematic effects like e.g., lever arm details or temperature-induced variations (see Chs. 2.2 and 4.2.3), etc.

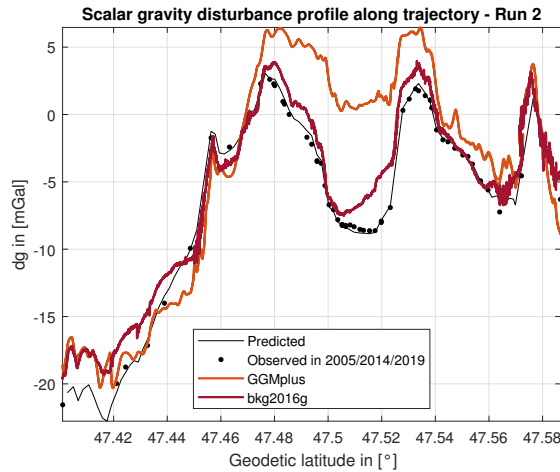
Before the 3D-gravity profiles are presented, the author elucidates how the accuracy assessment of the profiles is approached. Then, efforts made to acquire the final profiles are illustrated step-by-step to better understand the system's behavior on certain changes. The last part tackles possible bottlenecks, critical, and uncritical components w.r.t. the accuracy of the VDs and SGDs determined with the RQH.

⁴⁹spherical vs. ellipsoidal



(a) η profiles along the trajectory. Maximum gradient based on VD observations: $5'' \text{ km}^{-1}$.

(b) ξ profile along the trajectory. Maximum gradient based on VD observations: $5'' \text{ km}^{-1}$.



(c) dg profiles along the trajectory. Maximum gradient based on predicted data set: 20 mGal km^{-1} .

Figure 4.24: Modeled and observed 3D-gravity profiles along the trajectory (based on Run 2 in both directions). The observed values originate from the 2005 campaign for the VDs in (a) and (b) and from the 2005, 2014, and 2019 relative gravity measurements for the scalar component in (c). With the help of the 103 VD observations and the predicted SGDs, approximate maximum gradients for η , ξ , and dg were determined and added to the captions. Based on these values the EKF update standard deviations are linearly increased by 0 - 0.1'' or 0 - 0.5 mGal when the horizontal distance between the GNSS antenna and the update point is 0 - 25 m. Above 25 m no update is initiated.

4.3.3.1 Accuracy assessment The accuracy assessment of the 3D-gravity profiling results is realized with the help of 90 VDs observed in 2005 and with 50 relative gravity measurements conducted in 2005, 2014, and 2019, which serve as a reference. All these data sets are described in Ch. 4.3.2. At some points, relative gravity measurements were observed more than once, which helped to evaluate the consistency of the three data sets. In these cases, the most recent observation is chosen as a reference. The GGMplus and the bkg2016g solutions are also evaluated against these data sets. The reference points are selected under two criteria. Firstly, the points must not be used as EKF updates during the processing. At this point, it is stated that the analysis concerning an optimal spacing between update measurements revealed that three update points (No. 1, 7, and 12) suffice for accurate gravity profiles. In other words, the effort to provide reference data below 10 - 15 km intervals is not justified with regard to an accuracy improvement, at least for time-consuming VD observations. Secondly, the points have to be located close to the trajectory, which is verified during the evaluation and might lead to a slightly lower number of reference points used in the assessment, depending on the driven trajectory. The distance criterion between a reference point and the trajectory is set to <25 m.

The accuracy of each component is expressed as the RMS value⁵⁰ of the differences between each reference value and the closest 3D-gravity profiling/model value. The GGMplus and bkg2016g were calculated with high temporal/spatial resolution along the trajectory. Thus, the distance between the reference points and the closest model points are mostly rather small, compared to the 3D-gravity profiling results. As described in Ch. 3.2, the latter are averages over 0.001° -latitude-intervals, which translates to a spatial resolution of ~ 111 m. The author decided to linearly interpolate the 3D-gravity profiling results along latitude (longitude not considered⁵¹) onto the original GNSS-based latitudes along the trajectory, to obtain values close to the reference points. To avoid an over-weighting of differences in sections with dense reference value coverage in the RMS calculation, especially for the SGD (see Fig. 4.23 or Fig. 4.24(c)), the differences are averaged over 0.01° -sections afterward, resulting in 19 sections between 47.40° N and 47.59° N.

Some clarifications are added concerning the significance of the RMS error. First of all, the reference data are attributed with standard deviations of at least a magnitude two below the terrestrial 3D-gravity profiling results. VDs were determined with the accurate ($<\pm 0.1''$) zenith camera TZK2-D DZCS and the 2005, 2014, and 2019 Scintrex observations agreed to $<\pm 0.1$ mGal. Moreover, it can be stated that all data is consistently defined w.r.t. the GRS80 and, in the case of VDs, according to Helmert's definition. On the other hand, the measurement concept of terrestrial 3D-gravity profiling does not allow to drive exactly above each of the reference points. A simple gradient analysis revealed maximum changes of $\pm 0.1''$ and ± 0.5 mGal over 25 m along the trajectory, which are considered inside the EKF. Additionally, the reference data of the scalar component is not equally distributed. Only 15 (Run 1 with detour)/16 (Run 2 and 3) 0.01° -sections out of 19 provide reference values. And lastly, tides are not considered in the processing of the 3D-gravity profiles, since this effect only marginally changes the direction of the physical plumb line and the magnitude of gravity w.r.t. the accuracies achievable by terrestrial 3D-gravity profiling ($0.01 - 0.02''$ and $0.1 - 0.2$ mGal, respectively, cf. Torge and Müller (2012)).

To get more confidence in the upcoming RMS error evaluation, the author adds the RMS errors of constant, mean 3D-gravity profiles along the trajectory. Clearly, such curves contain no information about the profiles' variation, but would still reach reasonable RMS errors of $2.84''/1.15''$ and 5.95 mGal, see Table 4.8.

Note, another valuable precision indicator is the comparison between the results of two single runs. Due to the detour in Run 1, such a comparison only makes sense for Run 2 and Run 3. Values are provided for the final single Run solutions (cf. Figs. 4.27(b), (d), and (f)).

⁵⁰These values are called RMS error from now on.

⁵¹This approach is only applicable due to the strong north-south orientation of the trajectory.

4.3.3.2 3D-gravity disturbance profiles Before diving into the outcome of the campaign, it is stated that, if not specified otherwise, for the following results only three update points are used, namely No. 1, 7, and 12 from Fig. 4.23 and Table 4.7. In the following figures, these update points are located leftmost, rightmost, and at around 47.483° N, but they are not shown, since these update points are not used for the RMS error calculation.

Starting from the initial RTS solution, this section treats the effect of single adjustments inside the processing chain onto the final 3D-gravity profile quality. The RMS errors of the profiles after each adjustment are listed in Tables 4.12 and 4.13. Table 4.12 contains the results, when no gravity reduction is applied, Table 4.13 those when GGMplus is reduced during the processing. Moreover, each table includes two sections to separate the results gained with and without applying the temperature calibration parameters obtained in Ch. 4.2.3. Each row of the tables represents a certain system noise matrix (\mathbf{Q}) setup and includes the RMS errors for the three runs as well as for the combination of Run 2 and 3. The \mathbf{Q} -matrix column is assigned to Tables 4.9 (\bullet), 4.10 ($\bullet\bullet$), and 4.11 ($\bullet\bullet\bullet$). Selected solutions are visualized, too. All plots illustrate the predicted data set as visual support as well as the reference observations used for the RMS calculation, both in black color. The results of the three runs are presented in blue (Run 1), red (Run 2), and yellow (Run 3). For Run 1, two black vertical lines are added to each figure, which mark the section of the detour in between⁵².

Beforehand, Table 4.8 lists the RMS errors obtained from fictive constant signals, GGMplus, and bkg2016g. The constant signals are defined as the mean η , ξ and dg values of Run 2 presented in Figs. 4.27(b), (d), and (f). The table shows that bkg2016g performs best, while the GGMplus values are at least 50 % larger. Although the constant signals are the worst solution containing no information about the signal variation, the RMS errors of ξ and dg are not far off from GGMplus, along this trajectory.

Model	RMS of η in ["]	RMS of ξ in ["]	RMS of dg in [mGal]
Constant signal	2.84	1.15	5.95
GGMplus	0.78	1.03	4.71
bkg2016g	0.50	0.46	1.60

Table 4.8: RMS errors of fictive constant profiles, GGMplus profiles, and bkg2016g profiles.

Initial RTS solution and refinement At first, the basic solution of the VDs and the SGD is analyzed. The standard error covariance matrix \mathbf{P} (listed for the sake of completeness) and the initial \mathbf{Q} -matrix are defined in Table 4.9. \mathbf{Q} is based on empirical values and on Gauß-Markov parameters determined in Ch. 4.3.1. $v_{[hor]}$ represents the absolute horizontal velocity (in the n-frame) of the vehicle in m s^{-1} and transforms the inverse correlation length ($\beta_{[dg]}$) of the third-order Gauß-Markov processes into the inverse correlation time.

The left-hand figures in Figs. 4.25 present the outcome of the RTS smoother, resulting when no gravity reduction and no temperature calibration is applied inside the processing. Depicted are two profiles for each Run, one directed southward, the other directed northward. For the RTS solutions, no RMS errors are provided for the single directions due to the poor performance.

The right side illustrates the refined solution, meaning an averaged solution of both directions of each run according to Ch. 3.2. The corresponding RMS errors are included in Table 4.12.

⁵²Note that the gravity disturbance signal of the detour during Run 1 between the two vertical black lines significantly deviates from the signal of Run 2 and 3.

Error-state component	P -matrix	Q -matrix •
$\delta\varphi, \delta\lambda, \delta h$	2 cm	$0 \text{ cm s}^{-0.5}$
$\delta v_{[E]}^n, \delta v_{[N]}^n, \delta v_{[U]}^n$	10 cm s^{-1}	$0.005 \text{ cm s}^{-1.5}$
$\delta\phi^n, \delta\theta^n, \delta\psi^n$	$1^\circ, 1^\circ, 5^\circ$	$0.2^\circ \text{ h}^{-0.5}$
$\delta b_{[g,X]}, \delta b_{[g,Y]}, \delta b_{[g,Z]}$	$0.001^\circ \text{ h}^{-1}$	$0^\circ \text{ h}^{-1} \text{ s}^{-0.5}$
$\delta b_{[a,X]}, \delta b_{[a,Y]}, \delta b_{[a,Z]}$	30 mGal	$\sqrt{2 \frac{1}{3600} 0.45^2} \text{ mGal s}^{-0.5}$
$\delta dg_{[E]}^n, \delta dg_{[N]}^n, \delta dg_{[U]}^n$	1 mGal , 1 mGal , 0.1 mGal	$0 \text{ mGal s}^{-0.5}$
$\delta \dot{d}g_{[E]}^n, \delta \dot{d}g_{[N]}^n, \delta \dot{d}g_{[U]}^n$	$10 \mu\text{Gal s}^{-1}$	$0 \text{ mGal s}^{-1.5}$
$\delta \ddot{d}g_{[E]}^n, \delta \ddot{d}g_{[N]}^n, \delta \ddot{d}g_{[U]}^n$	$10 \mu\text{Gal s}^{-2}$	$\sqrt{\frac{16}{3} \left(\frac{2.903}{2800} v_{[hor]}\right)^5} 10.98^2 \text{ mGal s}^{-2.5}$, $\sqrt{\frac{16}{3} \left(\frac{2.903}{2600} v_{[hor]}\right)^5} 6.03^2 \text{ mGal s}^{-2.5}$, $\sqrt{\frac{16}{3} \left(\frac{2.903}{4300} v_{[hor]}\right)^5} 8.36^2 \text{ mGal s}^{-2.5}$

Table 4.9: Definition of the square root of the diagonal matrix elements of P and Q . The accelerometer and gyroscope biases are modeled as first-order Gauß-Markov processes, while the gravity disturbance components are modeled as third-order Gauß-Markov processes (see Chs. 2.2.1.2 and 4.3.1). The entries of the latter are based on the autocorrelation analyses in Fig. 4.20.

The VDs in Figs. 4.25 show that the initial settings cause a large variation in the estimated signal. The first thing to mention is that the results differ from Run to Run and depend on the driving direction. Individual dynamics of each drive might be responsible for the deviations of the results. Also interesting to see is that the results of Run 2 look far off in Figs. 4.25(a) and (c) but averaging helps to approximate the reference fairly good for ξ in Fig. 4.25(d) (RMS error of $1.16''$). In contrast, η cannot benefit from averaging (RMS error of $4.76''$).

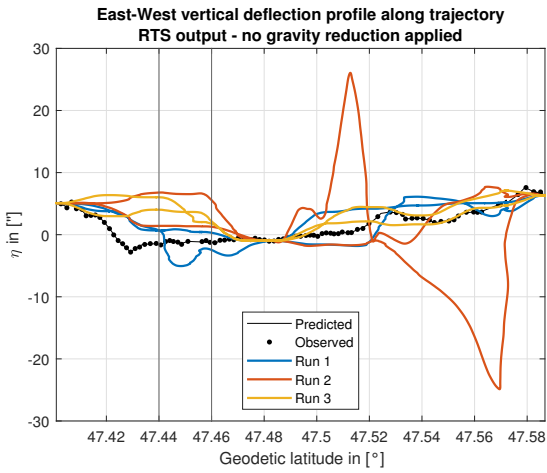
Concerning the SGD in Figs. 4.25(e) and (f), clearly each of the single profiles is dominated by the gravity signal but exhibits a bias in the northern section. In Fig. 4.25(e), single-directed profiles vary by up to 10 mGal. Overall, Run 2 performs best with a RMS error of 3.94 mGal, following the reference data the closest. The three SGD RMS errors (3.94 - 6.13 mGal) already compete with the one of GGMplus (see Table 4.8: 4.71 mGal). In comparison to that, the bkg2016g solution outperforms the others with a RMS error of 1.60 mGal.

Introducing gravity information to the EKF, to reduce the gravity signal, does not lead to large improvements, as can be seen by comparison of the first rows of Tables 4.12 and 4.13. This is no surprise at this point because the signal characteristics of the third-order Gauß-Markov process in $Q \bullet$ do not suit a reduced gravity signal.

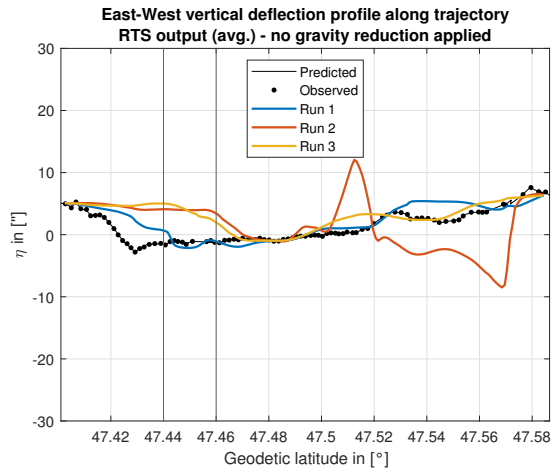
Q -matrix adaption Based on Table 4.9, two consecutive changes of Q -matrix entries are carried out. The first one, defined in Table 4.10, is based on the idea that if the gyroscope performance is underestimated, the EKF tries to improve the attitude by assigning (too large) corrections, which actually degrade the information about the RQH's orientation and thus the quality of the VDs. After adapting the gyroscopes' angle random walk by setting the Q -matrix entries of the attitude noise to a lower value, the EKF shall put more trust in the gyroscopes' output.

Error-state component	Q -matrix ••
$\delta\phi^n, \delta\theta^n, \delta\psi^n$	$0.01^\circ \text{ h}^{-0.5}$

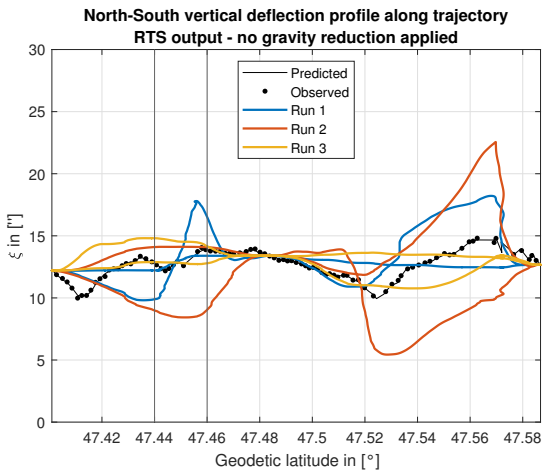
Table 4.10: Redefinition of the square root of the diagonal matrix elements of Q for the attitude.



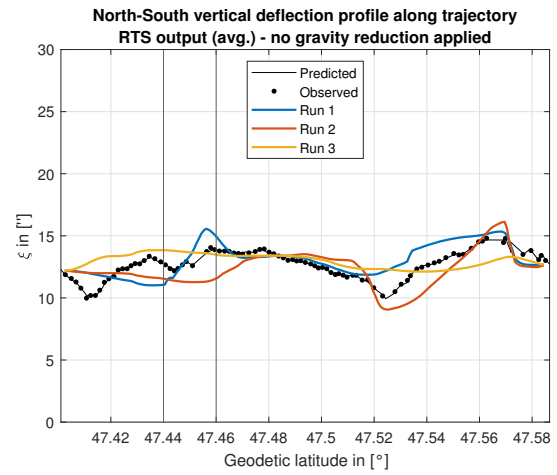
(a) η profiles - RTS smoother output



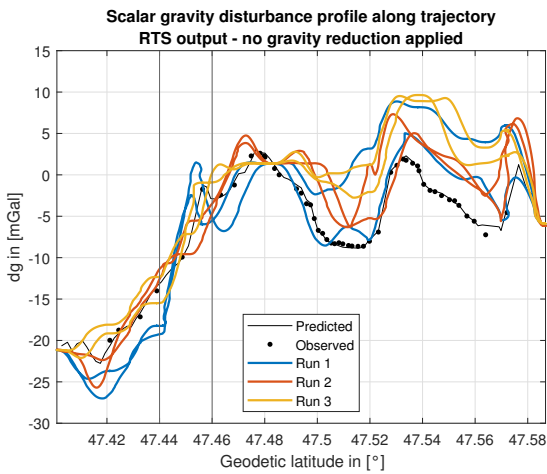
(b) η profiles - RTS smoother output, average of both directions



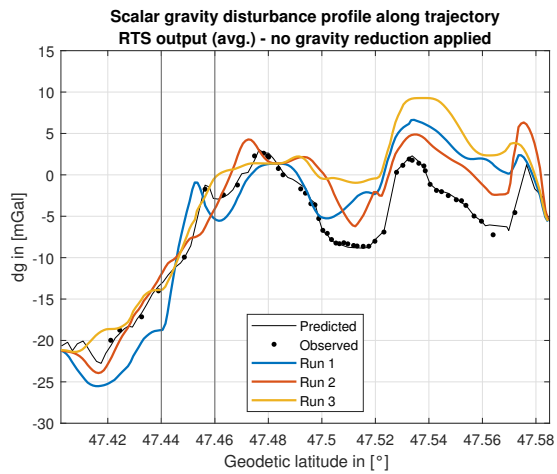
(c) ξ profiles - RTS smoother output



(d) ξ profiles - RTS smoother output, average of both directions



(e) dg profiles - RTS smoother output



(f) dg profiles - RTS smoother output, average of both directions

Figure 4.25: Initial 3D-gravity results of the three runs. On the left side, the RTS smoother output is visualized while on the right side the result after the profile refinement (Ch. 3.2) is depicted. No gravity reduction and no temperature correction were applied during the processing.

The new \mathbf{Q} -matrix clearly has a large impact on the horizontal components in Figs. 4.26(a) and (c). Overall, the RMS errors (second row of Tables 4.12 and 4.13) show that the quality of the estimated VDs improved by this adaption. The η profiles approach the reference fairly well. All RMS errors are below $1''$. Very promising is the consistent correlation of Run 1, 2, and 3 with the feature around 47.53° N in η . Unfortunately, ξ in Fig. 4.26(c) cannot benefit from the adaption the same way. The RMS error of Run 2 significantly increased. It appears that the current estimation misses flexibility and thus wrongly assigns a large portion of the error budget. It seems that the previous deviations in η are just forwarded to ξ here.

Regarding the SGD, the \mathbf{Q} -matrix adaption hardly affects the results as it is less sensitive to minor orientation errors naturally. Only slight improvements of 0.1 - 0.5 mGal in the RMS errors are gained. Still, a gravity reduction inside the EKF cannot significantly decrease the resulting RMS errors.

The next step is to adapt the characterization of the Gauß-Markov processes of the estimated gravity signal, to ensure a realistic behavior of the final profiles. By increasing the correlation distances or downsizing the elements of $\mathbf{B}_{[dg]}$, large short-term variations are not forwarded to the gravity estimates. The new definition is listed in the middle column of Table 4.11. Thereby, each \mathbf{Q} -matrix entry is not (only marginally) changed because $\sigma_{[dg]}$ is adapted accordingly (cf. $\frac{16}{3}\mathbf{B}_{[dg]}^5\sigma_{[dg]}^2$, p. 46). Still, the new $\mathbf{B}_{[dg]}$ influences the error propagation via the system and the transition matrix, see Eq. (3.41).

Error-state component	Q-matrix ●●●	
	w/o gravity reduction	w/ gravity reduction
$\delta\ddot{d}g_{[E]}^n, \delta\ddot{d}g_{[N]}^n, \delta\ddot{d}g_{[U]}^n$	$\sqrt{\frac{16}{3}\left(\frac{2.903}{5000}v_{[hor]}\right)^5 45^2} \text{ mGal s}^{-2.5},$ $\sqrt{\frac{16}{3}\left(\frac{2.903}{7500}v_{[hor]}\right)^5 85^2} \text{ mGal s}^{-2.5},$ $\sqrt{\frac{16}{3}\left(\frac{2.903}{12000}v_{[hor]}\right)^5 110^2} \text{ mGal s}^{-2.5}$	$\sqrt{\frac{16}{3}\left(\frac{2.903}{23224}v_{[hor]}\right)^5 100^2} \text{ mGal s}^{-2.5},$ $\sqrt{\frac{16}{3}\left(\frac{2.903}{23224}v_{[hor]}\right)^5 100^2} \text{ mGal s}^{-2.5},$ $\sqrt{\frac{16}{3}\left(\frac{2.903}{23224}v_{[hor]}\right)^5 100^2} \text{ mGal s}^{-2.5}$

Table 4.11: Redefinition of the square root of the diagonal matrix elements of \mathbf{Q} for the gravity disturbance.

In Figs. 4.26, the outcome without gravity reduction is visualized on the right side. η and dg appear unaffected but the large amplitudes in ξ for Run 2, and also Run 1 in the northern part, decreased. With this adaption, all VD RMS errors reduced to below $1''$.

The right column of Table 4.11 is applied as soon as GGMplus information is forwarded to the EKF during the processing, which is used to reduce the gravity signal upfront. Then, the EKF only estimates the remaining gravity signal that is not included in GGMplus. This signal has a completely different, more stochastic, and long-wavelength nature⁵³ and consequently, the Gauß-Markov parameters have to be adjusted with larger correlation distances.

The 3D-gravity profiles with the gravity reduction in the EKF are not visualized here, since both variants are illustrated next to each other in the following subsection, after applying the temperature calibration⁵⁴. With \mathbf{Q} ●●●, the RMS errors decrease w.r.t. \mathbf{Q} ●● (see Table 4.13, third row). For η the improvements are around $0.4''$, for ξ between $0.01''$ and $3.8''$, and for dg between 0.1 mGal and 0.6 mGal. The RMS errors outperform the solution without gravity reduction significantly, which reveals on the one hand that the updated Gauß-Markov characteristics fit to the residual gravity signals properly and on the other hand that the contribution of the GGMplus model is highly beneficial for 3D-gravity profiling.

⁵³High-frequency signal cannot be detected by the RQH due to the high level of quantization noise and white noise in the higher frequency bands. Thus, only the residual long-wavelength signal is "visible" for the EKF.

⁵⁴From now on, it will be focused more on the results with gravity reduction.

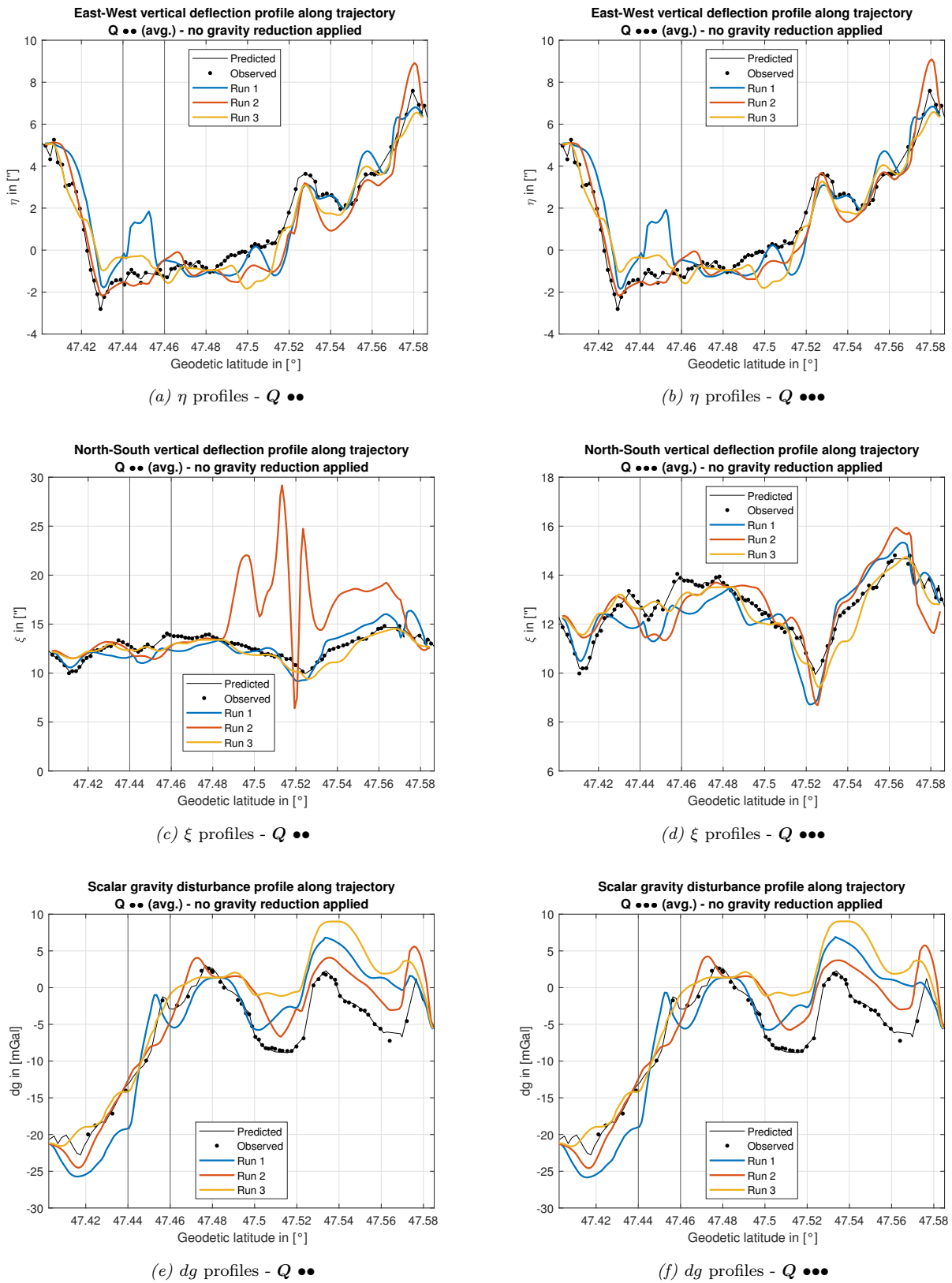


Figure 4.26: 3D-gravity results of the three runs after first (left) and second (right) Q -matrix adaption. No gravity reduction and no temperature correction were applied during the processing.

Temperature calibration A noticeable improvement is achieved for the SGD by applying the temperature calibration parameters of the strapdown rotation test from Ch. 4.2.3 (Savage, 2007), as presented in Figs. 4.27. Here, the reader is also given insight into the effects of the gravity reduction step inside the EKF, when comparing the left figures (no gravity reduction) with the right figures (with gravity reduction). While the long wavelengths are very similar between corresponding curves, the short-wavelength information on the right is contributed by GGMplus.

For Run 2 and 3, the previous bias of the SGD in the northern part diminished after applying the temperature calibration. The RMS errors decreased below 2 mGal. In Run 1, mainly the left side improved. It is not exactly clear, why the profile of Run 1 behaves differently, but it is assumed that the parallel CG-5 measurements are responsible. Firstly, because the measurements extended the run's duration, which led to fewer gravity updates per time. Secondly, several start-stop-maneuvers had to be performed and it is not clear how these dynamics influence the RQH sensor output. Finally, the CG-5 measurements affect the RQH temperature by opening the car doors and thereby cooling down the interior. As already mentioned earlier, the temperature calibrations cannot compensate effects of temperature gradients onto the RQH output.

In contrast to the large impact on the SGD, the horizontal components are hardly affected by the temperature calibration, cf. Fig. 4.26(b), (d) and 4.27(a), (c) or the RMS errors in Tables 4.12 and 4.13, row 3 and 6. Becker (2016, Ch. 8.2.2) made similar observations after applying an accelerometer temperature calibration. This result agrees with his studies on observability and estimability as well as on error propagation. Thereby, it was shown that a RQH attitude error would dominate the VD accuracy. However, the parameters of the strapdown rotation test not only cover the accelerometers but also gyroscope scale factors and cross-couplings. Here, the results in Ch. 4.2.3 could show that both errors are too small to affect 3D-gravimetry (cf. Becker (2016, Table 5.3)).

After this last adaption for single runs, it makes sense to compare the results of Run 2 and 3 (no detour), to evaluate the internal accuracy of the profiles. The agreement of the profiles is expressed in terms of the RMS values of the 0.001° -differences (Ch. 3.2, bullet 1 - 5): $\eta = 0.35''$, $\xi = 0.87''$, and $dg = 1.41$ mGal. The values of η and dg are close to the RMS errors of Table 4.13 in the last row, where the final RMS results are listed. ξ , in comparison, is about 1.1 - 2 times larger, representing larger inconsistencies between two runs than between the single runs and the reference data.

Combination of Run 2 and 3 Eventually, the final solution is created by combining the results of Run 2 and 3 (see Ch. 3.2). Run 1 is deliberately excluded for two reasons. Firstly, the detour is not covered by the other two runs and the alternative route is not representative for a campaign like this. Normally, one would avoid such narrow and steep tracks of the detour. However, it is acknowledged that the sharp gravity disturbance structures of the detour are well detected by the RQH in all three components, see Figs. A.2. Secondly, the conducted CG-5 measurements during Run 1 made it last for double the time of Run 2 and 3, which is assumed to be one of the reasons for the worse quality of the vertical component.

The combination does not necessarily yield the smallest RMS errors for each component in Tables 4.12 and 4.13. But, when no reference data is available to assess the profiles' quality in future campaigns, a robust strategy must be followed to gain gravity data that can be trusted. In this work, it was chosen to call the final solution the one where $\sqrt{RMS(\eta)^2 + RMS(\xi)^2 + RMS(dg)^2}$ is the smallest. Solutions with more accurate single components, e.g., the SGD of Run 2, exhibit a degraded performance in the other components. The final figures (Figs. 4.28) include the terrestrial 3D-gravity profiling results with and without gravity reduction as well as the GGMplus and bkg2016g profiles.

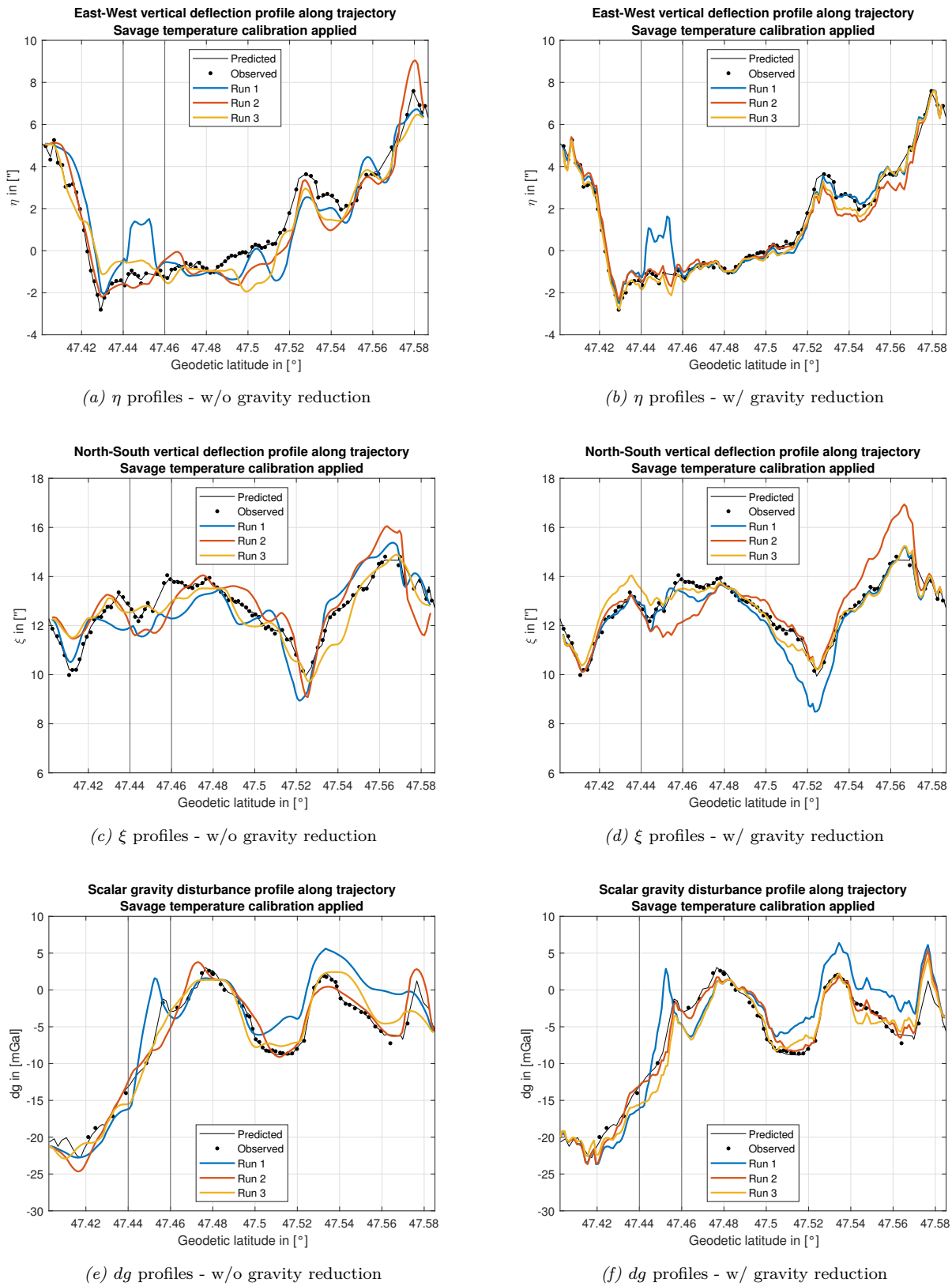


Figure 4.27: 3D-gravity results of the three runs, after applying the temperature calibration parameters (Ch. 4.2.3, Savage (2007)) to the RQH output. On the left side, no gravity reduction was applied during the processing.

The light blue η component in Fig. 4.28(a) shows two sections where it diverges from the reference. The section around 47.50° N offers poor sky-visibility and includes a tunnel below the "Bundesstrasse 2". Around 47.53° N, where also the dark blue profile deviates from the reference, no obvious reason for the degradation can be found. The road is smooth and runs fairly straight, with good sky-visibility. The only thing to mention is that the section includes one of the three mentioned hills. What is interesting to see is that in Fig. 4.27(b) the dark blue η profile of Run 1 is able to capture the structure in this section. The models also exhibit offsets over larger sections such that the final RMS errors are all quite similar, except for the dark blue curve. After introducing GGMplus information to the algorithm, the RMS error shrinks to $0.29''$, which is below the bkg2016g solution by 40 %.

Unfortunately, the 3D-gravity profiling results of ξ are less accurate. The profiles are biased between 47.55° N and 47.57° N and cannot follow the reference around 47.46° N. In this second section, the models also deviate. None of the profiles can map the sharp signal accurately, which coincides with the sharp peak in the ellipsoidal heights in Fig. 4.19(a). The RMS error of $0.44''$ of the dark blue curve is still far below the one of GGMplus and at the same level as bkg2016g.

From the light blue curve in Fig. 4.28(c), it can be concluded that the coarse structure of the SGD is already well captured when GGMplus is not forwarded to the EKF. Due to the RQH performance (see Allan deviation in Ch. 2.2.1.2), the spatial resolution is limited and no fine structures are included in this profile. Consequently, large deviations from the reference appear when sharp signal structures occur, e.g., the smoothed curve between 47.56° N and 47.58° N. The RMS errors give the impression that this solution is as good as the bkg2016g. But, one has to be aware that the two signals contain different frequency content. By forwarding GGMplus information to the EKF, a large portion of the missing high-frequency content is added. It allows the profile to follow the reference more accurately. Consequently, a comparison between the dark blue profile and the one of bkg2016g is more meaningful. Both reach RMS errors around 1.5 - 1.6 mGal.

The last illustration in Figs. 4.28 depicts the residual gravity signal estimated by the EKF/RTS routine when GGMplus is reduced (averaged, then the combination of Run 2 and 3) together with the difference between GGMplus and observed VDs, observed SGDs, and predicted SGDs. It shows the missing signal of GGMplus w.r.t. the reference and how well this remaining signal can be mapped by the RQH. It is no surprise that the high-frequency spectrum of the signal is not registered by the EKF/RTS routine due to the RQH performance. However, the majority of the long-wavelength signal is captured by the EKF/RTS, with only a few biased sections. These residual gravity curves are most probably emerging from deficiencies in the GGMplus mass-density assumption of 2670 kg m^{-3} .

So far, the spatial resolution of the final results was only briefly addressed and is specified here. It depends on whether an external gravity model is integrated for a gravity reduction step or not. If not, the spatial resolution is not precisely quantifiable, because it is depending on the (variable) velocity during the measurements and also on the RTS smoother, which is driven by optimal estimation and not by a specific spatial or temporal smoothing operation. Based on the RQH bias instability, the temporal resolution is around 100 s, which translates to a spatial resolution between 275 m and 2000 m for velocities between 10 km h^{-1} and 70 km h^{-1} (half wavelength). As soon as external gravity information is added, in this case, GGMplus, the spatial resolution is defined by the model (high resolution assumed) and the algorithm actually just estimates the missing gravity information of the model, which is limited to the "high-performance" bandwidth of the RQH accelerometers. For GGMplus, the spatial resolution is ~ 200 m and the missing signal is dominated, as just stated, by unmodeled density anomalies as well as inconsistencies in the underlying topography model.

Table 4.14 provides further statistical information about the 3D-gravity results depicted in Figs. 4.28. The "Min/Max"-values resemble the range of the differences w.r.t. the reference, while "Mean" hints towards a systematic offset in the differences. The RMS errors are repeated from Tables 4.8, 4.12, and 4.13 for convenience.

The numbers confirm that the terrestrial 3D-gravity profiling results can compete with the bkg2016g derived profiles. As already stated, the RMS errors are quite similar, but the mean values of Run 2+3 are below the ones of bkg2016g. In contrast, the bkg2016g "Min/Max"-values manifest a smaller range than Run 2+3.

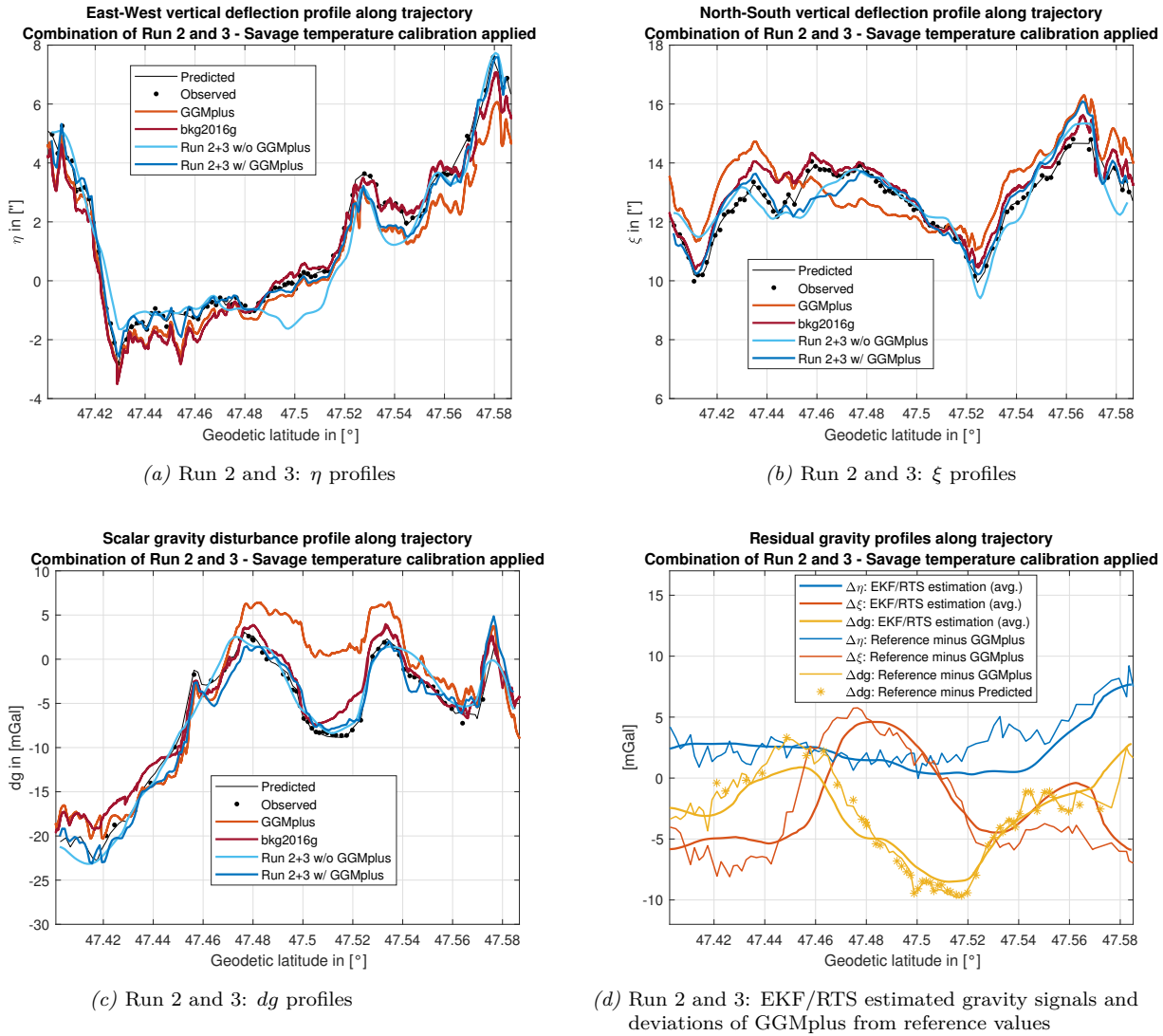


Figure 4.28: 3D-gravity results of the combination of Run 2 and 3 after applying the temperature calibration parameters (Ch. 4.2.3, Savage (2007)) to the RQH output (a-c). Additionally, the EKF/RTS contribution w.r.t. GGMplus is visualized (d).

Run	Q-matrix	RMS of η in ["]	RMS of ξ in ["]	RMS of dg in [mGal]
w/o temperature correction				
1/2/3/2+3	•	1.83/4.76/2.76/3.33	1.13/1.12/1.10/0.81	4.82/3.94/6.13/4.93
1/2/3/2+3	••	0.79/0.83/0.79/0.67	0.95/4.42/0.60/2.09	4.67/3.52/5.91/4.58
1/2/3/2+3	•••	0.78/0.69/0.78/0.58	0.73/0.85/0.58/0.59	4.64/3.57/5.92/4.61
w/ temperature correction				
1/2/3/2+3	•	1.73/4.86/2.69/3.36	1.21/1.23/1.07/0.79	3.78/2.00/1.76/1.71
1/2/3/2+3	••	0.84/0.95/0.85/0.77	0.94/4.57/0.58/2.19	3.57/1.87/1.70/1.60
1/2/3/2+3	•••	0.84/0.78/0.82/0.67	0.73/0.82/0.55/0.57	3.53/1.88/1.70/1.61

Table 4.12: RMS errors for all Runs without the gravity reduction applied in the EKF. The Q -matrix entries correspond to Tables 4.9, 4.10, and 4.11.

Run	Q-matrix	RMS of η in ["]	RMS of ξ in ["]	RMS of dg in [mGal]
w/o temperature correction				
1/2/3/2+3	•	1.30/4.69/1.01/2.69	1.38/1.06/0.84/0.79	4.57/3.74/5.64/4.63
1/2/3/2+3	••	0.64/0.77/0.57/0.56	0.96/4.46/0.46/2.15	4.45/3.24/5.43/4.26
1/2/3/2+3	•••	0.28/0.32/0.24/0.24	0.6/0.77/0.36/0.45	4.30/2.91/4.66/3.75
w/ temperature correction				
1/2/3/2+3	•	1.20/4.79/0.96/2.74	1.44/1.19/0.79/0.80	3.40/1.49/1.35/1.18
1/2/3/2+3	••	0.71/0.87/0.64/0.67	0.93/4.61/0.48/2.25	3.22/1.19/1.33/1.02
1/2/3/2+3	•••	0.24/0.40/0.25/0.29	0.57/0.77/0.35/0.44	3.12/1.33/1.90/1.50

Table 4.13: RMS errors for all Runs with the gravity reduction applied in the EKF. The Q -matrix entries correspond to Tables 4.9, 4.10, and 4.11.

Solution	Min/Max/Mean/RMS of η in ["]	Min/Max/Mean/RMS of ξ in ["]	Min/Max/Mean/RMS of dg in [mGal]
GGMplus	0.25/1.70/0.66/0.78	-1.57/1.13/-0.56/1.03	-9.44/3.29/-3.01/4.71
bkg2016g	-0.29/0.80/0.31/0.50	-1.01/0.01/-0.39/0.46	-2.71/0.89/-1.08/1.60
Run 2+3 w/	-0.20/0.80/0.14/0.29	-0.90/0.96/-0.09/0.44	-3.12/2.56/0.21/1.50
Run 2+3 w/o	-0.98/1.32/0.21/0.67	-1.08/1.07/0.06/0.57	-2.57/4.25/-0.28/1.61

Table 4.14: Statistical summary of the 3D-gravity profiles based on GGMplus, bkg2016g, and the $Q_{\bullet\bullet\bullet}$ temperature corrected solutions of the combination of Run 2 and 3. "w/" and "w/o" signify if a gravity reduction was applied in the EKF or not.

4.3.3.3 Crucial components In this section, further insights into the coherence between certain error sources and the quality of the 3D-gravity profiles are derived. Therefore, a number of errors are introduced to the processing chain. Bottle-necks for 3D-gravity accuracies below $1''/\text{mGal}$ identified through simulations by Becker (2016) (for airborne gravimetry) are verified with regards to the Estergebirge results. The author emphasizes that the current outcome of the refined SGD cannot reach these accuracies yet, which slightly shifts the error margins of Becker (2016, Table 5.3). Moreover, a major difference to airborne campaigns is the possibility to include gravity updates, reducing some of the effects mentioned in Becker (2016). Another goal is to trace back the divergence between the two 3D-gravity profiles when measuring in the opposite direction of the trajectory.

The following manipulations/adaptions are tested with Run 2 of the Estergebirge campaign. The temperature calibration parameters from the strapdown rotation test (Ch. 4.2.3) are applied. The gravity reduction is omitted because it is supposed that an error has a more distinct impact on the full gravity disturbance estimates, due to the more flexible Gauß-Markov parameters (cf. Table 4.11). The resulting RMS errors are listed in Tables 4.15 - 4.23, together with the RMS errors of the standard solution (called "None", meaning that no manipulations were applied).

- **RQH timestamp error:** under nominal conditions, the GNSS receiver provides timing information to the RQH via a PPS in combination with a NMEA message to reference the pulse with an absolute timestamp. The AsteRx-U receiver time offset is limited to ± 0.5 ms w.r.t. GPS time, which is considered unproblematic, but neglects internal delays. As soon as the receiver is unable to forward exact timing information due to signal loss, the time tagging of the RQH is solely based on its internal oscillator. During the Roll and Pitch calibration (Ch. 4.2.2) the RQH oscillator drift was tested and did not exceed $0.3 \mu\text{s s}^{-1}$. Consequently, a timestamp error larger than 2 ms, as assumed critically by Becker (2016), does not need to be expected for GNSS outages below ~ 2 min. The RMS errors in Table 4.15 reveal that even with a constant RQH timestamp offset of 2 ms the RMS errors remain at the same level. Regarding the divergence between the north-to-south and south-to-north solutions, a constant time offset does not result in a uniform, symmetric alteration of the two solutions.

Manipulation	RMS of η in $''$	RMS of ξ in $''$	RMS of dg in [mGal]
None	0.78	0.82	1.88
RQH timestamp -25 ms	1.14	1.25	1.91
RQH timestamp -10 ms	0.79	0.92	1.88
RQH timestamp +2 ms	0.81	0.82	1.88
RQH timestamp +10 ms	0.98	0.86	1.90
RQH timestamp +50 ms	2.40	1.87	2.16

Table 4.15: 3D-gravity profiling RMS errors when adding a constant time offset to the RQH time tags before processing.

- **Initial alignment error:** the coarse alignment with a navigation-grade IMU is sufficiently accurate so that the EKF performs nominally, see tab 4.16.

Manipulation	RMS of η in $''$	RMS of ξ in $''$	RMS of dg in [mGal]
None	0.78	0.82	1.88
Initial alignment error: Roll+2°, pitch +2°, yaw +5°	0.79	0.82	1.88

Table 4.16: 3D-gravity profiling RMS errors when manipulating the Euler angles after the initial alignment.

• **ISA non-orthogonality errors:** the observed effects of introducing errors to the orientation of accelerometer or gyroscope axes are mostly in accordance with Becker (2016, Table 5.3).

Accelerometer cross-couplings are of minor concern provided that the standard manufacturer calibration reduces the cross-couplings down to some tens of arcseconds. Only one RMS error is included in Table 4.17, but all of them were tested.

A $20''$ -misalignment of the accelerometer triad w.r.t. the gyroscope axes in the XZ- and YZ-plane deteriorates the SGD, whereas the VDs degrade only slightly by the same misalignment in the XY-plane. The findings for cross-couplings in the gyroscope axes only partly agree with Becker (2016). As expected, a $20''$ cross-coupling⁵⁵ in $\epsilon_{[XY]}/\epsilon_{[YX]}$ does not affect the scalar component but η degrades strongly. However, Table 4.17 shows that ξ is hardly affected, actually by none of the cross-coupling scenarios. The reason for this result is not quite clear. It might be that the larger accelerations along the Y axis (cf. A.1), which is mostly aligned in east-west direction in this example, cause this error mapping into the η component. Apart from that, the RMS error of the scalar component only increases when X or Y is bent towards the Z axis, not the other way around.

The differences between the two single-directed solutions of Run 2 are not affected.

Manipulation	RMS of η in ["]	RMS of ξ in ["]	RMS of dg in [mGal]
None	0.78	0.82	1.88
Acc. cross-coupling Y towards Z of $20''$	0.78	0.83	1.88
Acc. misalignment XY-plane of $20''$	0.96	0.87	1.87
Acc. misalignment YZ-plane of $20''$	0.80	0.80	2.38
Acc. misalignment ZX-plane of $20''$	0.78	0.82	2.37
Gyr. cross-coupling X towards Y of $20''$	3.55	0.76	1.87
Gyr. cross-coupling Y towards X of $20''$	3.63	0.80	1.86
Gyr. cross-coupling Y towards Z of $20''$	0.80	0.84	2.82
Gyr. cross-coupling Z towards Y of $20''$	0.98	0.87	1.87
Gyr. cross-coupling Z towards X of $20''$	0.78	0.82	1.88
Gyr. cross-coupling X towards Z of $20''$	0.96	0.86	2.33

Table 4.17: 3D-gravity profiling RMS errors after manipulating the ISA geometry. X, Y, and Z represent the RQH b-frame axes pointing in front-, left-, and up-direction.

⁵⁵It is reminded that Ch. 4.2.3 shows gyroscope cross-couplings of the RQH below $10''$ after the manufacturer's calibration.

- **Lever arm error:** a vertical lever arm error in the decimeter range hardly affects the VDs or the SGD in Table 4.18. When determining the SGD only, any lever arm error within the range of several centimeters is of no concern. On the contrary, the VDs are sensitive to errors in the horizontal components of the lever arm.

Apart from that, the differences between the outcomes in the two driving directions showed larger, although not uniform, changes depending on the lever arm error.

Manipulation	RMS of η in ["]	RMS of ξ in ["]	RMS of dg in [mGal]
None	0.78	0.82	1.88
Lever arm X/Y +3.5/+7.5 cm	0.62	1.06	1.89
Lever arm X/Y +10/-10 cm	1.58	1.14	1.92
Lever arm X/Y -10/+10 cm	1.46	0.98	1.85
Lever arm Z -50 cm	0.83	0.81	1.89

Table 4.18: 3D-gravity profiling RMS errors when introducing a wrong lever arm to the algorithm. X, Y, and Z represent the RQH b-frame axes pointing in front-, left-, and up-direction.

- **Gyroscope bias error:** in 2017 an unusual large gyroscope bias of $0.012^\circ \text{ h}^{-1}$ in the Y component was detected during the manufacturer’s calibration. Such a bias in any of the gyroscopes would not degrade the results of terrestrial 3D-gravity profiling. However, IMUs integrating less accurate gyroscopes with a larger bias by the order of one magnitude cannot reach similar RMS errors in the 3D-gravity disturbance estimates. From Table 4.19 it becomes clear that the accuracy requirement for the vertical gyroscope is not as stringent as for the horizontal ones.

The larger biases would influence the differences between the two solutions in opposite direction.

Manipulation	RMS of η in ["]	RMS of ξ in ["]	RMS of dg in [mGal]
None	0.78	0.82	1.88
Gyr. X, Y, Z bias $+0.01^\circ \text{ h}^{-1}$	0.79	0.81	1.88
Gyr. X, Y, Z bias $+0.1^\circ \text{ h}^{-1}$	1.49	1.02	2.27
Gyr. X bias $+1^\circ \text{ h}^{-1}$	7.80	3.38	20.06
Gyr. Z bias $+1^\circ \text{ h}^{-1}$	0.62	1.47	1.88
Gyr. X, Y bias $+1^\circ \text{ h}^{-1}$	7.55	8.69	96.30

Table 4.19: 3D-gravity profiling RMS errors when adding a constant bias to the gyroscope observations. X, Y, and Z represent the RQH b-frame axes pointing in front-, left- and, up-direction.

- **Savage temperature calibration removed:** the final 3D-gravity profiles (Fig. 4.28) can only be reached with the help of the strapdown rotation test in Ch. 4.2.3. Now, the effect of individual temperature calibration parameter types is assessed simply by not applying them. The results in Table 4.20 show that within the temperature range of Run 2 the accelerometer scale factors and non-orthogonalities have the largest influence on the SGD. The increased RMS error due to the non-orthogonality error is in accordance with the values of the accelerometer misalignments from Table 4.17 (cf. Fig. 4.16(f)). The reason why the accelerometer biases do not affect the RMS errors is that firstly, the accelerometer biases are still estimated inside the EKF as part of the error-state vector and secondly, the gravity estimates are not degraded by the residual long-wavelength bias changes due to the repeated gravity updates. As already noted before, the VDs do not noticeably benefit from the calibration.

An effect on the divergence of the single directed profiles cannot be observed.

Manipulation	RMS of η in ["]	RMS of ξ in ["]	RMS of dg in [mGal]
None	0.78	0.81	1.88
Savage w/o acc. biases	0.78	0.82	1.82
Savage w/o acc. non-orthogonalities	0.78	0.82	2.16
Savage w/o acc. scale factors (lin. and asym.)	0.78	0.84	3.36
Savage w/o gyr. cross-couplings	0.72	0.83	1.86
Savage w/o gyr. scale factors	0.78	0.82	1.88

Table 4.20: 3D-gravity profiling RMS errors when single temperature correction parameter types of the strapdown rotation test are not applied to the observations.

• **No ZUPT:** the reason why to apply a ZUPT is clear, in theory. The car's velocity is known with high confidence during these times. But, conducting a ZUPT means that the RQH is exposed to unnecessary dynamics when stopping and re-accelerating the car and it takes longer to drive off a certain distance. Additionally, GNSS observations can provide similar information, although with less confidence. Table 4.21 shows that no clear statement about the benefit of ZUPTs can be made for the Estergebirge campaign. ξ degrades while dg improves⁵⁶. Remember, Run 2 does not include additional standstill phases. For this reason, Run 3 is considered, too, since it comprises planned standstill phases. Consequently, the effect of ZUPTs should be more evident. Neglecting the ZUPTs in Run 3 increases only the VD RMS errors slightly⁵⁷. This outcome does not generally support a strategy that includes additional ZUPTs in terrestrial 3D-gravity profiling campaigns. However, this conclusion is not valid as soon as the GNSS availability is worse than along the trajectory in the Estergebirge. The variation of the single directed profiles remains unaffected.

Adaption	RMS of η in ["]	RMS of ξ in ["]	RMS of dg in [mGal]
None	0.78	0.82	1.88
W/o ZUPT	0.74	0.91	1.45

Table 4.21: 3D-gravity profiling RMS errors when standstill phases are not included as ZUPTs inside the EKF.

• **Accelerometer eccentricity neglected:** a special case for the RQH of the IAPG is that internally the installation offsets of the accelerometers from the b-frame's origin are not applied, see p. 23. Thus, rotational accelerations are coupling into the accelerometer observations. The offsets are about 5 cm in magnitude for the Y and Z sensors and have to be corrected for 3D-gravity profiling, as exemplified by the increased RMS errors in Table 4.22.

Manipulation	RMS of η in ["]	RMS of ξ in ["]	RMS of dg in [mGal]
None	0.78	0.82	1.88
Acc. eccentricity neglected	1.38	1.59	2.19

Table 4.22: 3D-gravity profiling RMS errors without correcting accelerometer observations for the geometric offset w.r.t. the b-frame origin.

⁵⁶For the results with the gravity reduction step, all RMS errors degraded slightly without ZUPTs.

⁵⁷RMS $\eta/\xi/dg$ - None: 0.82"/0.55"/1.70 mGal, w/o ZUPT: 0.93"/0.60"/1.70 mGal

• **Number of gravity ties:** it was mentioned before that three gravity updates suffice for an accurate profile determination for a ~ 23 km trajectory. As can be seen from Table 4.23 in the last row, a real gain in accuracy can only be achieved when updates are available every ~ 2 km. This effort is not justified for the VDs, where only slight improvements are obtained, but additional VD data would need at least two more nights of observing in case of the 23 km trajectory in the Estergebirge. Consequently, for future campaigns, QDaedalus observations can be separated by 10 - 15 km. When it comes to the vertical component, one might consider decreasing the distance between CG-5 measurement points from 10 - 15 km down to 2 km. The additional effort is reasonable, especially because it could be shown that 5 min observations can be trusted to ± 0.1 mGal.

Reducing the number of gravity update points to a single one, which would have to be located at the start/endpoint of the campaign to initialize the EKF, illustrates the importance of additional 3D-gravity observations along the trajectory for the VDs. The large RMS errors indicate that long-wavelength errors couple into VD estimation, which are not removable with a single gravity update point. The RMS of the SGD, in contrast, performs without any loss of accuracy⁵⁸.

Adaption	RMS of η in ["]	RMS of ξ in ["]	RMS of dg in [mGal]
None	0.78	0.82	1.88
Gravity ties: 7	6.13	4.50	1.86
Gravity ties: 1, 4, 7, 10, 12	0.68	0.82	1.89
Gravity ties: 1, 2, 3, 4, 5, 6, 7, 9, 10, 11, 12	0.59	0.68	1.46

Table 4.23: 3D-gravity profiling RMS errors with different amounts of gravity update points along the trajectory.

Unfortunately, the trigger for the differences between the two solutions per run is still an open question. The first possible cause that comes into mind is an attitude error/accelerometer misalignment, which is in general difficult to isolate from the horizontal components of the gravity disturbance, as derived in the observability analysis for airborne gravimetry in Becker (2016). However, in the case of terrestrial 3D-gravity profiling, it is possible to introduce additional information in terms of VD measurements, which solves this problem (except for short-term attitude errors in between the measurements). Another possible cause is the lever arm used in this thesis, which was determined by photogrammetric means and is supposed to be accurate within some centimeters. But as the analysis w.r.t. Table 4.18 showed, there is a correlation with the horizontal gravity components and therefore the lever arm should be verified again, either through geometric measurements or by estimating the lever arm inside the EKF as an additional error-state in combination with special maneuvers during the campaign. Additionally, a possible timestamp error due to internal delays might have an influence. Overall, it can be stated that the effect has to be symmetric w.r.t. the yaw angle since a combination of the two directions yields considerable results. In other words, the deviations have different signs depending on the driving direction. Other significant correlations (velocities, GNSS outages, GNSS statistics, Q -matrix entries, etc.) could not be found.

Apart from that, the Mahalanobis distance could explain some of the larger, non-symmetric deviations between the two solutions along both directions of the three runs. The Mahalanobis distance indicates an incorrect weighting of new observations w.r.t. the estimates. This is the case in a few spots where the sky-visibility is assumed to be poor. Here, probably the standard deviations of the GNSS solution are too optimistic.

⁵⁸Keep in mind that the temperature calibration was applied here.

5 Summary and conclusion

5.1 Summary

With the astrogeodetic campaign in Perth (Western Australia), described in Ch. 4.1 (Schack et al., 2018), for the first time, a digital VD data set in the Southern Hemisphere was established. The practical part of the campaign was realized by two observers with equipment that was transported to Australia via commuter aircraft and that fit into a small car. Observations were conducted during nighttime given cloudless skies. Thereby, 39 sets of VDs were determined with an average spacing of ~ 1 km. Repeated measurements with the QDaedalus system confirmed the VD standard deviation of $\sim \pm 0.2''$ determined by Hauk et al. (2016). For the height anomaly differences, calculated from the astrogeodetic observations, the available stochastic information revealed a standard deviation of $\pm 10 - 15$ mm over the 38 km traverse as a realistic assumption. The global and regional model analyses (AGQG2009, AGQG2017, GGMplus) showed that the models can predict VDs to an accuracy of $\sim 1''$ in flat areas. The transition between low bulk density and high bulk density rock at the Darling Fault is well resolved by QDaedalus, but only hardly visible in AGQG2017 and not observable in the AGQG2009 and GGMplus data. Moreover, the models revealed tilts of 1 mm over ~ 1 km in the height anomaly differences, which are either originating from deficiencies in the coastal zone gravity data or, less probable, from remaining systematic errors in the QDaedalus observations. Another outcome is that the smaller RMS values of the AGQG models in Table 4.1 indicate that the inclusion of local gravity information is beneficial for gravity field modeling in areas of steep geoid gradients and rather flat topography.

The second measurement campaign, described in Ch. 4.2, deals with the temperature calibration of the RQH inertial sensors, which was conducted by iMAR inside the thermal chamber of a two-axis calibration turntable. Initially, the idea was to quantify temperature-induced bias changes in the accelerometer output for different RQH orientations. Therefore, in 2017 an Up and Down calibration (Ch. 4.2.1) was realized, followed by a Roll and Pitch calibration (Ch. 4.2.2). The Up and Down calibration revealed that the estimated temperature-induced accelerometer bias and scale factor variations are relevant for gravimetry at the sub- $''$ /sub-mGal level. Apart from that, large trends in the accelerometer non-orthogonalities with rising temperatures were detected. This outcome indicated a rotation either between the inertial sensor triads, which would probably inhibit high-accuracy gravimetry or between the ISA and the RQH housing, which is less critical for terrestrial applications because VD measurements can compensate such a rotation. Unfortunately, the Roll and Pitch calibration could only confirm the results from the Up and Down calibration but could not provide any further insights into the origin of non-orthogonality changes.

Due to the outcome of these calibrations, in 2019 the Up and Down calibration (Ch. 4.2.1) was repeated to compare the results with 2017. Additionally, a strapdown rotation test (Savage, 2007) was conducted that evaluates accelerometer data in combination with gyroscope data (Ch. 4.2.3). As such, it allows analyzing rotations between the inertial sensor triads and rotations of the ISA w.r.t. the housing, to detect the cause of the non-orthogonality phenomenon. The repeated Up and Down calibration could reveal that even the temperature-induced accelerometer biases, scale factors, and non-orthogonality changes from 2017 to 2019 degrade gravimetric results if they remain uncompensated. Moreover, the non-orthogonality results of 2017 were not reproducible and showed a completely different scenario in 2019. But, with the help of the strapdown rotation test, a rotation between the inertial sensor triads was disproved. Instead, a rotation of the ISA w.r.t. the RQH housing could be made responsible for the non-orthogonality behavior extracted from the Up and Down measurements. This confirms that high-accuracy gravimetric data can be collected with the RQH. However, the temporal behavior of this phenomenon is still an open issue. In contrast, the gyroscope calibration parameters, estimated in the strapdown rotation test, are hardly affected by the temperature.

Lastly, a terrestrial 3D-gravity profiling campaign in the Estergebirge is assessed in Ch. 4.3. The Estergebirge provides a valuable geodetic database for validating such a campaign. Existing VD and absolute gravity values build the foundation for the accuracy assessment of the estimated 3D-gravity profiles obtained from the multi-sensor data fusion described in Chs. 3 and 4.3.3.2. During three measurement runs in 2019 different observation strategies were applied to identify the best way to collect accurate data that subsequently yields decent 3D-gravity results. Thereby, collecting relative gravity data in parallel to the RQH and GNSS observations led to a slightly decreased quality in the final gravity estimates, probably caused by the complex temperature variation from opening the car doors repeatedly.

The final results, which are based on two runs in both directions along the same trajectory, provide VD and SGD profiles with RMS errors of 0.2 - 0.5'' and 1.5 mGal, respectively, w.r.t. accurate reference data. The spatial resolution is equivalent to the resolution of the gravity model used for gravity reduction inside the processing. In this case, the GGMplus is applied with a spatial resolution of ~ 200 m. It could be shown that the major part of the residual long-wavelength signal, which is not included in GGMplus, is estimated by the EKF/RTS algorithm with good conformity. Furthermore, RMS errors reveal that the determined profiles reach a similar or even slightly better accuracy level than those of the bkg2016g model provided by the BKG. This outcome could only be achieved by tuning the system noise matrix, by applying the temperature calibration parameters derived in Ch. 4.2.3, and with the help of the profile refinement (Ch. 3.2). Single-directed runs in opposite direction yield a symmetric deviation in the gravity profiles. They do not reach a similar accuracy as the combined solution. Unfortunately, the origin of the rather large deviations of the single runs could not be determined.

Following this, specific manipulations and adaptations were applied to sensor- and metadata as well as to the software, to analyze the results' sensitivity with regards to these adaptations. It could be shown that the gravity estimates degrade under certain sensor axis non-orthogonalities (accelerometer misalignments and gyroscope non-orthogonalities). An accurate SGD estimate also highly depends on well-known accelerometer scale factors. Both, the non-orthogonalities and scale factors can be determined with the strapdown rotation test introduced in Ch. 4.2.3. Besides, no clear statement about the advantage or disadvantage of ZUPTs can be obtained by in-/excluding ZUPTs from the processing since it did not result in a consistent improvement or degradation of the results. Another important insight is that the number of gravity ties must be chosen within a trade-off: either highest accuracies with gravity updates every 2 km requiring more time for observations or less dense gravity updates every 10 - 15 km with a loss in accuracy of 20 - 30 % in the VDs and 80 % in the SGD, see Table 4.23.

5.2 Conclusion

The initial goal of the Perth study (Schack et al., 2018) was to establish the first digital VD data set in the Southern Hemisphere and to assess the deviations from existing global and regional gravity field models in a region with a dynamic geoid shape, with one of the steepest geoid gradients worldwide. Apart from successfully evaluating and validating GGMplus, AGQG2009, and AGQG2017, the campaign also proved that with QDaedalus hardly any restrictions concerning transport, costs, or accuracy apply. It was even capable of detecting the prominent geophysical feature at the Darling Fault. Thus, the instrument is an immense gain for local gravity field determination and validation in remote areas. Concerning the data evaluation, it is pointed out again that comparing VDs defined in Helmert with Molodensky VDs needs accurate information about the terrain slope, especially in areas with large gravity disturbances.

Apart from that, QDaedalus qualified as a precise zenith camera that is applicable for terrestrial 3D-gravity profiling, where high-quality VDs have to be gathered with little preparation and effort.

The temperature calibration analyses of the RQH suggest to continuously calibrate the accelerometer biases and linear scale factors w.r.t. temperature-induced effects. A series of Up and Down calibrations every one or two months, to observe the bias and scale factor variations in more detail, could help to find out a reasonable time interval between calibrations.

The Roll and Pitch analyses showed that some accelerometer readings depend on the sensor orientation. But having revealed the ISA movement, a Roll and Pitch calibration as described in Ch. 4.2.2 is more or less useless when it is evaluated against the turntable readings since the sensor alignment w.r.t. the turntable is not constant. An alternative would be to use the gyroscope data to calculate the accelerometer orientation. Unfortunately, this approach is not very promising since the angular random walk/white noise of the gyroscopes is too large to resolve the ISA rotation presented in Figs. 4.11.

The strapdown rotation test was successfully applied to determine the source of the accelerometer non-orthogonality variations detected by the Up and Down calibration in 2019. It is a promising calibration scheme, although a very time-consuming approach, that cannot be performed frequently simply due to logistic and economical reasons. A comparison with the estimated linear scale factors from the Up and Down calibration in Fig. 4.17(a) suggests that both types of parameters can be determined similarly accurate with the much simpler and less time-consuming Up and Down calibration. However, the strapdown rotation yields more parameters, including asymmetric scale factors.

The results presented in this work demonstrate that the concept of terrestrial 3D-gravity profiling is capable of providing high-accuracy gravity disturbance profiles along any trajectory with varying sky-visibility (forest sections, village roads). The assessment of the Estergebirge campaign showed that the current instrument setup generates 3D-gravity profiles that compete with dedicated regional gravity field models. Thereby, it is essential to apply the profile refinement and temperature calibration parameters, especially for accelerometer non-orthogonalities and scale factors. Consequently, the profiles may help to validate existing gravity field models or to model gravity locally/regionally. This can be realized independently of external gravity information (with lower spatial resolution) or with the inclusion of the GGMplus in a gravity reduction step (with a spatial resolution of ~ 200 m).

As a trade-off for future campaigns, it is advised to provide VDs update points every 10 - 15 km and SGD update points every 2 km. The author would conduct a VD night session comprising three VD update points (20 - 30 km trajectory) with relative gravimeter measurements every 2 km. The IMU/GNSS measurements should be accomplished on a separate occasion, at least two times in both directions. The general advice concerning ZUPTs is to keep their number low and to assign each (planned or unexpected, e.g., red light) standstill phase as ZUPT for an EKF update. This approach helps to minimize the amount of dynamic start/stop-phases and to keep the measurement period short.

6 Outlook

The astrogeodetic campaign of Perth (Schack et al., 2018) is kind of a pioneering example for possible future VD campaigns. Local gravity field determination in terms of VD or height anomaly profiles with QDaedalus becomes realizable in nearly any terrain. Of course, such data can also be used to assess the local quality of existing gravity field models. Concerning the outcome of the campaign, for Perth a dedicated airborne gravimetry campaign along the coastal area could give deeper insights if the observed tilt in the gravity models is due to the different gravity data quality at the sea-land border. In Featherstone et al. (2019), the authors bring up vertical land motion as a cause of the tilts, which cannot definitely be resolved with the GPS and leveling approach applied in this paper. Another interesting study based on Ch. 4.3 of this work would be a terrestrial 3D-gravity profiling campaign along the traverse in Perth to compare results, but also along the coast, which would be helpful to study the origin of the tilts in the gravity field models in more detail.

Based on the outcome and discussion of Ch. 4.2, a calibration scheme is derived for the RQH that is supposed to yield robust calibration parameter estimates. First of all, the RQH temperature range can be limited to 30 - 50 °C operating temperature of the RQH for terrestrial campaigns⁵⁹, according to Fig. 4.21. A strapdown rotation test sequence should be passed for the highest and lowest temperature, to linearly interpolate the derived parameters afterward. The curves in Figs. 4.16(c), 4.16(d), and 4.17(b) justify a linear interpolation. The asymmetric linear scale factors, the non-orthogonalities of the accelerometer axes w.r.t. the MARS and the ISA misalignment w.r.t. the housing are of major interest since they cannot be determined otherwise. Additionally, the Up and Down calibration and the Roll and Pitch calibration are conducted for 30 °C, 35 °C, 40 °C, 45 °C, and 50 °C operating temperature, with roll and pitch angles <10°. With this strategy, the accelerometer biases and linear scale factors are robustly estimated from the Up and Down sequence. Subsequently, the determined calibration parameters can be applied to the Roll and Pitch data, which then allows the calibration of remaining orientation-dependent errors inside the accelerometer data.

The successful establishment of a system, including software and hardware that determines the gravity disturbance vector along the Earth's surface with high accuracy, was the ultimate goal of this thesis. The final thoughts address an outlook on follow-up analyses, on possible improvements of the results of the Estergebirge campaign, and on terrestrial as well as on airborne 3D-gravimetry.

Pending analyses

- Due to time restrictions, an analysis based on height anomaly differences, as for the Perth campaign, could not be finished. The accurate and dense VD reference data set would allow a meaningful analysis of the cumulative error from the models and the profiling data in a mountainous region.
- Regarding Fig. 4.28(d), it was stated that these differences are supposed to originate from deviations of the GGMplus density model from the real density. A location-based comparison with a geophysical data set regarding the local density distribution can give further insight.
- Assuming that absolute gravity values exist every 2 km as suggested by the author, it can be questioned, based on Fig. 4.28(d), if a combination of GGMplus together with these absolute values reaches similar results for the SGD as terrestrial 3D-gravity profiling.

⁵⁹ → measuring inside of a car, with a warm-up phase for the RQH, without parallel gravity measurements.

- One of the next investigations should be a verification of the lever arm, as it is a possible error source that affects the results depending on the driven direction. Several approaches are conceivable, but the author tends to augment the error-state vector inside the EKF for the lever arm components and possibly conduct a local maneuver (e.g., to drive off a large eight-figure) where the VDs can be considered constant.

Future improvements

- In hindsight, the author recommends correcting the ISA rotation w.r.t. the housing. Although it was concluded that this effect is not critical when providing enough VD update points, other error effects might get more apparent after removing the rotation. Additionally, the distance between update points might be increased.
- For future campaigns, the evaluation should be realized along the driven distance and not w.r.t. the latitude as it was possible along this north-south directed trajectory.
- Instead of performing the profile refinement according to Ch. 3.2, the gravity result of one run can be forwarded to the EKF to reduce gravity (instead of GGMplus) when processing the second run. However, in this case, the Gauß-Markov parameters have to be tuned accordingly, which might not be trivial.
- A promising possibility to improve the results would be the implementation of a tightly-coupled algorithm. By combining RQH and GNSS observations based on pseudo-ranges and pseudo-range rates, GNSS observations to less than four satellites can still contribute to the state estimation.
- To become even more independent of the required four GNSS satellites for a positioning solution, additional sensors can be added to the four standard instruments. As such, an odometer or a tiltmeter can provide update information in terms of distance and inclination to become more resilient to GNSS outages.

3D-gravimetry

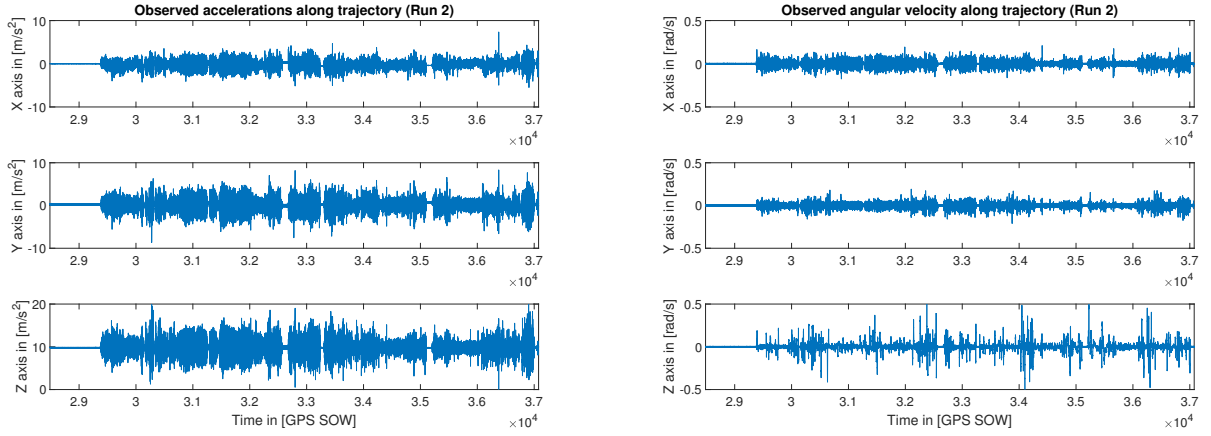
- In this thesis, the practical realization and evaluation of a terrestrial 3D-gravimetry concept yield precise VD and SGD profiles. The statistics reveal that the quality is comparable to profiles derived from dedicated regional gravity models. As mentioned before, certain enhancements will increase the quality and robustness of the concept even more. Thus, by following the recommendations of the author concerning the implementation and realization of future campaigns, the concept allows collecting high-quality data along defined trajectories, even in remote areas. This data can either help to validate existing gravimetric data sets or simply to provide new independent gravimetric information. Thereby, a validation of gravity models, airborne gravimetry campaigns, or GNSS leveling results is conceivable and e.g., a 3D-gravity profiling network that links existing gravity tie points might bring new and independent insights to local gravity studies. Hereby, the major advantage of the concept is its quick realization, its reliability through repeated measurements, and the geoid evaluation along profiles without the need for areal data. Such reliability can otherwise only be provided by dedicated local/regional gravity models or with lower resolution and more organizational efforts (at least for smaller areas), by airborne campaigns. Moreover, the concept would principally allow determining VDs, SGDs as well as height anomaly differences throughout a tunnel. Of course, the sacrifice of GNSS observations must be compensated by appropriate additional sensors.

-
- The uprise and employment of minimized high-quality inertial sensors/IMUs in combination with the advances in unmanned aerial vehicles brings new possibilities to 3D-gravimetry. Provided that an IMU with navigation-grade characteristics can be fixed to and flown by a copter system or a fixed-wing system with the ability of "vertical take-off and landing", the concept of this thesis can also be realized in an airborne scenario, including periodical landings near gravity tie points. In this case, the requirements w.r.t. certain error margins and the long-term stability of the applied IMU would be reduced. Table 4.23 indicates that especially the VDs quality would benefit if more than one gravity tie is provided throughout a campaign.

A Appendix

Raw RQH data

Raw inertial RQH observations of Run 2 are visualized in Figs. A.1. Run 2 does not include a detour or scheduled stops. The measurement took about 2.5 h. One can identify the alignment phase of about 15 min in the beginning, which is needed for the self-alignment of the RQH w.r.t. gravity (for roll and pitch) and the Earth's rotation axis (for yaw), to define \mathbf{R}_n^b from Eq. (2.3). The ZUPT periods are selected from these plots before the main processing is carried out. ZUPTs are identified where the acceleration amplitude in Fig. A.1(a) is significantly decreased for all three time series. The remaining parts represent the dynamics while driving superimposed by sensor noise. Except for the Z gyroscope, noise dominates the shape of the curves amplified by the dynamics. The overall amplitudes and ranges of the Z components are the largest, due to surface irregularities (accelerometer) and the curve shape of the trajectory (gyroscope). For the horizontal components, the Y accelerations are slightly larger than those of X, which states that the lateral dynamics, including amplified noise, are larger than the longitudinal ones. The X angular velocities slightly exceed those of Y, claiming that there is more rotation around the roll axis of the car than the pitch axis. The final VDs and SGDs are hidden inside the time series on the left with magnitudes smaller than 100 mGal or 0.001 m s^{-2} .



(a) Raw RQH accelerations.

(b) Raw RQH angular velocities.

Figure A.1: Raw inertial RQH observations (after manufacturer calibration) during Run 2 of the terrestrial 3D-gravity profiling campaign in the Estergebirge.

Scintrex CG-3 2005

Geodetic latitude [°]	Geodetic longitude [°]	Ellipsoidal height [m]	Absolute gravity [$\frac{m}{s^2}$]
47.559643	11.293605	865.40	9.8057864
47.556870	11.292568	868.53	9.8057810
47.553829	11.292427	873.86	9.8057742
47.552189	11.293138	876.76	9.8057694
47.550241	11.292694	879.45	9.8057605
47.547230	11.291149	883.09	9.8057516
47.544716	11.290639	886.14	9.8057447
47.542830	11.289448	888.34	9.8057377
47.540448	11.288450	897.38	9.8057150
47.538140	11.287179	917.40	9.8056733
47.536224	11.285749	928.62	9.8056403
47.533753	11.285342	939.29	9.8056088
47.532631	11.284608	941.34	9.8056029
47.530261	11.283983	941.95	9.8055913
47.527904	11.283984	944.95	9.8055715
47.523204	11.284602	912.66	9.8055947
47.519849	11.283713	914.11	9.8055771
47.517535	11.283786	913.09	9.8055711
47.515460	11.281446	914.73	9.8055641
47.513184	11.280390	918.49	9.8055508
47.511860	11.278449	919.45	9.8055473
47.509693	11.276048	921.85	9.8055399
47.508198	11.274615	924.05	9.8055331
47.506549	11.273137	925.61	9.8055265
47.505257	11.271824	926.31	9.8055239
47.503601	11.270484	928.28	9.8055198
47.502020	11.269707	935.19	9.8055045
47.500353	11.269596	940.40	9.8054906
47.498829	11.268359	955.08	9.8054582
47.497425	11.266798	970.41	9.8054262
47.495884	11.265471	973.11	9.8054184
47.493865	11.264126	985.46	9.8053907

Table A.1: Absolute gravity determined by the 2005 Scintrex CG-3 relative gravity campaign. Bold: Identical points of 2014 and/or 2019.

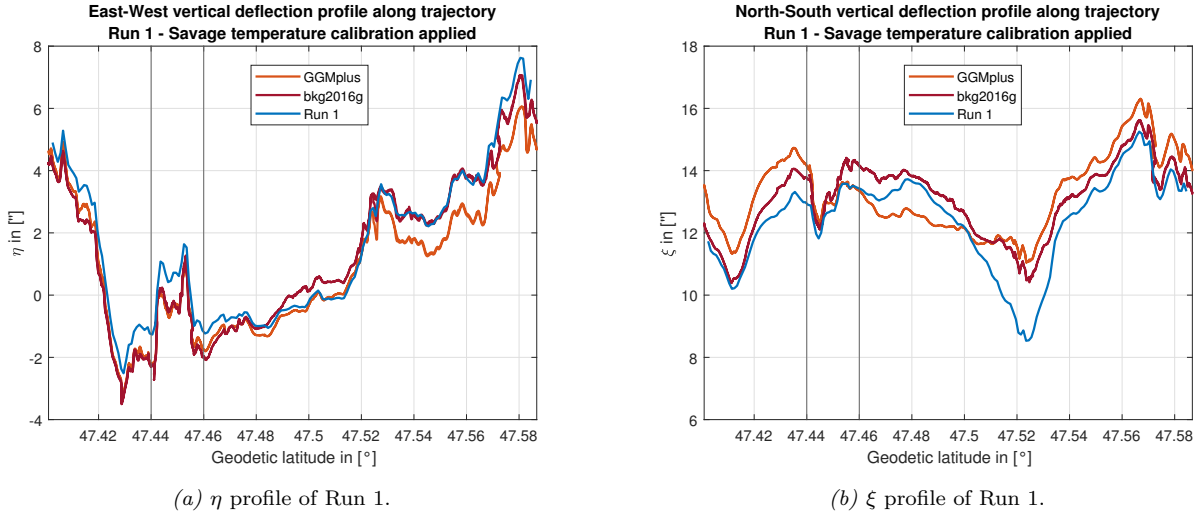
Scintrex CG-3 2014

Geodetic latitude [°]	Geodetic longitude [°]	Ellipsoidal height [m]	Absolute gravity [$\frac{m}{s^2}$]
47.5065485	11.2731371	925.61	9.80552566
47.5052569	11.2718236	926.31	9.80552335
47.4958837	11.2654706	973.11	9.80541782
47.4920937	11.2641736	990.99	9.80537723
47.4854760	11.2632190	1010.34	9.80532856
47.4837323	11.2636578	1020.84	9.80530220
47.4800991	11.2641375	1038.82	9.80525723
47.4782347	11.2642969	1036.41	9.80526767
47.4684589	11.2655207	1000.71	9.80533061
47.4632079	11.2656290	984.07	9.80536529
47.4486086	11.2662721	956.18	9.80536290
47.4326361	11.2599572	967.88	9.80524031
47.4244728	11.2573340	974.22	9.80519732

Table A.2: Absolute gravity determined by the 2014 Scintrex CG-3 relative gravity campaign. Bold: Identical points of 2005 and/or 2019.

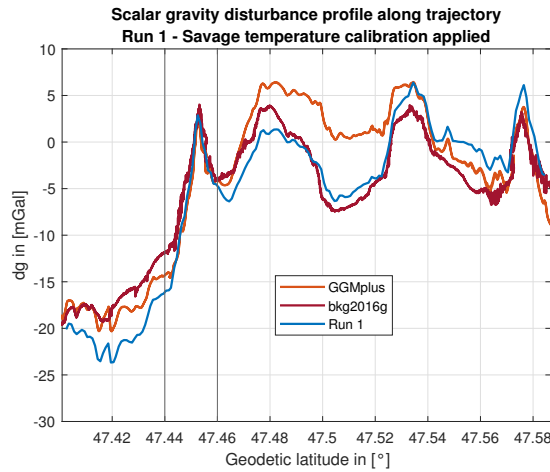
Profiles of Run 1

Figures A.2 show that the RQH offers reasonable data along the steep and curvy detour. The detour is marked by the two vertical black lines. In between, no reference data is available, but it becomes clear that the structure of GGMplus, bkg2016g, and Run 1 are very similar.



(a) η profile of Run 1.

(b) ξ profile of Run 1.



(c) dg profile of Run 1.

Figure A.2: η , ξ , and dg of Run 1 based on $Q \bullet \bullet \bullet$, with temperature correction and with gravity reduction by GGMplus. Here, the GGMplus and bkg2016g data are calculated along the trajectory of Run 1.

B Co-author confirmations

Co-author confirmation: Christian Hirt

12 December 2020

To whom it may concern,

Re: Schack, P., C. Hirt, M. Hauk, W.E. Featherstone, T.J. Lyon and S. Guillaume (2018) A high-precision digital astrogeodetic traverse in an area of steep geoid gradients and close to the coast of Perth, Western Australia, *Journal of Geodesy* 92(10): 1143-1153

This letter is to confirm Peter Schack's author contribution to the above manuscript as

- Campaign design, preparation and organisation: 25%
- Measurement campaign and computations: 33%
- Data analysis and interpretation: 25%
- Preparation and editing of text, figures and tables : 25%

This paper resulted from a collaborative project between Technische Universität München and Curtin University, titled "Gravity field validation in Australia using a German digital astronomical camera" and funded by DAAD (German Academic Exchange Service) Joint Research Cooperation Scheme.

This allowed Peter to visit Australia and conduct the night-time surveys. The paper was then written after his return to Germany.

Yours faithfully,



Dr. Christian Hirt
Hans-Fischer-Fellow of the Institute of Advanced Study, TU München

Co-author confirmation: Markus Hauk

12 December 2020

To whom it may concern,

Re: Schack, P., C. Hirt, M. Hauk, W.E. Featherstone, T.J. Lyon and S. Guillaume (2018) A high-precision digital astrogeodetic traverse in an area of steep geoid gradients and close to the coast of Perth, Western Australia, *Journal of Geodesy* 92(10): 1143-1153

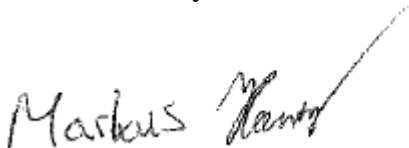
This letter is to confirm Peter Schack's author contribution to the above manuscript as

- Campaign design, preparation and organisation: 25%
- Measurement campaign and computations: 33%
- Data analysis and interpretation: 25%
- Preparation and editing of text, figures and tables : 25%

This paper resulted from a collaborative project between Technische Universität München and Curtin University, titled "Gravity field validation in Australia using a German digital astronomical camera" and funded by DAAD (German Academic Exchange Service) Joint Research Cooperation Scheme.

This allowed Peter to visit Australia and conduct the night-time surveys. The paper was then written after his return to Germany.

Yours faithfully,

A handwritten signature in black ink that reads "Markus Hauk". The signature is written in a cursive style with a long, sweeping flourish extending upwards and to the right.

Markus Hauk

Co-author confirmation: Will Featherstone



12 December 2020

To whom it may concern,

Re: Schack, P., C. Hirt, M. Hauk, W.E. Featherstone, T.J. Lyon and S. Guillaume (2018) A high-precision digital astrogeodetic traverse in an area of steep geoid gradients and close to the coast of Perth, Western Australia, *Journal of Geodesy* 92(10): 1143-1153

This letter is to confirm Peter Schack's author contribution to the above manuscript as

- Campaign design, preparation and organisation: 25%
- Measurement campaign and computations: 33%
- Data analysis and interpretation: 25%
- Preparation and editing of text, figures and tables : 25%

This paper resulted from a collaborative project between Technische Universität München and Curtin University, titled "Gravity field validation in Australia using a German digital astronomical camera" and funded by DAAD (German Academic Exchange Service) Joint Research Cooperation Scheme.

This allowed Peter to visit Australia and conduct the night-time surveys. The paper was then written after his return to Germany.

Yours faithfully,

Professor Will Featherstone
Professor of Geodesy

Co-author confirmation: Todd Lyon



12 December 2020

To whom it may concern,

Re: Schack, P., C. Hirt, M. Hauk, W.E. Featherstone, T.J. Lyon and S. Guillaume (2018) A high-precision digital astrogeodetic traverse in an area of steep geoid gradients and close to the coast of Perth, Western Australia, *Journal of Geodesy* 92(10): 1143-1153

This letter is to confirm Peter Schack's author contribution to the above manuscript as

- Campaign design, preparation and organisation: 25%
- Measurement campaign and computations: 33%
- Data analysis and interpretation: 25%
- Preparation and editing of text, figures and tables : 25%

This paper resulted from a collaborative project between Technische Universität München and Curtin University, titled "Gravity field validation in Australia using a German digital astronomical camera" and funded by DAAD (German Academic Exchange Service) Joint Research Cooperation Scheme.

This allowed Peter to visit Australia and conduct the night-time surveys. The paper was then written after his return to Germany.

Yours faithfully,

Todd Lyon

Co-author confirmation: Sébastien Guillaume

12 December 2020

To whom it may concern,

Re: Schack, P., C. Hirt, M. Hauk, W.E. Featherstone, T.J. Lyon and S. Guillaume (2018) A high-precision digital astrogeodetic traverse in an area of steep geoid gradients and close to the coast of Perth, Western Australia, *Journal of Geodesy* 92(10): 1143-1153

This letter is to confirm Peter Schack's author contribution to the above manuscript as

- Campaign design, preparation and organisation: 25%
- Measurement campaign and computations: 33%
- Data analysis and interpretation: 25%
- Preparation and editing of text, figures and tables : 25%

This paper resulted from a collaborative project between Technische Universität München and Curtin University, titled "Gravity field validation in Australia using a German digital astronomical camera" and funded by DAAD (German Academic Exchange Service) Joint Research Cooperation Scheme.

This allowed Peter to visit Australia and conduct the night-time surveys. The paper was then written after his return to Germany.

Yours faithfully,



Sébastien Guillaume

List of figures

2.1	RQH housing with cable port on the backside. The b-frame axes are marked on top with the X axis pointing in front direction, the Y axis to the left, and the Z axis upwards.	23
2.2	Allan deviations of static inertial measurement data exemplified by four static data sets. Thin-solid lines: X axis pointing downwards, RQH cold start. Thin-dashed lines: Z axis pointing upwards, RQH cold start. Thick-solid lines: X axis pointing downwards, RQH after warm-up. Thick-dashed lines: Z axis pointing upwards, RQH after warm-up. Accelerometer data is depicted in (a) and gyroscope data in (b).	26
2.3	Normalized autocorrelation of the RQH ISA sensors. The underlying data originates from the 30 h data set, where a calm period of ~ 5.5 h was selected.	27
2.4	Illustration of QDaedalus components (a) and operational setup (b).	29
2.5	Scintrex CG-5 relative gravimeter in operation, leveled via tripod.	30
3.1	Schematic overview of the terrestrial 3D-gravity profiling software. Theory components are linked in gray and the EKF sequence is depicted in more detail on the right side of the figure.	40
4.1	Study area in Perth, Western Australia. (a) Surface geology digitized from Davidson (1995) with elevations contoured from SRTM, (b) AGQG2017 height anomaly in meters, showing the steep east-west gradient (~ 70 ppm) due to the juxtaposition of the Perth Basin and Yilgarn Craton along the north-south Darling Fault, (c) AGQG2017 north-south VDs in arcsecond, (d) AGQG2017 east-west VDs in arcsecond. The astrogeodetic traverse is represented by black dots. (Schack et al., 2018)	59
4.2	VDs along the Perth traverse. Units in arcsecond. (a) north-south component ξ , (b) east-west component η . Astronomically measured VDs (black circles), GGMplus RCR-combination (magenta), and SRTM RCR-combination (blue). The large east-west VDs reflect the steep quasigeoid gradient in the Perth region due to the Darling Fault. (Schack et al., 2018)	62
4.3	VDs along the Perth traverse. Units in arcsecond. (a) north-south component ξ , (b) east-west component η . GGMplus-predicted deflections (blue), AGQG2009-predicted deflections (red), AGQG2017-predicted deflections (black), astronomically observed VDs (green). (Schack et al., 2018)	64
4.4	Differences between observed and modeled VDs. Units in arcsecond. (a) north-south component ξ , (b) east-west component η . (Schack et al., 2018)	64
4.5	(a) Height anomaly differences (in meters) along the Perth traverse from GGMplus (blue), AGQG2009 (red), AGQG2017 (black), and VD survey (green). (b) Differences between height anomalies (in meters) from the astronomical-topographical solution and from the models (GGMplus, AGQG2009, and AGQG2017). The height anomaly of each solution or model was set to zero at the beginning of the traverse. (Schack et al., 2018)	66
4.6	Gravity anomaly errors used in AGQG2017. Units in mGal. Rectangular projection. (Schack et al., 2018)	67
4.7	Sketch of the calibration scenario. In black the RQH is depicted with its b-frame indicated in blue. The gray parts abstract the two-axis calibration turntable. When $\theta_{[0]}$ and $\theta_{[1]}$ are set to 0 rad the platform is nominally leveled and the RQH X axis points southward (to the reader), the Z axis upwards, and the Y axis eastward.	69
4.8	Up and Down calibration: Averaged accelerometer output over temperature in six different orientations (each axis pointing up and down once) in 2017 and 2019.	71

4.9	Up and Down calibration: Accelerometer biases over temperature in 2017 and 2019.	72
4.10	Up and Down calibration: Accelerometer linear scale factors over temperature in 2017 and 2019.	73
4.11	Up and Down calibration: Accelerometer non-orthogonalities over temperature in 2017 and 2019.	74
4.12	Roll and Pitch calibration: RQH orientations during calibration, for all temperatures. The FLU-frame states that the roll and pitch rotations are assigned to the b-frame X and Y axes, respectively.	76
4.13	Roll and Pitch calibration: Accelerometer output (averaged values) over temperature for all orientations. Additionally, roll (left) and pitch (right) angles are clustered and color-coded.	79
4.14	Roll and Pitch calibration: Accelerometer biases and non-orthogonalities over temperature, based on all roll and pitch combinations during the calibration.	80
4.15	Strapdown rotation test: Gyroscope linear scale factors and cross-couplings over temperature.	83
4.16	Strapdown rotation test: Accelerometer parameters over temperature.	84
4.17	(a) Comparison of linear scale factors, determined with the Up and Down calibration and the strapdown rotation test, referenced to 10 °C. (b) Misalignments: ISA - RQH housing (relative).	86
4.18	Location of the terrestrial 3D-gravity profiling trajectory east of Garmisch-Partenkirchen, in the Estergebirge. The trajectory (red) starts at lake Walchensee towards Mittenwald and ends just north of the Austrian border. The map was created with the help of the "Bayern Atlas" and can be viewed online via https://v.bayern.de/Myxvg	87
4.19	Ellipsoidal heights and roll-pitch orientations of the RQH along the trajectory (both directions) in the Estergebirge.	89
4.20	VD and SGD autocorrelations of a complete measurement session (blue) and along the trajectory from south to north (red). The underlying data originates from GGMplus. Also included is a horizontal line at σ^2/e to determine the correlation distances and an empirical "intermediate" third-order Gauß-Markov model. The variance σ^2 and the Gauß-Markov β -values of the black curves for η , ξ , and dg are: $\sigma^2 = 5.33(\prime\prime)^2$; $1.61(\prime\prime)^2$; 69.83 mGal^2 and $\beta = \frac{2.903}{2.8} \text{ km}^{-1}$; $\frac{2.903}{2.6} \text{ km}^{-1}$; $\frac{2.903}{4.3} \text{ km}^{-1}$	90
4.21	RQH temperature sensor outputs during the three runs in the Estergebirge.	92
4.22	Inertial Explorer output: number of GNSS satellites used in solution and PDOP for Run 2.	93
4.23	Gravimetric and astrogeodetic observation points along the trajectory (red). Orange: VD observation points from 2005. Blue, green, and black: Relative gravimeter observation points from 2005, 2014, and 2019, respectively.	94
4.24	Modeled and observed 3D-gravity profiles along the trajectory (based on Run 2 in both directions). The observed values originate from the 2005 campaign for the VDs in (a) and (b) and from the 2005, 2014, and 2019 relative gravity measurements for the scalar component in (c). With the help of the 103 VD observations and the predicted SGDs, approximate maximum gradients for η , ξ , and dg were determined and added to the captions. Based on these values the EKF update standard deviations are linearly increased by 0 - 0.1" or 0 - 0.5 mGal when the horizontal distance between the GNSS antenna and the update point is 0 - 25 m. Above 25 m no update is initiated.	98
4.25	Initial 3D-gravity results of the three runs. On the left side, the RTS smoother output is visualized while on the right side the result after the profile refinement (Ch. 3.2) is depicted. No gravity reduction and no temperature correction were applied during the processing.	102

4.26	3D-gravity results of the three runs after first (left) and second (right) \mathbf{Q} -matrix adaptation. No gravity reduction and no temperature correction were applied during the processing.	104
4.27	3D-gravity results of the three runs, after applying the temperature calibration parameters (Ch. 4.2.3, Savage (2007)) to the RQH output. On the left side, no gravity reduction was applied during the processing.	106
4.28	3D-gravity results of the combination of Run 2 and 3 after applying the temperature calibration parameters (Ch. 4.2.3, Savage (2007)) to the RQH output (a-c). Additionally, the EKF/RTS contribution w.r.t. GGMplus is visualized (d).	108
A.1	Raw inertial RQH observations (after manufacturer calibration) during Run 2 of the terrestrial 3D-gravity profiling campaign in the Estergebirge.	123
A.2	η , ξ , and dg of Run 1 based on $\mathbf{Q} \bullet \bullet \bullet$, with temperature correction and with gravity reduction by GGMplus. Here, the GGMplus and bkg2016g data are calculated along the trajectory of Run 1.	126

List of tables

2.1	Descriptive sensor parameters of the Honeywell QA-2000 accelerometers (Dorobantu and Gerlach, 2004).	24
2.2	Descriptive sensor parameters of the Honeywell GG1320 gyroscopes (Dorobantu and Gerlach, 2004).	25
3.1	Error-state vector setup together with its mathematical notation and the selected physical units of the error-state vector and the error covariance information.	41
4.1	Descriptive statistics of the VDs along the Perth traverse: observed, GGMplus, AGQG-2009, and AGQG2017, and differences between the observations and models. Units in arcsecond. (Schack et al., 2018)	63
4.2	Descriptive statistics of the height anomaly differences along the traverse. Units in millimeter. (Schack et al., 2018)	66
4.3	Temperature stages for calibrations conducted in 2017 and 2019.	68
4.4	Upwards pointing b-frame axes and nominal turntable orientation angles during Up and Down calibration.	69
4.5	Upwards pointing accelerometer axes and nominal turntable orientation angles at the start of each sequence of the strapdown rotation test. Additionally, rotations executed during the calibration are listed in terms of the nominal b-frame rotation axis and angle.	81
4.6	Classification of Inertial Explorer standard deviations (σ) for each component of the GNSS positions of Run 2.	92
4.7	VDs and absolute gravity values based on the measurements that were performed in 2005 and on November 7, 2019. The standard deviation of the VDs is set to $\pm 0.25''$ and those of the absolute gravity values are empirically estimated with ± 0.1 mGal. Bold: Identical points of 2005 and/or 2014. Note: No. 7 and 12 got assigned with predicted VDs.	96
4.8	RMS errors of fictive constant profiles, GGMplus profiles, and bkg2016g profiles.	100
4.9	Definition of the square root of the diagonal matrix elements of \mathbf{P} and \mathbf{Q} . The accelerometer and gyroscope biases are modeled as first-order Gauß-Markov processes, while the gravity disturbance components are modeled as third-order Gauß-Markov processes (see Chs. 2.2.1.2 and 4.3.1). The entries of the latter are based on the autocorrelation analyses in Fig. 4.20.	101
4.10	Redefinition of the square root of the diagonal matrix elements of \mathbf{Q} for the attitude.	101
4.11	Redefinition of the square root of the diagonal matrix elements of \mathbf{Q} for the gravity disturbance.	103
4.12	RMS errors for all Runs without the gravity reduction applied in the EKF. The \mathbf{Q} -matrix entries correspond to Tables 4.9, 4.10, and 4.11.	109
4.13	RMS errors for all Runs with the gravity reduction applied in the EKF. The \mathbf{Q} -matrix entries correspond to Tables 4.9, 4.10, and 4.11.	109
4.14	Statistical summary of the 3D-gravity profiles based on GGMplus, bkg2016g, and the $\mathbf{Q}_{\bullet\bullet\bullet}$ temperature corrected solutions of the combination of Run 2 and 3. "w/" and "w/o" signify if a gravity reduction was applied in the EKF or not.	109
4.15	3D-gravity profiling RMS errors when adding a constant time offset to the RQH time tags before processing.	110
4.16	3D-gravity profiling RMS errors when manipulating the Euler angles after the initial alignment.	110

4.17	3D-gravity profiling RMS errors after manipulating the ISA geometry. X, Y, and Z represent the RQH b-frame axes pointing in front-, left-, and up-direction.	111
4.18	3D-gravity profiling RMS errors when introducing a wrong lever arm to the algorithm. X, Y, and Z represent the RQH b-frame axes pointing in front-, left-, and up-direction.	112
4.19	3D-gravity profiling RMS errors when adding a constant bias to the gyroscope observations. X, Y, and Z represent the RQH b-frame axes pointing in front-, left- and, up-direction.	112
4.20	3D-gravity profiling RMS errors when single temperature correction parameter types of the strapdown rotation test are not applied to the observations.	113
4.21	3D-gravity profiling RMS errors when standstill phases are not included as ZUPTs inside the EKF.	113
4.22	3D-gravity profiling RMS errors without correcting accelerometer observations for the geometric offset w.r.t. the b-frame origin.	113
4.23	3D-gravity profiling RMS errors with different amounts of gravity update points along the trajectory.	114
A.1	Absolute gravity determined by the 2005 Scintrex CG-3 relative gravity campaign. Bold: Identical points of 2014 and/or 2019.	124
A.2	Absolute gravity determined by the 2014 Scintrex CG-3 relative gravity campaign. Bold: Identical points of 2005 and/or 2019.	125

Bibliography

- M. Albayrak, C. Hirt, S. Guillaume, K. Halicioglu, M. Özlüdemir, and C. K. Shum. Quality assessment of global gravity field models in coastal zones: A case study using astrogeodetic vertical deflections in Istanbul, Turkey. *Studia Geophysica et Geodaetica*, 64:306–329, 2020. doi:10.1007/s11200-019-0591-2.
- D. W. Allan. Statistics of atomic frequency standards. *Proceedings of the IEEE*, 54(2):221–230, 1966. doi:10.1109/PROC.1966.4634.
- L. Bastos, P. Tomé, T. Cunha, M. J. Fernandes, and S. Cunha. Gravity anomalies from airborne measurements - experiments using a low cost IMU device. In *Gravity, Geoid and Geodynamics 2000*, pages 253–258, Berlin, Heidelberg, 2002. Springer Berlin Heidelberg. doi:10.1007/978-3-662-04827-6_42.
- D. Becker. *Advanced Calibration Methods for Strapdown Airborne Gravimetry*. PhD thesis, Technische Universität Darmstadt, Fachbereich Bau- und Umweltingenieurwissenschaften, Schriftenreihe der Fachrichtung Geodäsie Heft 51, 2016. ISBN 978-3-935631-40-2.
- D. Becker, J. E. Nielsen, D. Ayres-Sampaio, R. Forsberg, M. Becker, and L. Bastos. Drift reduction in strapdown airborne gravimetry using a simple thermal correction. *Journal of Geodesy*, 89(11): 1133–1144, 2015. doi:10.1007/s00190-015-0839-8.
- G. Boedecker, F. Leismüller, T. Spohnholtz, J. Cuno, and K. H. Neumayer. Tests Towards Strapdown Airborne Gravimetry. In *International Symposium on Kinematic Systems in Geodesy, Geomatics and Navigation*, pages 457–462, 1994.
- W. Bosch and H. Wolf. Über die Wirkung von topographischen Lokal-Effekten bei profilweisen Lotabweichungs-Prädiktionen. *Mitteilungen aus dem Institut für Theoretische Geodäsie der Universität Bonn*, 1974.
- B. Bürki. *Integrale Schwerefeldbestimmung in der Ivrea-Zone und deren geophysikalische Interpretation*. 40. Geodätisch-geophysikalische Arbeiten in der Schweiz, 1989. Schweizerische Geodätische Kommission.
- J. M. Brockmann, T. Schubert, T. Mayer-Gürr, and W.-D. Schuh. The Earth’s gravity field as seen by the GOCE satellite - an improved sixth release derived with the time-wise approach (GO_CONS_GCF_2_TIM_R6). *GFZ Data Services*, 2019. doi:10.5880/ICGEM.2019.003.
- C. G. Brown, K. Sarabandi, and L. E. Pierce. Validation of the Shuttle Radar Topography Mission height data. *IEEE Transactions on Geoscience and Remote Sensing*, 43(8):1707–1715, 2005. doi:10.1109/TGRS.2005.851789.
- R. G. Brown and P. Y. C. Hwang. *Introduction to Random Signals and Applied Kalman Filtering*. John Wiley & Sons, Inc., 2012. 4th edition.
- W. A. Davidson. Hydrogeology and groundwater resources of the Perth region, Western Australia. *Curtin University of Technology, School of Applied Geology*, 1995. PhD thesis.
- R. Deurloo, L. Bastos, and M. Bos. On the use of UAVs for Strapdown Airborne Gravimetry. In *Geodesy for Planet Earth*, pages 255–261, 2012. ISBN 978-3-642-20338-1. doi:10.1007/978-3-642-20338-1_31.

-
- R. Dorobantu and C. Gerlach. Investigation of a Navigation-Grade RLG SIMU type iNAV-RQH. Technical report, Institut für Astronomische und Physikalische Geodäsie / Forschungseinrichtung Satellitengeodäsie, 2004.
- M. R. Drinkwater, R. Floberghagen, R. Haagmans, D. Muzi, and A. Popescu. GOCE: ESA's first Earth Explorer Core Mission. 17, 2003. doi:10.1007/978-94-017-1333-7_36.
- B. Eissfeller. *Analyse einer geodätischen raumstabilisierten Inertialplattform und Integration mit GPS*. PhD thesis, Universität der Bundeswehr München, Studiengang Vermessungswesen, Schriftenreihe Heft 37, 1989.
- M. El-Diasty and S. Pagiatakis. Calibration and Stochastic Modelling of Inertial Navigation Sensor Errors. *Journal of Global Positioning Systems*, 7(2):170–182, 2008.
- N. El-Sheimy, H. Hou, and X. Niu. Analysis and Modeling of Inertial Sensors Using Allan Variance. *IEEE Transactions on Instrumentation and Measurement*, 57(1):140–149, 2008. doi:10.1109/TIM.2007.908635.
- W. E. Featherstone. On the use of Australian geodetic datums in gravity field determination. *Geomatics Research Australasia*, 62:17–36, 1995. ISSN 13249983.
- W. E. Featherstone and D. D. Lichti. Fitting gravimetric geoid models to vertical deflections. *Journal of Geodesy*, 83(6):583–58, 2009. doi:10.1007/s00190-008-0263-4.
- W. E. Featherstone and J. M. Rüeger. The importance of using deviations of the vertical in the reduction of terrestrial survey data to a geocentric datum. *The Trans-Tasman Surveyor*, 1(3): 46–61, 2000. doi:10.1080/00050326.2000.10440341 [Erratum in *The Australian Surveyor* 47(1): 7] 10.1080/00050356.2002.10558836.
- W. E. Featherstone, J. F. Kirby, C. Hirt, M. S. Filmer, S. J. Claessens, N. J. Brown, G. Hu, and G. M. Johnston. The AUSGeoid09 model of the Australian Height Datum. *Journal of Geodesy*, 85(3):133–150, 2011. doi:10.1007/s00190-010-0422-2.
- W. E. Featherstone, J. C. McCubbine, N. J. Brown, S. J. Claessens, M. S. Filmer, and J. F. Kirby. The first Australian gravimetric quasigeoid model with location-specific uncertainty estimates. *Journal of Geodesy*, 92(2):149–168, 2018. doi:10.1007/s00190-017-1053-7.
- W. E. Featherstone, T. J. Lyon, and J. C. McCubbine. Potentially Misleading GPS Leveling–Based Assessment of Gravimetric Geoid or Quasigeoid Models due to Vertical Land Motion and Different GPS Processing Software. *Journal of Surveying Engineering*, 145(4), 2019.
- I. Fischer, M. Slutsky, F. Shirley, and P. W. III. New pieces in the picture puzzle of an astrogeodetic geoid map of the world. *Bulletin Géodésique*, 88(1):199–221, 1968. doi:10.1007/BF02525661.
- F. Flechtner, K.-H. Neumayer, C. Dahle, H. Dobsław, E. Fagiolini, J.-C. Raimondo, and A. Güntner. What Can be Expected from the GRACE-FO Laser Ranging Interferometer for Earth Science Applications? *Surveys in Geophysics*, 37:453–470, 2016. doi:10.1007/s10712-015-9338-y.
- J. Flury. *Schwerefeldfunktionale im Gebirge Modellierungsgenauigkeit, Messpunktdichte und Darstellungsfehler am Beispiel des Testnetzes Estergebirge*. PhD thesis, Deutsche Geodätische Kommission Reihe C, 2002.
- J. Flury. Relativistic geodesy. *Journal of Physics: Conference Series*, 723:012051, 2016. doi:10.1088/1742-6596/723/1/012051.

-
- R. Forsberg. A study of terrain reductions, density anomalies and geophysical inversion methods in gravity field modelling. *Department of Geodetic Science and Surveying, Ohio State University, Columbus, USA*, Report 355, 1984.
- R. Forsberg, A. A. Vassiliou, K. P. Schwarz, and R. V. C. Wong. Inertial gravimetry - a comparison of Kalman filtering-smoothing and post-mission adjustment techniques. *Bulletin Géodésique*, 60(2): 129–142, 1986. doi:10.1007/BF02521013.
- C. Förste, S. L. Bruinsma, O. Abrikosov, J.-M. Lemoine, J. C. Marty, F. Flechtner, G. Balmino, F. Barthelmes, and R. Biancale. EIGEN-6C4 The latest combined global gravity field model including GOCE data up to degree and order 2190 of GFZ Potsdam and GRGS Toulouse. *GFZ Data Services*, 2014. doi:10.5880/icgem.2015.1.
- J. G. Fryer. The Australian Geoid. *The Australian Surveyor*, 24(4):203–214, 1972. doi:10.1080/00050326.1972.10440630.
- A. Gelb. *Applied Optimal Estimation*. The M.I.T. Press, 1974. ISBN 978-0-262-20027-1.
- C. Gerlach, R. Dorobantu, and M. Rothacher. A Testbed for Airborne Inertial Geodesy: Terrestrial Gravimetry Experiment by INS/GPS. *Proceedings-CD, IAG Symposium on Gravity, Geoid and Space Missions (GGSM 2004)*, 2004.
- C. Gerlach, R. Dorobantu, and M. Rothacher. Results of a combined INS/GPS experiment for geodetic application. *Navigation (Paris)*, 53(212):31–47, 2005. ISSN 0028-1530.
- C. Gerlach, R. Dorobantu, C. Ackermann, N. Kjörsvik, and G. Boedecker. Gravimetri med treghetssystemer: Oversikt og testresultater - Gravimetry with Inertial Navigation Systems: Overview and Test Results. *KART OG PLAN*, 70:46–59, 2010a. ISSN 0047-3278.
- C. Gerlach, R. Dorobantu, C. Ackermann, N. S. Kjörsvik, and G. Boedecker. Preliminary Results of a GPS/INS Airborne Gravimetry Experiment Over the German Alps. *Gravity, Geoid and Earth Observation, Springer Berlin Heidelberg*, pages 3–9, 2010b. doi:10.1007/978-3-642-10634-7_1.
- C. L. Glennie, K. P. Schwarz, A. M. Bruton, R. Forsberg, A. V. Olesen, and K. Keller. A comparison of stable platform and strapdown airborne gravity. *Journal of Geodesy*, 74(5):383–389, 2000. doi:10.1007/s001900000082.
- P. D. Groves. *Principles of GNSS, inertial, and multisensor integrated navigation systems*. Artech house, 2008.
- S. Guillaume. *Determination of a Precise Gravity Field for the CLIC Feasibility Studies*. PhD thesis, Eidgenössische Technische Hochschule ETH Zürich, Switzerland, 2015.
- S. Guillaume, B. Bürki, S. Griffet, and H. Mainaud-Durand. QDaedalus: Augmentation of total stations by CCD sensor for automated contactless high-precision metrology, 2012. URL http://fig.net/resources/proceedings/fig_proceedings/fig2012/papers/ts09i/TS09I_guillaume_buerki_et_al_6002.pdf. Accessed: 2020-12-05.
- M. Hauk. Erprobung des astrogeodätischen Messsystems QDaedalus zur Bestimmung von genauen Lotabweichungen. Master thesis, Technical University of Munich, 2014.
- M. Hauk, C. Hirt, and C. Ackermann. Experiences with the QDaedalus system for astrogeodetic determination of deflections of the vertical. *Survey Review*, 49(355):294–301, 2016. doi:10.1080/00396265.2016.1171960.

-
- W. A. Heiskanen and H. Moritz. *Physical geodesy*. W.H. Freeman, San Francisco, 1967.
- F. R. Helmert. *Die mathematischen und physikalischen Theorien der höheren Geodäsie*. Teubner, Leipzig (reprint Minerva, Frankfurt a.M. 1961), 1880/1884.
- C. Hirt. Monitoring and analysis of anomalous refraction using a digital zenith camera system. *Astronomy and Astrophysics*, 459(1):283–290, 2006. doi:10.1051/0004-6361:20065485.
- C. Hirt and J. Flury. Astronomical-topographic levelling using high-precision astrogeodetic vertical deflections and digital terrain model data. *Journal of Geodesy*, 82(4-5):231–248, 2008. doi:10.1007/s00190-007-0173-x.
- C. Hirt and G. Seeber. High-Resolution Local Gravity Field Determination at the Sub-Millimeter Level using a Digital Zenith Camera System. In: Tregoning P., Rizos c. (eds) *Dynamic Planet. International Association of Geodesy Symposia*. Springer, 130:316–321, 2007. doi:10.1007/978-3-540-49350-1_47.
- C. Hirt, H. Denker, J. Flury, A. Lindau, and G. Seeber. Astrogeodetic validation of gravimetric quasigeoid models in the German Alps – first results. *Proc. First Int. Symp. of the International Gravity Field Service*, pages 84–89, 2007. Istanbul, Turkey, 28. Aug.- 01. Sept. 2006, Harita Dergisi, 18.
- C. Hirt, U. Feldmann-Westendorff, H. Denker, J. Flury, C.-H. Jahn, A. Lindau, G. Seeber, and C. Voigt. Hochpräzise Bestimmung eines astrogeodätischen Quasigeoidprofils im Harz für die Validierung des Quasigeoidmodells GCG05. *Zeitschrift für Vermessungswesen*, page 133:108–119, 2008.
- C. Hirt, B. Bürki, A. Somieski, and G. Seeber. Modern determination of vertical deflections using digital zenith cameras. *Journal of Surveying Engineering*, 136(1):1–12, 2010a. doi:10.1061/(ASCE)SU.1943-5428.0000009.
- C. Hirt, U. Marti, B. Bürki, and W. E. Featherstone. Assessment of EGM2008 in Europe using accurate astrogeodetic vertical deflections and omission error estimates from SRTM/DTM2006.0 residual terrain model data. *Journal Geophysical Research– Solid Earth*, 115(B10), 2010b. doi:10.1029/2009JB007057.
- C. Hirt, M. Schmitz, U. Feldmann-Westendorff, G. Wübbena, C.-H. Jahn, and G. Seeber. Mutual validation of GNSS height measurements from high-precision geometric-astronomical levelling. *GPS Solutions*, 15(2):149–159, 2011. doi:10.1007/s10291-010-0179-3.
- C. Hirt, S. J. Claessens, T. Fecher, M. Kuhn, R. Pail, and M. Rexer. New ultra-high resolution picture of Earth’s gravity field. *Geophysical Research Letters*, 40(16):4279–4283, 2013. doi:10.1002/grl.50838.
- B. Hofmann-Wellenhof and H. Moritz. *Physical Geodesy*. Springer-Verlag Vienna, 2006. doi:10.1007/978-3-211-33545-1.
- B. Hofmann-Wellenhof, K. Legat, and M. Wieser. *Navigation - Principles of Positioning and Guidance*. Springer-Verlag Wien NewYork, 2003. doi:10.1007/978-3-7091-6078-7.
- Honeywell. Q-Flex QA-2000 Single Axis Quartz Accelerometer, a. URL <https://aerospace.honeywell.com/en/learn/products/sensors/qa-2000-single-axis-quartz-accelerometer>. Accessed: 2020-12-29.

-
- Honeywell. GG1320AN Digital Ring Laser Gyroscope, b. URL <https://aerospace.honeywell.com/en/learn/products/sensors/gg1320an-digital-ring-laser-gyroscope>. Accessed: 2020-12-29.
- H. Jamil, M. Kadir, R. Forsberg, A. Olesen, M. N. Isa, S. Rasidi, A. Mohamed, Z. Chihat, E. Nielsen, F. Majid, K. Talib, and S. Aman. Airborne geoid mapping of land and sea areas of East Malaysia. *Journal of Geodetic Science*, 7(1):84–93, 2017. doi:10.1515/jogs-2017-0010.
- C. Jekeli. Airborne vector gravimetry using precise, position-aided inertial measurement units. *Bulletin G eod esique, Springer-Verlag*, 69(1):1–11, 1994. doi:10.1007/BF00807986.
- C. Jekeli. An analysis of vertical deflections derived from high-degree spherical harmonic models. *Journal of Geodesy*, 73(1):10–22, 1999. doi:10.1007/s001900050213.
- C. Jekeli. *Inertial Navigation Systems with Geodetic Applications*. Walter der Gruyter, Berlin, New York, 2001. ISBN 3-11-015903-1.
- C. Jekeli. Airborne Gradiometry Error Analysis. *Surveys in Geophysics*, 27:257–275, 2006. doi:10.1007/s10712-005-3826-4.
- C. Jekeli and J. H. Kwon. Results of airborne vector (3-d) gravimetry. *Geophysical Research Letters*, 26(23):3533–3536, 1999. doi:10.1029/1999GL010830.
- C. Jekeli and X. Li. INS/GPS Vector Gravimetry Along Roads in Western Montana. *The Ohio State University*, Report No. 477, 2006.
- T. E. Jensen. *Airborne Strapdown Gravity Measurements for Geodesy and Geophysics*. PhD thesis, Technical University of Denmark, National Space Institute, 2018.
- F. Johann, D. Becker, M. Becker, R. Forsberg, and M. Kadir. The Direct Method in Strapdown Airborne Gravimetry - a Review. *zfv – Zeitschrift f ur Geod sie, Geoinformation und Landmanagement*, 5:323–333, 2019. doi:10.12902/zfv-0263-2019.
- F. Johann, D. Becker, M. Becker, and E. S. Ince. Multi-Scenario Evaluation of the Direct Method in Strapdown Airborne and Shipborne Gravimetry. In *Proceedings of the 5th IAG Symposium on Terrestrial Gravimetry: Static and Mobile Measurements. International Association of Geodesy Symposia*. Springer, 2020. accepted.
- E. T. Knickmeyer. *Vector Gravimetry by a Combination of Inertial and GPS Satellite Measurements*. PhD thesis, University of Calgary, Department of Surveying Engineering, Report No.20035, 1990.
- V. N. Koneshov, M. I. Evstifeev, I. B. Chelpanov, and O. M. Yashnikova. Methods for Determining Deflections of the Vertical on a Moving Base. *Gyroscopy and Navigation, Pleiades Publishing*, 7(4): 326–336, 2016. doi:10.1134/S2075108716040076.
- C. Kotsakis. A study on the reference frame consistency in recent Earth gravitational models. *Journal of Geodesy*, 83(31), 2009. doi:10.1007/s00190-008-0227-8.
- J. Kouba and P. H eroux. Precise Point Positioning Using IGS Orbit and Clock Products. *GPS Solutions*, 5(2):12–28, 2001. doi:10.1007/PL00012883.
- J. Kuipers. *Quaternions and rotation sequences: a primer with applications to orbits, aerospace, and virtual reality*. Princeton University Press, 1999. ISBN 0-691-05872-5.

-
- A. Lawrence. *Modern Inertial Technology - Navigation, Guidance and Control*. Second Edition. Springer-Verlag, 1998. ISBN 0-387-98507-7.
- X. Li. *Moving Base INS/GPS Vector Gravimetry on a Land Vehicle*. PhD thesis, The Ohio State University, Geodetic Science and Surveying, Report No. 486, 2007.
- X. Li, J. Crowley, S. Holmes, and Y. Wang. The contribution of the GRAV-D airborne gravity to geoid determination in the Great Lakes region. *Geophysical Research Letters*, 43(9):4358–4365, 2016. doi:10.1002/2016GL068374.
- I. M. Longman. Formulas for Computing the Tidal Accelerations Due to the Moon and Sun. *Journal of Geophysical Research*, 64(12), 1959. doi:10.1029/JZ064i012p02351.
- U. Marti. *Geoid der Schweiz 1997*. 56. Geodätisch-geophysikalische Arbeiten in der Schweiz, 1997. Schweizerische Geodätische Kommission.
- M. F. Middleton, A. Long, S. A. Wilde, M. Dentith, and B. A. Evans. A preliminary interpretation of deep seismic reflection and other geophysical data from the Darling Fault zone, Western Australia. *Exploration Geophysics*, 24(3-4):711–717, 1993. doi:10.1071/EG993711.
- H. Moritz. Geodetic Reference System 1980. *Journal of Geodesy*, 74(1):128–133, 2000. doi:10.1007/s001900050278.
- A. Noureldin, T. B. Karamat, and J. Georgy. *Fundamentals of Inertial Navigation, Satellite-based Positioning and their Integration*. Springer, 2013. ISBN 978-3-642-30465-1.
- N. K. Pavlis, S. A. Holmes, S. C. Kenyon, and J. K. Factor. The development and evaluation of the Earth Gravitational Model 2008 (EGM2008). *Journal of Geophysical Research - Solid Earth*, 117(b4), 2012. doi:10.1029/2011JB008916.
- N. K. Pavlis, S. A. Holmes, S. C. Kenyon, and J. K. Factor. Correction to "The development and evaluation of the Earth Gravitational Model 2008 (EGM2008)". *Journal of Geophysical Research - Solid Earth*, 118(b5):2633–2633, 2013. doi:10.1002/jgrb.50167.
- S. Petrovic, F. Barthelmes, and H. Pflug. Airborne and Shipborne Gravimetry at GFZ with Emphasis on the GEOHALO Project. In *IAG 150 Years*, pages 313–322, 2016. ISBN 978-3-319-30895-1. doi:10.1007/1345_2015_17.
- H. E. Rauch, F. Tung, and C. T. Striebel. Maximum Likelihood Estimates of Linear Dynamic Systems. *AIAA Journal*, 3(8):1445–1450, 1965. doi:10.2514/3.3166.
- C. Reigber, P. Schwintzer, and H. Lühr. The CHAMP geopotential mission. *BOLLETTINO DI GEOFISICA TEORICA ED APPLICATA*, 40(3-4):285–289, 1999.
- D. T. Sandwell, R. D. Müller, W. H. F. Smith, E. Garcia, and R. Francis. New global marine gravity model from Cryosat-2 and Jason-1 reveals buried tectonic structure. *Science*, 346(6205):65–67, 2014. doi:10.1126/science.1258213.
- P. G. Savage. *Strapdown Analytics*. Strapdown Associates, Inc., 2007. 2nd edition, Part 1 and 2.
- P. Schack, C. Hirt, M. Hauk, W. E. Featherstone, T. J. Lyon, and S. Guillaume. A high-precision digital astrogeodetic traverse in an area of steep geoid gradients close to the coast of Perth, Western Australia. *Journal of Geodesy*, 92(10):1143–1153, 2018. doi:10.1007/s00190-017-1107-x.

-
- U. Schirmer, J. Schwabe, G. Liebsch, and H. Denker. DHHN2016 Die Erneuerung des Deutschen Haupthöhennetzes und der einheitliche integrierte geodätische Raumbezug 2016. Documentation, Arbeitsgemeinschaft der Vermessungsverwaltungen der Länder der Bundesrepublik Deutschland, Arbeitskreis Raumbezug, Projektgruppe "Erneuerung des DHHN", 2018. URL <http://www.adv-online.de/AdV-Produkte/Integrierter-geodaetischer-Raumbezug/broker.jsp?uCon=b7f20578-49e8-7961-f5a6-4d2601fa2e0c&uBasVariant=11111111-1111-1111-1111-111111111111>. Accessed: 2020-12-05.
- K. P. Schwarz and Y. C. Li. What can airborne gravimetry contribute to geoid determination? *Journal of Geophysical Research – Solid Earth*, 101(8):17873–17881, 1996. doi:10.1029/96JB00819.
- K. P. Schwarz and M. Wei. *INS/GPS Integration for Geodetic Applications*. Department of Geomatics Engineering - University of Calgary, 2001. Lecture Notes ENGO 623 (Copy at IAPG).
- Scintrex Limited. CG-5 Scintrex Autograv System - Operation Manual - Revision 8, 2017. URL https://scintrexltd.com/wp-content/uploads/2017/02/CG-5-Manual-Ver_8.pdf. Accessed: 2020-12-04.
- E.-H. Shin and N. El-Sheimy. A New Calibration Method for Strapdown Inertial Navigation Systems. *Zeitschrift Vermessungswesen*, 127(1):1–10, 2002.
- D. A. Smith, S. A. Holmes, X. Li, S. Guillaume, Y. M. Wang, B. Bürki, D. R. Roman, and T. M. Damiani. Confirming regional 1 cm differential geoid accuracy from airborne gravimetry: The geoid slope validation survey of 2011. *Journal of Geodesy*, 87(10-12):885–907, 2013. doi:10.1007/s00190-013-0653-0.
- S. Stoll. Reaktivierung des Testgebietes Estergebirge. Bachelor's thesis, Technische Universität München, 2014. Lehrstuhl für Astronomische und Physikalische Geodäsie.
- B. Tapley, S. Bettadpur, M. Watkins, and C. Reigber. The Gravity Recovery and Climate Experiment: Mission overview and early results. *Geophysical Research Letters*, 31:4 PP., 2004. doi:10.1029/2004GL019920.
- P. J. G. Teunissen and O. Montenbruck. *Springer Handbook of Global Navigation Satellite Systems*. Springer International Publishing, 2017. ISBN 978-3-319-42926-7. doi:10.1007/978-3-319-42928-1.
- W. Torge and J. Müller. *Geodesy*. De Gruyter, Berlin/Boston, 2012. 4th Edition.
- C. van Loan. Computing Integrals Involving Matrix Exponential. *Transactions on Automatic Control*, AC-23(3):395–404, 1978. doi:10.1109/TAC.1978.1101743.
- S. Vignudelli, A. Kostianoy, P. Cipollini, and J. Benveniste. *Coastal altimetry*. Springer, Berlin, Heidelberg, 2011. doi:10.1007/978-3-642-12796-0.
- C. Voigt. *Astrogeodätische Lotabweichungen zur Validierung von Schwerefeldmodellen*. PhD thesis, Deutsche Geodätische Kommission C 702, München, 2013.
- C. Voigt and H. Denker. Validation of second generation GOCE gravity field models by astrogeodetic vertical deflections. *In: IAG Proceedings*, 139:291–296, 2013. doi:10.1007/978-3-642-37222-3_38.
- C. Voigt, H. Denker, and C. Hirt. Regional astrogeodetic validation of GPS/levelling data and quasi-geoid models. *in: Sideris, M. G. (ed.) Observing Our Changing Earth, Springer, Berlin*, pages 413–420, 2009.

-
- Y. M. Wang, C. Becker, G. Mader, D. Martin, X. Li, T. Jiang, S. Breidenbach, C. Geoghegan, D. Winester, S. Guillaume, and B. Bürki. The Geoid Slope Validation Survey 2014 and GRAV-D airborne gravity enhanced geoid comparison results in Iowa. *Journal of Geodesy*, 2017. doi:10.1007/s00190-017-1022-1.
- A. Watts. *Isostasy and Flexure of the Lithosphere*. Cambridge University Press, Cambridge, 2001.
- M. Wei and K. P. Schwarz. Flight test results from a strapdown airborne gravity system. *Journal of Geodesy*, 72(6):323–332, 1998. doi:10.1007/s001900050171.
- J. Wendel. *Integrierte Navigationssysteme - Sensordatenfusion, GPS und Inertiale Navigation*. Oldenbourg Verlag München, 2011. ISBN 978-3-486-70439-6.
- R. Wielen, H. Schwan, C. Dettbarn, H. Lenhardt, H. Jahrei, and R. Jhrling. Sixth Catalogue of Fundamental Stars (FK6). *Astronomisches Rechen-Institut Heidelberg*, Part I, Basic Fundamental Stars with Direct Solutions(35), 1999.
- R. Yu, S. Cai, M. Wu, J. Cao, and K. Zhang. An SINS/GNSS Ground Vehicle Gravimetry Test Based on SGA-WZ02. *Sensors*, 15(9):23477–23495, 2015. doi:10.3390/s150923477.
- J. F. Zumberge, M. B. Hefflin, D. C. Jefferson, M. M. Watkins, and F. Webb. Precise point positioning for the efficient and robust analysis of GPS data from large networks. *Journal of Geophysical Research - Solid Earth*, 102(B3):5005–50017, 1997. doi:10.1029/96JB03860.